Cyclic steam oxidation of a steel for biomass power plant application

UNIVERSITY OF BIRMINGHAM

By

REBECCA-LOUISE MOBBS

A thesis submitted to the

University of Birmingham

for the degree of

DOCTOR OF ENGINEERING

Department of Metallurgy and Materials

College of Engineering and Physical Sciences

University of Birmingham

February 2018

UNIVERSITY OF
BIRMINGHAM

University of Birmingham Research Archive

e-theses repository

This unpublished thesis/dissertation is copyright of the author and/or third parties. The intellectual property rights of the author or third parties in respect of this work are as defined by The Copyright Designs and Patents Act 1988 or as modified by any successor legislation.

Any use made of information contained in this thesis/dissertation must be in accordance with that legislation and must be properly acknowledged. Further distribution or reproduction in any format is prohibited without the permission of the copyright holder.

In loving memory of my Mom,
Wendy Mobbs
27/03/1966 – 17/05/2013

Abstract

Austenitic stainless steels are commonly used as heat exchanger tubing in coal fired power plants. As a result, this class of steels have been optimised to withstand high temperatures and pressures. However, under these conditions, the alloy will experience oxidation which greatly affects the lifetime of the materials. The increased likelihood of more cyclic operating conditions means a greater level of understanding of the oxidation and spallation behaviour of these alloys is required. High temperature oxidation studies available in the literature principally have an emphasis on isothermal oxidation of flat plates rather than curved surfaces representative of boiler tubing.

The isothermal and cyclic steam oxidation and spallation behaviour of TP347H FG has been studied in this thesis. Electron microscopy and elemental characterisation showed the oxide encompasses an inner Fe-Cr-Ni spinel and an outer magnetite layer. A haematite layer forms during the initial stages of oxidation in air-saturated steam conditions similar to the oxides formed in plant conditions.

The use of a novel technique, termed STORME, made it possible to identify the chemistry of the spalled oxide and also allowed calculations of the interfacial fracture energy to be made and the mechanism for spallation to be identified. Modelling of the spallation observed enables predictions of spallation behaviour to be made.

Acknowledgements

Endless gratitude is given to my supervisors Professor Hugh Evans and Dr Mary Taylor, both for their academic support and emotional support at difficult times. Without their continued care and encouragement over the last four years this thesis would not exist.

My appreciation is also extended to Professor Paul Bowen for helping me to overcome certain obstacles throughout my EngD and Dr Steve Osgerby for valuable discussions throughout the course of the project.

I am grateful for the help and technical support given by Andy Bradshaw, Dave Price, Tim Perry and Chris Cooper. Rengen Ding is also thanked for his TEM help and skills.

Thanks are also given to Gary Newbolt for assistance with MATLAB coding, Danial Khoshkou and Tom Reynolds for extensive oxidation chats, Johnathon Morrison for all that he continuously helped me with and Fiona Schulz for offering support through difficult times. I am also thankful to the office for making the last couple of years enjoyable.

Finally, I would like to thank my father, Paul Mobbs, and husband, Robert Clarke for never giving up on me and encouraging me to pursue my dreams even when it felt impossible.

Publications

The following paper was produced for publication in a peer reviewed journal:

- The Effect of Thermal Cycling on Steam Oxidation Behaviour of TP347H FG at 650 °C, R-L. Mobbs, S. Osgerby, M. P. Taylor, H. E. Evans, Materials at High Temperatures, 2018, 35: 1-3, pp. 291-298.

Table of Contents

List of Figures

List of Tables

List of Abbreviations and Nomenclature

BCC	Body Centred Cubic
FCC	Face Centred Cubic
HCP	Hexagonal Close Packed
TTT	Time Temperature Transformation
CCT	Continuous Cooling Transformation
SEM	Scanning Electron Microscope
TEM	Transmission Electron Microscope
EDS	Energy Dispersive X-Ray Spectroscopy
WDS	Wavelength Dispersive X-Ray Spectroscopy
XRD	X-Ray Diffraction
STORME	Simultaneous Thermographic and Optical Recording Media Examination
MRS	Micro-Raman Spectroscopy
AFM	Atomic Force Microscopy
BSE	Back Scattered Electron
SE	Secondary Electron
at.%	Atomic percent
wt.%	Weight percent
C_0	Concentration in equilibrium with the vapour pressure/ at.%
C_S	Surface concentration/ at.%
C_B	Bulk concentration/ at.%
t	Time/ s
erfc	Error function complement
x	Distance from the surface/ m
α	Transfer coefficient/ $m.s^{-1}$
h	Substrate thickness/ m
t_D	Time at which delamination occurs/ s
t_{SP}	Time at which complete localised spallation occurs/ s
T	Temperature/ K
R	Radius of spalled site/ m
ξ	Oxide thickness/ m
γ_F	Fracture energy/ $J.m^{-2}$
ΔT_d	Oxidation temperature – delamination temperature
ΔT_p	Oxidation temperature – propagation temperature
ΔT_{SP}	Oxidation temperature – spallation temperature
ΔT_b	Temperature drop required to initiate buckle
ΔT_w	Temperature drop required to initiate wedging
ΔT_{ub}	Temperature drop required to initiate unstable buckling
CTE, α	Coefficient of Thermal Expansion/ K^{-1}
α_{ox}	Coefficient of thermal expansion of the oxide
α_m	Coefficient of thermal expansion of the metal
E_{ox}	Young's modulus/ Pa
σ	Stress
σ_{ox}	Stress within the oxide

ε	Strain
v	Poisson's ratio
D	Diffusion coefficient/ $m^2.s^{-1}$
D_{eff}	Effective diffusion coefficient/ $m^2.s^{-1}$
k_n	Rate constant
k_p	Parabolic rate constant
k_l	Linear rate constant
p_{O_2}	O partial pressure

Chapter 1 – Introduction

Understanding the effect of steam containing environments on the oxidation behaviour of austenitic stainless steels is important for several industries including power generation, petrochemical and aerospace industries. Of particular interest is the steam side of heat exchanger tubes in power plant boilers since the prediction of scale integrity is an important objective in corrosion studies. Severe spallation in boiler tubing leads to tube blockages and erosion of turbine blades which can result in tube overheating and ruptures [1], [2].

The increased demand for greener energy in the UK has sparked further interest in utilising biomass as a fuel. However, it is thought that biomass power plants will not be used for baseload operation and will therefore become more cyclic in nature. The effect of cyclic loading on the oxidation and spallation behaviour of the inner surface of superheater and reheater tubing, i.e. steam side, is not fully understood.

This thesis explores the steam oxidation and spallation behaviour of an austenitic stainless steel, TP347H FG, under isothermal and cyclic conditions at 923 K for superheater and reheater applications through the use of a novel technique developed during the Eng.D. The effect of Cr depletion on the cyclic oxidation behaviour was also studied.

Chapter 2 – Literature Review

2.1. Biomass in the Energy Industry

2.1.1. Introduction

As the demand for energy in the UK continues to grow, so too does the threat to our energy security. The rate at which conventional fossil fuels are being used is higher than that at which reserves are being discovered. There is therefore, an ever increasing need to diversify away from coal, oil and natural gas, and move towards a more renewable future. The possible impact of climate change, as a result of high carbon dioxide emissions, has further intensified the desire for a greener energy mix. Biomass energy has the potential to satisfy both of these aspirations. The UK government have set targets to meet 15% of the energy demand from renewables by 2020 [3]. Of this 15%, biomass will make up a large proportion.

Biomass can be described as material resulting from living or once living organisms and includes agricultural wastes, animal residues and sewage, and is the most common form of renewable energy. For millions of years humans have been utilising biomass as a fuel, burning wood for heat and cooking purposes. The third world still widely utilise this form of fuel but in recent years it has been more widely used in the western world. Motivation for the increased use of biomass in Europe stems from firstly, the technological developments in crop production and conversion into usable fuels, commonly wood pellets, sawdust and straw bales etc. As a result of this progression, biomass can be used to generate heat and power at a lower cost and higher efficiency than was possible before. Secondly, the surplus production of food

crops in the US and Europe and related policies associated with reducing the surplus has led to the production of energy crops being more desirable [4]. Thirdly, and probably most importantly, the threat of climate change has had a major influence over the use of biomass as an energy source.

2.1.2. Biomass Versus Conventional Fossil Fuels

Utilising biomass as an energy source has several advantages over conventional resources such as oil and gas, and has the possibility of using the existing infrastructure from coal fired plants. However, changing the type of fuel used in the plant will alter some of the plant characteristics and will, for instance, have an effect on steam flow rates and temperature of the steam. This will have some impact on alloy performance and subsequently affect the efficiency.

One of the major benefits of biomass is the renewability. When efficiently processed, biomass can be termed as carbon neutral. It is a cyclical method and so the same amount of carbon released into the atmosphere during combustion is then absorbed by new plant growth. Fossilised biomass on the other hand releases new CO_2 into the atmosphere that has been stored as a hydrocarbon for millions of years. Because fossil fuels take so long to form, they cannot be considered as renewable in terms of a usable time-scale.

However, despite its renewability and carbon neutrality, there is one major disadvantage for using biomass as an alternative to conventional fuels and that is in its energy density by volume. Typical house coal has energy densities in the range of 6400-7300 $kWh.m^{-3}$ whereas wood only has an energy density in the region of 2100-3200 $kWh.m^{-3}$ [5]. More biomass has to be burned in order to achieve the same

amount of energy as you would from burning coal which increases the amount that has to be burnt and also transported.

As already mentioned, there are different forms of biomass that can all be used to produce energy and these can be split into four main groups; woody plants, herbaceous plants/ grasses, aquatic plants, and manures. Determining the most appropriate type of biomass for different end uses requires the consideration of several properties:

- Moisture content (intrinsic and extrinsic)
- Calorific value
- Proportions of fixed carbon and volatiles
- Ash/ residue content
- Alkali metal content
- Cellulose/ lignin ratio

There are several ways in which biomass can be converted into energy and the method used depends on the type of biomass being converted, the end requirement for the biomass, environmental factors, and economic conditions [6]. It is normally the end requirement of the energy that dictates which conversion process is most suitable.

Altering the fuel will also affect the operation of the plant including operating temperature and loading with biomass plants expecting to operate under more cyclic loading conditions. The focus of the work presented in this thesis was steam side of the heat exchanger tubing. Although the fuel does not come into direct contact with this area of the plant, the cyclic loading conditions will have consequences for the

behaviour and lifetime of the material. It is therefore important to consider all implications that could arise from modifying operational conditions.

2.2. Materials

2.2.1. Microstructure of Steel

The origin of good thermal and electrical conductivity in a metal comes from the free movement of valance electrons that are attracted to positive metal ions. The ions within a metal will arrange themselves to minimise the amount of - - and + + repulsions and maximise the number of - + attractions, hence reducing the level of entropy. This rearrangement therefore can lead to different structures being formed. The crystal structure that Fe takes is dependent on temperature and treatment processes which in turn will dictate the properties of the material. The following Section summarises the structures that Fe and steel can form and the properties associated with each of them with emphasis being placed on the microstructure and properties relevant to the main alloy used in this project. The three most common crystal structures for metals are body centred cubic, face centred cubic and hexagonal close packed, each of which are shown in Figure 2-1.

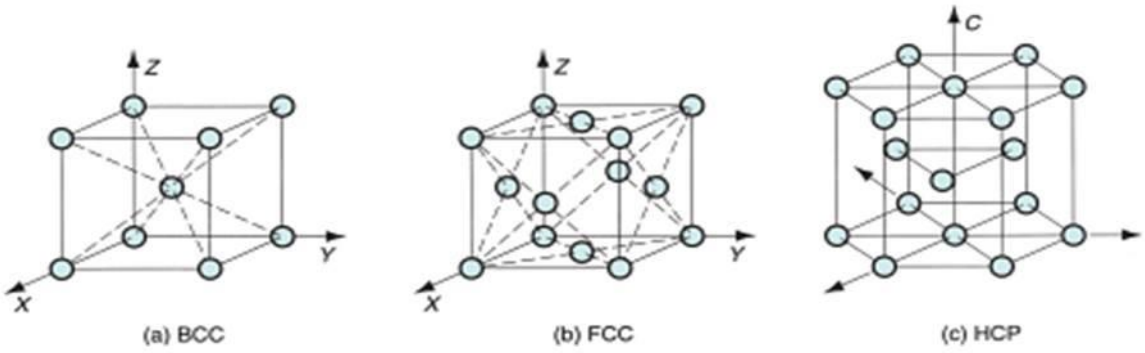

Figure 2-1 Schematic representation of three types of metallic crystal structure: a) Body centred cubic (BCC) b) face centred cubic (FCC) and c) hexagonal close packed (HCP) [6].

Steel is formed through the addition of carbon to Fe on interstitial sites which has the effect of strengthening. Different types of steel are classified according to carbon content since differing compositions result in behavioural differences. The Fe carbon phase diagram can be seen in Figure 2-2 [7] which was calculated with Thermocalc software, coupled with PBIN database.

The solubility of carbon in Fe is dependent on temperature and crystal structure. Below 912 °C, i.e. in the α-ferrite form, a maximum of 0.02 wt.% carbon is soluble in Fe at 738 °C (A_1 on Figure 2-2). This is due to the carbon atoms being located on interstitial sites where the atom is approximately twice as large as the interstitial space leading to a strong local strain field surrounding the carbon atom. As can be seen from the phase diagram shown below in Figure 2-2, α-ferrite is stable at room temperature, up to temperatures of 912 °C and takes the BCC form. Above this temperature the FCC crystal structure, γ-austenite is stable up to temperatures of 1394 °C and a maximum of 2.14 wt.% carbon is soluble in Fe up to this point. This phase is not stable below the eutectoid temperature of 912 °C unless cooled rapidly to room temperature. The difference in solubility of carbon in Fe in these two phases is due to the interstitial sites available for carbon to occupy which is dependent on the packing of the Fe ions in the lattice, i.e. the crystal structure. There are two possible interstitial sites; the tetrahedral site which, when occupied is surrounded by four atoms, or the octahedral site which is surrounded by six atoms. It is possible to calculate the size of the interstitial spaces hence determining how large an atom can be accommodated without causing distortion of the lattice. For a close packed crystal lattice such as FCC or HCP, the largest atom diameter that can be accommodated is 0.568 Å and 1.044 Å in the tetrahedral and octahedral sites, respectively. Carbon

atoms are 1.54 Å in diameter and so to cause minimal distortion they prefer to be located on octahedral sites in FCC. In the body centred cubic crystal lattice however, carbon atoms prefer to occupy tetrahedral sized spaces. Despite the closer packing seen in the FCC structure compared to BCC, the octahedral sites are larger. Hence, carbon is more soluble in γ-Fe than α-Fe. Above the upper limit of the austenite region at 1394 °C, Fe again forms the BCC crystal structure and is known as δ-ferrite. This phase is stable only at high temperatures and will begin to melt at 1538 °C. Another phase that can be seen in the phase diagram is Fe_3C known as cementite. This forms when there is excess carbon and the solubility of carbon in Fe has reached its maximum. Below 738 °C a reaction of γ → α + Fe_3C occurs which is known as pearlite [8].

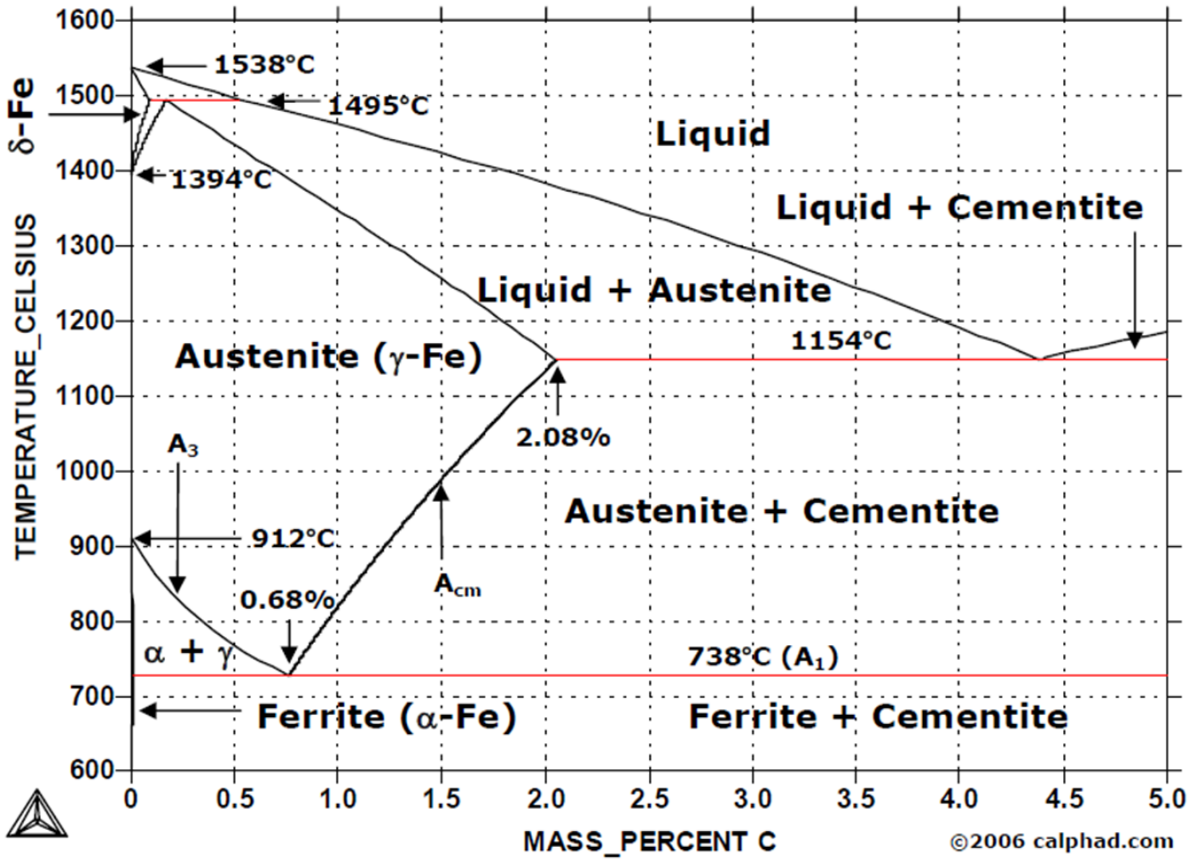

Figure 2-2 Fe-C phase diagram [7].

Time-Temperature-Transformation, 'TTT', curves such as the one seen in Figure 2-3 for 316 austenitic stainless steel, of similar composition to the alloy of interest for this work [9], shows the kinetics of isothermal transformations and are obtained through rapid quenching of the steel to the desired temperature followed by the measurement of the constituent volume fraction [8]. Such a curve is applicable to the alloy of interest in this study where the suppliers water quenched the steel subsequent to a heat treatment of 1473 °C. TTT curves are mainly used to interpret the behaviour of austenite for a particular heat treatment which then allows predictions to be made as to which treatment is required to form a desirable microstructure [10]. The main disadvantage of a TTT diagram is that the composition of the alloy is required.

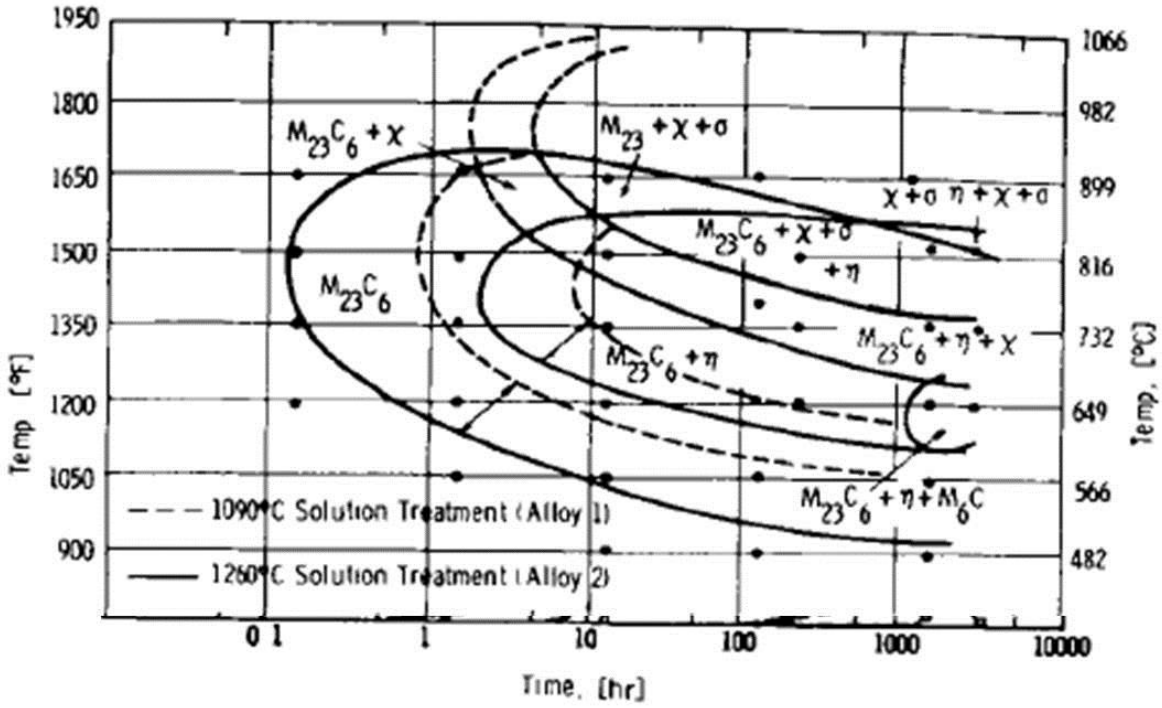

Figure 2-3 Time-temperature-transformation diagram of 316 austenitic stainless steel [9].

The position of the curve can be altered by alloying elements. For instance, the addition of Ni, an austenite stabiliser, moves the position of the ferrite line down and to the right, i.e. the temperature at which the transformation occurs is decreased and the time to nucleation is increased. The addition of Cr on the other hand has the opposite effect since it is a ferrite stabiliser. The effect of alloying additions will be discussed in further detail in Section 2.2.2. The effect of austenite and ferrite forming elements is demonstrated with the use of a Schaeffler diagram [11] such as that shown in Figure 2-4 [12]. As can be seen here, large amounts of Cr can eradicate the austenite phase at all temperatures, i.e. an increase in the ratio of Cr_{eq}:Ni_{eq} increases the preference for ferrite formation.

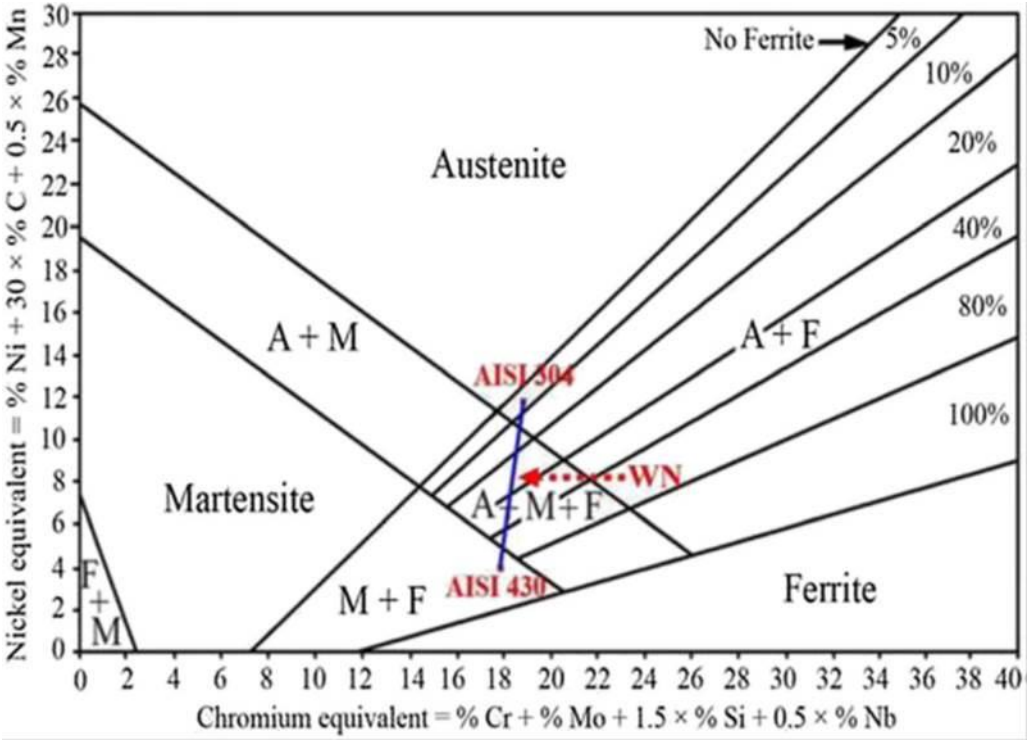

Figure 2-4 Example of a Schaeffler diagram [12].

2.2.1.1. Ferritic Steels

Ferritic Fe, which is also known as ferrite and is denoted by α on a phase diagram, Figure 2-2, possesses a body centred cubic (BCC) crystal structure at room temperature and is stable up to 1183 K. At this temperature pure Fe transforms to austenite and possesses an FCC crystal structure. At 1663 K Fe will revert back to the BCC form and is known as δ-ferrite. This high temperature phase is stable up to the melting temperature of 1809 K.

Adding carbon to Fe is a well-established method in steel making and it is used for its abilities to improve strength. Further details of alloying elements and their effects on materials properties will be given later in Section 2.2.2. As already mentioned above, the carbon content of α-Fe is low, with a maximum of 0.02 wt.%. The improvement of

strength and hardness is not able to be achieved through heat treatments for ferritic steels [13].

Metals used in commercial applications tend to be alloyed with other elements to improve the overall properties. Ferritic stainless steels typically contain between 11 and 17 wt.% Cr and little to no Ni.

This class of alloys have good tensile strength [10], [14] and good creep strength at temperatures below 823 K but also exhibit poor oxidation resistance in steam because of their lower Cr contents relative to austenitic steels, as demonstrated later.

2.2.1.2. Austenitic Steels

Austenitic steels possess a face centred cubic (FCC) crystal structure and typically contain between 0.08 and 2.14 wt.% carbon as shown in Figure 2-2 [9], although they can contain much less, down to 0.01 wt.% such as those shown in Table 2-1. The compositions of some common austenitic alloys are given in Table 2-1. These materials are able to be used over a wide range of temperatures due to their higher Cr content [10], i.e. increased oxidation resistance. The application of cold work, i.e. deformation at low temperature [15], can significantly increase strength [16], Table 2-2. This is due to the difficulty in generation and movement of these dislocations through the FCC lattice. Generally austenitic steels have poor thermal conductivity and increased thermal expansion coefficients compared to ferritic and martensitic alloys [17]. As a result, the oxide layer formed has a tendency to spall which could mean that austenitic steels are not able to withstand cyclic oxidation as well as ferritic steels whose thermal expansion coefficients are not as high, see Table 2-2. A move to biomass energy and more cyclic operating conditions could therefore

cause problems in terms of oxide scale spallation which is the main motivation for this work.

Austenitic steels can also undergo stress corrosion cracking if the corrosion resistance is not adequate enough for the environment in which it is being used. Elements such as Cr and Si are therefore added or the composition of Cr and Si are increased to increase oxidation resistance. This will be discussed in further detail in Sections 2.2.2 and 2.3. Another weakness with this class of materials is that they are only able to endure fatigue at around 30% of the tensile strength compared to ferritic steels which can endure up to 60% of its tensile strength [16].

This particular class of alloy is more expensive compared to ferritic steels due to the increased Ni content, but have an increased oxidation resistance and so tend to be used in the hotter Sections of the superheater and reheater tubing in power plants where oxidation resistance is an important consideration. However, in the nuclear industry where oxidation resistance is important, ferritic steels are used because of their high strength properties.

Austenitic stainless steel TP347H FG, where TP is tube piping, H is high carbon and FG is fine-grained, was used in this thesis, the composition of which is shown in Table 2-1 [18]. FG is used to denote the alloy is different to the coarse-grained counterpart TP347H. This particular alloy is commonly used as heat exchanger tubing in coal fired power plants that are expected to be converted to biomass power plants. The material is manufactured through hot extrusion followed by cold finishing. Finally, solution annealing is carried out followed by quenching to form the

fine-grained structure. The finished product is a seamless steel tube formed through cold-drawing or cold-rolling processes [19].

Table 2-1 Nominal compositions of common austenitic alloys (wt.%).

Alloy	Fe	C	Cr	Ni	Mn	Si	Cu	Mo	N	Other
TP347H FG [18]	bal	0.1	18	10	1.5	0.6	-	-	-	Trace amounts S, P
Super 304H [20]	bal	0.1	18	9	0.8	0.2	3	-	0.1	0.1 Co
304L [21]	bal	0.015	19.0	10.0	1.0	0.38	-	-	0.05	-
HR3C [20]	bal	0.01	25	20.0	2.0	0.75	-	-	-	-
1714CuMo [22]	bal	0.11	15.8	13.7	0.74	0.51	3.07	1.83	-	-
800H [22]	Bal	0.09	21.15	32.31	1.21	0.5	-	-	-	0.5 Ti, 0.48 Al

2.2.1.3. Martensitic steels

In order to increase the solubility of carbon in Fe the metal must be heated to its austenitic phase. Martensitic steel, which exhibits a fine needle like structure and possesses a body centred tetragonal crystal structure [10], is then formed when the metal is quenched rapidly and the austenitic field does not have time for diffusion-controlled decomposition processes to occur [8]. During the transformation process laths are formed in order to reduce the strain energy present as a result of the transformation. Whether or not the transformation is complete depends on the quench medium used, the start and finish temperature of the martensite and the composition of the material. Typical quenching mediums for martensitic transformations include oil and water. It is possible to control the start and finish temperatures of martensite through the addition of alloying elements which also enables the fraction of martensite formed to be controlled. As-quenched martensitic steels are rarely used in industrial applications because of their brittle nature and high dislocation density. Tempering is used to increase the toughness which unfortunately has a negative effect on the hardness but means these materials have more use in industry since the brittle nature has been reduced.

Table 2-2 Typical values of mechanical properties for ferritic, austenitic and martensitic steels.

	Ferritic	Austenitic	Martensitic
Tensile Strength (MPa)	416-540 [10], [14]	600 [10], [23]	570-1850 [10], [14]
Thermal expansion coefficients ($x10^{-6}$ K^{-1})	12-13 [24]	18.1 [10]	9.5-12 [24]
Thermal conductivity (W m^{-1} K^{-1})	23-28 [25]	13.8 [10]	26-29 [25]
Hardness (Hv)	150 – 270 [10], [14], [26]	150-185 [23], [26]	252 [14]
Yield Strength (MPa)	240-483 [26]	200-2000 [16], [26]	276-1089 [27]
Elongation (%)	20-30 [26]	1-60 [26]	20-34 [25]
Fatigue Strength (MPa)		110-210 [28]	170-330 [28]
Reduction of area of fracture (%)	30-45 [25]	35-45 [25]	40-65 [25]

2.2.2. Effect of Alloying Elements on Microstructure and Properties of Stainless Steel

Table 2-3 shows common alloying elements and the effect of such additions on steels. Materials used as superheater and reheater tubing in power plants are exposed to aggressive environments with high temperatures and pressures and corrosive atmospheres. As a result of the harsh operating conditions, elements are added to the steel in order to improve oxidation resistance, creep strength and toughness. The following Section gives details about the elements found in commonly used austenitic stainless steels and the effect they have on the microstructure and properties of the steel. More detail has been given on the elements found in TP347H FG which is the material used throughout this study. Elements such as copper and aluminium which are found in other austenitic steels such as Super 304 H have also been included in the table below.

Table 2-3 Properties of typical alloying elements [29].

Element	Properties
Carbon (C)	Increases strength and hardness.
Nickel (Ni)	Austenite former responsible for providing toughness and strength and also increases resistance to oxidation.
Chromium (Cr)	Ferrite former which increases oxidation resistance through the formation of a protective chromia layer.
Copper (Cu)	Produces precipitation hardening properties and enhances corrosion resistance.
Silicon (Si)	Improves steam oxidation resistance and can be used as a ferrite stabiliser.
Molybdenum (Mo)	Gives increased strength, minimises temper brittleness.
Vanadium (V)	Can induce secondary hardening.
Tungsten (W)	Reduces grain size and stabilises ferrite.
Manganese (Mn)	Improves hot working properties. Increases strength, toughness and hardenability. Austenite forming element.
Titanium (Ti)	Useful for carbide stabilisation.
Niobium (Nb)	Carbide stabilisation.
Aluminium (Al)	Increases oxidation resistance and is known as a ferrite stabiliser.

2.2.2.1. Carbon

Small amounts of carbon are added to stainless steel to increase strength. In austenitic stainless steels carbon is normally found in quantities of around 0.08 wt.%.

Carbon can be incorporated in the alloy at interstitial sites where it improves the strength of the steel through solid solution strengthening.

Carbon is also able to combine with Fe to form Fe carbide, also known as cementite, when it precipitates out of the matrix resulting in precipitation strengthening. As the time at temperature increases, Fe is replaced by other alloying elements such as Mo, Cr and V [30]. Precipitation hardening is brought about by a specific heat treatment whereby a metastable supersaturated solid solution is produced resulting in precipitate formation via diffusion of solute atoms. During the diffusion stage, when the precipitate is undergoing the transition to be coherent, the parent metal lattice experiences strain, hampering dislocations, hence strengthening the metal [31].

Other common carbide precipitates found in steels include $M_{23}C_6$, where M = Cr, MC, where M = Nb, Ta or W, M_7C_3, where M = Fe, Cr , M_6C, where M = Fe, Mo and W, and M_3C where M = W, some of which provide precipitation strengthening in the same way as cementite. These precipitates however can lead to other issues. $M_{23}C_6$ commonly precipitates on grain boundaries and as a result ‘provides favourable nucleation sites for creep damage’ [32]. Also to note is that after long exposure times at high temperature, precipitates begin to coarsen due to transformation to Z phase resulting in decreased levels of strengthening [32], [33].

Creep strength is also improved with the presence of carbon in amounts higher than 0.04 wt.% where carbides of niobium, NbC, are formed through interactions of dislocations that are brought on by creep [34]. Niobium is therefore added because of its ability to readily form carbides and nitrides. NbC carbides make the steel stronger through precipitate hardening. Niobium has a stronger affinity for carbon than Cr

does and so it prevents Cr carbide formation. Since the addition of carbon results in an increase in strength, and increased strength means reduced ductility, it is only possible to achieve good levels of ductility at lower carbon levels [10].

2.2.2.2. Chromium

Cr is a ferrite stabiliser and at most temperatures will lead to Fe having a ferritic microstructure, as shown in Figure 2-5. It was mentioned earlier in Section 2.2.1 that a critical concentration of Cr can be reached in which an austenite phase is no longer able to be formed.

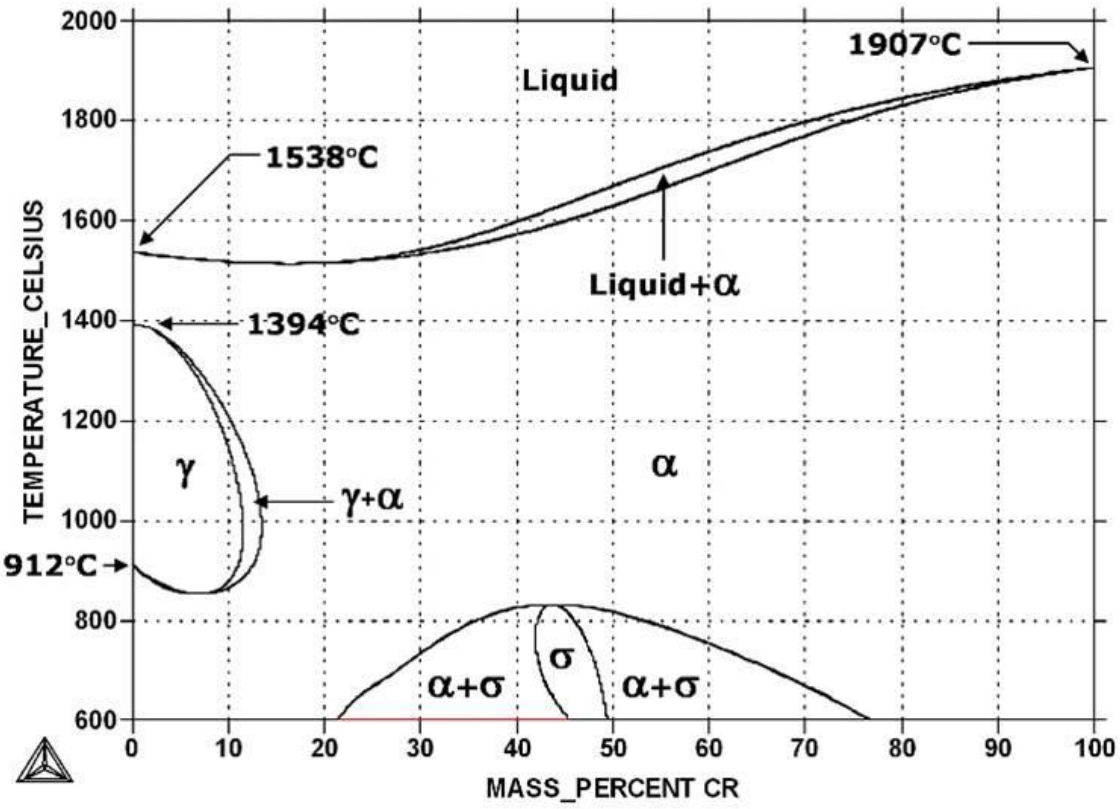

Figure 2-5 Fe-Cr phase diagram [35] where γ is austenite phase, α is ferrite phase and σ is an intermetallic FeCr compound.

Cr is added to stainless steels to provide resistance against oxidation and corrosion through the formation of a thin, stable Cr_2O_3 layer which prevents further oxidation [10]. This is evident in Figure 2-6 which shows that oxide thickness decreases with increasing Cr content as a function of time for various steels in a water vapour/ steam environment, [21], [36], [37].

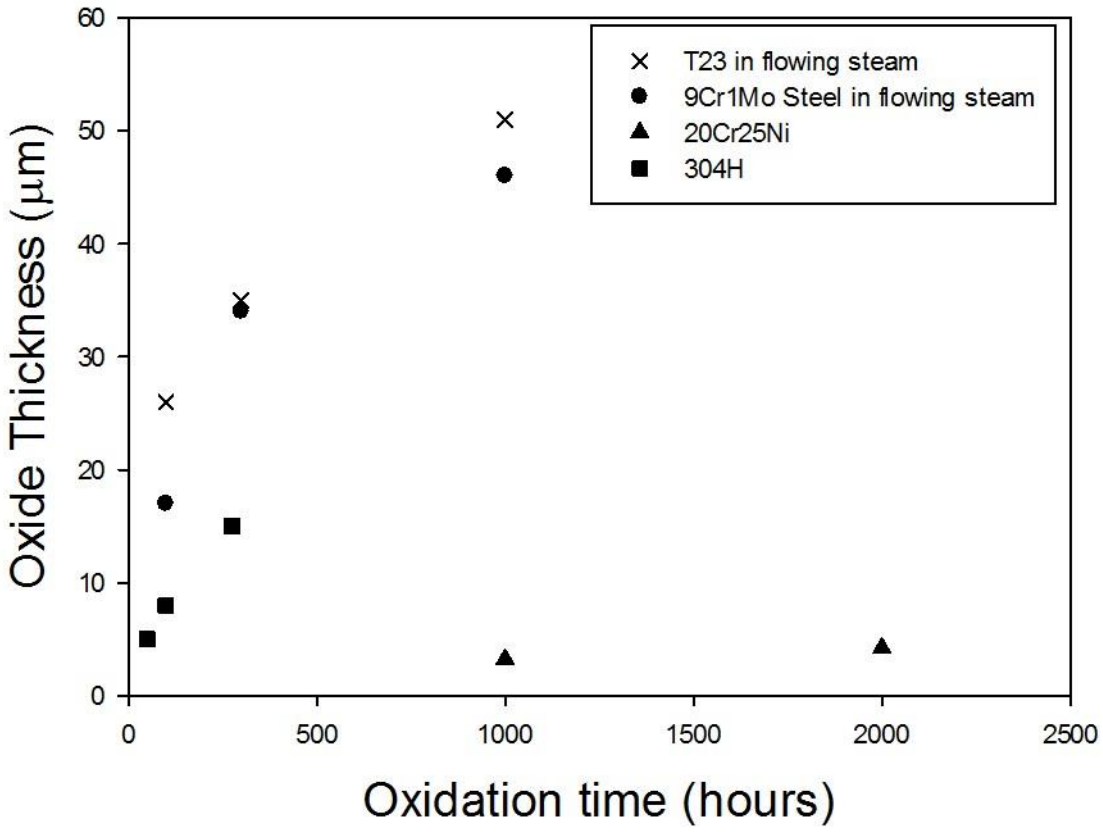

Figure 2-6 Oxide thickness as a function of time for T23 (2.25Cr) in flowing steam at 823 K [36], 9Cr1Mo steel in flowing steam at 823 K, 20Cr25Ni steel in humid air at 1073 K [37] and 304H (18Cr) in steam at 873 K [21].

This chromia layer reduces the rate of diffusion of metal out to the oxide/ gas interface and also the diffusion of O into the metal [38]. Further detail on the diffusion of Cr will be given in Section 2.4. Sensitisation of the metal, i.e. diffusion of Cr to form $Cr_{23}C_6$ and Cr_2N, can begin to occur if the steel is kept within the temperature range

of 823 – 1073 K for a long period of time [39]. A result of this carbide and nitride formation is a reduction in the ductility of the material and also an increase in the corrosion rate because of a reduction in the amount of Cr available to form a chromia layer. As already mentioned above, the addition of niobium prevents the formation of Cr carbides. Evidence of this is seen in alloys such as 20Cr-25Ni-Nb stabilised stainless steels used in the nuclear industry [40].

The formation of a protective layer is also dependent on the microstructure of the underlying alloy and not simply concentration of the alloying element, Cr or Si, for example [41]. For instance, in the case of austenitic stainless steel TP347H FG, the finer grains within the alloy allow an increased rate of Cr diffusion relative to the original alloy and so the rate of oxidation is decreased again despite the same level of Cr concentration [2].

2.2.2.3. Nickel

Ni is another element that is commonly found in stainless steels and is added as an austenitic stabiliser. The amount of Ni required to stabilise the austenitic structure is dependent on the percentage of Cr found within the steel because Cr is considered to be a ferritic stabiliser as seen in the Fe-Cr phase diagram in Figure 2-5 [35]. Austenitic steels used for superheater and reheater tubing in power plants commonly contain 18 wt.% Cr and 8 wt.% Ni. An alteration in the amount of Cr content means the Ni concentration has to also be modified in order to maintain an austenitic structure. Other common austenite compositions include 20 wt.% Cr 25 wt.% Ni [40] for use in the nuclear industry. The addition of Ni also has a positive impact on

toughness and strength at a wide range of temperatures whilst also improving oxidation and corrosion resistance.

2.2.2.4. Manganese and copper

Other elements added to the alloy to stabilise the austenitic structure are Mn and copper although copper is usually added because of its ability to increase creep strength. The stabilising effect of Mn is not as strong as that of Ni and a larger amount is therefore required to achieve the same effect. Both of these elements have the effect of coarsening carbide precipitates which decreases the creep strength over a long period of time.

2.2.2.5. Silicon

As already mentioned in the introduction, oxidation resistance is vital when these materials are exposed to harsh operating conditions found in steam operated power plants. Although Cr is the main element used to increase oxidation resistance Si can also be added to aid with this effect. Si is also added because it can reduce the amount of O and gas bubbles in the alloy during the manufacturing process. Si also has the effect of hardening the steel through solid solution strengthening [42]. It has been suggested that Si has a beneficial effect on the rate of Cr depletion in alloys exposed to water vapour containing environments, therefore extending the time to breakaway oxidation [43].

2.2.2.6. Phosphorus

The final element found in TP347H FG is phosphorus. Unlike the other elements found in this steel phosphorus is not an alloying element but is an impurity.

Phosphorus has negative effects on the steel such as giving the steel a brittle nature, increasing the likelihood of fracturing and also weakening of the metal when phosphides form on grain boundaries as occurs during hot working.

2.3. High Temperature Oxidation

2.3.1. Introduction

The general oxidation reaction for a metal, M, can be written as [44]:

$$aM + \frac{b}{2}O_2 \rightarrow M_aO_b$$ Equation 2-1

where ‘a’ and ‘b’ are integers. This is a very simple equation and high temperature oxidation is often more complex when factors such as multi component alloys and the presence of numerous deposits which can alter the surface chemistry are taken into consideration [44].

Unsurprisingly, most materials will oxidise at high temperatures leading to degradation and is therefore of concern in industry. Means of slowing down these processes and controlling the morphology of the oxides formed is of great interest in the scientific community. As previously mentioned, Cr is added to alloys in order to increase their oxidation resistance. Formation of protective oxides such as chromia, Cr_2O_3, or $FeCr_2O_4$ spinel form, limit the oxidation of the Fe rich alloy to form non protective oxides such as haematite, Fe_2O_3, and magnetite, Fe_3O_4.

The following Section of the literature review will discuss the thermodynamics, kinetics and mechanisms of oxidation of steels in various atmospheres.

2.3.2. Thermodynamic Fundamentals

Thermodynamic calculations are important in gaining an understanding of the processes that an oxidation reaction will go through, determining which reactions can occur between the steel and the oxidant and also in acquiring the ability to envisage the likely products formed.

The general oxidation reaction for a metal is shown in Equation 2-1 above. Whether or not a reaction occurs is dependent on the second law of thermodynamics and the change in Gibbs free energy being ≤0, at which point a reaction is expected to be spontaneous. The second law of thermodynamics, expressed in terms of Gibbs free energy, *G*, is shown below [44]:

$$G = H - TS \qquad \textbf{Equation 2-2}$$

where *S* is the entropy and this term must overcome the enthalpy, *H*, in order for the reaction to occur. If ΔG^0 is greater than zero then the reaction is thermodynamically impossible and if it is equal to zero then the reaction is in equilibrium.

From standard thermodynamics, a reaction between a pure metal and O results in the following [44]:

$$\Delta G = \Delta G^\circ + RT\, ln\left(\frac{a_{M_aO_b}}{a_M^a a_{O_2}^{b/2}}\right) \qquad \textbf{Equation 2-3}$$

where ΔG^0 is the difference in Gibbs free energy when all the species are present in their standard states, *R* is the gas constant, *T* is the temperature and $a_x = {p_x}/{p_x^0}$ is the thermodynamic activity, where p_x is the vapour pressure and p_x^0 corresponds to the standard state of x. The thermodynamic stability of the oxides can be expressed

in terms of the dissociation oxygen partial pressure which can be found from the equilibrium constant for the reverse reaction of that shown in Equation 2-1 [45]:

$$logk_1 = log\left[(pO_2)_{dissoc}^{y/2}\right] = -\frac{\Delta G^0}{2.303RT}$$ **Equation 2-4**

Once equilibrium has been reached, ΔG is equal to zero and ΔG^0 can be expressed as [16]:

$$\Delta G° = -RT\,ln\left(\frac{a_{M_aO_b}}{a_M^a a_{O_2}^{b/2}}\right)$$ **Equation 2-5**

K_p, the equilibrium constant for the reaction at constant pressure, can be related to the activity of the reacting species, as follows:

$$K_P = \frac{a_{M_aO_b}}{a_M^a P_O^{b/2}}$$ **Equation 2-6**

Equation 2-5 can then be rewritten as:

$$\Delta G^0 = -RTlnK_P$$ **Equation 2-7**

For the oxide to form, the oxygen partial pressure must be greater than the dissociation pressure of the oxide when in equilibrium with its metal.

The likelihood of an oxide forming is able to be determined through the use of an Ellingham diagram, a crucial tool in understanding the conditions for which a particular oxidation product will form [44].

The relationship between Gibbs free energy and temperature when all elements are in their standard states can be seen in the following equation.

$$\Delta G^0 = \Delta H^0 - T\Delta S^0$$ Equation 2-8

It is this Equation 2-8 that forms the basis of the Ellingham diagram which is a plot of the standard Gibbs free energy as a function of temperature. The Ellingham diagram for some common oxides is shown in [46]. The gradient of the lines on the Ellingham diagram is the standard change in entropy, -ΔS°, and the intercept is the standard change in enthalpy, ΔH°, and it is assumed that neither of these parameters vary significantly with temperature.

The negative entropy of the reaction is due to the entropy of gases being much higher than that of liquids and solids. The elimination of the gas phase during the reaction of metals with their oxides increases the free energy with increasing temperature. The lower the line on the graph, the more stable the oxide. The Ellingham diagram can therefore also be used to compare the stabilities of different oxides which are dependent on the enthalpy of the reaction at equilibrium.

It is also possible to acquire oxygen partial pressure data from an Ellingham diagram since the partial pressure can be written in terms of Gibbs free energy:

$$P_{O_2} = exp\left(\frac{\Delta G^\circ}{RT}\right)$$ Equation 2-9

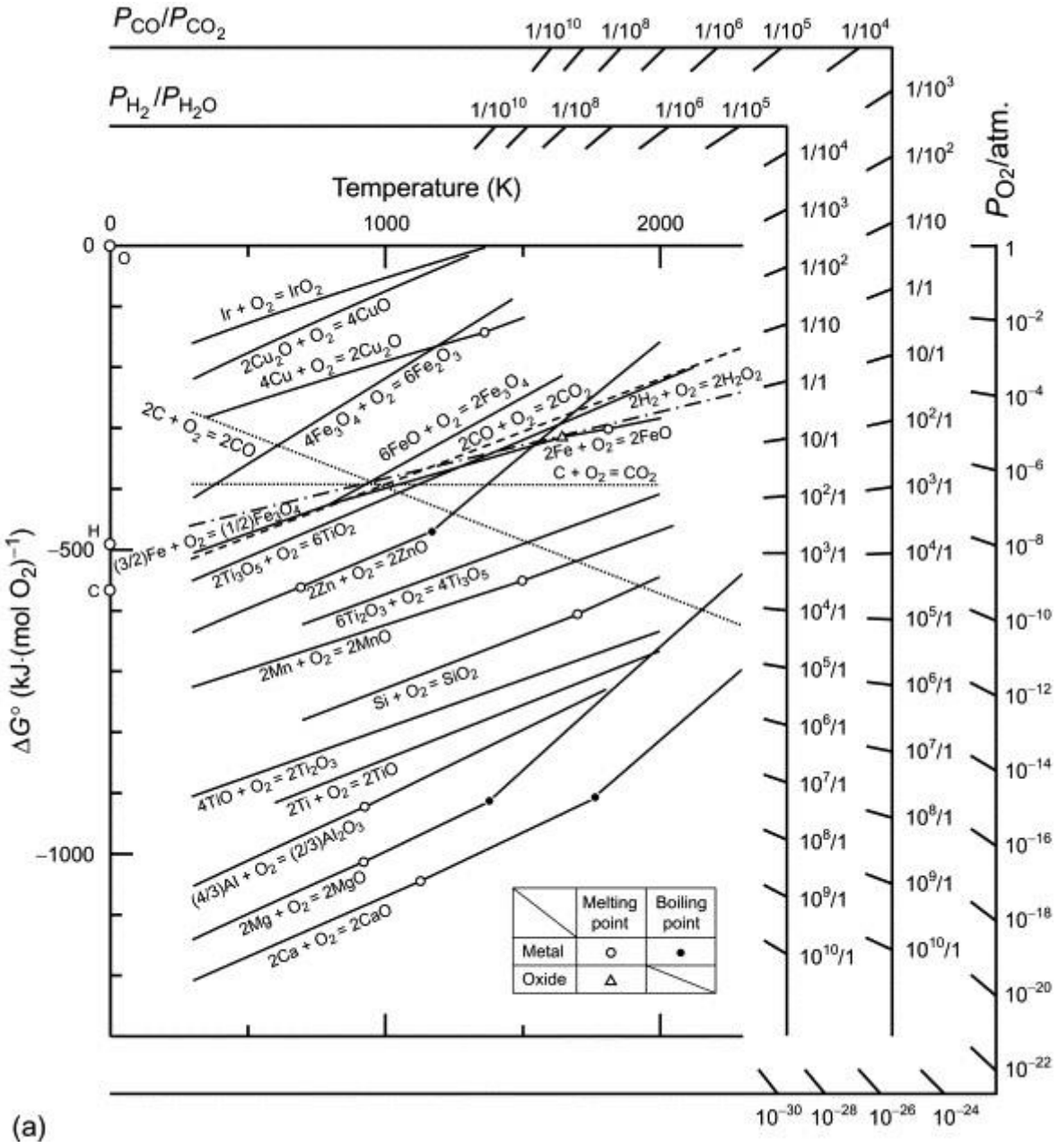

Figure 2-7 Ellingham diagram for some typical oxide reactions [46].

2.3.3. Mechanisms of Oxidation

Several mechanisms exist for the oxidation of an alloy and the route through which it occurs will be dependent on the composition of the alloy, the environment in which the oxidation is taking place, the condition of the surface and the microstructure of the alloy [47].

The first stage of the oxidation process is adsorption of O on to the clean metal surface where, on average, there are circa 10^{15} adsorption sites per square centimetre [47]. This adsorption can be either physical adsorption (physisorption) whereby the gas binds to the metal surface through van der Waals forces and can be reversible, or chemical adsorption (chemisorption), involving the transfer of electrons through a chemical reaction with the surface. Physisorption is generally easier as a continuous layer can be formed that is not necessarily achieved with chemisorption where a patchy layer normally grows. It is possible for physisorption to occur on any surface at low temperatures and generally does not have an activation energy associated with it since there is no barrier to prevent the reaction from occurring. Chemisorption on the other hand, due to a chemical reaction taking place, is dependent on activation energy. As a result, this mode of adsorption normally occurs at high temperatures and at an active site.

Once the surface is completely oxidised, an alternative mechanism, diffusion, takes place if oxidation continues. As can be seen from Figure 2-8 [45], the metal and the gas are separated by the oxide scale.

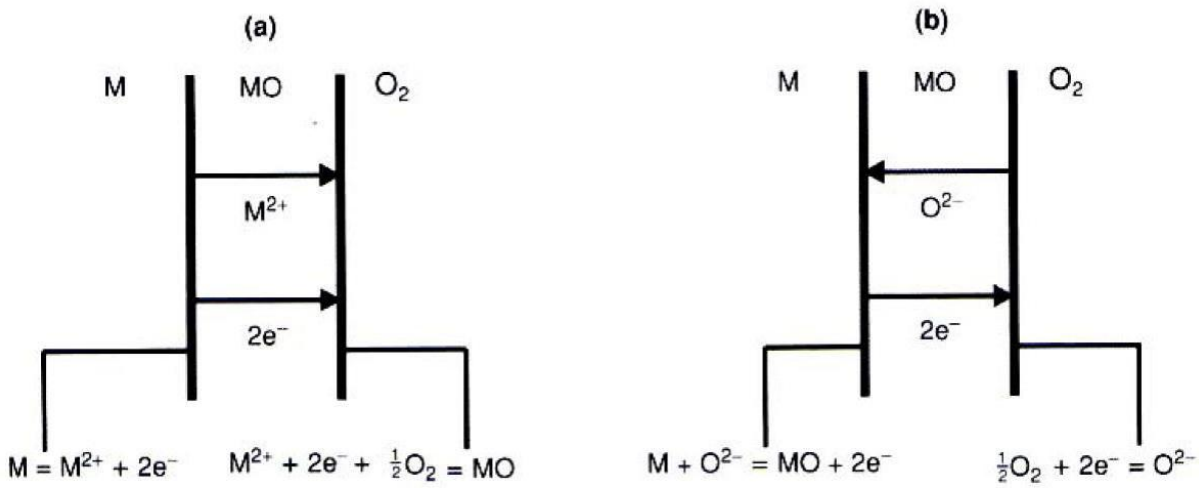

Figure 2-8 Interfacial reactions and transport processes for high-temperature oxidation mechanisms: (a) cation mobile and (b) anion mobile [45].

Either the metal ions diffuse through the oxide layer to the air/ oxide interface and react with O there or the O ions diffuse through the oxide layer to the metal/ oxide interface to react with the metal. If the oxide scale is thin, then the driving force for diffusion can be due to 'electric fields in or across the film' [47]. On the other hand, if the oxide scale is thick, the driving force is the chemical potential gradient across the scale.

2.3.4. Kinetics

The reaction kinetics are important in order to provide a full understanding of the oxidation process. For instance, the rate equations can provide assistance in determining the mechanism through which the oxidation has occurred by classifying the oxidation behaviour [47]. There are two ways in which the kinetics can be measured: either through observing the mass change, or determining the thickness of the oxide layers, which requires sectioning of the sample. In this study, oxide thickness is the preferred method since the samples have a total of 3 surface finishes

and therefore different rates of reaction. Using this method is also advantageous in that it provides information on each of the oxides formed and examination of subsurface and changes in the alloy.

Several rate laws can be identified but the three main laws are parabolic, linear and logarithmic. In the case of austenitic stainless steels and those discussed in this thesis, parabolic rate laws are dominant and so only this mechanism will be discussed in further detail. For more information on linear and logarithmic rate laws see [47].

If the rate of oxidation is restricted as a result of diffusion of the element that forms the protective oxide layer, through the compact scale then the parabolic rate law is found to be obeyed. For instance, chromia and alumina scales. This can be expressed by:

$$\xi^2 = k_p t \qquad \text{Equation 2-10}$$

where k_p is the parabolic rate constant, $m^2.s^{-1}$, ξ is oxide thickness, m, and t is time, s. Certain assumptions, according to Wagner's theory, can be made in order to determine the rate constant, k_p [47]:

1. The oxide layer is compact and perfectly adherent,
2. Migration of ions or electrons across the oxide is the rate controlling process,
3. Thermodynamic equilibrium is established at both the metal-scale and scale-gas interfaces,
4. The oxide scale shows only small deviations from stoichiometry and, hence, the ionic fluxes are independent of position within the scale,

5. Thermodynamic equilibrium is established locally throughout the scale,
6. The scale is thick compared with the distances over which space charge effects occur,
7. Oxygen is insoluble in the metal.

Kofstad's description of Wagner's theory [47] also suggests that reactions occurring at phase boundaries are rapid since the diffusion through the scale is rate determining[1].

Mass balance and diffusion theory along with the assumptions from Wagner's theory can be used to show that:

$$k_P = \frac{1}{RT}\int_{\mu_0'}^{\mu_0''}\left(D_O + \frac{Z_M D_M}{Z_0}\right) d\mu_0$$ Equation 2-11

where k_p is the parabolic rate constant, R is the gas constant, T is temperature, Z_M is the valence of the metal, D_M is the diffusivity of the metal in the oxide, D_O is the diffusivity of O in the oxide, μ_0' is the chemical potential of O at the metal/ oxide interface and μ_0'' is the chemical potential of O at the gas/ oxide interface.

It is possible for the oxidation reaction to follow a combination of rate laws. If oxidation kinetics are slow then a thin oxide scale layer is formed compared to a thick oxide for fast kinetics. Ultimately, oxide thickness is dependent on length of time at temperature.

[1] N.B. Information gathered on Wagner's theory has been taken from Birks, Meier and Pettit 'High Temperature Oxidation of Metals' who provided a detailed review of the original paper [44].

2.3.5. Oxide Formation

A thin protective oxide scale will be formed on austenitic stainless steels exposed to mild conditions such as in air environments and grows at a declining rate which can be seen by the line OAD in Figure 2-9 [48]. However, when the reaction conditions are more severe, such as in steam environments, there is the initial protective period (line OA) followed by an increase in the rate of reaction (line AB), known as breakaway, leading to either self-healing (line BC), which is a further decrease in reaction rate, or, continuation of the formation of a non-protective oxide (line BE) can be seen instead. It is also possible for the line AB to be followed immediately when the alloy is in extremely aggressive conditions.

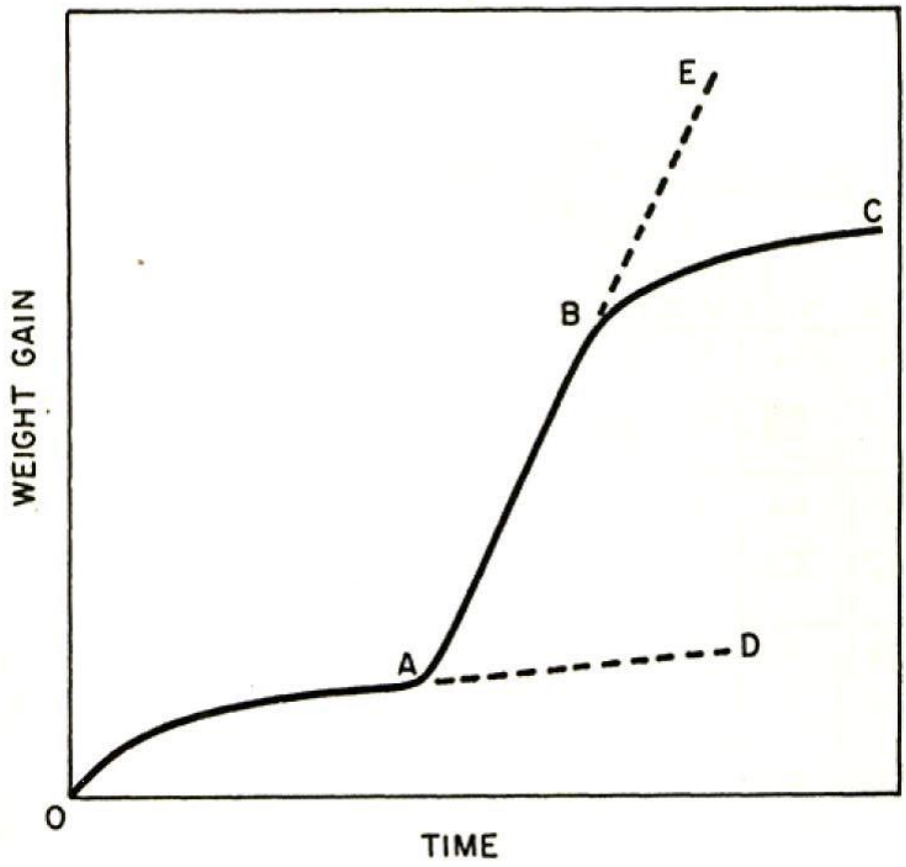

Figure 2-9 Diagram of weight gain as a function of time [48].

When austenitic alloys are oxidised the different oxides that can form are FeO, stable above 843 K, Fe_2O_3, Fe_3O_4, $Fe_xCr_{2-x}O_4$, Cr_2O_3 and CrO_3. The amount of each oxide formed and where on the alloy it is formed will be dependent on alloy composition, impurities, atmosphere, effective oxygen partial pressure, temperature, specimen geometry, surface finish and method of exposure to the atmosphere [49-56]. Each oxide and its formation will be considered below.

2.3.5.1. Fe Oxides

The phase diagram for Fe and O is shown below in Figure 2-10 [45] and indicates which phase is thermodynamically stable at a given temperature and O weight percent. Fe is able to exist in a range of oxidation states from +2 to +6 but +2 and +3 are the most common. As a result of this array of oxidation states, it is possible for several types of oxide to form; FeO (wüstite), Fe_3O_4 (magnetite), and Fe_2O_3 (haematite). When Fe is oxidised, the subsequent oxides occupy more volume than the pure Fe potentially causing it to spall and revealing a fresh surface for reactions to transpire. It is apparent that wüstite exists as $Fe_{1-\delta}O$, where δ varies dependent on temperature, magnetite, at high temperature, digresses from its nominal stoichiometry, but haematite is stoichiometric at most temperatures. The diagram also reveals that at high levels of O content the different phases can co-exist with one another. Wüstite, at temperatures above 843 K, is present with magnetite, below this temperature wüstite is unstable, magnetite coexists with haematite, and haematite with O gas. It is in this order that the oxide layers are disposed within a scale grown isothermally on Fe [2], [44], [45].

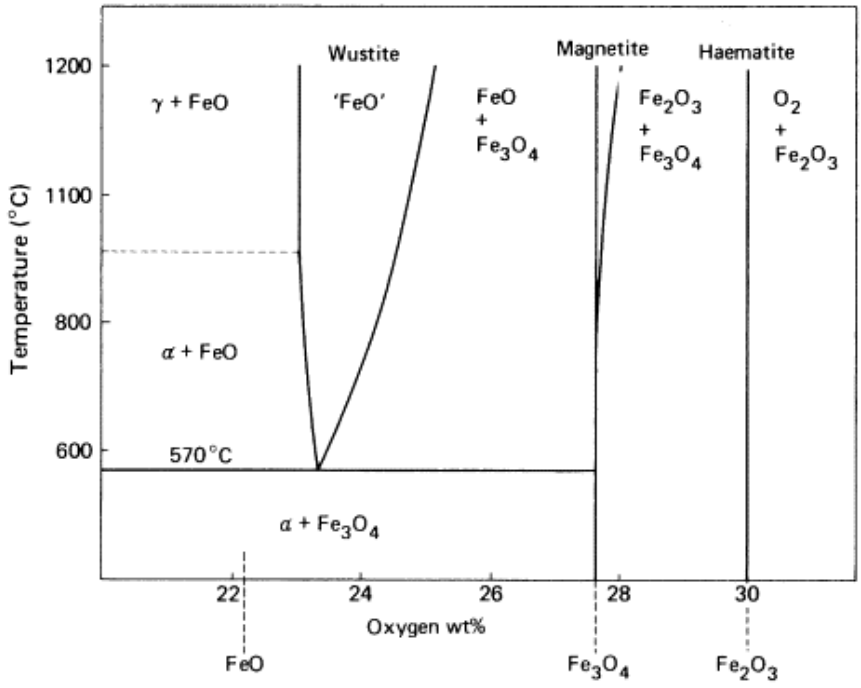

Figure 2-10 Fe-O phase diagram [45]

It is possible for magnetite to be further oxidised to form haematite because of its thermodynamic instability [57], the mechanism of which is shown in Figure 2-11 [45] and described by the following equation:

$$2Fe_3O_4 + H_2O \rightarrow 3Fe_2O_3 + H_2$$

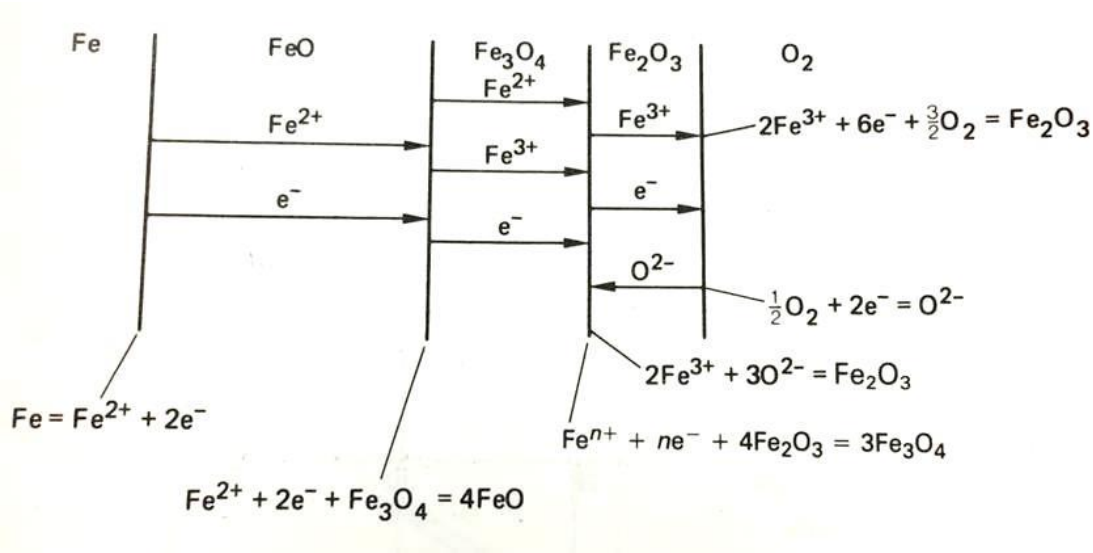

Figure 2-11 Mechanism of oxidation of magnetite to haematite [45]

2.3.5.2. Chromium

When the Cr content is sufficiently high in Cr containing alloys, a protective layer is formed, Cr_2O_3, when the alloy undergoes oxidation in air and steam. If the O content is high enough then the chromia scale can further react to form a volatile species, CrO_3, at temperatures over 1173 K, shown schematically in Figure 2-12 [45]. This mechanism will be discussed in further detail in Section 2.4.

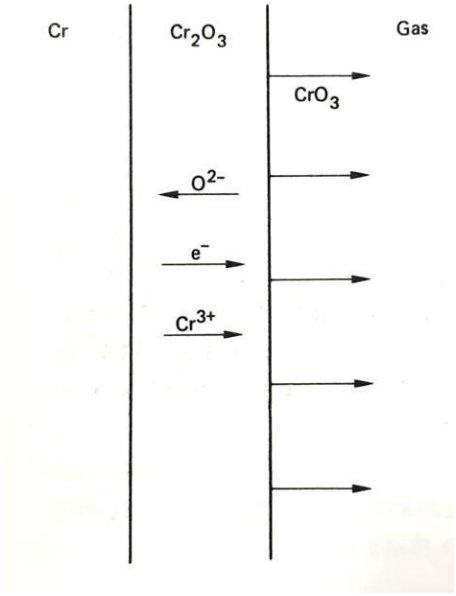

Figure 2-12 Volatilisation of Cr [45]

2.3.5.3. Nickel

Although it has been reported [58] to be possible to form Ni in multiple valence states, +2, +3 and +4, the only well characterised oxide that forms on pure Ni is a single layered oxide, NiO which is a p-type semiconductor [45].

In the case of stainless steels however, Ni often oxidises to form Fe-Cr-Ni spinel oxides [59-61].

2.3.5.4. Typical Oxide Microstructure for Oxides Formed on TP347H FG

Exposure of TP347H FG, the alloy of interest in this thesis, to steam environments typically results in the formation of a duplex oxide scale consisting on an inner Fe-Cr-Ni spinel and an outer layer of magnetite and an outer decoration of haematite [22]. With longer times at temperature a Cr rich oxide, Cr_2O_3, is observed at the base of the Fe-Cr-Ni spinel.

The mixed metal oxide, Fe-Cr-Ni spinel, possesses a spinel structure and is formed through the inward diffusion of oxygen from within the oxidising atmosphere. The Cr rich oxide, Cr_2O_3, possesses a corundum structure [62] and is formed through outward diffusion of chromium from within the alloy. It forms as a dense, compact layer at the base of the Fe-Cr-Ni spinel and as a result leads to a decrease in the oxidation rate, as will be discussed later. Haematite, Fe_2O_3, and magnetite, Fe_3O_4, are both outwardly growing oxides that rely upon the outward diffusion of iron from within the alloy. Fe_2O_3 possesses a rhombohedral crystal structure [63] whilst Fe_3O_4 on the other hand possesses a spinel type structure [64]. The reason behind the ordering of the oxide layers lies within the Ellingham diagram shown earlier in Figure 2-7. Haematite and magnetite can be found towards the top of the Ellingham diagram meaning that they are more thermodynamically stable than other oxides. Cr_2O_3 on the other hand is found lower down on the Ellingham diagram.

2.3.6. Oxidation in Air and Dry O_2

Oxidation of steels in air generally results in the formation of a duplex oxide scale consisting of an outer Fe rich oxide and an inner spinel layer.

The rate of oxidation for steels exposed to air or O_2 environments is dependent upon the other reactive elements within the steel. Comparisons have been made in the literature between 9Cr-1Mo steels that have varying concentrations of Si as well as different grain sizes [65]. It was found that alloys containing higher amounts of Si (up to 0.75 wt.%) and larger grain sizes were more oxidation resistant and therefore had lower oxidation kinetics at 973 K. However, at lower temperatures of 773 K the grain size does not play a considerable role in the oxidation resistance. It was also shown that for 9Cr-1Mo steels the oxidation rates are higher at 873 K compared to 973 K [66] . This is as a result of a switch over from general oxidation at 873 K to selective oxidation of Cr at 973 K.

In the case of austenitic stainless steels, Fe_2O_3 was found to form at the outer surface when exposed to dry air within the temperature range of 600 - 873 K [67], [50]. Other studies have found, through transmission electron microscopy (TEM) examination, that when 316 stainless steel was oxidised in air at 873 K a complex multi-layer structure formed with an outer layer of Fe oxide and an inner layer of Cr oxide. Both of these layers were shown to include high concentrations of both Ni and Mo [68]. For Cu-bearing austenitic stainless steel 304H precipitates of Cu-rich particles were found in the oxide when oxidised in air at 923 K. The composition of the oxides was found to comprise of binary oxides of Fe, Cr, Mn and Nb as well as the spinel oxides $FeCr_2O_4$ and $MnCr_2O_4$ [69]. At 1273 K, oxidation of 304 was shown to form external chromia but this layer was not continuous [70]. Oxidation of 304L at 600 K showed that rapid diffusion of Fe through the oxide scale resulted in a concentration gradient of Fe within the oxide. Co, Mn, Ti and Ni were also shown to play a role in the oxidation process however as oxidation time increased, the relative

level of these elements within the oxide decreased as a result of depletion of the minor elements [50]. Si was also found in higher concentrations of 1 wt.% at the oxide grain boundaries, as was the case for the 9Cr-1Mo steels mentioned earlier, compared to 0.8 wt.% for the corresponding grain centres. Oxidation kinetics were shown to be parabolic for 304H in air at 923 K. For high Cr containing steel TP347H FG with a small grain size, a single, slow growing Cr_2O_3 layer formed when oxidised in air at 1023 K [71]. This was as a result of the finer grains leading to increased Cr diffusion. Austenitic stainless steels oxidised in dry O_2 were found to form a thin protective Cr rich oxide scale on the surface in the temperature range 773 – 923 K [67].

2.3.7. Steam Oxidation

2.3.7.1. Introduction

The primary focus of the work in this thesis is oxidation of austenitic stainless steel, TP347H FG, in a steam environment. Understanding the effect of water vapour on the oxidation of steels is important in the power generation industry since it can cause material thinning and down-stream erosion as a result of spallation [72]. The efficiency of steam turbines is greatly dependent on steam temperature and pressure. Generally, it is accepted that steam exacerbates oxidation kinetics [73] compared to air and O environments but the cause of this is not fully understood.

This Section of the literature review will consider the mechanism of steam oxidation, the effect of different steam oxidation environments on the oxidation behaviour of commonly used boiler steels and the effect of Cr concentration.

2.3.7.2. Mechanisms of Steam Oxidation

Steel can be oxidised by steam because steam generates a higher oxygen partial pressure during dissociation compared to the oxygen partial pressure generated by the dissociation of Fe oxides.

It is well documented in the literature that the oxidation mechanism of metals exposed to steam differs to that in air [74] and that the oxidation kinetics are dramatically increased. However, the cause of such exacerbated kinetics in a steam environment is not fully understood and several mechanisms explaining the oxidation process in water vapour containing environments have been suggested in the literature including [75]:

- H_2/ H_2O bridges in voids at the scale/ alloy interface leading to dissociation processes,
- Incorporation of hydrogen in the scale in the form of H^+/ OH^- ,
- Formation of volatile Fe-hydroxides or volatile Cr-oxyhydroxides,
- Enhanced surface reaction and preferential adsorption at inner scale surfaces,
- Enhanced growth stresses leading to scale cracking.

Each of these mechanisms will be discussed in turn below.

The dissociation mechanism was proposed by Fujii and Meussner in 1964 and is shown schematically in Figure 2-13 [76]. A series of oxidation tests were performed on 0-25Cr Fe-Cr alloys in Ar-10%H_2O between 973 and 1373 K. Linear kinetics were observed for steels with lower Cr contents and attributed to rates of incorporation of O from the water vapour, Figure 2-13.

Oxidation of these alloys under steam conditions resulted in the formation of an outwardly growing wüstite layer and an inwardly growing, porous wüstite + spinel phase.

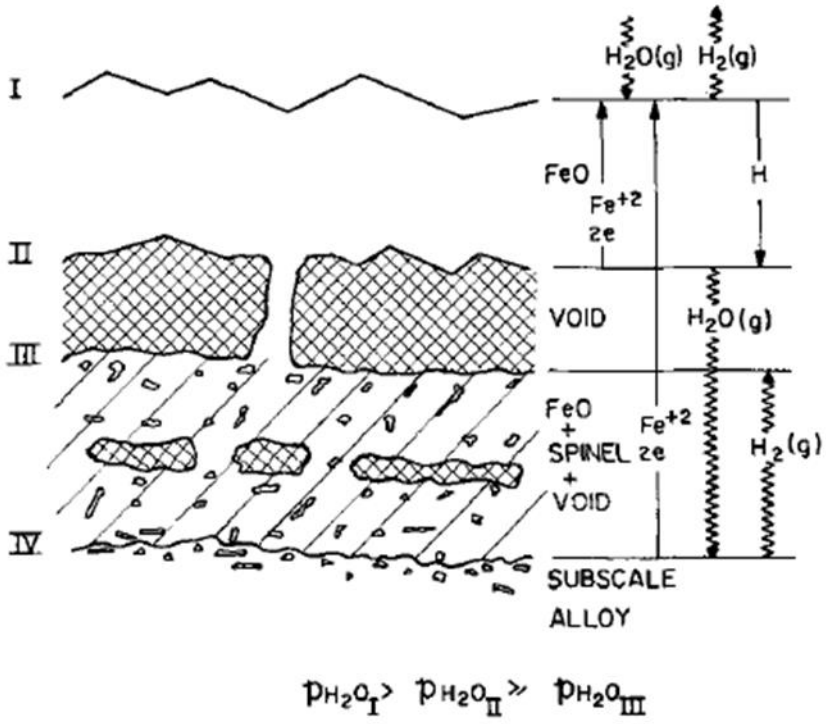

Figure 2-13 Dissociation mechanism proposed by Fujii and Meussner [76].

Investigative studies into the oxide scale structure indicated a dissociative process operating within the voids separating the two oxide scales observed. At the oxide/ gas interface, interface I, water vapour was adsorbed on to the surface and reacted with Fe ions diffusing outwardly. This resulted in the formation of FeO as well as defects in the oxide and adsorbed hydrogen as shown in Figure 2-13 and described by the following equations.

$$H_2O\ (g) \rightarrow H_2O(ads)$$

$$H_2O\ (ads) + Fe^{2+} + 2e^- \rightarrow' FeO' + Fe_{vac} + 2 \oplus + H_2\ (ads)$$

$$H_2\ (ads) \rightarrow H_2(g)$$

$$H_2\ (ads) \rightarrow 2H^*(ox)$$

where $\oplus$ is an electron defect.

At the oxide/ oxide interface, i.e. interface II, the Fe oxide is thought to dissociate and oxide ions are adsorbed. The reactions occurring at this interface were described by the following equations:

$$FeO + Fe_{vac} + 2\oplus \rightarrow Fe^{2+} + O^{2-}$$

$$2H^*_{2(ox)} \leftrightarrow H_{2(ads)}$$

$$H_{2(ads)} \leftrightarrow H_2\ (g)$$

$$H_{2(ads)} + O^{2-} \rightarrow H_2O\ (g) + 2e^-$$

H_2O is formed as a carrier gas for O transport in the voids.

The dissociative mechanism described by Fujii and Meussner has been found to be applicable to alloys containing 0-15 wt.% Cr. This mechanism however has not been as successful in describing the oxidation of alloys containing more than 15 wt.% Cr in water vapour containing environments between 1023 and 1173 K. It is thought under these conditions cracks and pores form within the chromia layer resulting in the formation of a spinel-type oxide. Spinel oxides are not as protective in nature as chromia scales and so allow transport of Fe ions to the oxide/ gas interface and as such an Fe rich oxide is able to form [56].

Surman and Castle indicated three possible transport mechanisms in steam oxidation:

- Solid state diffusion of Fe ions outwards to the oxide-gas interface,
- Solid state diffusion of O^{2-} inwards to the metal-oxide interface, or
- Vapour phase diffusion of volatile $Fe(OH)_2$.

The formation of volatile species has been suggested to account for the increased oxidation kinetics of alloys exposed to steam compared to air [77]. Examples of volatile species found in different steam atmospheres and the possible reactions leading to their formation include:

$$\frac{1}{2}Cr_2O_3 + H_2O\ (g) + \frac{3}{4}O_2(g) \rightarrow CrO_2(OH)_2(g) \quad [78]$$

$$FeO + H_2O \rightarrow Fe(OH)_2\ (g) \quad [79]$$

$$Fe_3O_4 + 3H_2O \rightarrow 3Fe(OH)_2\ (g) + \frac{1}{2}O_2 \quad [79]$$

$$Fe_2O_3 + 2H_2O \rightarrow 2Fe(OH)_2(g) + \frac{1}{2}O_2 \quad [79]$$

$Fe(OH)_2$ has been proposed to be the cause for the increase in oxidation rate of P91 exposed to environments containing 2-7% water vapour [79]. That work concluded that H_2O creates porosity through the evaporation of $Fe(OH)_2$. These pores can provide a route for O transport through the reactions shown in Figure 2-14.

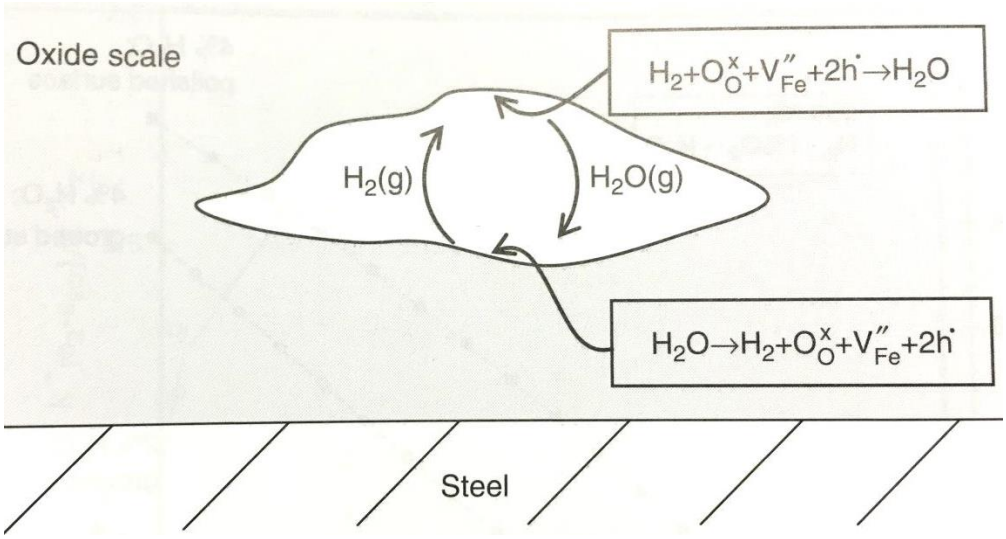

Figure 2-14 Transport of water vapour through the scale [44].

Another possible oxidation mechanism for steam environments is the dissociation of H_2O (g) [22]:

$$H_2O(g) \leftrightarrow 2H^+ + O^{2-}$$

$$H_2O\ (g) \leftrightarrow OH^- + H^+$$

The first of the two dissociation routes above is considered to be the most appropriate in the literature [22]. The second of the two equations shown above has been suggested to result in oxidation occurring at the oxide/ metal interface as a result of the inward diffusion of OH^- ions [80].

Evaporation of Cr containing gas species such as $CrO_2(OH)_2$ will lead to scale loss [72]. The enhanced Cr depletion caused by volatilisation of Cr is then thought to bring about breakaway oxidation more quickly hence increasing oxidation kinetics. This was shown by Asteman *et al*. who studied oxidation of 304L in 10% water vapour at 873 K [81].

Scales grown in water vapour containing environments are generally more porous than those grown in dry O [82]. It is commonly believed in the literature that this formation of voids is caused by the difference in the rate of diffusion of cations and anions. The rapid diffusion of cations outwards leaves behind vacancies which coalesce to form voids [1], [83], [84], [85], [86]. Over time these voids accumulate and a gap forms. Further work on pores, voids and cracks showed they play an important role in further oxidation and that the size of them should be correlated to oxide thickness if voids have formed through the vacancy migration mechanism [83], [87], [88]. It has also been suggested that voids can form as a result of weakening of the grain boundaries [1]. Formation of these pores in the inner scale results in a decrease in the area available for diffusion [89] since ions cannot diffuse through the pores. The effect of void coalescence on stresses and spallation of oxide scales will be discussed in Section 2.5. Gorman and Fry [41] observed extensive laminar porosity on 9Cr steels after 1000 hours which resulted in the spallation of the outer magnetite layer and that this porosity was considerably reduced after 3000 hours suggesting that there is a healing mechanism for pore formation.

2.3.7.3. Oxide Formation in Different Steam Environments

A wide variety of steam and water vapour containing atmospheres has been studied in the literature ranging from 10%H_2O-Ar to oxygenated and deoxygenated steam. The term deoxygenated steam refers to ‘O free’ water where the O has been removed from the environment usually by purging with nitrogen [20], [21]. A selection of environments will be discussed with the main focus on oxygenated and

deoxygenated steam since these are the atmospheres used in the work presented in this thesis.

Generally, increasing the concentration of water vapour increases oxidation kinetics, as shown in Figure 2-15 for an Fe-15Cr alloy at 1173 K.

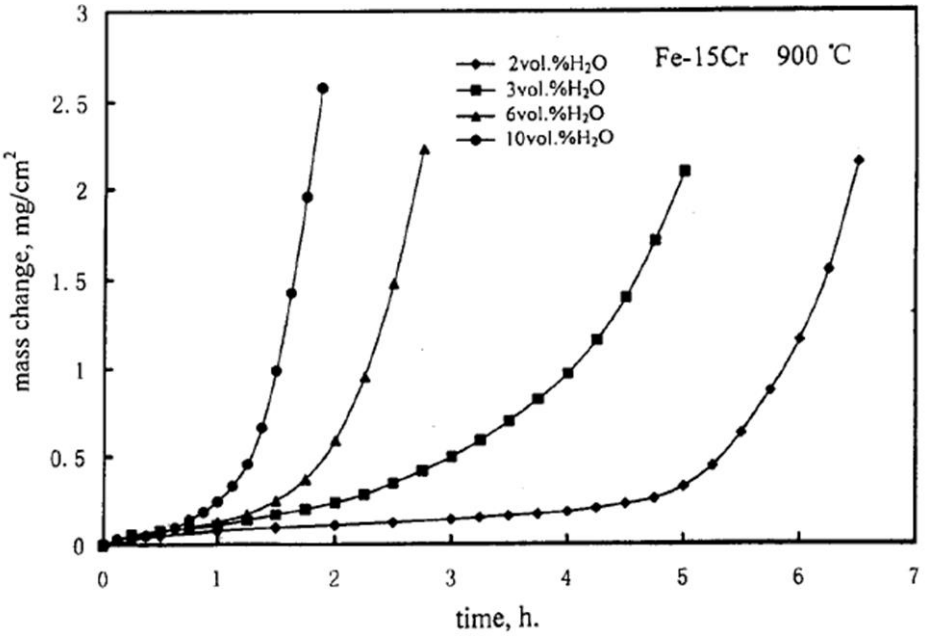

Figure 2-15 Oxidation kinetics of Fe-15Cr in O with various amounts of water vapour [53].

The literature shows that haematite, Fe_2O_3, is normally only formed after long periods of time in plant or under air saturated steam in laboratory conditions [90]. There is evidence in the literature to suggest that there is no haematite formation when the steam environment is O free. Table 2-4, from [73], shows the oxides formed on binary alloys exposed to four different atmospheres with increasing amounts of H_2O. Othman *et al.* show that steam promotes the formation of Fe containing oxides and haematite only formed when O was present. When this O was replaced with

hydrogen, effectively deoxygenating the atmosphere, there was no haematite formation.

Table 2-4 Oxides formed on three different binary alloys exposed isothermally to various steam containing environments at 973 K [73]**.**

Alloy	Ar-20O_2	Ar-20O_2-5H_2O	Ar-5O_2-20H_2O	Ar-10H_2-5H_2O
Fe-9Cr	Cr_2O_3	Fe_2O_3, $(Fe,Cr)_3O_4$	Fe_2O_3, Fe_3O_4,FeO	$(Fe,Cr)_3O_4$, FeO
Fe-17Cr	Cr_2O_3	Cr_2O_3	Cr_2O_3	Cr_2O_3
Fe-25Cr	Cr_2O_3	Cr_2O_3	Cr_2O_3	Cr_2O_3

Further evidence for this observation was provided by Rosser *et al*. [21] and Lukaszewicz *et al*. [91] who both found that in deoxygenated environments, where nitrogen was used to purge the water of O, there was no indication of haematite formation for austenitic stainless steels oxidised for up to 1000 hours at 923 K.

Lukaszewicz and Nicholls *et al*. [91] however did also find that for alloys T23 and TP347H FG they were able to detect haematite when the steam flow rate was increased from 4 to 40 $mm.s^{-1}$. They have postulated the reason for this was that higher steam flow rates resulted in an increased oxidising condition. The mechanism for steam oxidation in this case was assumed to be the dissociation of water to form H_2 and O_2 where H_2 will sit on the surface of the alloy whilst O_2 diffuses into the alloy. The higher steam flow rate then therefore sweeps the hydrogen away which has been suggested to suppress the formation of haematite. More recently, the same observations have again been reported by Dudziak and Nicholls *et al.* [20] where increased steam flow rates resulted in the formation of Fe_2O_3 and was thought to be

as a result of an increased oxygen partial pressure at the oxide/ gas interface due to a higher concentration of oxidising species with the higher steam flow rate. The reason for the higher oxygen partial pressure however could be as a result of ineffective removal of O from the water with a higher steam flow rate. The O content of the water was not measured neither before nor during the testing period. Results of this work could therefore be improved by measuring the O content of the water to provide further evidence that haematite is forming as a result of a different mechanism. Other studies have shown that gas flow direction also has some effect on the oxide scale morphology. For a 10 wt.% ferritic steel exposed in environments containing up to 50% steam for 5 hours a thin haematite layer formed at the front of the sample where the gas started to react [92]. On alloy T23 the oxide is 8-10% thicker in areas facing direct steam flow compared to the rest of the sample facing indirect steam flow [91].

Asteman *et al*. on the other hand found that higher steam velocities result in a destabilised Cr rich oxide [52] when 304L, of similar composition to TP347H FG, was oxidised in H_2O/ O_2 mixtures at 873 K for 168 hours. The explanation for that observation was Cr evaporation which will be discussed in further detail in Section 2.4. In a later paper Asteman *et al*. [93] reported haematite formed on 304L during isothermal oxidation at 1073 K in O_2 + 40% H_2O, Figure 2-16.

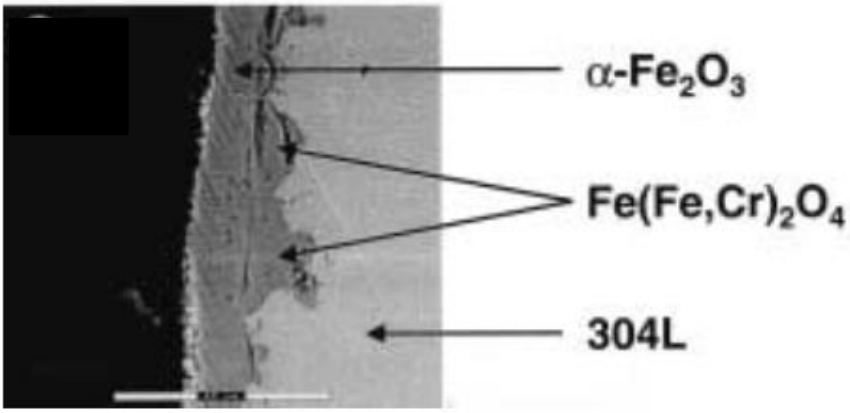

Figure 2-16 304L oxidised for 168 hours at 1073 K in O_2 + 40% H_2O with a flow rate of 4000 ml.min^{-1} [93].

Increasing the amount of water vapour in the carrier gas exacerbates the oxidation kinetics and results in the formation of a much thicker duplex oxide, as demonstrated in Figure 2-17 [67] where TP347H FG had been exposed to different water vapour containing environments for 336 hours at 873 K. The increased water vapour concentration also resulted in an alteration in the oxide morphology.

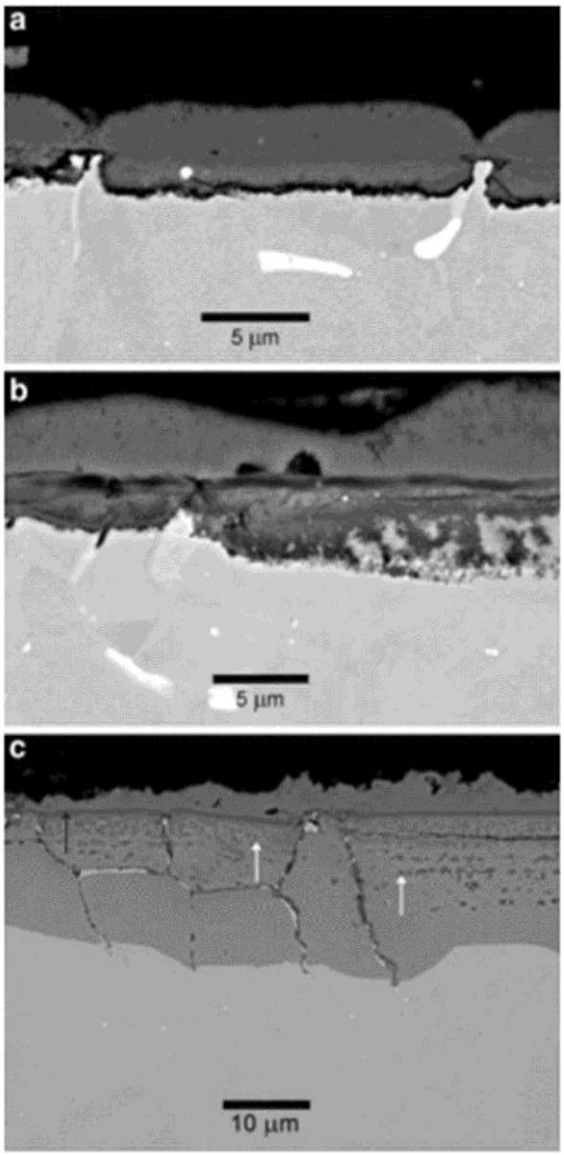

Figure 2-17 BSE images of TP347H FG oxidised in a) dry air, b) air-8% H_2O and c) air-46% H_2O for 336 hours at 873 K [67].

This study also found that when the oxidising environment contained humidified air + Ar, haematite formed whereas when the atmosphere was humidified H_2 + Ar the outer Fe rich oxide was found to be only magnetite [67]. This was attributed to the partial pressures of oxygen being too low when air is removed from the system since thermodynamic calculations for the Fe-O system have shown that Fe_2O_3 is only able to form where the partial pressure is above 2.16×10^{-15}.

Gorman and Fry [41] also stated that high O potentials lead to the formation of haematite which in turn reduces the diffusion rate of O and prevents further haematite formation. Figure 2-18 and Figure 2-19 indicate the calculated oxygen partial pressures at various temperatures in steam containing environments and the Fe oxides expected to form at those oxygen partial pressures. The values determined were consistent with those found by Hansson *et al*. [67].

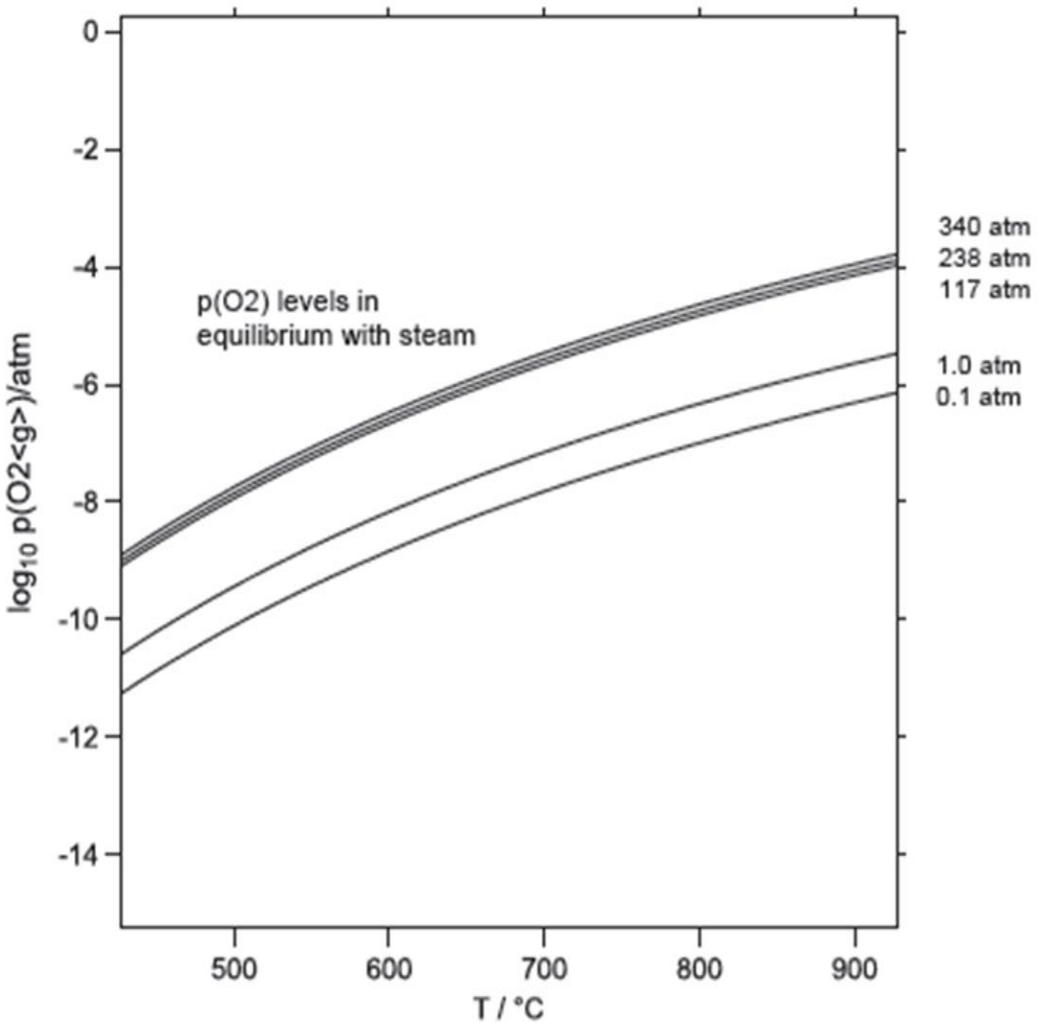

Figure 2-18 Calculated oxygen partial pressure in equilibrium with steam at various pressures [53].

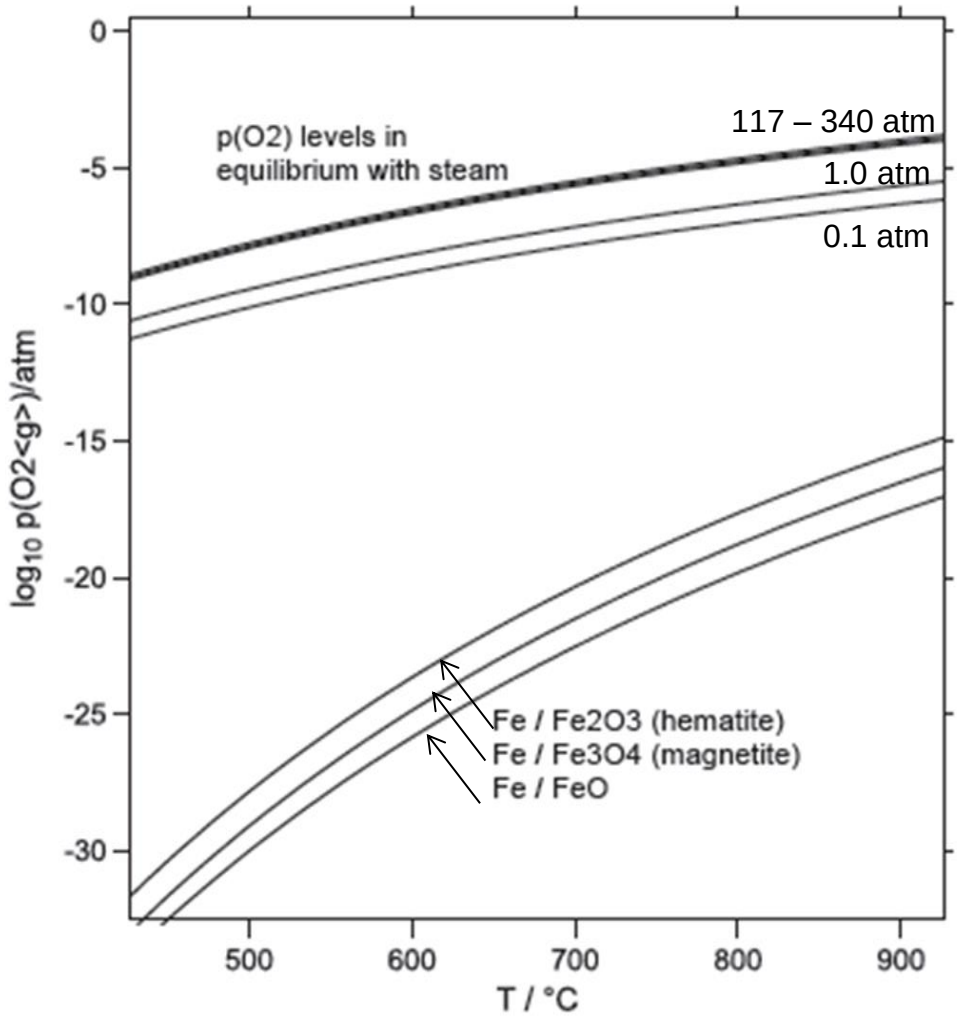

Figure 2-19 Calculated oxygen partial pressures required to form various Fe oxides [53].

2.3.7.4. Steam Oxidation of Steels and the Effect of Cr Concentration

Much research has been carried out on the effect of steam containing environments on high temperature oxidation of steels. The composition of the alloy has been shown in the literature to have a significant effect on steam oxidation resistance even within the same class of alloys [56]. It has been widely shown in the literature that an increase in the oxidation temperature results in an increase in mass gain [91].

The oxidation resistance of low Cr steels such as T23 (2.25 wt.% Cr) has been studied between 873 and 1023 K. Results have shown an increase in temperature led to a decrease in the amount of haematite present when T23 was exposed to deoxygenated steam for up to 1000 hours [54]. For the higher temperatures investigated in that study no spallation was observed. Figure 2-20 summarises the scale growth kinetics for 2.25 wt.% Cr containing steels.

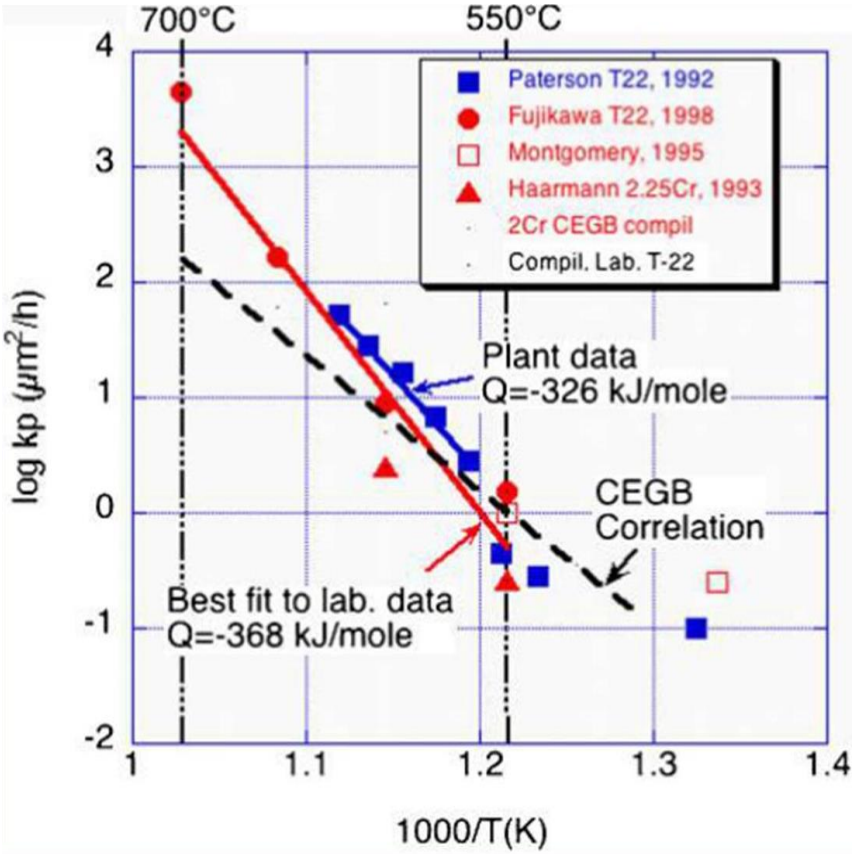

Figure 2-20 Summary of scale growth kinetics for 2.25Cr alloys (total scale thickness) [89].

Oxidation resistance of grade 91 steel is achieved by the 9% Cr level. Exposure to steam at 923 K grade 91 results in the formation of an outwardly growing Fe_3O_4 layer and an underlying growing $(Fe,Cr,Mn)_3O_4$ layer [41]. Steam oxidation of 9Cr steels was also shown to be affected by various alloying elements. Finally, steam flow was

also shown to have some impact on the oxidation behaviour of steels with mass change increasing with increasing flow rate [91].

Oxidation resistance has also been shown in the literature to be improved when the steel surface is coated prior to oxidation. However, this is dependent on the coating used. Figure 2-21 and Figure 2-22 present the cross sectional images of uncoated and Al coated samples, respectively. These images indicate that when coated with Al alloys 316 and 304 do not form Fe rich oxides which are seen when exposed to steam without coating. The mass gain of Al coated 300 series austenitic stainless steels was reduced up to 100 times compared to uncoated samples [90]. This was as a result of Al_2O_3 formation on coated samples which prevented spinel formation. Direct Current Magnetron Sputtering (DCMS) was used to deposit a 30 μm thick nanocrystalline coating with an identical composition to 304 stainless steel [91]. Use of this coating was shown to prevent the onset of breakaway oxidation when 304 stainless steel was exposed to flowing air + 40% H_2O. This was attributed to the coating having an abundance of grain boundaries therefore improving Cr diffusion. Coatings of this nature provide further benefits in that the additional problem of interdiffusion between the coating and substrate seen with other coatings is non-existent since the compositions are identical [96]. Other researchers have also shown beneficial effects to oxidation resistance when a coating has been used [97], [98], [99], [100].

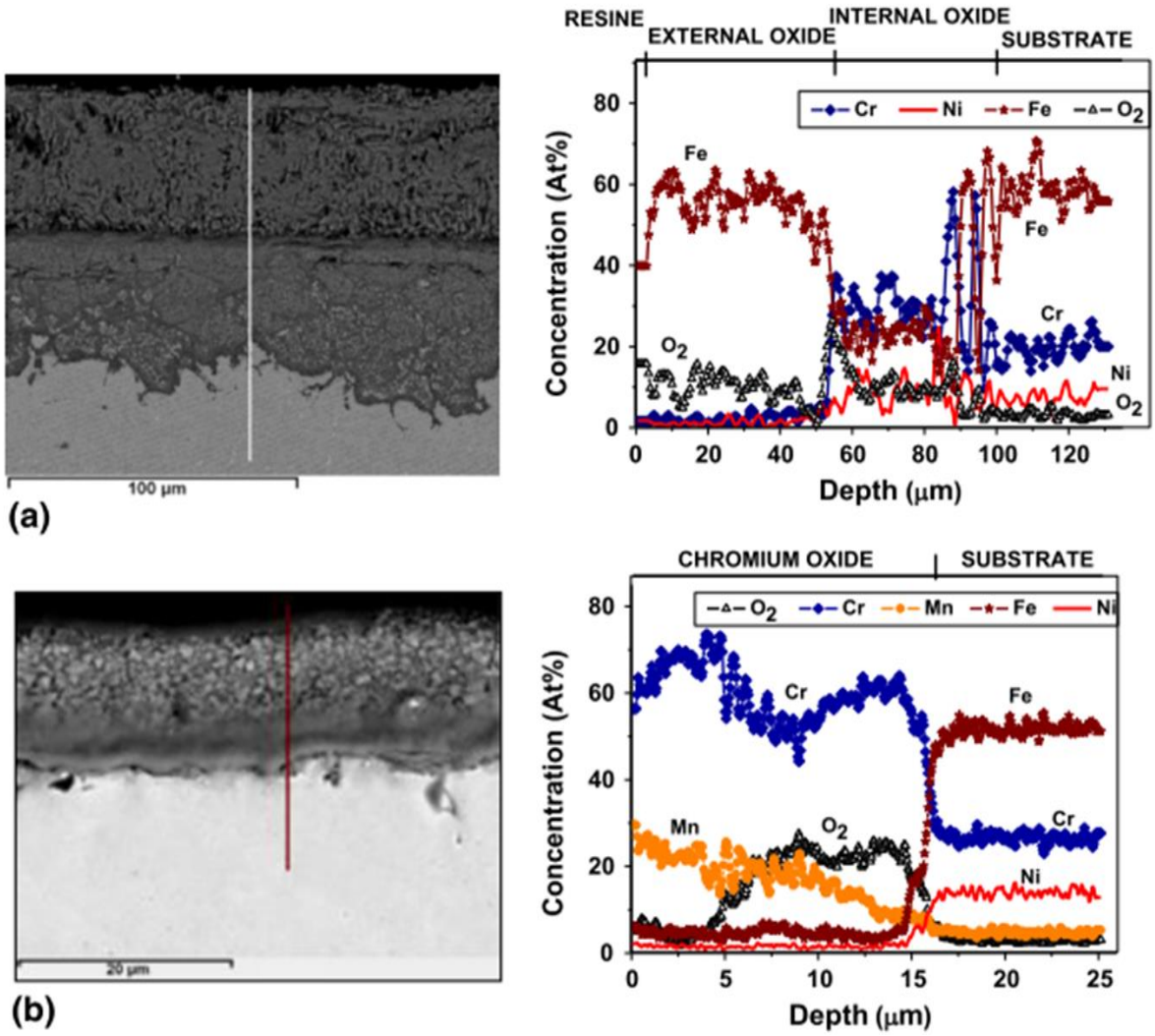

Figure 2-21 BSE micrographs and line scan analysis of cross sections after steam oxidation at 750 °C for 600 hours of steel without coating (a) AISI 316 and (b) AISI 304 [94].

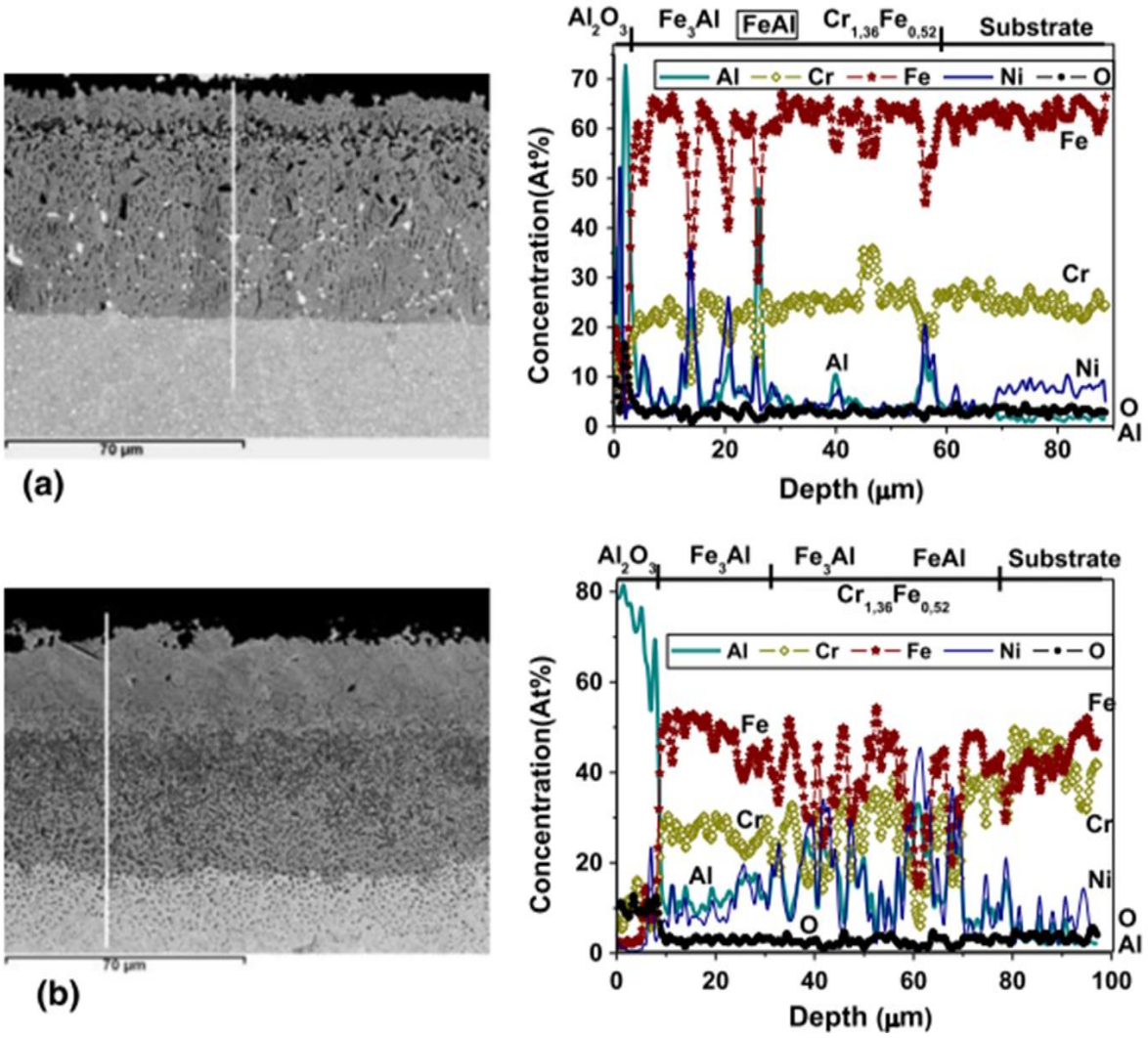

Figure 2-22 BSE micrographs and line scan analysis of cross-section of austenitic steels with Al-CVD-FBR coating oxidised 1023 K for 1000 hours: (a) Al/AISI 316 and (b) Al/AISI 304 [94].

The compositions of some common austenitic steels are given in Table 2-1 and the differences in oxidation behaviour with respect to the concentration of Cr within the alloy will be discussed since it has been postulated that the effect of water vapour on the oxidation behaviour is dependent on alloy composition [76].

Oxidation of 18/8 austenitic steels in steam environments at temperatures between 773 and 1073 K leads to the development of double layered oxide scales where the outer oxide is an Fe rich oxide and the inner oxide containing the remaining alloying elements [67].

Recent work on three different austenitic steels, TP347H FG, Super 304 H and HR3C, has been carried out to investigate their steam oxidation resistance at 923 K and 973 K and it was found that the most resistant of the three alloys investigated was HR3C, with TP347H FG showing the least resistance [20]. Of these three alloys, HR3C is the most Cr rich with 25 wt.% Cr compared to 18 wt.% for Super 304H and TP347H FG. This study found that there was also a temperature dependence on the steam oxidation resistance which was most pronounced with the lower Cr containing steels and showed mass gain increased with increasing temperature.

Investigations have been carried out into the effect of specimen surface finish on the steam oxidation resistance. It was found that ground surface finishes provided the best oxidation resistance and as received the worst as a result of enhanced Cr diffusion through dislocation paths. Samples with pickled surface finishes have been shown to cause an increase in the oxidation kinetics compared to ground surfaces [41], [55]. For this thesis, only as-received samples have been considered since this is the most applicable for industry and so the effects of surface finish will not be discussed in any further detail. For more information see [20], [101 – 103].

Figure 2-23 shows a schematic representation of the steam oxidation behaviour of TP347, the coarse grained version of the austenitic stainless steel used in this thesis, and TP347H FG. This schematic indicates a decrease in the oxidation rate for the fine grained version of the alloy [104]. Grain boundary diffusion is quicker than diffusion of elements through the bulk. Therefore the increased number of grain boundaries in the fine-grained version of the alloy results in faster formation of a protective scale hence limiting the amount of further oxidation.

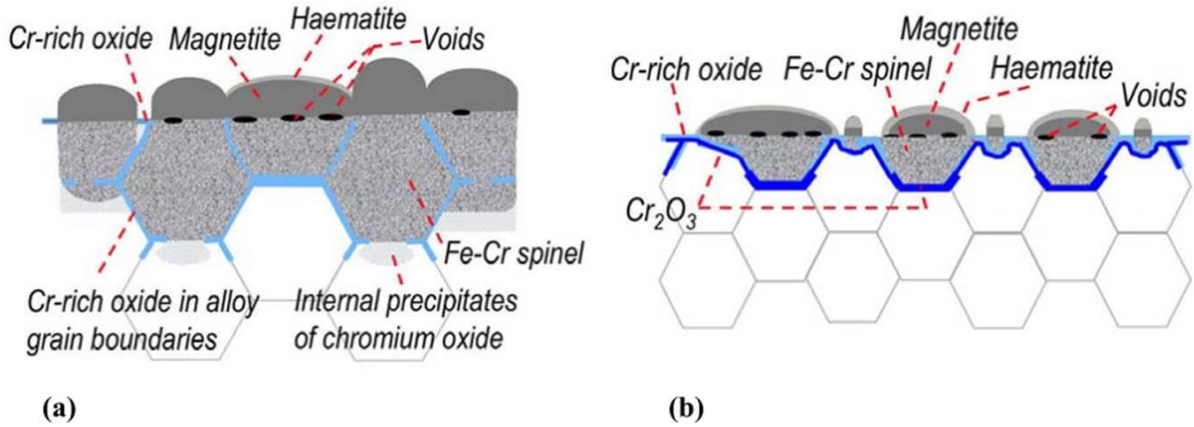

Figure 2-23 'Schematic representation of the oxide scale formed on TP347 in steam' where a) is for the coarse grained alloy and b) is for the fine grained alloy [105].

Figure 2-24 indicates the weight gain of model alloys at different temperatures and shows that for increasing Cr content there is a decrease in weight gain. The highest weight gain values observed are for the lower Cr containing steels studied. Increasing the Cr content allows the formation of protective oxides such as Cr_2O_3 which prevents further oxidation from occurring and hence reduces the weight gain. Spallation also results in the lower Cr containing alloys to have an increased mass gain due to the formation of large voids and coagulation between them. For higher Cr containing alloys, > 12%, there is also a reduced amount of temperature dependence compared to the lower Cr alloys.

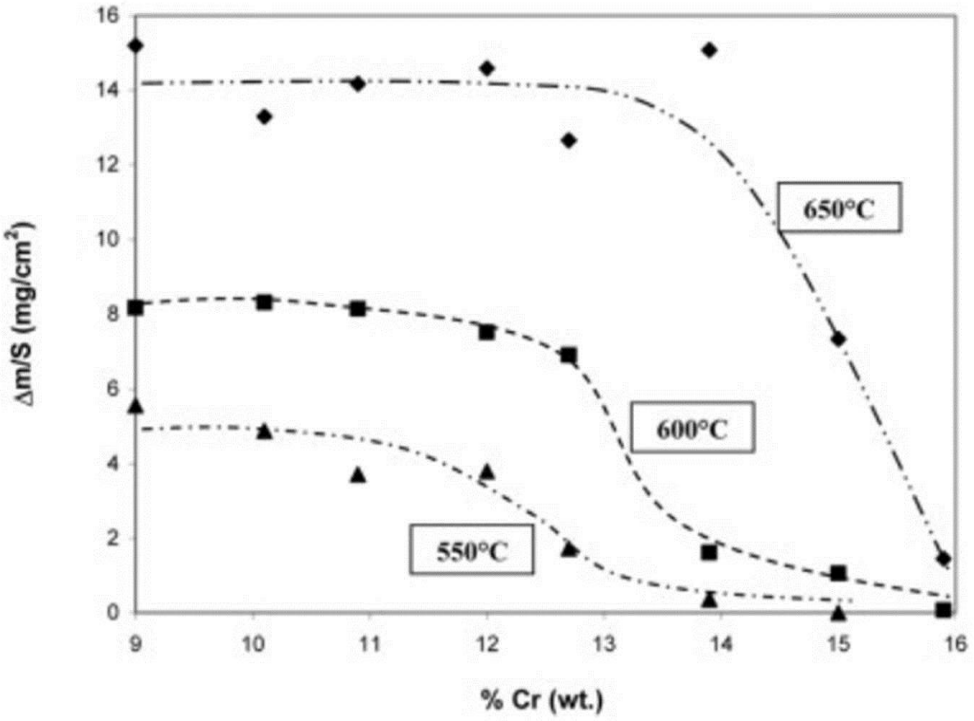

Figure 2-24 Weight gain of the Fe-Cr model alloys after 250 hours exposure in Ar-50%H_2O vs their Cr content [83].

2.3.7.5. Summary of Steam Oxidation

There is extensive data in the literature on steam oxidation that shows there is much to be considered when understanding the behaviour of steels exposed to this environment including the class of alloy, the concentration of Cr within the alloy and the O potential of the oxidising environment.

Generally, austenitic stainless steels show greater oxidation resistance to steam than do ferritic and martensitic steels [106]. Within the same class of alloys it has also been shown that a higher Cr concentration shows increased oxidation resistance [83].

Oxide growth and composition is also dependent on the steam conditions and oxygen partial pressure. Higher oxygen partial pressures lead to the formation of haematite which is not seen in deoxygenated steam environments. The effect of this haematite formation on steels will be discussed in further detail in Section 2.5.

2.3.8. Cyclic Oxidation

Material lifetime is greatly affected by thermal cycling and so it is important to consider oxidation behaviour under cyclic operating conditions. High thermal stresses may be developed during cyclic oxidation as a result of the mismatch in thermal expansion coefficients between the oxide scales and the underlying alloy [107], [108]. These stresses can then result in oxide scaling cracking and spallation. Further exposure under oxidising conditions may then result in breakaway oxidation and accelerated oxidation kinetics due to scale loss and depletion of protective elements.

A three-stage oxidation kinetic regime was observed when 9Cr-1Mo steel was exposed to Ar-10% water vapour at 873 K for up to 290 cycles consisting of 1 hour at temperature and 15 minutes cooling in an alumina tube [109]. Initially Cr favours the formation of $(Fe,Cr)_3O_4$ and is expected to limit the diffusion of cations outwards. As oxidation continues, the Cr concentration within the alloy depletes and is not high enough to maintain the formation of a protective oxide. At this stage, Fe diffuses outwardly and there is an increase in the oxidation kinetics. When the concentration of Fe reduces and the Cr concentration has again reached a level where a more protective oxide can form, kinetics decrease. Spallation was also observed in that study which could provide further cause for the increase in oxidation kinetics during the second stage.

Yan *et al*. [86] investigated the cyclic oxidation behaviour of 3 austenitic alloys, TP347H FG, wrought Super 304H (w304) and recrystallised Super 304H (r304). When w304 was exposed to a steam containing environment at 893 K for up to 1000 hours, a single chromia layer formed. TP347H FG and r304 on the other hand formed $(Fe,Cr)_3O_4$ and Fe_3O_4 oxides. Mass gain data from that work showed a decrease for TP347H FG after 100 hours oxidation but an increase with increasing cycle number for both 304 alloys. This was thought to be as a result in spallation of the outer oxide for TP347H FG.

Thermal cycling of 20Cr25NiNb stabilised stainless steel was studied when exposed to CO_2 atmospheres at 1123 K [110]. That work showed that the amount of spallation decreased with increasing number of thermal cycles and was at a minimum after 3 or 4 exposures.

Cyclic oxidation identified in the literature mainly considers thermogravimetric results during cycles. It is only when the final thermal exposure has been completed that the samples are examined in cross Section. It is therefore unclear whether or not, in some cases, spallation occurs on cooling after every cycle or only in the final one. The oxide chemistry is also unknown between each cycle.

2.4. Cr Evaporation

Selective oxidation of elements such as aluminium and Cr to form dense alumina and chromia oxides provide further oxidation resistance and increase a materials lifetime. Of particular interest for this thesis is the formation of Cr_2O_3. The establishment of Cr rich oxides is dependent upon the diffusion coefficient of Cr and also the concentration of Cr at the surface [111]. Several authors have used vacuum

annealing to evaporate Cr from the surface of steels [112], [113], since the evaporation of Cr has been suggested to be analogous to the selective oxidation of Cr [114]. The selective oxidation or evaporation of elements results in the surface being initially depleted and creates a depletion profile through the bulk. It was mentioned earlier in Section 2.3.7.4 that the lower the Cr concentration within an alloy, the faster the oxidation kinetics. This is also shown in Figure 2-25 below. An increase in oxidation kinetics can reduce the lifetime of a material. It is therefore important to understand the evaporation and selective oxidation of Cr and how this affects prolonged oxidation.

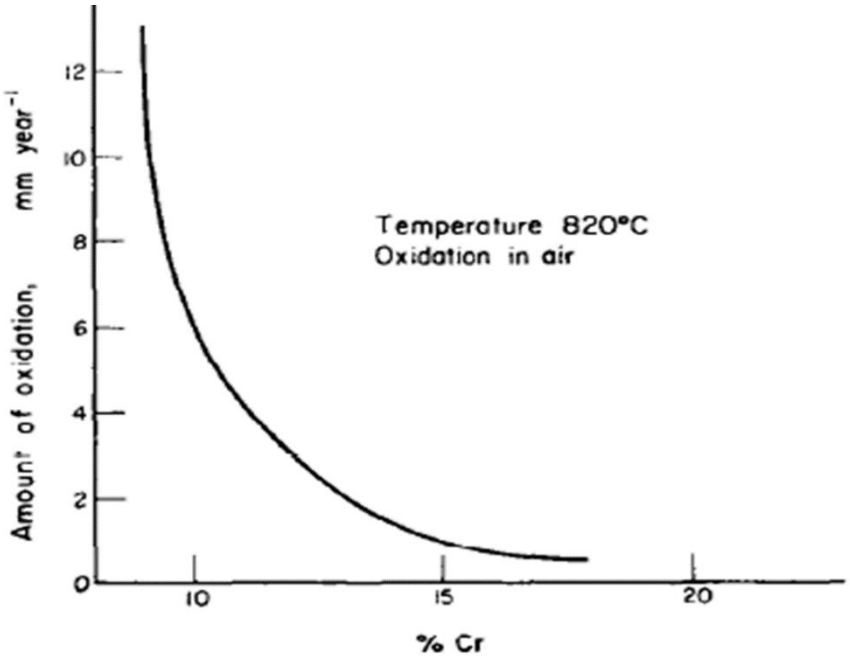

Figure 2-25 Rate of oxidation as a function of varying Cr content in Fe-Cr alloys [115].

The technique of vacuum annealing has previously been used to evaporate Cr for 20Cr-25Ni-Nb stabilised stainless steel [112], [113]. It was assumed in those investigations that the loss of Cr from the surface, i.e. the flux of Cr ions being evaporated, was proportional to the difference between the Cr concentration in

equilibrium with the vapour pressure, C_0, and the concentration of Cr at the surface, i.e.:

$$-D\left(\frac{dc}{dx}\right) = \alpha(C_0 - C_S) \quad \text{Equation 2-12}$$

where D is the diffusion coefficient of Cr in the alloy, $m^2.s^{-1}$, C is the concentration, at.%, x is the distance into the alloy where the surface is 0, m, α is the transfer coefficient of Cr leaving the surface, $m.s^{-1}$ and C_0 is the concentration in equilibrium with the vapour pressure, at.%. The transfer coefficient defines the evaporative mass loss.

The above equation along with $C_S = C_B$ at t = 0 where C_B is the bulk concentration in a semi-infinite solid describe the boundary conditions. The results of such conditions were given by Crank as [116]:

$$\frac{C_B - C}{C_B - C_0} = \boldsymbol{erfc}\left\{\frac{x}{2\sqrt{Dt}}\right\} - \boldsymbol{exp}\{\boldsymbol{hx} + \boldsymbol{h^2 Dt}\}.\boldsymbol{erfc}\left\{\frac{x}{2\sqrt{Dt}} + \boldsymbol{h}\sqrt{\boldsymbol{Dt}}\right\} \quad \text{Equation 2-13}$$

where erfc is the error function complement, t is time, s, and h=α/D.

Mathematical modelling, using the above equations, of depletion profiles obtained from experimental investigations allowed the transfer and diffusion coefficients for Cr to be determined for various steels.

Volatilisation of Cr oxides and degradation of Cr_2O_3 occurs during high-temperature oxidation above 1273 K to form CrO_3, CrO_2OH and $CrO_2(OH)_2$ through the following equations [72], [117], [118]:

$$\frac{1}{2}Cr_2O_3 + \frac{3}{4}O_2 \rightarrow CrO_3$$

$$\frac{1}{2}Cr_2O_3 + H_2O + \frac{3}{4}O_2 \rightarrow CrO_2(OH)_2$$

$$\frac{1}{2}Cr_2O_3 + \frac{1}{2}H_2O + \frac{1}{2}O_2 \rightarrow CrO_2OH$$

Research available in the literature suggests the increase in oxidation kinetics as a result of Cr volatilisation is due to the lack of a Cr rich protective scale preventing further [77].It has been shown that Cr volatilisation increases when alloys are oxidised in water vapour containing environments compared to air at temperatures between 1273 and 1473 K [119]. Results from work carried out by Caplan and Cohen [119] show that Cr_2O_3 evaporates to CrO_3.

It has been shown in the literature that generally, a higher concentration of Cr is required to form a protective healing layer for alloys exposed to steam and water vapour containing environments compared to air [47], [119], [120], [121]. It has been suggested that this is as a result of H_2O causing the protective Cr_2O_3 layer to decompose leading to the formation of volatile Cr species [75]. 20Cr25Ni steel exposed to CO/ CO_2 and 25Cr20Ni2.8Si and 304 steel exposed to air in the temperature ranges of 923 – 1286 K were found to require 16wt.% Cr to form a healing layer [59], [122], [123]. The protective nature of Cr_2O_3 has been suggested to be lost in water vapour because of its abilities to dissolve hydrogen ions [124].

Asteman *et al*. [81] investigated the oxidation behaviour of austenitic stainless steel 304L at 873 K when exposed to O_2 + 10%H_2O and found that after prolonged exposures, a mass loss was observed as a result of Cr evaporation. In that study, Cr evaporation was confirmed through the use of XPS analysis of a condensed phase on a cooled probe.

2.5. Oxide Stresses and Spallation

It has been suggested that spallation is dependent on the number and morphology of macroscopic defects present in the scale rather than scale thickness [92]. For example, voids within the outer oxide scale, the formation of which was discussed in Section 2.3.7.2, can cause a plane of weakness [1], [2], [125]. Once there is through scale cracking in the oxide and the voids have reached a critical value to coalesce leading to separation at the oxide/ oxide interface, decohesion of the outer oxide scale may occur [54], [83], [126], [86], [127], [128]. Zurek *et al*. showed that exposure of ferritic steels at 823 - 923 K formed voids which concentrated at the interface between the inner and outer oxide scales which resulted in spallation [129].

2.5.1. Introduction and Concerns in Industry

Oxides tend to be brittle in nature and so when they undergo stress, cracking and decohesion of the scale can occur potentially leading to spallation [130]. Failure of these oxides on the steam side of boiler tubing can compromise the safety of a power plant [131] since a build-up of spalled oxide can lead to erosion of turbine blades further downstream and tube overheating which will eventually result in tube rupturing such as that shown in Figure 2-26.

Figure 2-26 Example of tube rupture from plant experience [128].

The failure of oxide scales can occur when the oxide/ metal system undergoes compressive/ tensile stresses or strains [133] and the most commonly accepted reason as to why spallation occurs is the mismatch in coefficients of thermal expansion (CTE) between the metal and oxides [134]. Generally, alloys have much larger expansion coefficients compared to oxides as is shown in Table 2-5. On cooling from high temperatures these large differences result in the alloy contracting at a quicker rate than the oxide, putting the oxide under compression. There are various types of stresses in which the alloy/ oxide system can experience and lead to failure which will be discussed in this Section of the literature review.

Table 2-5 Average thermal expansion coefficients for a range of oxides and alloys.

Oxide/ Alloy	α x 10^{-6} /K^{-1}	Temperature range (K)
Fe_3O_4	12.0	373-923 [135]
Fe_3O_4	15.4	298-973 [136]
Fe_3O_4	18.4	373-973 [136]
Fe_3O_4	17	373-1273 [137]
Fe_2O_3	10.8	373-573 [137]
Fe_2O_3	12.2	373-1273 [2]
Fe_2O_3	11.0-14.1	298-1273 [138]
FeO	15	673-1073 [130]
FeO	12.2	373-1273 [139]
Cr_2O_3	7.3	373-1273 [139]
Cr_2O_3	8.5	673-1073 [130]
Fe	15.3	273-1173 [139]
Cr	9.5	273-1273 [139]
TP 347H FG	19.9	373 – 923 [2]

2.5.2. Stress Generation

The sources of stress can be split into two main categories: internal and external. Internal stresses can be developed through oxide scale growth, transformations or a mixture of the two. External stresses on the other hand are developed as a result of mechanical and/ or thermal stresses. Of these, the two most common routes of stress are growth and thermal stresses, closely followed by transformational stresses, each of which will be discussed in turn below.

2.5.2.1. Growth stresses

Growth stresses may be developed in a number of ways and the proposed mechanisms include [45]:

a) Volume differences between the oxide and metal from which it forms,
b) Epitaxial stresses,
c) Oxide formation within the scale, and
d) Specimen geometry.

In 1923, Pilling and Bedworth developed a model describing the origin of growth stresses in oxide layers. Their model suggests that the oxide growth takes place via O diffusion through the lattice. The Pilling-Bedworth ratio (PBR) is the ratio of the volume of oxide formed per metal atom to the volume of metal consumed per metal atom:

$$\boldsymbol{\Phi} = \frac{\boldsymbol{V_{ox}}}{\boldsymbol{V_m}}$$ Equation 2-14

where Φ is the PBR and V_{ox} and V_m are the molar volumes of oxide and metal, respectively. The PBR for some common oxide/ substrate combinations can be seen in Table 2-6.

Table 2-6 PBR values for common oxides and substrates [140].

System	PBR
FeO/ α-Fe	1.68
Fe_3O_4/ α-Fe	2.1
Fe_2O_3/ α-Fe	2.14
$Fe(Fe,Cr)_2O_4$/ Fe-Cr	2.1
$FeCr_2O_4$/ Fe-18Cr-8Ni	2.1
Fe_3O_4/ FeO	1.2
Fe_2O_3/ Fe_3O_4	1.02
Cr_2O_3/ Cr	2.07
Cr_2O_3/ Fe-25Cr-20Ni	2.1
SiO_2/ Si	2.15
Al_2O_3/ Al	1.28
NiO/ Ni	1.65
CoO/ Co	1.86
TiO_2/ Ti	1.73

When the PBR is greater than unity, such as with the FeO/ α-Fe combination shown in Table 2-6, the oxide, FeO, would be expected to be in compression. When the ratio is less than unity however, the oxide would be expected to be in tension. This model suggests when oxides are under tension and hence tensile stresses are present, the system is unable to maintain the protective oxide layer.

2.5.2.2. Transformational stresses

Transformational stresses are those which arise from a physiochemical or compositional change within the oxide which leads to a change in volume. This can be due to changes in the lattice parameter, changes in scale composition, and dissolution of O in metals such as Nb, Ta and Zr.

2.5.2.3. Thermal stresses

Even when there are no stresses present in the system whilst at the oxidation temperature, stresses can still be generated on cooling as a result of the difference in thermal expansion coefficients between the alloy and the oxide and this is the most significant form of stress generation in an oxidising environment.

The following equation was used by Tien and Davidson [141] to calculate the stress arising from a temperature drop. The oxide in this case is under biaxial compression and is planar.

$$\sigma_{ox} = -\frac{E_{ox}\Delta T(\alpha_m - \alpha_{ox})}{(1-\nu)\left(1+\frac{E_{ox}\xi}{E_m h}\right)}$$ **Equation 2-15**

where σ_{ox} is the stress in the oxide, Pa, E_{ox} is the Young's modulus, Pa, α_m and α_{ox} are the thermal expansion coefficients for the metal and oxide, respectively, K^{-1}, ν is the Poisson's ratio and h is the thickness, m.

The calculated stress will have a negative sign when the oxide is placed under compression, i.e. when the metals thermal expansion coefficient is higher than that of the oxide.

Equation 2-15 can be further simplified to the thin film approximation when the thickness of the metal is much larger than that of the oxide:

$$\sigma_{ox} = -\frac{E_{ox}\Delta T(\alpha_m - \alpha_{ox})}{(1-\nu)}$$ **Equation 2-16**

This equation assumes that each layer in a multi layered oxide system will all be reduced to the same dimensions as the alloy substrate. The strain, ε, in each of these oxide layers can then be calculated using:

$$\varepsilon_r = -\frac{\sigma_{ox}(1-\nu)}{E_{ox}} = -(\alpha_m - \alpha_{ox})\Delta T$$ **Equation 2-17**

2.5.3. Stress Relief

2.5.3.1. Failure in tension

When oxide fracture and spallation occurs as a result of tension it is more likely to be on heating past the oxidation temperature as opposed to cooling down. As already mentioned above, oxides with a Pilling-Bedworth ratio of less than 1, are expected to grow under tension.

Through scale cracks that originate at pre-existing flaws are likely to cause an oxide scale to fail in tension [130].

If the energy release rate, G, of a flaw exceeds the critical energy release rate of the material, G_{1c}, then the flaw will continue to grow under a stress, σ.

$$G > G_{1c}$$ Equation 2-18

and,

$$G = \frac{K^2}{E}$$ Equation 2-19

where E is the Young's modulus and K is the stress intensity factor of the flaw which is given by:

$$K = F\sigma\sqrt{(\pi c)}$$ Equation 2-20

where F is a numerical factor which is dependent on the shape and disposition of the flaw.

G_{1c} is also related to the surface fracture energy, γ:

$$G_{1c} = 2\gamma$$ Equation 2-21

Therefore, the flaw will continue to grow if:

$$\frac{\sigma^2 F^2 \pi c}{E} = 2\gamma$$ Equation 2-22

2.5.3.2. Failure in compression

When cooling from high temperature, the oxide is normally under compression, as mentioned earlier. There are two possible routes to consider for failure in compression known as wedging (route I) and buckling (route II), as shown schematically in Figure 2-27 and each of these mechanisms will be considered in turn.

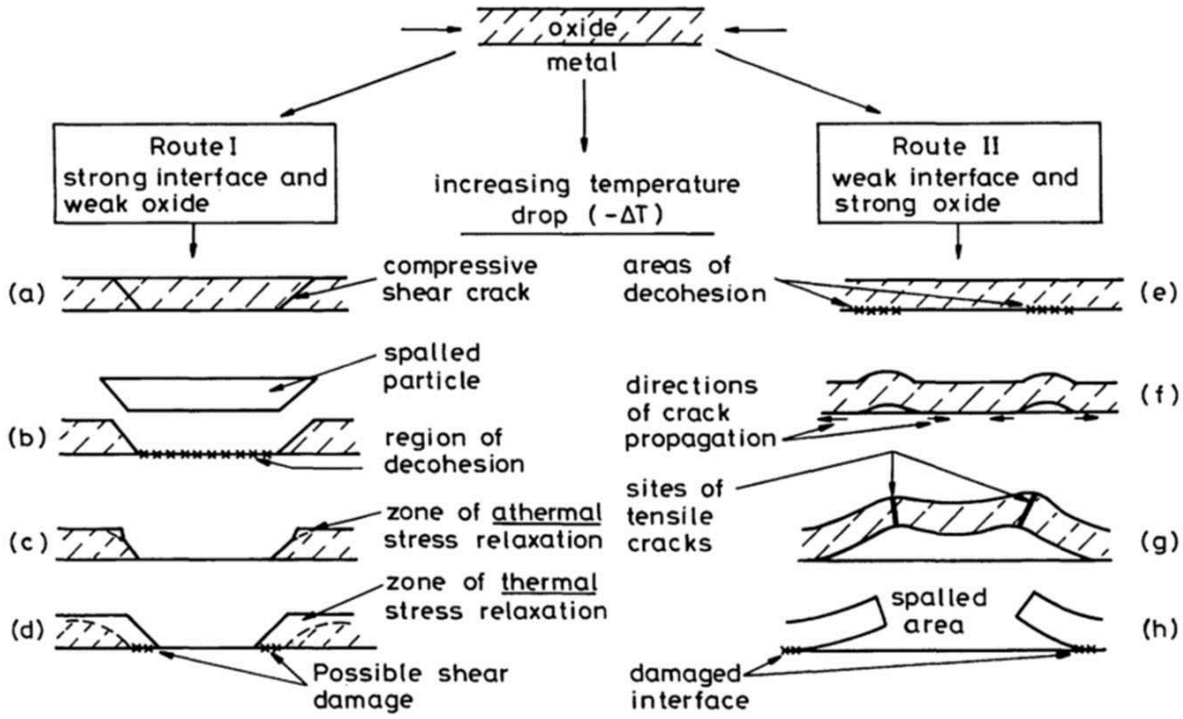

Figure 2-27 Failure in compression [142].

2.5.3.2.1. Wedging mechanism – route I

The wedging mechanism occurs when the interface is stronger than the oxide and requires no pre-existing defects to be present interfacially [143]. The formation of inclined shear cracks reduces the strain energy within the oxide. This mechanism is shown schematically in Figure 2-28 proposed by Evans *et al.* [144]. Growth of a tensile wedge crack at the oxide-metal interface will cause the oxide to spall when stimulated by subsequent cooling. The stress is thought to arise intrinsically from growth processes such as those mentioned above and will develop during a temperature change as a result of the differences in thermal expansion coefficients between the oxide and the metal.

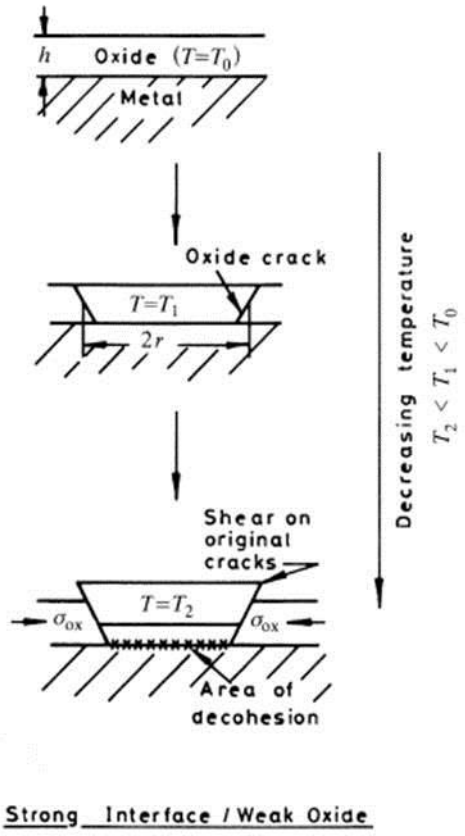

Figure 2-28 Wedging mechanism [144].

Until the spallation event has occurred, the oxide remains adherent and is planar. The oxide layer is also assumed to be 'stressed under equal biaxial conditions, i.e. for principal stresses σ_1, σ_2' [144]:

$$\sigma_1 = \sigma_2 = \sigma_{ox} \qquad \text{Equation 2-23}$$

As already mentioned above, the stresses are brought about by the difference in thermal expansion coefficient between the metal and the oxide but it is also thought to be caused intrinsically by the growth process. Therefore, the oxide stress can be given by:

$$\sigma_{ox} = (\sigma_i + E_{ox}\Delta T\Delta\alpha)$$ Equation 2-24

where E_{ox} is the Young's modulus of the oxide and is equal to the ratio of tensile stress over extensional strain, and σ_i is the intrinsic growth stress, both of which can be assumed to have negligible temperature dependence.

It is then possible to get the elastic stored energy, W^*, from the above equation and also from the fact that the Poisson contraction produces strains:

$$\varepsilon_1 = \varepsilon_2 = \left(\frac{\sigma_{ox}}{E_{ox}}\right)(1-\nu)$$ Equation 2-25

The elastic stored energy is then:

$$W^* = \frac{1}{2}\sigma_1\varepsilon_1 + \frac{1}{2}\sigma_2\varepsilon_2$$ Equation 2-26

Substituting Equations 2-24 and 2-25 into 2-26 gives:

$$W^* = \frac{1}{2}\sigma_{ox}\left[\left(\frac{\sigma_{ox}}{E_{ox}}\right)(1-\nu)\right] + \frac{1}{2}\sigma_{ox}\left[\left(\frac{\sigma_{ox}}{E_{ox}}\right)(1-\nu)\right]$$ Equation 2-27

Hence,

$$W^* = \frac{(\sigma_i + E_{ox}\Delta T\Delta\alpha)^2}{E_{ox}}(1-\nu)$$ Equation 2-28

Growth stresses, σ_i, can be considered to have a negligible contribution to the strain energy and so Equation 2-8 then becomes:

$$W^* = (\Delta T)^2(\Delta\alpha)^2(1-\nu_{ox})E_{ox}$$ Equation 2-29

$$\Delta T_w = \left(\frac{\gamma_F}{\xi E_{ox}(\Delta\alpha)^2(1-\nu)}\right)^{1/2}$$ Equation 2-30

This route of failure is more commonly associated with thicker oxides and strong interfaces. An example of the cracks that form in the first stages of wedge cracking are shown in Figure 2-29 [145].

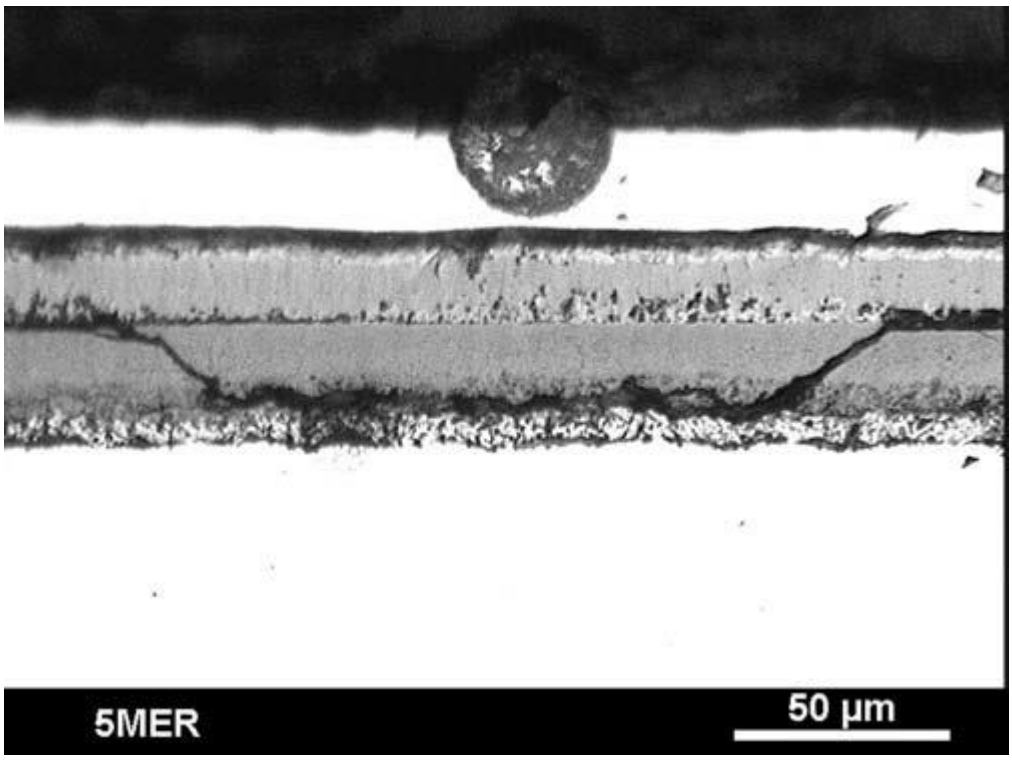

Figure 2-29 Cracks in the oxides formed on P92 steel oxidised in steam for 500 hours at 873 K [145].

2.5.3.2.2. Buckling mechanism – route II

The buckling mechanism occurs when the oxide is stronger than the interface and is favoured by thinner oxide. This mechanism is shown schematically in Figure 2-30 proposed by Evans *et al*. [144]. The strength of the interface is relatively low either intrinsically or as a result of void formation or the segregation of trace elements.

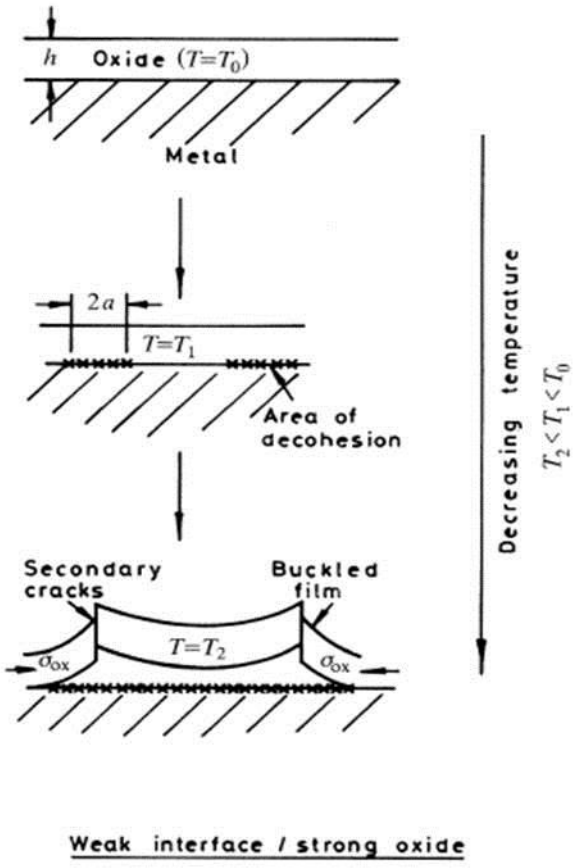

Figure 2-30 Buckling mechanism [140].

Assuming elastic conditions, the critical compressive stress to form a buckle over an area of interfacial decohesion of radius R is given by:

$$\sigma_b = \frac{1.22\ x\ E_{ox}}{(1-\nu^2)}\left(\frac{\xi}{R}\right)^2$$ Equation 2-31

where σ_b is stress, Pa, E_{ox} is the Young's modulus of the oxide, Pa, v is Poisson's ratio and ξ is thickness, m.

Here it is being assumed that the only source of stress is that deriving from differential thermal contraction. Therefore, the critical temperature drop required to initiate a buckle demonstrated by A.G. Evans and J. W. Hutchinson [142] is:

$$\Delta T_b = \frac{1.22}{\Delta\alpha(1-\nu)^2}\left(\frac{\xi}{R}\right)^2$$ Equation 2-32

The critical temperature drop required to initiate a buckle therefore increases with the increasing thickness of oxide for a given R value, as can be seen in Equation 2-32.

An example of failure by buckling on P92 steel in steam can be seen in Figure 2-31 [145].

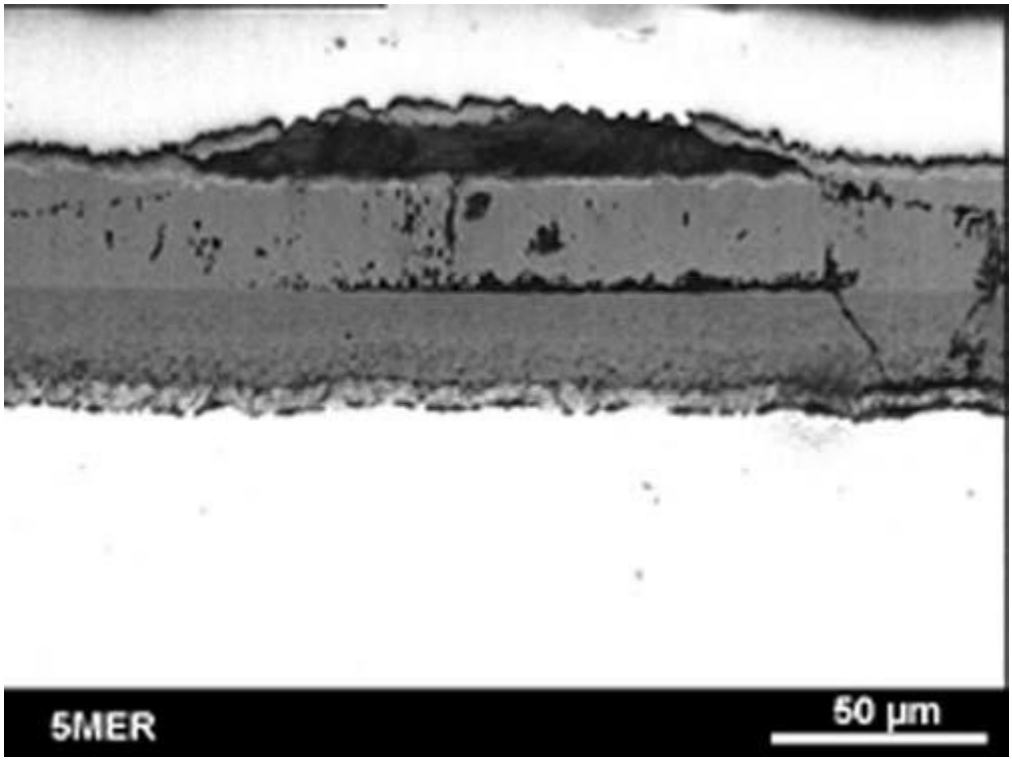

Figure 2-31 Buckling failure at the haematite/ magnetite interface in P92 steel oxidised in steam for 500 hours at 873 K [145].

2.5.3.2.3. Unstable Buckling

Spallation can sometimes not occur immediately at the time of buckling but is still possible if lateral propagation of the buckle occurs. Propagation of areas of decohesion may occur as a result of several buckle sites coalescing, shown

schematically in Figure 2-27(f). Crack propagation can be described by the following equation [143]:

$$\Delta T_{ub} = \left(\frac{1.052\xi^4}{R^4} + \frac{1.041\gamma_F}{E_{ox}\xi}\right)^{1/2} \frac{1}{\Delta\alpha} \quad \text{Equation 2-33}$$

where the first term in the equation relates to that to initiate the first buckle and the second term relates to its propagation.

2.5.4. Monitoring of Spallation

Osgerby [145] used acoustic emission to monitor the spallation behaviour of P92 at 873 K and found that cracking occurs over a range of temperatures at a ΔT of 373 – 423 K where ΔT is oxidation temperature – decohesion temperature [145]. In that study, only haematite was found to spall which was confirmed through X-ray Diffraction (XRD). SEM also revealed that tensile cracks could be seen in magnetite and spinel oxides. Further analysis of the results presented in that work showed maximum tensile stress in magnetite and maximum compressive stress in haematite coincides with the increased AE signals observed during cooling hence indicating that is the critical temperature drop required to initiate spallation. Singh Raman *et al*. [61] also used acoustic emission to monitor spallation and found that a sudden increase in activity was observed after around 4 hours isothermal oxidation of a high-Si steel.

Hayashi *et al*. [148] recently used the technique of dynamic visual observation to detect spallation on cooling for ferritic and austenitic stainless steels exposed to air environments at 1273 K for times up to 1000 hours. A camera was used to take images of the samples on cooling at 50 K intervals in order to detect a temperature

range in which spallation first occurred. An improvement to this technique would be to image the samples at 10 K intervals rather than 50 K to get a clearer idea of what is occurring between these temperatures. However, the cooling rate may be too high to allow such images to be taken.

Raman and Micro-raman spectroscopy have been used to study stresses. Galerie *et al*. [149] determined a value of thermal expansion coefficient for chromia on stainless steel as 10.8 x 10^{-6} K^{-1}. Guerain *et al.* [150] used micro-raman spectroscopy (MRS) to study delamination and spallation using stress maps as well as Atomic Force Microscopy (AFM) to determine the geometrical characteristics of buckle types. It was found in that study that buckle propagation is dependent on the local toughness value. In both of the studies mentioned here using a form of raman spectroscopy, spallation of chromia was able to be studied because of its ideal fluorescence wavelength. As a result, other oxides such as magnetite and haematite that do not fluoresce at the appropriate wavelength cannot be studied using this technique.

Despite the extensive research that has been carried out on the various techniques discussed to observe spallation there is no technique in the literature that has been described to both detect and image the point at which spallation occurs.

2.5.5. Spallation models

2.5.5.1. Oxide Scale Failure Diagram

Several oxide scale failure diagrams exist in the literature to predict the onset of spallation. The most relevant one to the work presented in this thesis is that developed by Evans *et al.* [144] shown in Figure 2-32 which uses Equations 2-30 and 2-32 to plot the boundaries for wedging and buckling failure mechanisms, respectively.

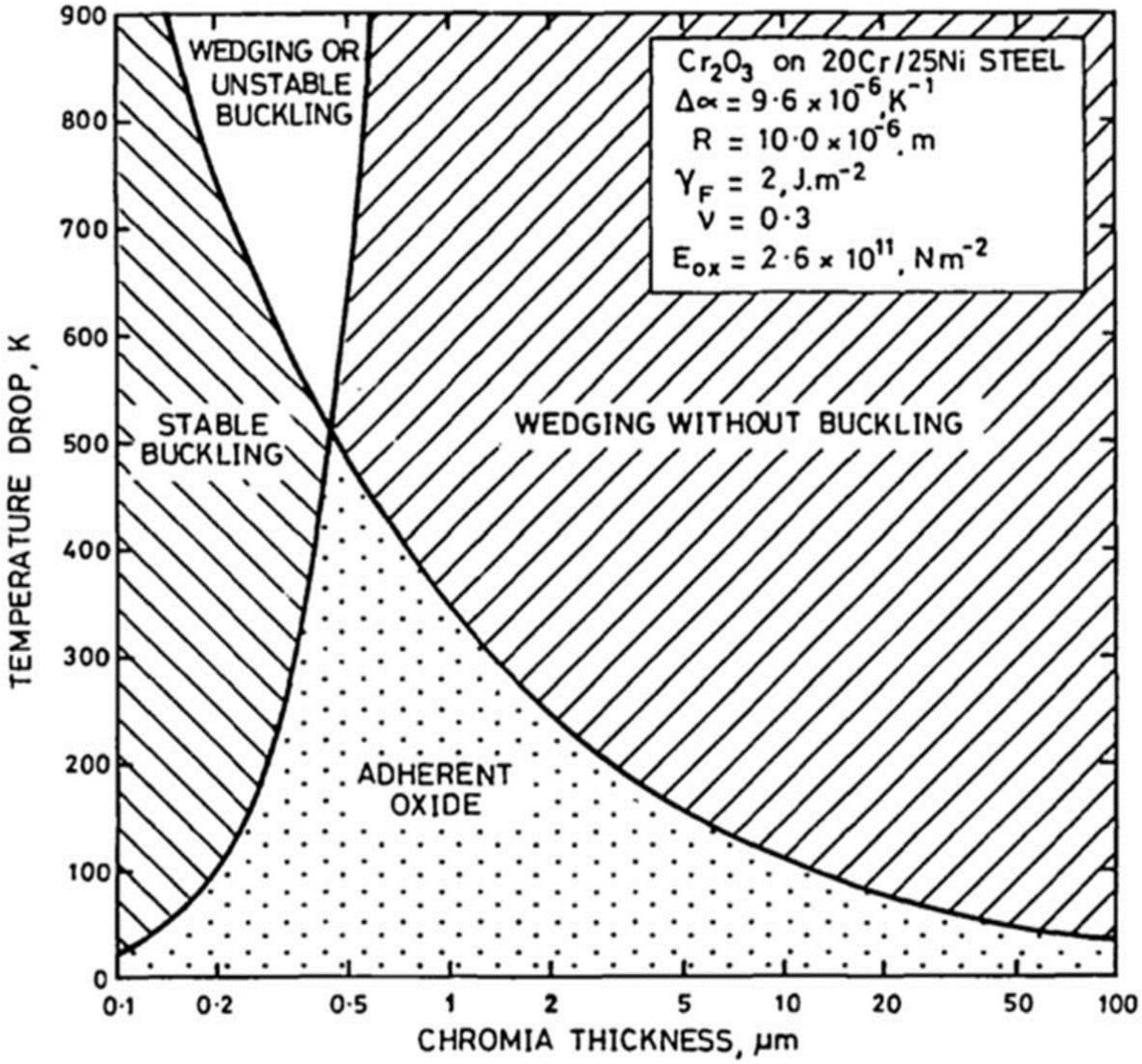

Figure 2-32 Spallation map developed by Evans *et al*. for a chromia scale on a 20Cr-25Ni-Nb stabilised stainless steel [144].

Another approach to oxide scale failure diagrams is shown in Figure 2-33 developed by Armitt *et al*. [136] in EPRI report FP-686 which identifies critical strain values as a function of spalled oxide thickness.

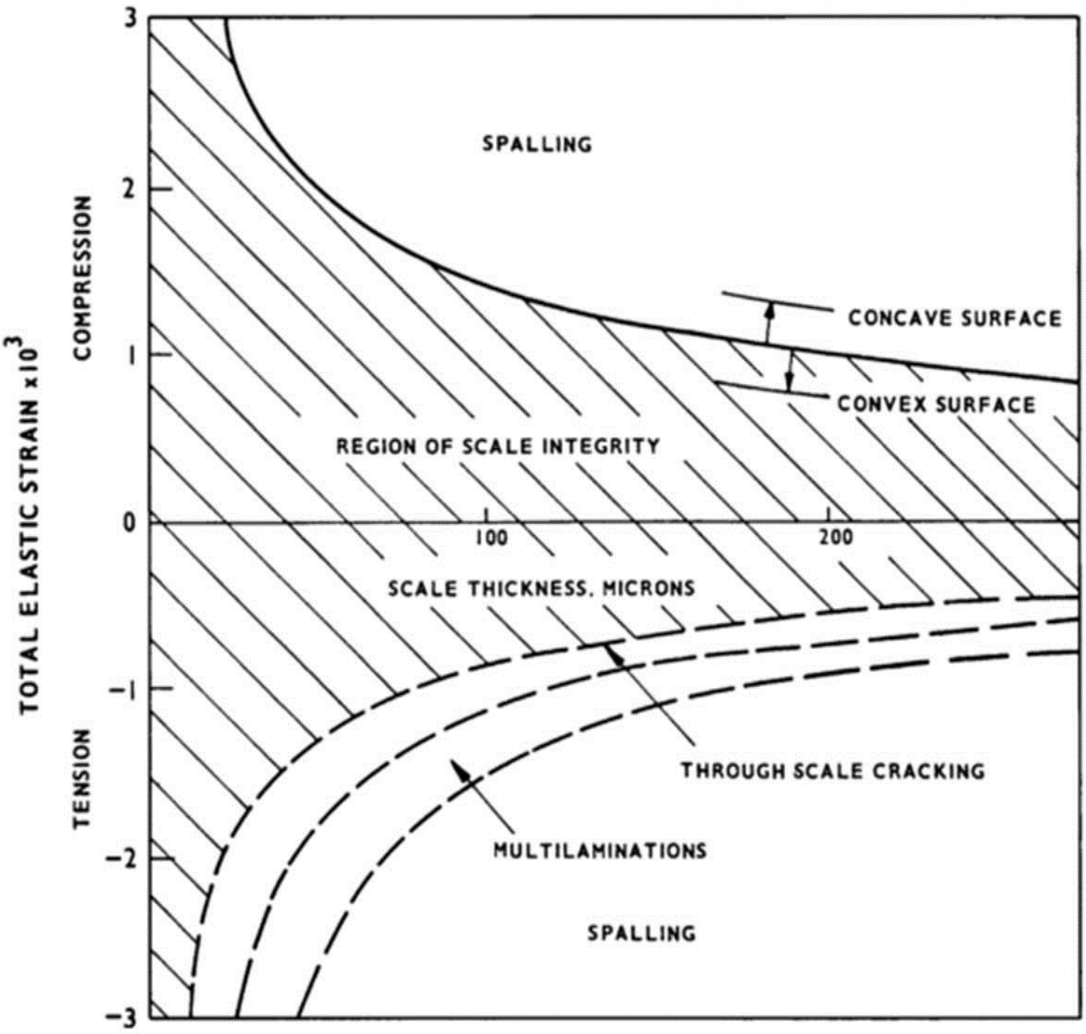

Figure 2-33 Scale failure diagram developed by EPRI in report FP686 [136].

Schutze *et al.* [133] developed a model that takes into consideration the defects of the oxide scale and reflects the effect of operational history. This scale failure diagram can be seen in Figure 2-34 and has used the original EPRI approach shown in Figure 2-33 as a foreground diagram. Sub planes then exist beneath the original approach to describe parameters such as physical defect size, porosity and interface roughness. A single parameter ω_0 is used to quantify “high impact” parameters that

are dependent on operational history and η(m) is used to quantify "low impact" parameters that are not completely dependent on temperature and so can be considered quasi-constant.

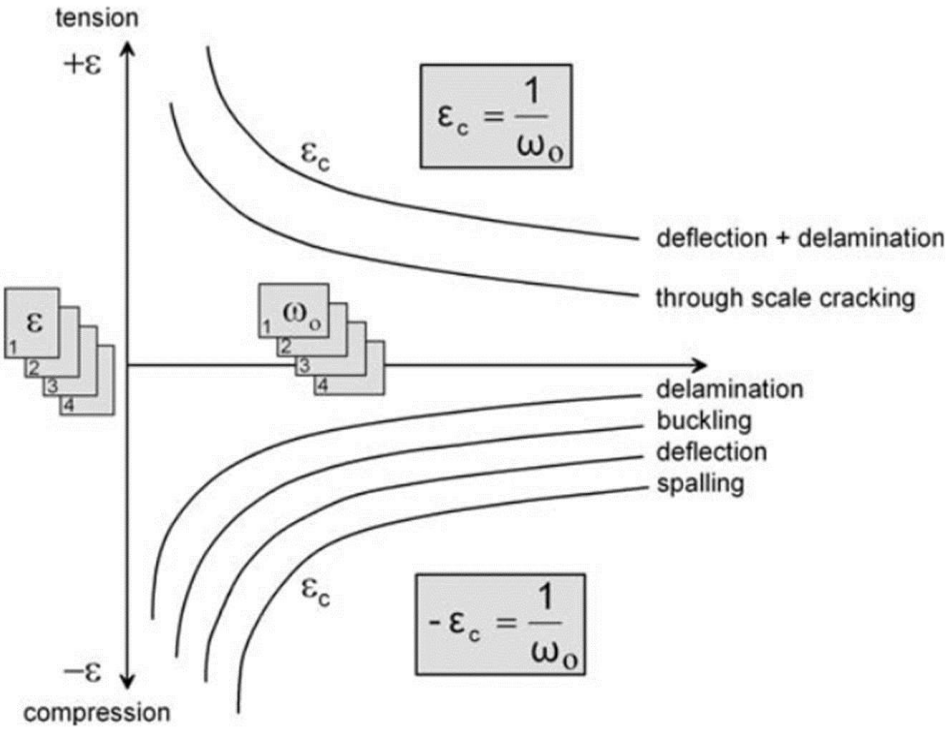

Figure 2-34 Example of an advanced scale failure diagram developed by Schutze *et al*. [133]

2.5.5.2. Cyclic Oxidation Failure Models

There are several models in the literature that predict the way in which an alloy will behave when it undergoes cyclic oxidation and the effect this has on spallation. One such model is known as COSP, and is a 'Program which models the Cyclic Oxidation weight gain and Spallation process' [151]. That model was developed by J. Smialek [134] who proposed the model for cyclic oxidation that predicted net weight change, amount of O and metal consumed and amount of oxide spalled. The model was based upon the assumption that a constant area fraction will spall at the oxide/ metal interface to produce bare metal surface at each cycle [134].

2.6. Research Gaps in the Literature

Austenitic stainless steels are commonly used as boiler tubing in coal and biomass power plants, particularly as heat exchanger tubing in the boiler. The cyclic nature of the biomass fired power plants will affect the materials lifetime. Much of the research already available in the literature analyses the end result of a series of cyclic oxidation experiments rather than inspecting the behaviour between cycles to determine trends in behaviour. This demonstrates the need for further work to be carried out into the cyclic oxidation of steels commonly exposed to harsh operating conditions such as those seen in power plants.

Numerous methods have been explored in the literature to determine the temperature at which oxide spallation occurs. However, it has not yet been possible to simultaneously image and detect localised delamination and spallation events with one technique. This inability has resulted in a generalisation being made when modelling spallation. This highlights the need to develop a method that can identify a delamination and spallation event whilst at the same time ascertain the temperature required to initiate such events. Understanding the spallation behaviour of commonly used materials will help to produce a model used to predict the onset of spallation.

2.7. Research Aims and Objectives

Based on the gaps in the literature identified in this review, the main aims and objectives of this thesis were as follows:

- Study the oxide spallation behaviour under isothermal conditions. Studying the oxidation behaviour under isothermal conditions will lead to a deeper

understanding of the spallation mechanism and allow further understanding of how this will affect the oxidation behaviour in subsequent cycles.

- Investigate the oxide growth kinetics of TP347H FG in steam. There is minimal data available in the literature on the oxidation kinetics of individual oxide layers since it is mostly reported as mass gain data. The determination of kinetics for the oxide layers will allow a better understanding of the oxidation process.
- To investigate the cyclic steam oxidation and spallation behaviour of austenitic stainless steel, TP347H FG, commonly used as heat exchanger tubing in coal fired power plants. Investigations of oxide chemistry and behaviour between each thermal cycle will allow a greater understanding of the oxidation mechanism.
- Compare the effects of oxygen partial pressure on oxidation behaviour subsequent to the initial spallation event.
- Determine the effect of depletion/ segregation zones within the alloy substrate. Depletion of Cr during oxidation may result in breakaway oxidation therefore increasing the oxidation kinetics.
- Determine the critical Cr concentration required to form a healing layer to understand the oxidation behaviour under thermal cycling conditions.

Chapter 3 – Experimental Procedure

3.1. Introduction

The main focus of this work was on a 300 series austenitic stainless steel known as TP347H FG, the nominal composition of which is shown in Table 3-1. This material is commonly used in superheater and reheater tubing within fossil fired power plants that are expected to be converted to biomass plants.

Table 3-1 Nominal composition of TP347H FG provided from the data sheet supplied.

	C	Si	Mn	S	P	Ni	Cr	Nb	Fe
wt.%	0.09	0.4	1.48	0.001	0.026	11.34	18.21	0.88	balance
at.%	0.41	0.79	1.49	0.002	0.046	10.66	19.32	0.52	balance

This chapter describes the methods and analytical techniques used to investigate oxide growth kinetics and spallation behaviour on the chosen material, TP347H FG, where TP is tube piping, H is high carbon content and FG is fine grained. Although this material is described as fine-grained this is only meant in terms of grain size relative to the standard alloy TP347H where the grain sizes are 110 μm [104] or 5.5 (ASTM) [152] and 20 μm [104] or 9.1 (ASTM) [152] for the original alloy and the fine grained version, respectively. The tubing provided was pickled using a commercially sensitive method. Common methods for pickling include hydrochloric acid and the less commonly used sulphuric acid [21].

This chapter is split into two main sections where the details of sample preparation prior to both oxidation and vacuum annealing are given in Section 3.2 followed by details on the steam oxidation rigs including set up and operation, given in

Section 3.3. The rest of the chapter will discuss vacuum annealing in Section 3.4 and sample preparation post experimental work and analysis carried out for the work in Sections 3.5 – 3.6.

3.2. Sample preparation prior to steam oxidation and vacuum annealing

Specimens of TP347H FG for both steam oxidation and vacuum annealing experiments were prepared from standard tubes as installed in plant, supplied by Sumitomo Metal Industries Ltd. The tubing had an internal diameter of 14 mm and a wall thickness of 4.5 mm. The tubing was cut into 10 mm lengths using an aluminium carbide disc on a Struers Ltd. Accutom-5 precision cutting machine at a low speed, <0.05 mm.min^{-1}. These were subsequently sectioned into arcs of approximately 60° using the same method. Typical specimen dimensions can be seen in Figure 3-1 and were measured using a Fisher Scientific Model FB 70250 digital micrometer accurate to ±0.03 mm.

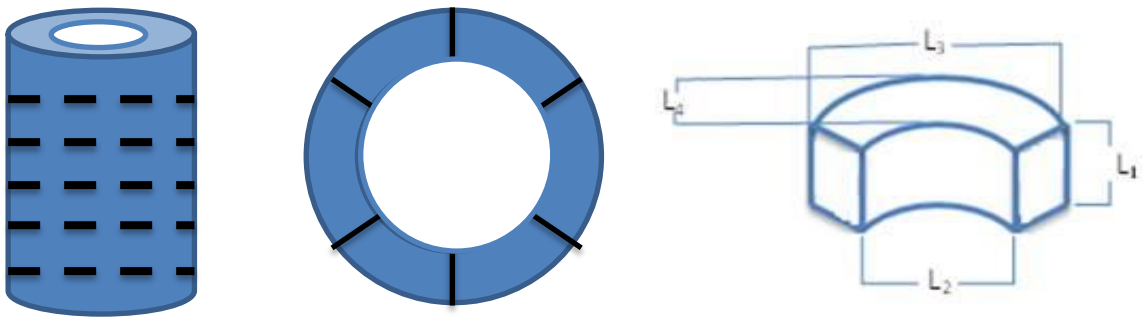

Figure 3-1 Typical sample dimensions and the measurements taken to calculate the surface area of the sample (L1 = 10 mm; L2 = 14 mm; L3 = 18 mm; L4 = 4.5 mm).

Before the samples underwent either steam oxidation or vacuum annealing small incisions were made on the side of each specimen, L_2, using a Si carbide disc on a South Bay Technology Model 650 low speed diamond saw to aid site location during

surface analysis between each experimental exposure and cycle. Typical incisions made on each specimen can be seen in Figure 3-2. These incisions were also useful in spall site identification using the thermal imaging camera, as discussed later.

Prior to steam oxidation or vacuum annealing tests the samples, once cut and incisions made, are cleaned in ethanol in a James Products sonic 3D ultrasonic cleaning tank for three minutes per sample. Each specimen was then weighed using a top-pan Sartorius MC1 research RC210P analytical balance accurate to ±0.000005 g.

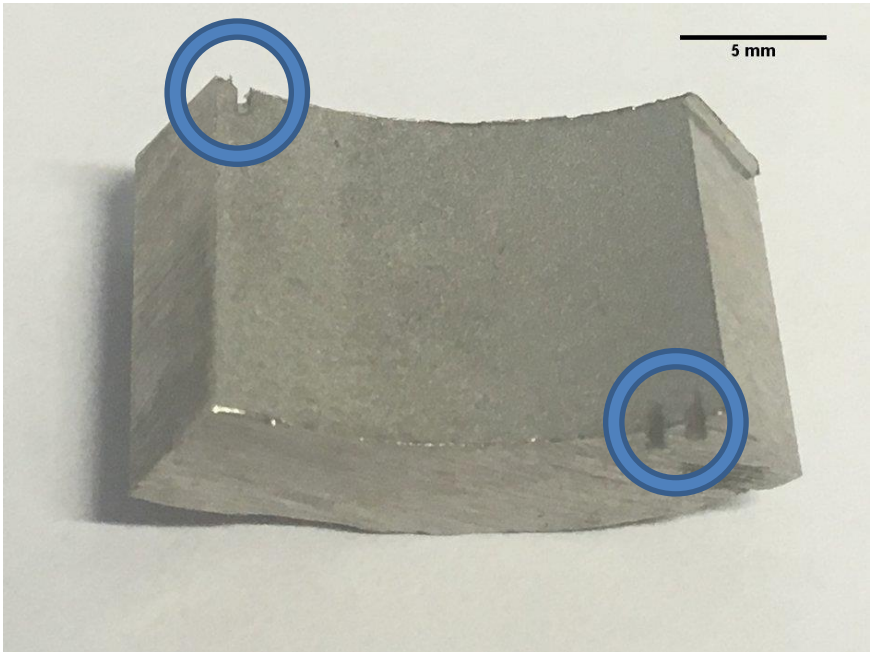

Figure 3-2 Optical image of TP347H FG specimen with incisions along L2.

3.3. Steam oxidation

3.3.1. Introduction

This section describes both the equipment and procedure used for steam oxidation experiments performed throughout this study.

The steam oxidation rigs were fully operational at the start of this work and were assembled for use in a previous project [21]. They were originally based on the facilities used at NPL although some modifications have been made throughout this project. Plan preventative maintenance has also been carried out throughout the duration of this work.

3.3.2. Steam Oxidation Equipment

This section will discuss the equipment involved in steam oxidation experiments. A schematic of the current set up of the steam rigs is shown in Figure 3-3 and the purpose of each of the major components is discussed below.

The water for the steam oxidation experiments was supplied from a deionised water reservoir into two pressurised water storage tanks labelled Barrel A and Barrel B on Figure 3-3. Water quality in power plants is monitored to ensure high purity and this was replicated for this work.

Several one way valves, 1-4 on the schematic, were used within the set-up of the steam rigs. Relief valve 2 controlled the inlet of gas into the water barrels and was set to a pressure of 0.3 bar. The gas cylinders were controlled with pressure regulators that were set to 1 bar. Relief valve 1 was in place to reduce too much pressure and would be activated at a level of 2 bar. Valves 3 and 4 were set to a

pressure of 0.5 bar and controlled the water inlet and pressure relief of the barrels, respectively. The valves were maintained throughout the duration of this study to ensure they were in a good working condition.

A Grundfos DDE6/10-B-SS/T/SS-X9772-31AAFG digital dosing pump controlled the input of water from the barrel into the steam oxidation furnaces to approximately 5 $ml.min^{-1}$ per work tube.

The work tube used for these tests was made of Kanthal APM, an FeCrAl alloy which is an alumina former. This material was chosen to prevent further reactions occurring with the samples. Both ends of the work tube were sealed. This is important for deoxygenated environments to ensure that no air is entering the tube during oxidation. End 1 of the work tube is also positioned slightly higher than End 2 to ensure a downward flow of water/ steam.

A stainless steel T junction is attached to the end of the work tube to which a stainless steel water trap is fitted. The T junction also allows a calibrated n-type thermocouple to be inserted into the work tube and enables in situ temperature monitoring. Readings were taken from the in situ thermocouple. Measurements were recorded in a log book at regular intervals during both set up and for the duration of the test.

The final segment of the rigs is a condensing water trap. The water trap is manually emptied periodically. The shape of the tubing from the furnace to the condensing water trap is designed to ensure the steam condenses at the bottom of the tube since there is a cold water reservoir in the trap, up to the line shown in the schematic. The role of the condensing water trap is to prevent a steam hammer from forming and

also to ensure that no steam flowed back in the opposite direction which was particularly important for deoxygenated steam tests. The elevated level of End 1 of the work tube also aided in the prevention of steam hammer formation.

3.3.3. Procedure Prior to Oxidation

Before testing was started, a reservoir of deionised water was provided to the work barrels and filling, where water is fed by a pump, and emptying was controlled manually with a control box. The deionised water in Barrels A and B, shown in Figure 3-3, were purged with either air or O-free nitrogen to produce air-saturated or deoxygenated environments, respectively. This purging lasted at least 24 hours to ensure the desired environment was achieved and the purging process continued for the duration of the test. The O levels were previously monitored using a Hach Orbisphere 410 O meter and it was found that the time period of 24 hours was required to achieve a satisfactory deoxygenated steam environment of 10 ppb O; this is similar to that which is seen in plant [153]. Degassing was controlled by a check relief valve under approximately 0.3 bar of pressure, shown as relief valve 2 on Figure 3-3.

The use of the barrels was alternated where one was filled from the reservoir whilst the other was providing water to the furnace. At the beginning of this work, a flow meter was attached only to furnace one and was used to manage the water flow between the two furnaces but this was decided not to be adequate enough and so a second flow meter was included in the rig set-up on the second furnace to more accurately balance the water flow.

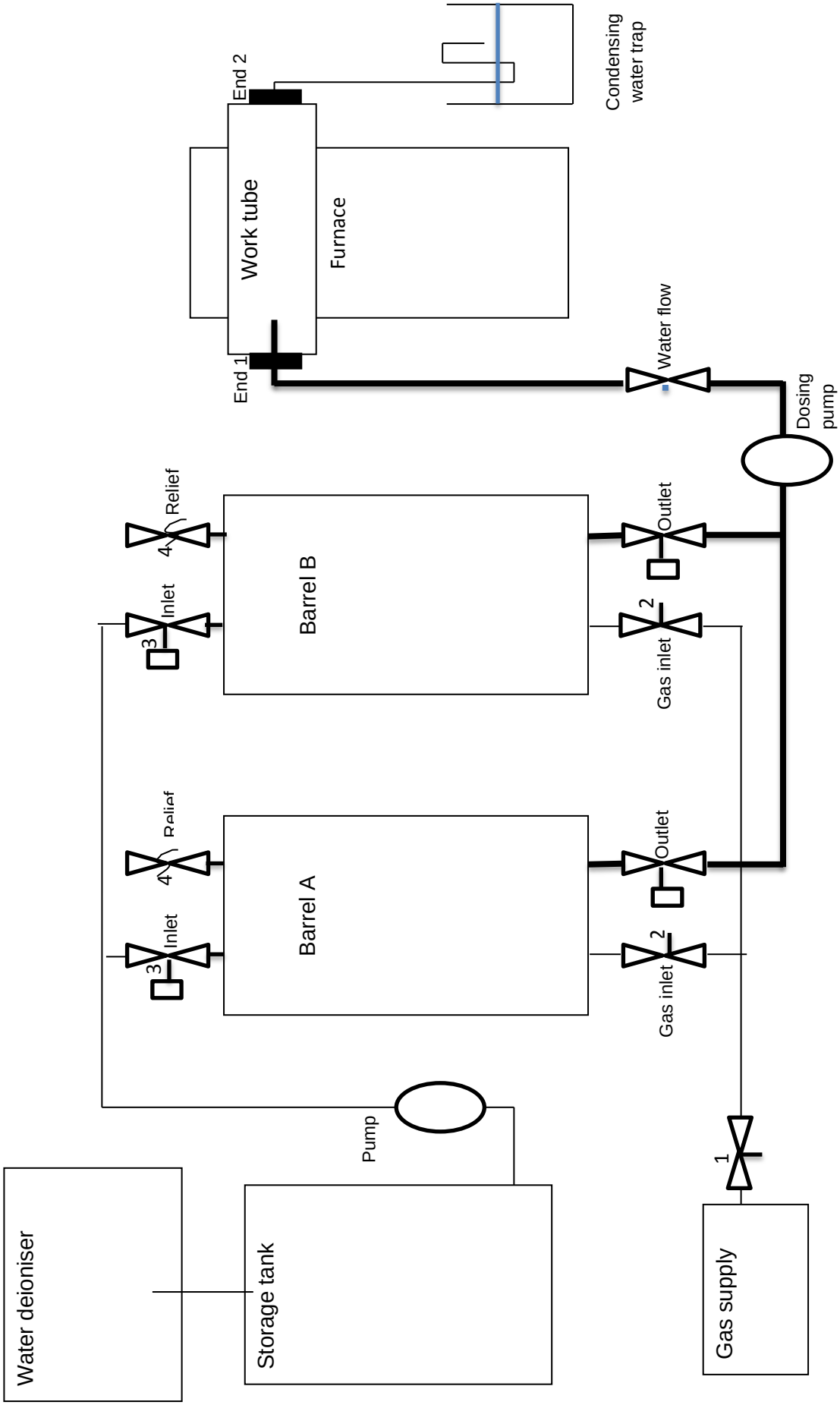

Figure 3-3 Schematic of the current set up of the steam rigs.

The furnaces were switched on prior to sample insertion and the temperatures were monitored alongside steam flow for a minimum of two days prior to the beginning of a test to ensure the conditions were stable.

3.3.4. Oxidation Testing

All tests for this study were carried out at 923 K and at atmospheric pressure. Current service conditions in plant are 813 K and 160 bar. The chosen experimental conditions were agreed upon with industrial collaborators and produce an oxide thickness equivalent to that of 20000 hours service time.

Specimens of TP347H FG, once prepared using the method outlined in Section 3.2, were placed in an alumina crucible with the inner surface of each sample facing upwards. The boat was placed in the furnace at temperature, thus the surfaces were parallel to the axial direction of the steam as shown in Figure 3-4.

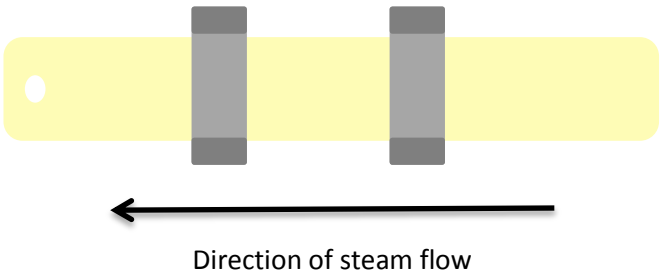

Figure 3-4 Sample layout in alumina boat for steam oxidation tests.

A maximum of two samples per crucible and one crucible per rig was exposed at any one time so as to minimise the turbulence within the steam and to ensure the oxidation conditions for each specimen were equally maximised. Both ends of the work tube were sealed as shown in the schematic in Figure 3-3.

The exposure time at temperature varied during the course of the project for times up to 1000 hours per cycle.

3.3.5. Post Oxidation

At the end of the steam oxidation experiments, the samples were removed from the furnace whilst at temperature using appropriate personal protective equipment and were allowed to cool to room temperature in air. Immediately after the samples were extracted from the furnace they were removed from the alumina crucible and stood up on end using tongs, such as that shown in Figure 3-1. Air quenching is said to provide the ideal conditions to initiate spalling [154]. During cooling the samples were recorded using an infrared thermal imaging camera and optical video camera, as described below.

3.3.6. Simultaneous Thermographic and Optical Recording Media Examination (STORME)

On removal from the steam furnace samples were monitored using a Microepsilon TIM400 thermal imaging camera with a 38° lens and a thermal resolution of 0.08 K. An emissivity of 0.89 was used and this was calibrated using an R-type thermocouple. The typical set up for the thermal imaging camera and video camera used to record the temperature profile on cooling can be seen in Figure 3-5.

Some short term steam oxidation experiments were carried out to optimise the operating conditions of the thermal imaging camera. Three temperature ranges are available in record mode: 253 – 373 K, 273 – 523 K and 423 – 1173 K. Initial results showed 273 – 523 K was a useful temperature range for this study. However, further analysis showed delamination events sometimes occurred above 523 K and hence were undetectable with the thermal camera in spite of spallation occurring within this range.

Figure 3-5 Typical set up for the thermal imaging camera (left) and video camera (right).

Since all steam oxidation experiments were performed at 923 K, it was decided that the 423 – 1173 K range would be used initially and recording would temporarily be stopped at approximately 523 K where the configuration of the thermal imager would be updated to record in the 273 – 523 K range. This was found to be the optimal conditions under which both delamination and spallation of localised events could be captured; hence the ΔT for the individual events could be determined.

Before the samples undergoing steam oxidation are removed from the furnace the IR and video cameras have to be focused in order to optimise the recording conditions to allow accurate detection of the delamination and spallation sites. Four dummy samples, such as those shown in Figure 3-5, are used to focus the cameras. Once the cameras have been focused, the two samples positioned at the front are removed. The two at the back are then used as a marker to identify where the

oxidised samples being removed from the furnace need to be positioned. Details of the data obtained from the IR camera are given later in Section 3.6.1.

In addition to this data, the IR camera also allowed cooling curves for the gross sample to be determined and compared. An example cooling curve is shown in Figure 3-6.

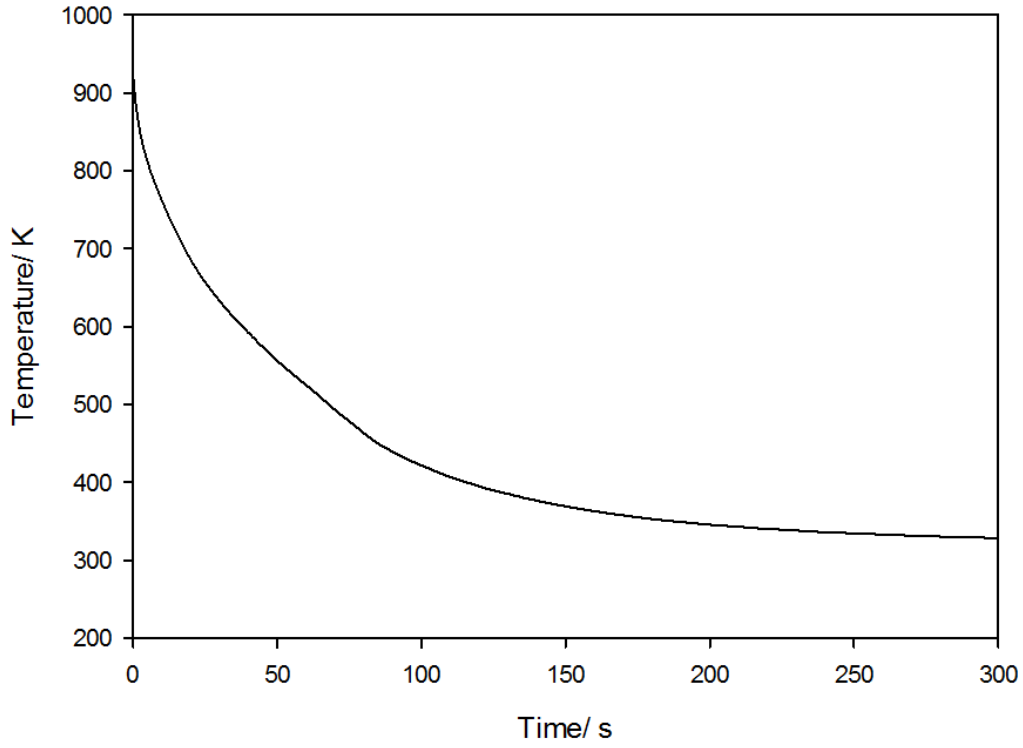

Figure 3-6 Example of a cooling curve obtained from the IR camera.

3.4. Vacuum annealing

The method of vacuum annealing to evaporate Cr from the surface of a specimen was used previously [108], [151] and the same method was utilised in this work. This technique was used here to promote Cr evaporation from the surface of specimens to mimic the effect of Cr depletion during oxidation. Specimens of TP347H FG were

placed in an alumina crucible, the layout of which can be seen in Figure 3-7, and vacuum anneals were carried out in an alumina furnace tube.

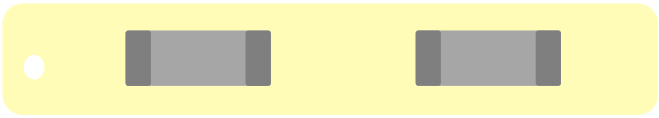

Figure 3-7 Sample layout in alumina boat for Cr evaporation experiments.

A pressure of 0.01 Pa at 1273 K was used to perform the vacuum annealing since the vapour pressure of Cr is 0.01 Pa at 1265 K [156]. To begin with, the samples were inserted into the alumina tube which was then clamped to the vacuum system. A roughing pump was used to evacuate the system down to 1 Pa before switching to a diffusion pump to achieve a vacuum of 0.01 Pa. A maximum of two specimens were vacuum annealed at any one time. At the end of the vacuum annealing experiment, the furnace was cooled at a rate of 10 $K.min^{-1}$ whilst still under vacuum. Only when the furnace had cooled to room temperature was the vacuum pump switched off and the samples removed from the alumina tube. After vacuum annealing the samples were reweighed in order to obtain weight change data.

3.5. Analytical Techniques and Sample Preparation Post Exposure

3.5.1. Surface Scanning Electron Microscopy (SEM) Analysis

Topographical examination of the surface of the samples was performed using a JEOL 6060 SEM. During surface analysis, samples were positioned in the SEM in the same orientation between each cycle to allow differences in surface morphology to be determined more easily. Images were taken across the whole of each sample to ensure there was a complete record of oxidation and spallation behaviour between each exposure.

3.5.2. Focused Ion Beam (FIB) Microscopy

Examination of samples of TP347H FG post steam oxidation was carried out using an FEI Quanta 3D FIB-SEM with EDS facilities attached. Because FIB microscopy is a destructive analytical technique, only a small selection of specimens were analysed using this method. The focused ion beam microscope was used to investigate areas of spallation post steam oxidation.

3.5.3. Cross Section Sample Preparation

After each thermal cycle in steam oxidation a section of approximately 1 mm is taken using the South Bay Technology Model 650 low speed diamond wheel saw using a Metprep HNF abrasive cut off wheel. Subsequent to the vacuum annealing experiments, each sample was sectioned into 3 parts using the same technique, two of which were used for subsequent steam exposures and the third was used for cross sectional analysis.

A standardised procedure was used to mount and polish all samples, details of which were as follows. Cross sections were mounted in Struers epoxy resin, which possesses low shrinkage and low viscosity properties, using a Struers Epovac vacuum impregnator at a pressure of 400 mbar. Once the mounting procedure was complete the sections were ground using SiC grinding paper of 240, 400, 800 and 1200 grit and polished using 6, 3 and 1 μm diamond suspension. Final polishing was completed with OPA alumina suspension.

Cross sections were prepared in this way to allow thorough analysis of oxide morphology, composition and thickness as well as to investigate the Cr depletion profiles in the alloy.

3.5.4. Cross Section Scanning Electron Microscopy (SEM) Analysis

Cross sectional examination was performed using a JEOL 7000 Field Emission Gun (FEG) SEM fitted with Energy Dispersive X-ray Spectroscopy (EDS) and Wavelength Dispersive X-ray Spectroscopy (WDS) Oxford Instruments. Prior to cross sectional examination samples were coated with platinum using an Emscope SC500 coater. The corners of the samples that were not of interest were painted with silver to increase the conductivity. Both secondary electron and back scattered electron modes were used to examine microstructural changes. For cross sectional examination the back scattered electron mode was preferred as this gave the best contrast between each of the oxide layers and the underlying alloy. An accelerating voltage of 20 keV was used throughout examination.

Accurate detection of lighter elements in the oxide layers, such as O, was measured using quantitative WDS analysis to ensure the Fe rich layers were more easily distinguishable. Calibrated standards are used to be able to measure the O and Cr content. This was of particular importance in accurately distinguishing between haematite, Fe_2O_3, and magnetite, Fe_3O_4, where the O compositions are 60.0 at.% and 57.1 at.%, respectively.

Oxide thicknesses, depth of penetration and concentration profiles were obtained from cross sectional analysis.

3.5.5. Optical Microscopy

Examination of the cross sections of the samples was performed using a monochromatic Zeiss microscope fitted with a CCD camera and 50x lens. There is a difference in contrast between haematite and magnetite when observed using an optical microscope and so this method was chosen to investigate the oxide thicknesses of the outer Fe rich oxides for samples where there was no visible spallation on cooling. This gave data used to determine the oxidation kinetics.

3.6. Data Analysis

3.6.1. Simultaneous Thermographic and Optical Recording Media Examination (STORME)

A thermal profile was obtained on cooling for each sample by measuring the average temperature across the surface of each sample using the area function on the TIM connect software provided with the thermal imaging camera. The temperature was measured at five second intervals down to room temperature.

Synchronisation of the IR monitor with a video camera enabled the precise time at which localised spallation occurred to be determined. In addition to the area function in the TIM connect software, it is also possible to obtain a temperature for a localised point within the working area, therefore allowing the temperature at which localised spallation events have occurred to be determined once the time at which spallation occurred was known. On examination of the IR videos it was noticed that the spall sites appear as a temperature gradient across the surface and the entire spall site can be detected. Monitoring the spallation events on the IR camera in reverse revealed that the reduced temperature at the localised spall sites is visible up to one

minute prior to the spallation event taking place. It was therefore determined that this was the delamination of the oxide at the spall site enabling the temperature at which both delamination and spallation occurred to be obtained.

A snapshot of the recording taken using the thermal imaging camera at a known time can be taken in the TIM connect software provided with the thermal imaging camera. These images were then imported to ImageJ where the diameter, and hence the radius, of both the delamination and spallation sites can be measured. The scale bar was calibrated to the length of each sample (L_1). The incisions on the specimens, shown earlier in Figure 3-2, were used to locate the event site between the optical video camera and the thermal imaging camera.

3.6.2. Spalled Oxide Thickness Measurements

Spall particles were collected for each specimen once cooled to room temperature. As mentioned above, synchronised IR and video cameras were used to detect delamination and spallation events. Once the initial spallation event had been identified from the video recording, the spall particle from that area was located. Magnetic tweezers were then used to collect the spalled particles and attach them, end on, to carbon adhesive tape mounted on an aluminium stub, as shown in Figure 3-8.

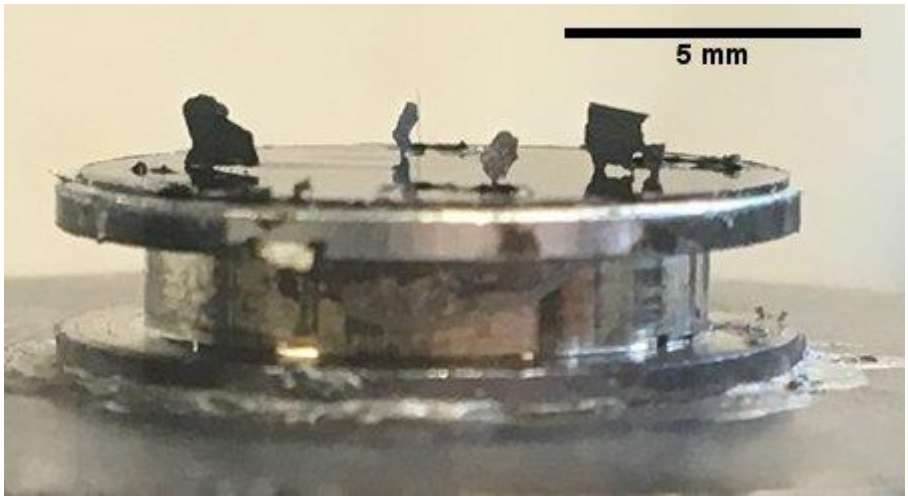

Figure 3-8 Spall particles stood on end, mounted on carbon adhesive tape.

The spalled oxides were coated with platinum for SEM analysis. The JEOL 7000 F, with stage manipulation, was used to image the spalled oxide end on to obtain oxide thickness measurements.

3.6.3. Micrograph Image Analysis

3.6.3.1. Oxide thickness measurements

Image analysis was performed using ImageJ software [157], [158] with a grid overlay plugin on backscattered electron (BSE) and optical microscope images. Firstly, the scale was set using the embedded scale bar from the microscope. The plugin was then used to place lines over the image at equal spacings. Oxide thickness measurements were then taken for both the haematite and magnetite oxides in the case of spall particles and both FeCrNi spinel oxide and Cr rich oxide in the direction of oxide growth. A total of 100 measurements were taken for each sample at intervals of 2 μm. The number of measurements taken per image was dependent upon the magnification at which the images were taken.

3.6.3.2. Depletion profiles

For samples where a profile was measured by means of point scans using EDS/ WDS, images were exported from the INCA software and imported into ImageJ where the scale bar was set. The distance away from the oxide/ metal interface, i.e. the point for which 0 μm was set, was then measured for each point in the profile using the micrograph, where into the oxide was a positive distance and into the metal was negative. For vacuum annealed specimens the outer surface was taken to be 0 μm and all measurements into the alloy were taken as a positive distance away from the surface.

3.6.3.3. Grain Size Analysis

Post vacuum annealing samples were cross sectioned, mounted and polished to a mirror finish using the method outlined in Section 3.5.3. Subsequently the samples were etched using 10% oxalic acid in deionised water for 30 seconds with a voltage of 2.5 Vdc to make the grain boundaries clearly visible. Cross sectional micrographs obtained from the JEOL 7000F SEM were then printed to perform grain size analysis where tracing paper was used to highlight the grain boundaries. Once all the grains had been traced by hand the images were then scanned and imported into ImageJ [157]. The scale was set using the scale bar from the SEM image and then cropped to include only the surface grains. The image was then converted to binary and inverted so the grain centre was black and the grain boundaries white. The analyse particles function in ImageJ was then used where the edges of the grains were excluded. Results were outputted as an area which was then converted to an equivalent radius, r, assuming a circular shape using Equations 3-1 and 3-2.

$$area = \pi r^2$$ Equation 3-1

$$r = \sqrt{\left(\frac{area}{\pi}\right)}$$ Equation 3-2

3.6.4. Oxidation Kinetics

Oxidation kinetics were determined through the measurement of oxide thickness for each individual oxide layer and can be described using the following equation.

$$\xi^n = k_n t$$ Equation 3-3

where ξ is oxide thickness, m, k_n is the rate constant, $m^n.s^{-1}$, and t is oxidation time, s. The value of n was determined using a logξ versus logt plot where the gradient of the line is 1/n as shown in Figure 3-9 below.

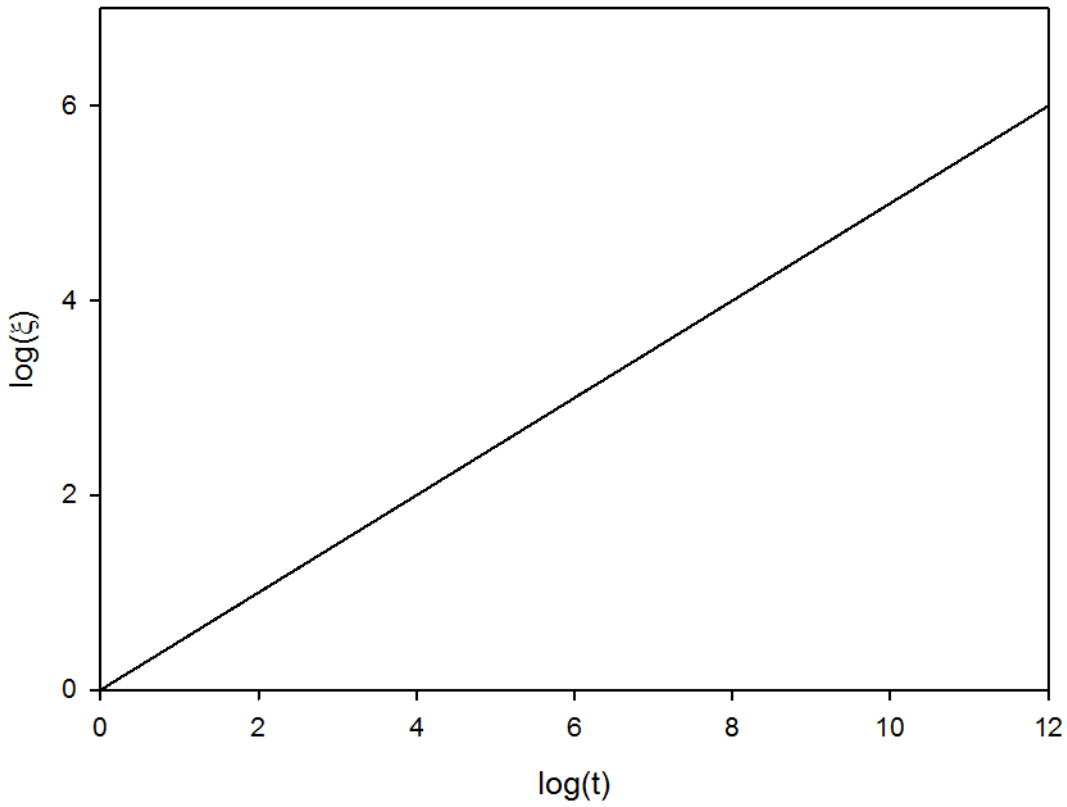

Figure 3-9 Example of log log plot where the gradient = 1/n.

A value for k_n was determined using a plot of oxide thickness, ξ, against oxidation time where the equation of the curve is

$$\xi = (k_n t)^{1/n} \qquad \text{Equation 3-4}$$

3.6.5. Curve fitting using MATLAB

Cr depletion profiles were obtained from SEM/ EDS analysis for samples which had undergone vacuum annealing. These depletion profiles are shown to fit the following equation [159]:

$$\frac{C_B - C_x}{C_B - C_0} = erfc\left\{\frac{x}{2\sqrt{Dt}}\right\} - exp\{hx + h^2 Dt\}\, X\, erfc\left\{\frac{x}{2\sqrt{Dt}} + h\sqrt{Dt}\right\} \qquad \text{Equation 3-5}$$

where C_B is bulk concentration, at.%, C_x is the concentration at a distance, x, away from the surface, m, C_0 is the concentration in equilibrium with the vapour pressure, erfc is the error function complement, D is the diffusion coefficient, $m^2.s^{-1}$, t is vacuum annealing time, s, and h=α/D where α is the transfer coefficient, $m.s^{-1}$.

Given that $C_0 << C_B$, Equation 3-3 can be rearranged to give the following:

$$C_x = C_B\left[1 - erfc\left\{\frac{x}{2\sqrt{Dt}}\right\} - exp\{hx + h^2Dt\}\ X\ erfc\left\{\frac{x}{2\sqrt{Dt}} + h\sqrt{Dt}\right\}\right] \quad \text{Equation 3-6}$$

The determination of $C_0 << C_B$ is given in Appendix A. The information obtained from the EDS analysis includes C_x and x. The vacuum annealing time, t, is already known for each specimen. A MATLAB script using the optimisation function was written to determine the values of D and h using the Cr depletion profiles obtained from each sample by optimising the fit of the curve to the data for Equation 3-4. The MATLAB script has been included in Appendix C.

Chapter 4 – Steam Oxidation and Spallation Behaviour of TP347H FG

4.1 Introduction

Austenitic stainless steels are commonly used as boiler tubing in steam power plants where the alloys undergo oxidation under harsh operating conditions.

Spallation of the oxides is seen in plant after 5000 – 50000 hours operation [136]. As a result of plant environments being difficult to reproduce under laboratory conditions, accelerated testing at 923 K was used here to produce oxides similar to those seen in plant, as discussed earlier in Section 3.3.4. The effect of pressure is unknown but work in the literature suggested there is a negligible difference between the oxides formed under pressure and those formed at atmospheric pressure [104]. Spalled oxide particles collected from boiler tubes in service were characterised in the literature and are known to be haematite [136]. Under laboratory conditions it is necessary to use air-saturated environments to form this oxide. The requirement for higher O potentials to form haematite was discussed in Section 2.3.7.3.

The spallation mechanism for TP347H FG oxidised in air saturated steam at 923 K was the main focus of the work for this chapter. A novel technique for monitoring spallation, known as STORME, was developed during the course of the project and the results obtained are included in this chapter. The observations made during isothermal testing of TP347H FG under the aforementioned conditions are discussed. Oxide chemistry and oxidation kinetics were investigated and the results are also included.

4.2 Isothermal Oxidation Behaviour

4.2.1 Observations

Prior to exposure the samples were a dull grey colour such as that shown in Figure 4-1. Subsequent to steam oxidation exposures when the samples were removed from the furnace the sample surface was matte grey.

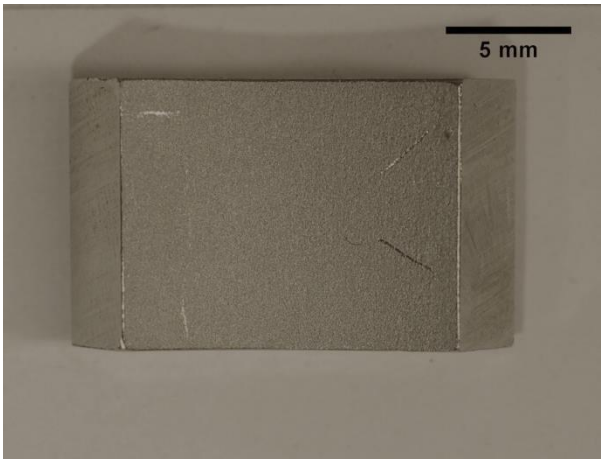

Figure 4-1 Macro image of a typical specimen of TP347H FG prior to exposure.

Samples were removed from the furnace whilst still at temperature and cooled in laboratory air. On cooling, significant spallation of the inner concave pickled surface of the samples occurred. In some cases, spallation was also observed from the outer convex surface of the samples but analysis from this surface was not carried out since that would be the fireside of the tubing and steam side oxidation and spallation was of interest for this thesis.

4.2.2 Surface SEM analysis

The surface of each specimen was examined post oxidation using a JEOL 6060 SEM to inspect spallation sites. Figure 4-2 shows representative images of the surface for each oxidation time carried out. It can be seen from these images that for the shorter

oxidation times tested, 50 and 100 hours (Figure 4-2(a) and (b)), one oxide morphology had spalled whereas for longer times at temperature, 300 – 1000 hours (Figure 4-2(c)-(f)), there were two oxide morphologies visible in areas of adherent oxide. This was most obvious in the 1000 hour experiment, Figure 4-2(f), where in some localised regions magnetite was still adherent. The three oxide morphologies, haematite, magnetite and mixed oxide spinel, have been labelled 1, 2 and 3 in the figure. Needles were also observed on higher magnification images of the surface in regions where spallation had not occurred. In some regions, the outer oxide had cracked but not completely spalled. This is shown in Figure 4-2(a) where the outer oxide looks to have buckled.

The whole of the inner concave surface of the sample was imaged using SEM and the images were then used to determine the area fraction of spallation, Table 4-1.

Table 4-1 Area fraction of spallation observed from surface SEM images of TP347H FG after isothermal oxidation in air saturated steam at 923 K.

Oxidation time/ hours	Area fraction of spallation (%)
50	95.2
100	80.8
300	74.5
500	72.3
750	27.0
1000	50.2

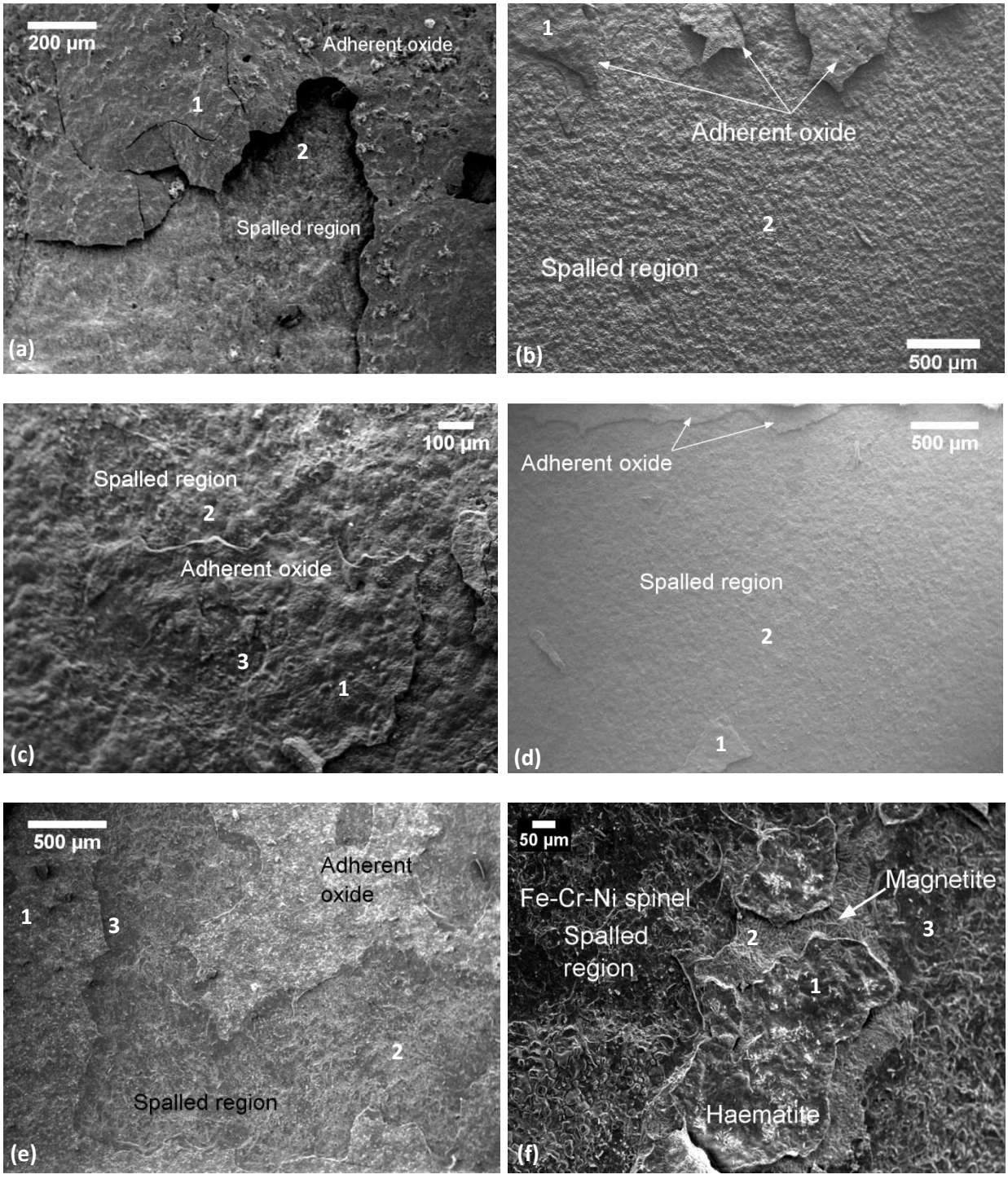

Figure 4-2 Secondary electron microscope images of the concaved surface of TP347H FG exposed to air saturated steam at 923 K for (a) 50 hours, (b) 100 hours, (c) 300 hours, (d) 500 hours, (e) 750 hours and (f) 1000 hours where 1 is haematite, 2 is magnetite and 3 is Fe-Cr-Ni spinel surface.

4.2.3 Cross Sectional Analysis

Cross sectional analysis using SEM was carried out to investigate the oxide thickness and chemistry for samples exposed isothermally to air saturated steam at 923 K for 50 – 1000 hours. Back scattered electron images of samples exposed for each time tested are shown in Figure 4-3. A duplex oxide consisting of an inwardly growing Fe-Cr-Ni spinel and an outwardly growing magnetite oxide grew during isothermal oxidation. Also visible in the cross sections are voids within the magnetite layer for shorter oxidation times (a-c) and at the magnetite/ spinel interface for oxidation times above 500 hours (d-f). The area fraction of voids and diameter between void walls were measured and are shown in Table 4-2.

Table 4-2 Area fraction of voids and the maximum diameter measured between void walls for each oxidation time in air-saturated steam at 923 K.

Oxidation time/ hours	Area fraction of voids/ %	Diameter of voids/ µm
50	4.4	2.9
100	5.7	3.3
300	4.9	3.4
500	-	3.6
750	-	4.7
1000	6.9	4.9

Figure 4-3(b) also shows evidence of buckle formation for the sample exposed to air-saturated steam at 923 K for 100 hours. In addition, some crack extension is visible beyond the original buckle. This buckled morphology was evident in cross sectional examination for all of the oxidation times investigated in this thesis.

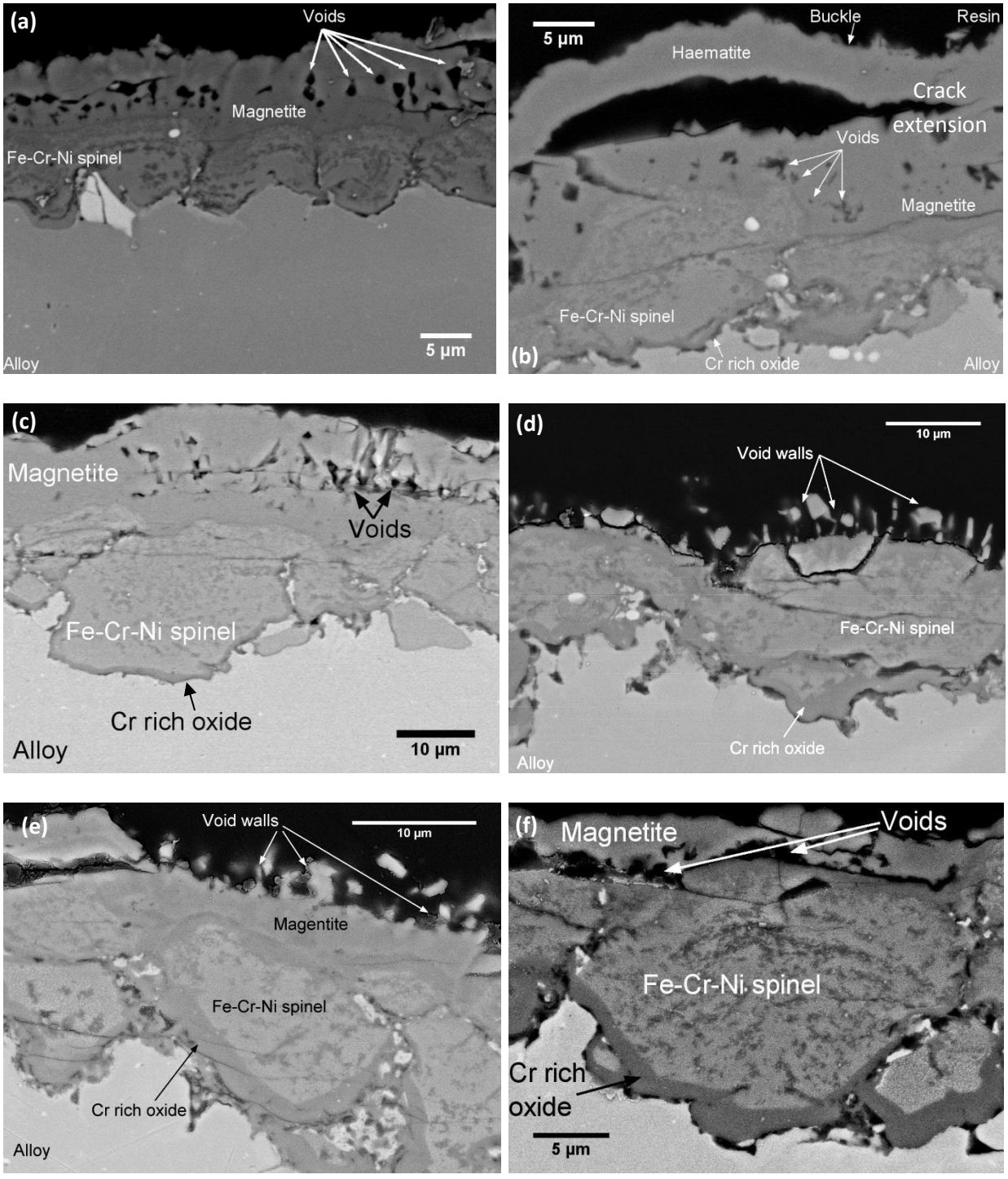

Figure 4-3 Cross sectional BSE micrographs of TP347H FG post oxidation in air saturated steam at 923 K for (a) 50 hours, (b) 100 hours, (c) 300 hours, (d) 500 hours, (e) 750 hours and (f) 1000 hours.

EDS and WDS analyses were also carried out on cross sections to confirm the oxide chemistry.

Optical microscopy of cross sections was also carried out since it was not possible to distinguish between haematite and magnetite using SEM analysis, Figure 4-4. Results from micrographs of unspalled regions show that haematite appeared as a marginally darker grey than magnetite and confirmed the presence of both Fe oxides.

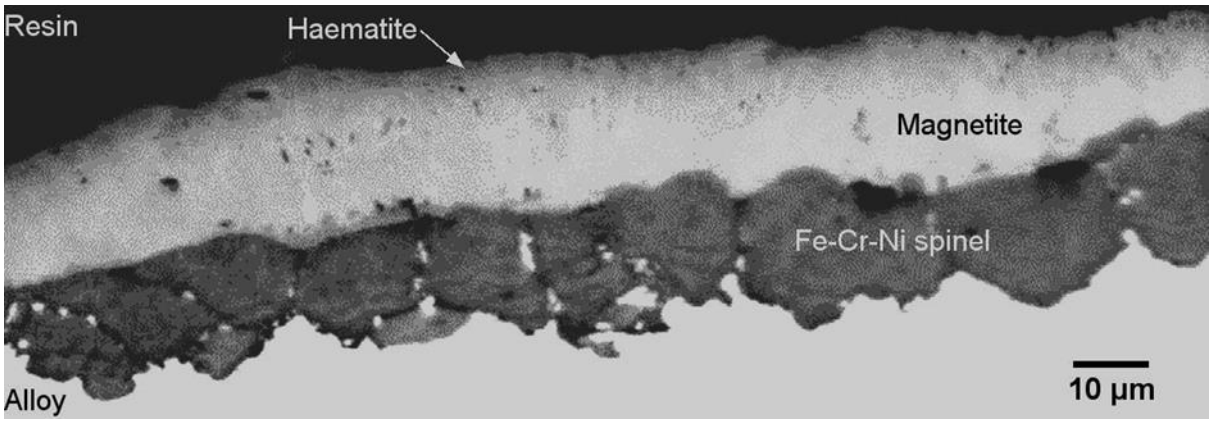

Figure 4-4 Optical cross sectional micrograph of an unspalled region of TP347H FG exposed to air saturated steam at 923 K for 1000 hours.

Haematite formation was also confirmed using WDS analysis. Figure 4-5 shows the concentration profile of a sample of TP347H FG exposed to air saturated steam at 923 K for 100 hours. At the oxide/ gas interface it is clear that there is an increase in O concentration confirming the haematite/ magnetite interface seen similarly in optical cross sectional analysis.

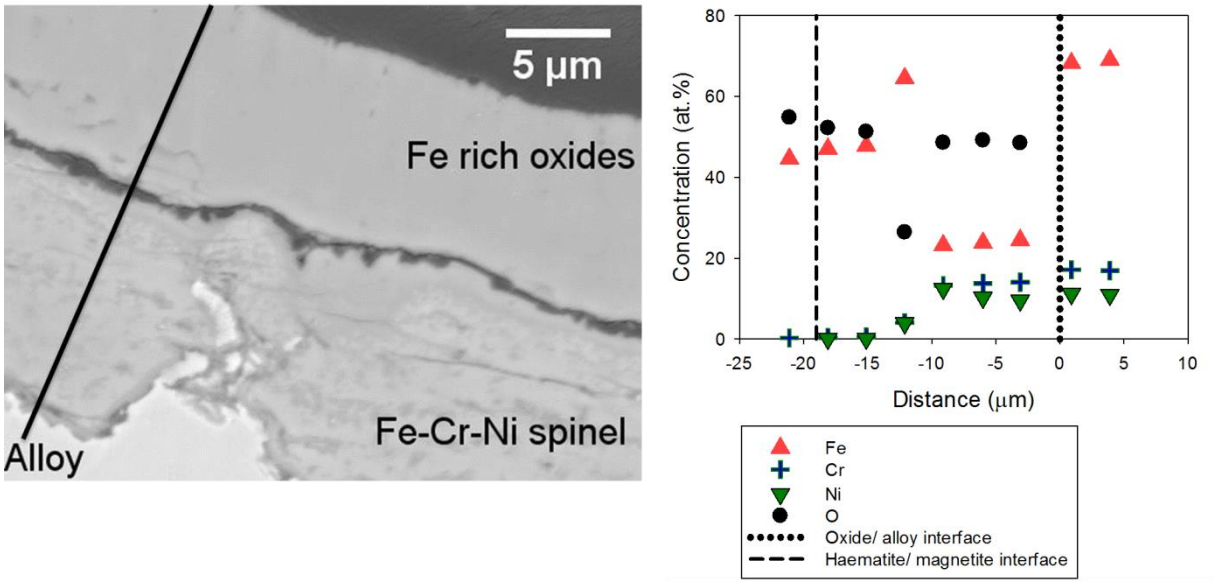

Figure 4-5 BSE image and concentration profile of the oxides formed on TP347H FG during oxidation in air saturated steam at 923 K for 1000 hours where the O and Cr concentrations have been obtained using WDS analysis (from [160]).

Identification of the Cr rich layer at the base of the Fe-Cr-Ni spinel was found early on in this project but the resolution of the EDS on the SEM was not high enough to determine the chemistry of the layer. Access to a Transmission Electron Microscope (TEM) with EDS capabilities later on in the project allowed the full characterisation and identification of Cr rich oxides. Further investigation was carried out on a sample of TP347H FG that had undergone 1000 hours oxidation in air saturated steam at 923 K. The oxide grown under these conditions was thick enough at approximately 1.5 µm to use a Focused Ion Beam (FIB) microscope to mill out a small section. The TEM foil produced is shown in Figure 4-6. Higher magnification dark field images of the TEM foil indicated there were two layers of oxide present at the base of the Fe-Cr-Ni spinel, Figure 4-7(a).

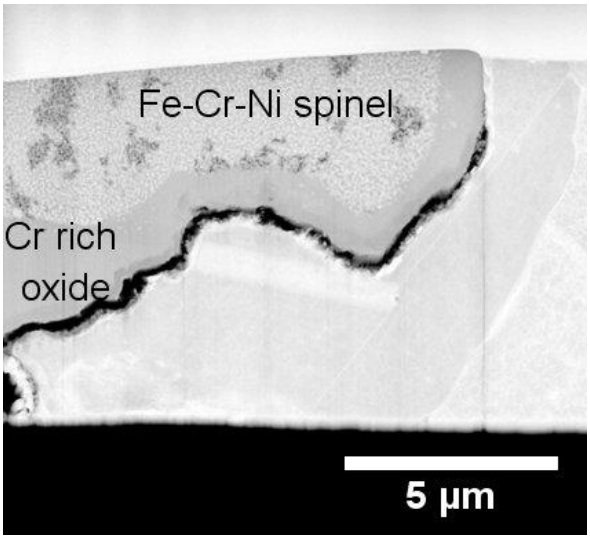

Figure 4-6 TEM foil of Cr rich oxide at the base of the Fe-Cr-Ni spinel produced using a FIB microscope.

EDS analysis from this sample indicated the thicker Cr rich oxide layer adjacent to the Fe-Cr-Ni spinel to be that of chromite, $FeCr_2O_4$. The oxide layer beneath that was found to be that of Cr_2O_3, indicated on the concentration profile at approximately 1350 nm. The width of the Cr rich peak was measured to be approximately 115 µm. Using approximate values, the following equation was used to determine the rate constant k_p for the Cr_2O_3 layer found in this study [161] which was calculated to be 5.25 x 10^{-21} $m^2.s^{-1}$:

$$k_p = 2.07x10^{-6}\ x\ exp\left(-\frac{31020}{T}\right) \qquad \text{Equation 4-1}$$

Using this value of k_p the theoretical chromia oxide thickness for 1000 hours could then be calculated based on Equation 4-2 and was found to be approximately 140 µm.

$$\xi^2 = k_p t \qquad \text{Equation 4-2}$$

The theoretical value is in good agreement with the value measured from the Cr peak in the concentration profile.

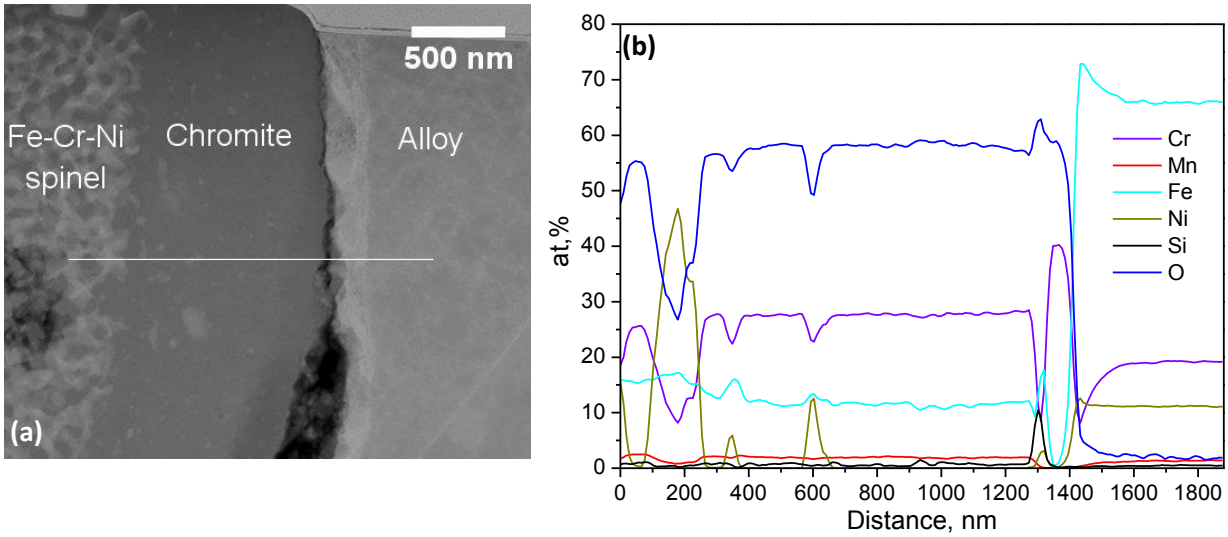

Figure 4-7 (a) Dark field cross sectional TEM image of TP347H FG exposed to air saturated steam for 1000 hours at 923 K and (b) the corresponding linescan which was taken from left to right on the cross sectional image.

The concentration profile shown in Figure 4-7(b) also indicated an enhancement in Fe directly beneath the Cr_2O_3 layer at approximately 1450 nm. The Cr_2O_3 layer was therefore thought to be behaving protectively, preventing further diffusion of Fe from within the alloy outwards.

4.2.4 Oxidation Kinetics

Isothermal oxidation kinetics for the Fe-Cr-Ni spinel oxide were determined but the thicknesses of magnetite and haematite were difficult to interpret as a result of the extensive spallation. Oxidation kinetics were therefore not determined for those oxides.

A plot of oxide thickness as a function of oxidation time was used to calculate n, the rate constant, using the following equation, Figure 4-8:

$$\xi = (k_n t)^{1/n} \qquad \textbf{Equation 4-3}$$

where ξ is oxide thickness, m, k_n is the rate constant, $m^n.s^{-1}$ and t is time, s.

The value of n in Equation 4-3 was calculated to be 2.9 for isothermal oxidation in air saturated steam at 923 K showing near-cubic behaviour. The value of k_n was found to be 1.3 x 10^{-15} $m^{2.9}.s^{-1}$. Data found in the literature for the same alloy stated that the oxidation kinetics were parabolic with k_p values of 1.7x10^{-17} $m^2.s^{-1}$ [2]. However, this literature value is for total oxide thickness for TP347H FG from plant trials rather than just the Fe-Cr-Ni spinel. The steam environment is also slightly different and so this value is not a true comparison. Shorter term testing has also been said to result in higher rate constants than do long term testing. Data for spinel on Super 304 H, which has a similar composition to the alloy studied in this thesis, was also found to be parabolic with a k_p value of 1.9 x 10^{-16} $m^2.s^{-1}$ when exposed to deoxygenated steam at 923 K. This discrepancy may again be as a result of the different steam conditions used. Insufficient data on spinel growth in the literature impedes further comparisons to be made. The cause for the near-cubic oxidation kinetics is thought to be as a result of the Cr rich oxides formed at the base of the spinel.

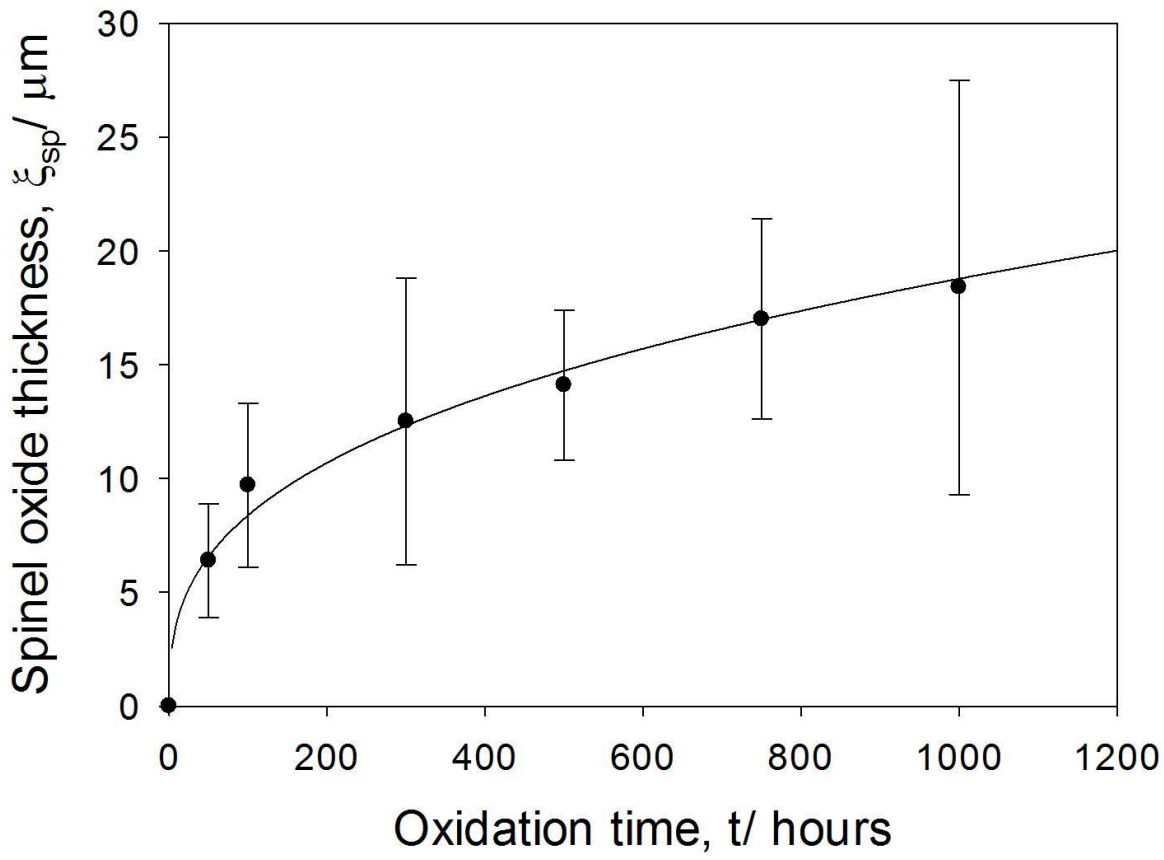

Figure 4-8 Plot of mean and standard deviation of Fe-Cr-Ni spinel oxide thickness against time at temperature in air saturated steam at 923 K.

4.3 Spallation Behaviour after Isothermal Oxidation

4.3.1 STORME Analysis

4.3.1.1 Introduction

As was mentioned in Section 2.5.4 of the literature review, techniques previously used to monitor delamination and spallation lacked the ability of imaging the samples and detect the localised temperature changes for individual spallation events at the same time. The technique of Simultaneous Thermal and Optical Recording Media Examination (STORME) was developed during this project and used in this thesis to record the temperature of samples during cooling in laboratory air. Samples were removed from the hot furnace and placed on a heat proof surface such that the inner

concave surface was facing the infrared and optical cameras, shown earlier in Figure 3-5, Section 3.3.6. Further details of the technique can be found in Chapter 3.

4.3.1.2 50 hours isothermal oxidation

Thermographic images of the inner concave pickled surface during cooling after 50 hours exposure in air saturated steam are shown in Figure 4-9 where the site of spallation is highlighted. These images indicate the sample (a) 1 second prior to delamination, t_{D-1}, (b) at the time of delamination for the highlighted localised site, t_D, (c) 1 second prior to complete spallation of that localised site, t_{SP-1}, and (d) at the time of complete localised spallation, t_{SP}. There was a temperature gradient across the surface where the bottom of the sample, in contact with the heat proof surface, cooled at a faster rate than the rest of the sample surface. This was the case for all specimens examined using this technique. As cooling time increased the number of localised delamination areas also increased.

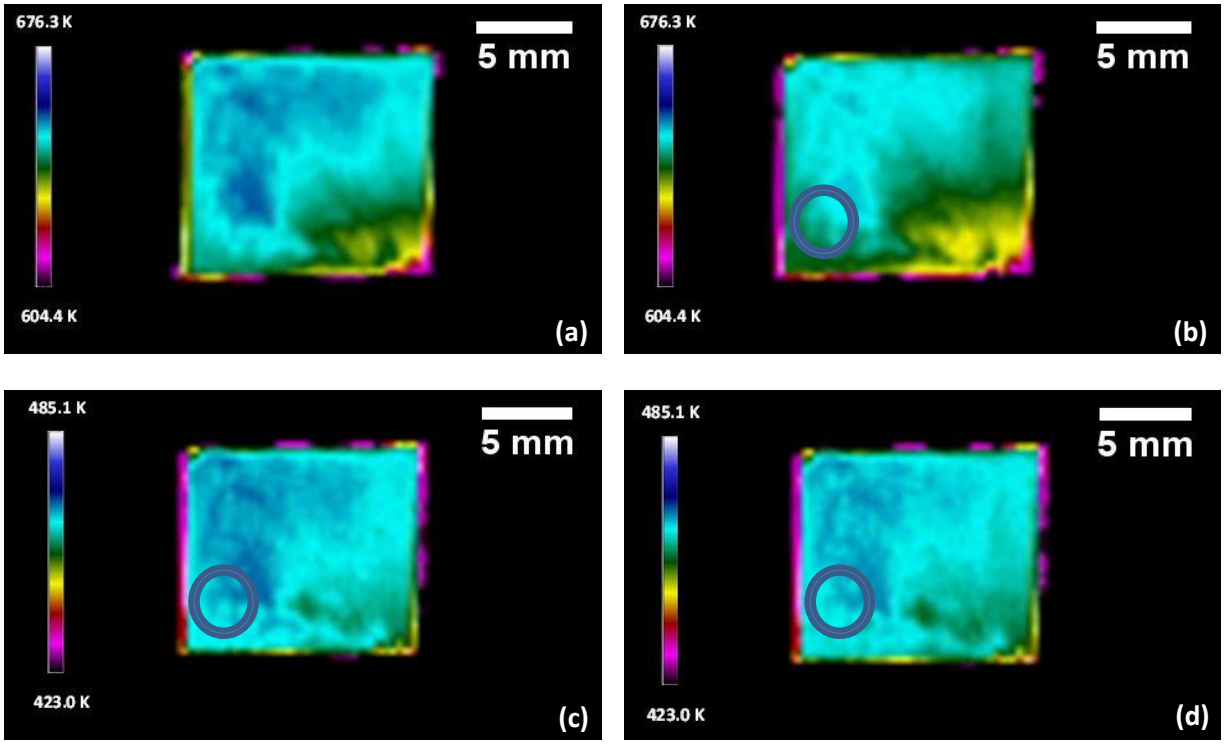

Figure 4-9 Thermographic images of the inner concave surface of TP347H FG during cooling after oxidation in air saturated steam at 923 K for 50 hours where (a) is 1 second prior to delamination, (b) is at the time of delamination, (c) is 1 second prior to complete localised spallation and (d) is at the time of complete localised spallation.

The STORME technique enabled measurements of the radius of the spalled sites, R, to be recorded from the time at which delamination occurs, t_D, to the time at which complete localised spallation of that site occurs, t_{SP}. There was 40 seconds between the delamination event and complete local spallation for this site. R was then plotted as a function of ΔT of the localised site, Figure 4-10. Also included in the plot is the critical strain energy criterion (CSEC) which assumes that strain energy builds up from the time at which delamination occurred until a critical ΔT value of 557.8 K was achieved. At that point the localised site would be completely spalled and all the strain energy released at once. The horizontal line is representative of the radius of curvature at which delamination occurs and the vertical line indicates the temperature at which spallation occurred. However, results from the thermal imaging camera

showed a gradual increase in R was observed indicating that strain energy was released gradually as ΔT increased.

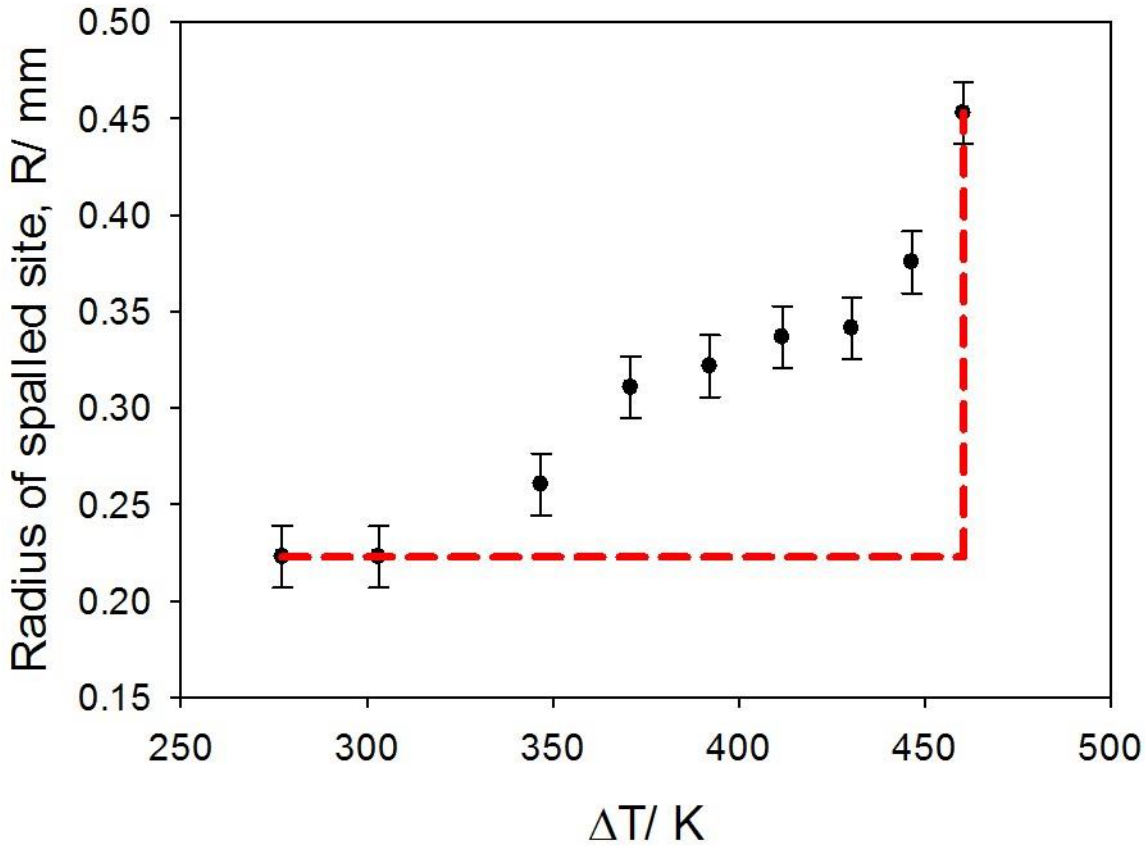

Figure 4-10 Radius of spalled site, R, highlighted in Figure 4-9 as a function of ΔT after 50 hours oxidation in air-saturated steam at 923 K. The error bars included in the figure are the error associated with the IR camera. Also included in this plot is the CSEC.

4.3.1.3 100 hours isothermal oxidation

Thermographic images of a sample exposed to air saturated steam for 100 hours at 923 K are shown in Figure 4-11. Again a series of images are shown from (a) 1 second prior to delamination to (d) the time at which complete spallation of that localised site occurred and the spalled region of interest is highlighted in the images. This example shows more clearly the increase in radius of the buckled region visible

in the thermographic images compared to the sample shown for 50 hours. It can also be seen in these images that the number of delaminated sites increased with cooling time.

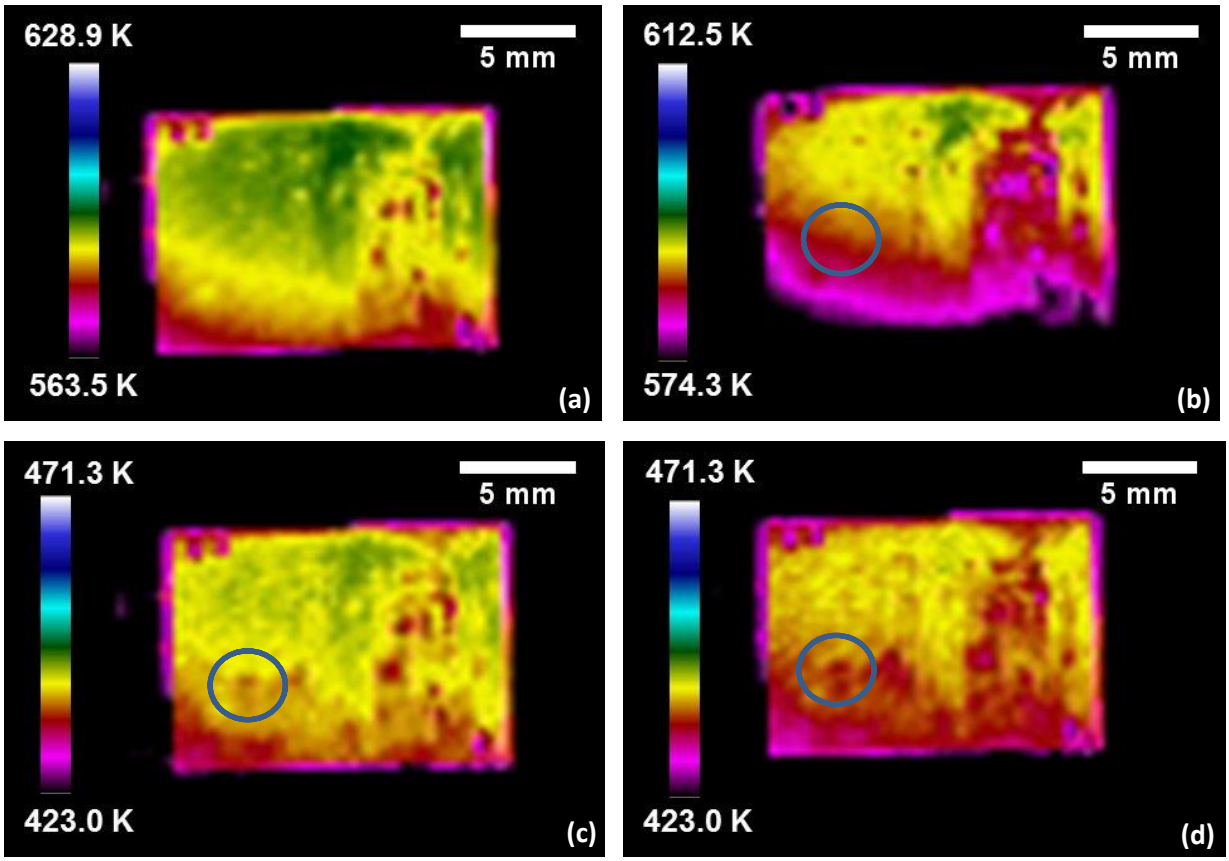

Figure 4-11 Thermographic images of the inner concave surface of TP347H FG during cooling after oxidation in air saturated steam at 923 K for 100 hours (a) is 1 second prior to delamination, (b) is at the time of delamination, (c) is 1 second prior to complete localised spallation and (d) is at the time of complete localised spallation.

The radius of the spalled region was measured from t_D to t_{SP} and plotted as a function of ΔT for the localised site, Figure 4-12. Measurements of R for this sample showed the site was stable for 10 seconds after the initial delamination and then there was a general increase to t_{SP}. Complete spallation occurred 70 seconds after the delamination event. Again the CSEC is included in the plot and assumes for this sample strain energy would build up for this site until a critical ΔT of 487.9 K was

achieved. R was also shown to increase gradually for this sample rather than follow the CSEC lines plotted.

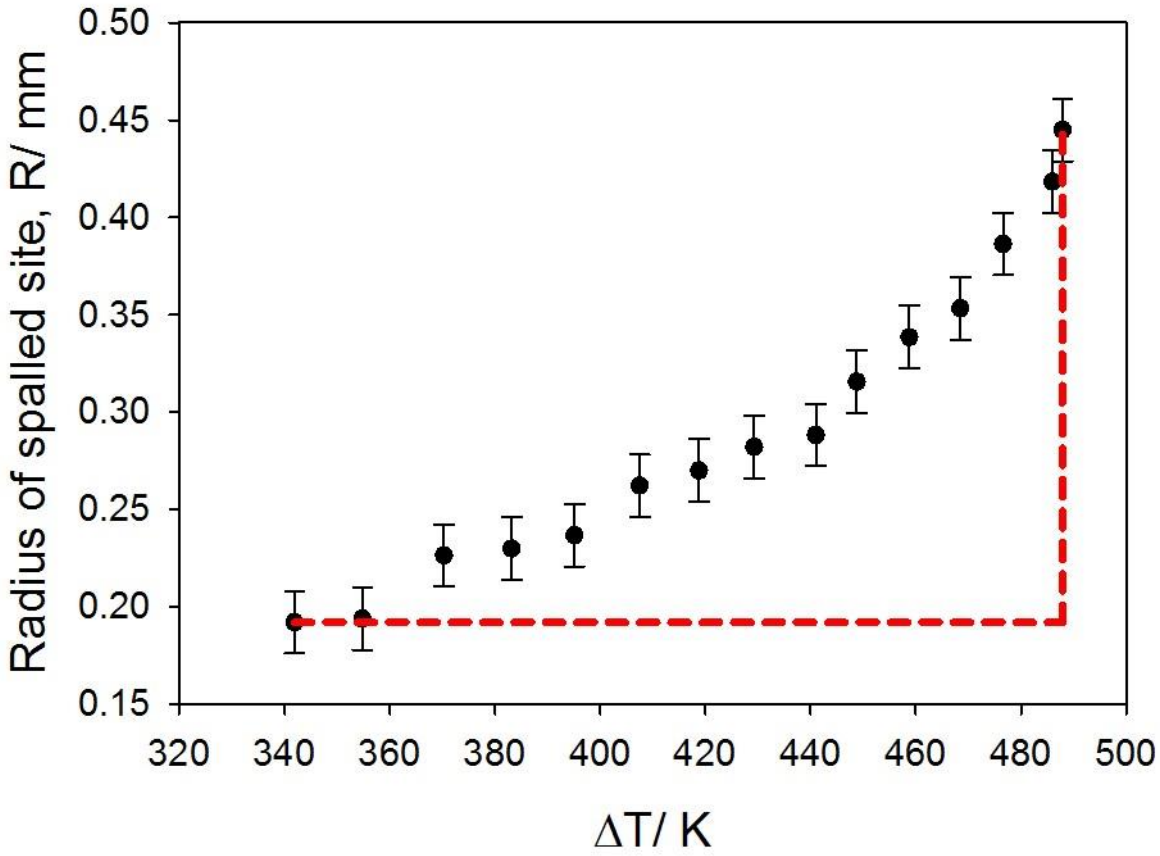

Figure 4-12 Radius of spalled site, R, highlighted in Figure 4-11 as a function of ΔT after 100 hours oxidation in air-saturated steam at 923 K. The error bars included in the figure are the error associated with the IR camera. Also included in this plot is the CSEC.

4.3.1.4 300 hours isothermal oxidation

Thermographic images for the sample exposed for 300 hours in air-saturated steam are shown in Figure 4-13 and include snapshots from t_{D-1} to t_{SP}. The spallation event of interest is highlighted in the figures. Again there was an increase in the number of delaminated areas as cooling time increased.

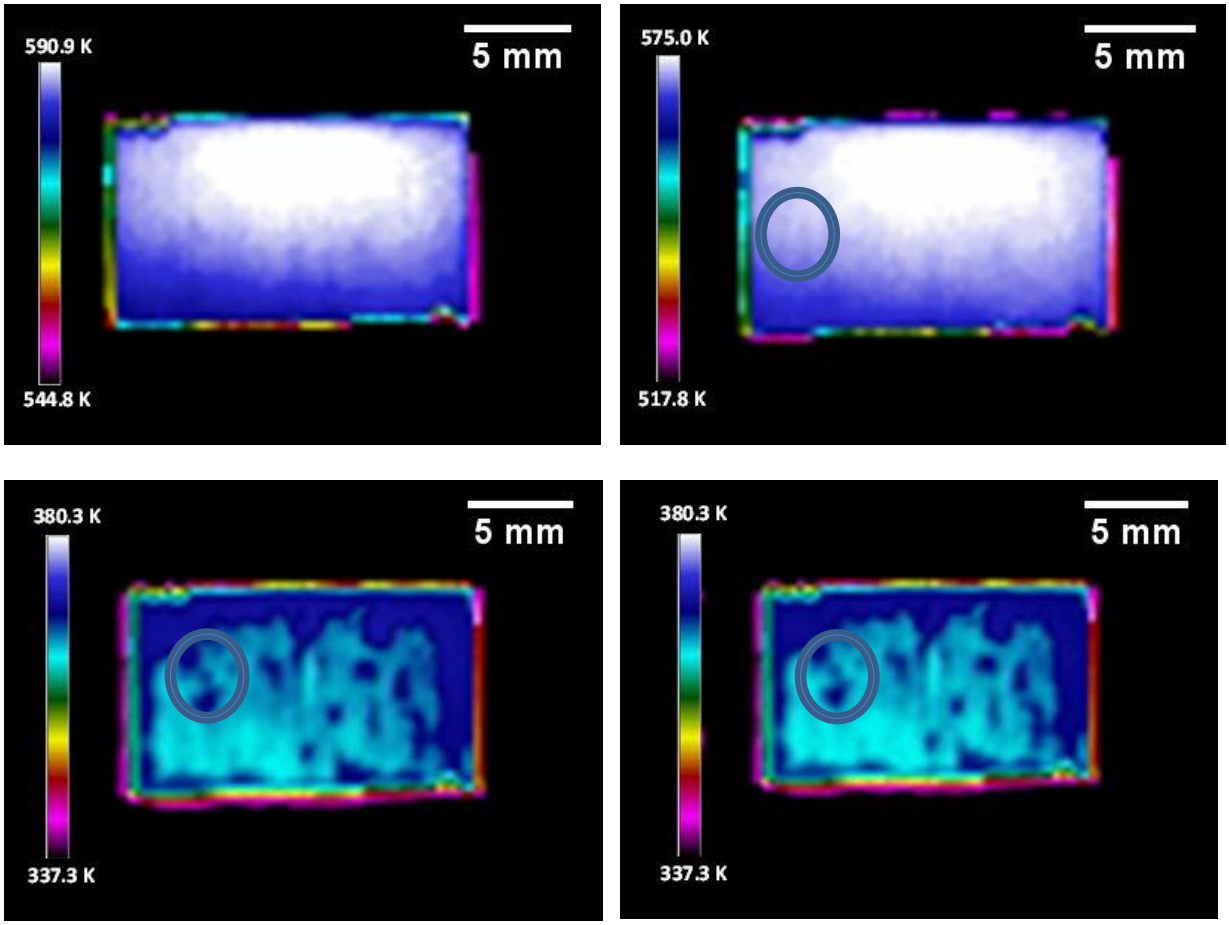

Figure 4-13 Thermographic images of the inner concave surface of TP347H FG during cooling after oxidation in air saturated steam at 923 K for 300 hours where (a) is 1 second prior to delamination, (b) is at the time of delamination, (c) is 1 second prior to complete localised spallation and (d) is at the time of spallation.

R was measured between t_D and t_{SP} and plotted as a function of ΔT of the localised spall site, Figure 4-14. For this sample, R steadily increased for approximately one minute before there was a sudden drop in temperature of around 80 K and another spike in the increase in radius of the site. It was found that there were 90 seconds between delamination and spallation events for this sample. Also included in the plot is the CSEC which for this sample assumes strain energy would build up until a critical ΔT value of 555.3 was achieved for spallation.

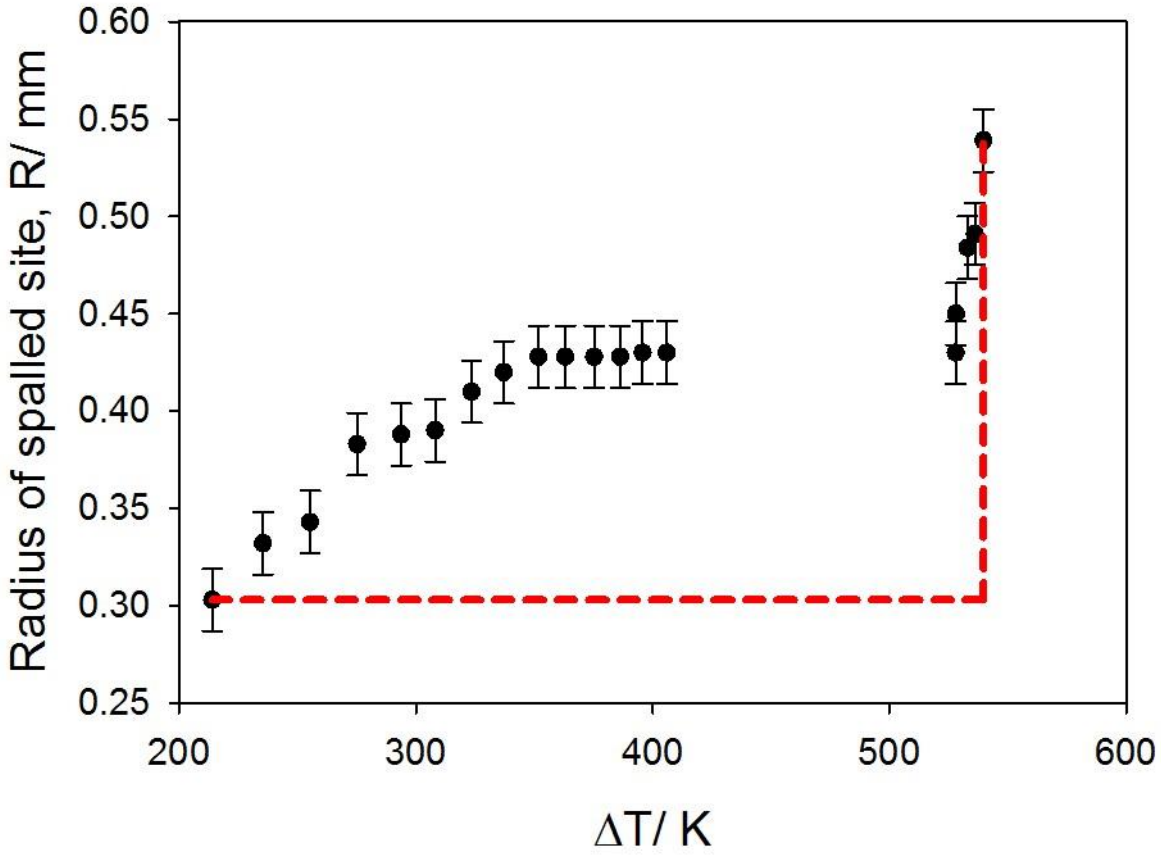

Figure 4-14 Radius of spalled site, R, highlighted in Figure 4-13 as a function of ΔT after 300 hours oxidation in air-saturated steam at 923 K. The error bars included in the figure are the error associated with the IR camera. Also included in this plot is the CSEC.

4.3.1.5 500 hours isothermal oxidation

For the sample exposed for 500 hours the thermographic images indicate only 1 delaminated area in the early stages of cooling, Figure 4-15, compared to the several that have been observed in some short term oxidation testing. The images shown in the figure below include snapshots of the sample at t_{D-1}, t_D, t_{SP-1} and t_{SP} and again the site of interest is highlighted.

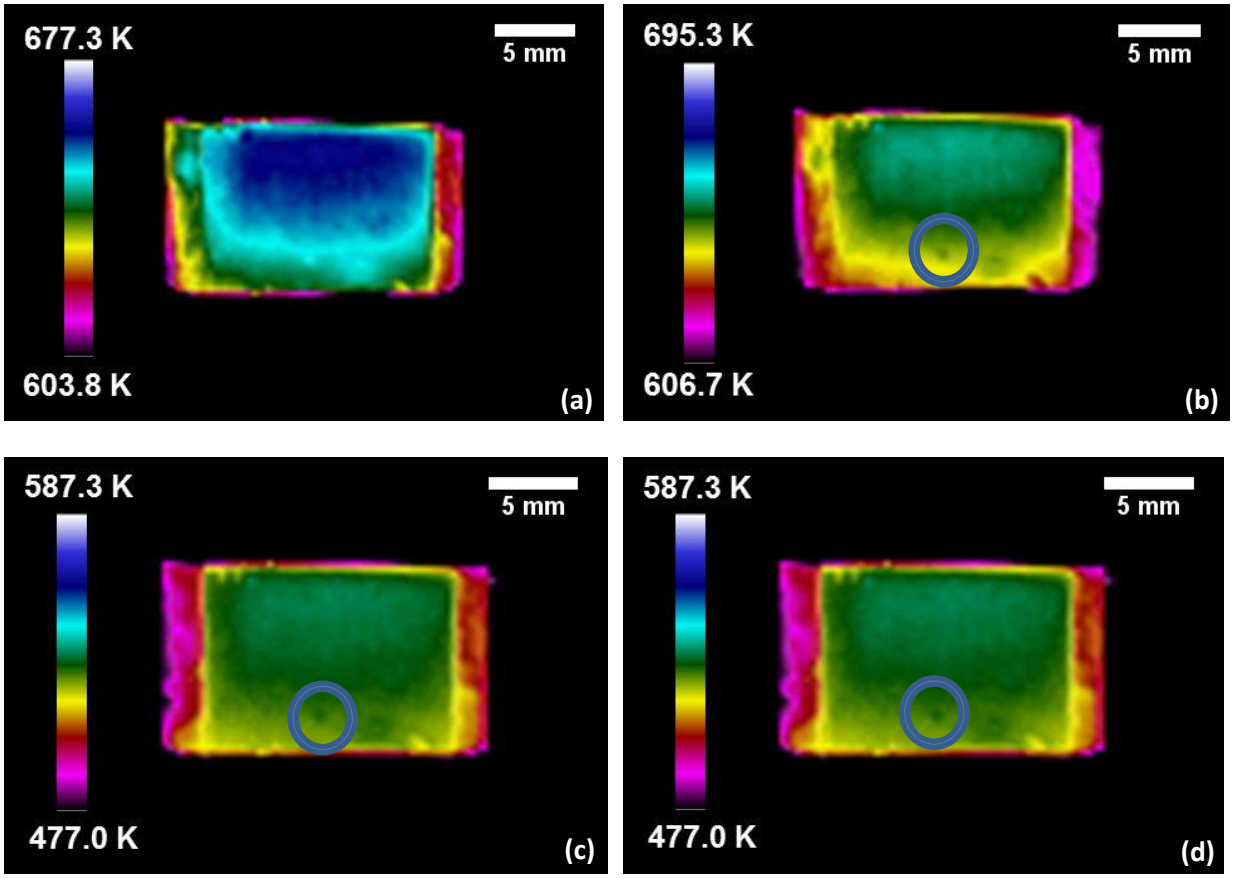

Figure 4-15 Thermographic images of the inner concave surface of TP347H FG during cooling after oxidation in air saturated steam at 923 K for 500 hours where (a) is 1 second prior to delamination, (b) is at the time of delamination, (c) is 1 second prior to complete localised spallation and (d) is at the time of spallation.

R was measured for this site and was plotted as a function of ΔT, Figure 4-16. The radius of that sample remained stable for 15 seconds and increased gradually thereafter until a ΔT of 390 K was achieved and the oxide completely spalled from the localised area. Complete spallation occurred 40 seconds after the delamination event in this case. Also included in the plot is the CSEC for this site which assumes that strain energy for this sample would not be released until a ΔT of 394.5 was reached.

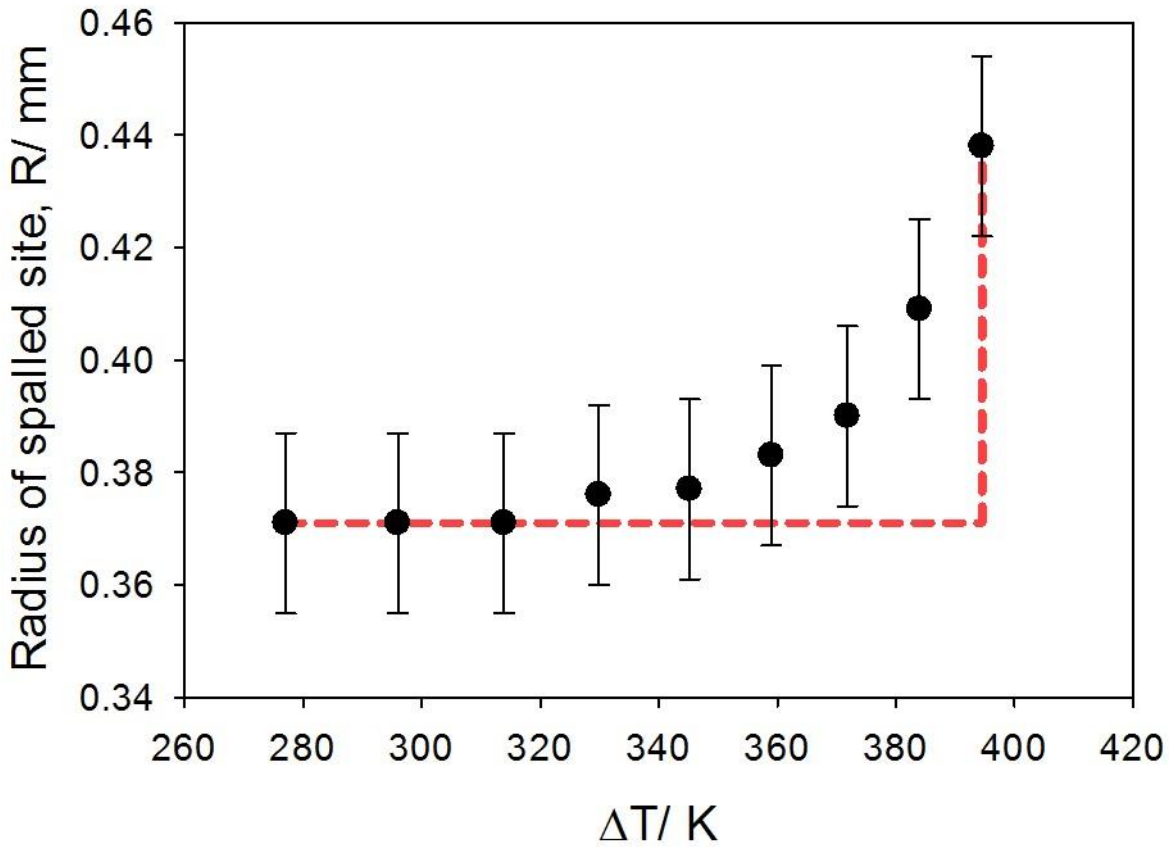

Figure 4-16 Radius of spalled site, R, highlighted in Figure 4-15 as a function of ΔT after 500 hours oxidation in air-saturated steam at 923 K. The error bars included in the figure are the error associated with the IR camera. Also included in this plot is the CSEC.

4.3.1.6 750 hours isothermal oxidation

Thermographic images taken during cooling after 750 hours isothermal oxidation in air saturated steam at 923 K are shown in Figure 4-17. The images were taken 1 second prior to delamination, at the time of delamination, 1 second prior to complete localised spallation and at the time of complete spallation. The area of interest is highlighted in the image and is shown to increase as cooling continues. One delaminated area was observed in the early stages of cooling, similar to that seen for 500 hours. The number of delamination sites identifiable on the surface had not

increased during the time between delamination and spallation for the highlighted site of interest.

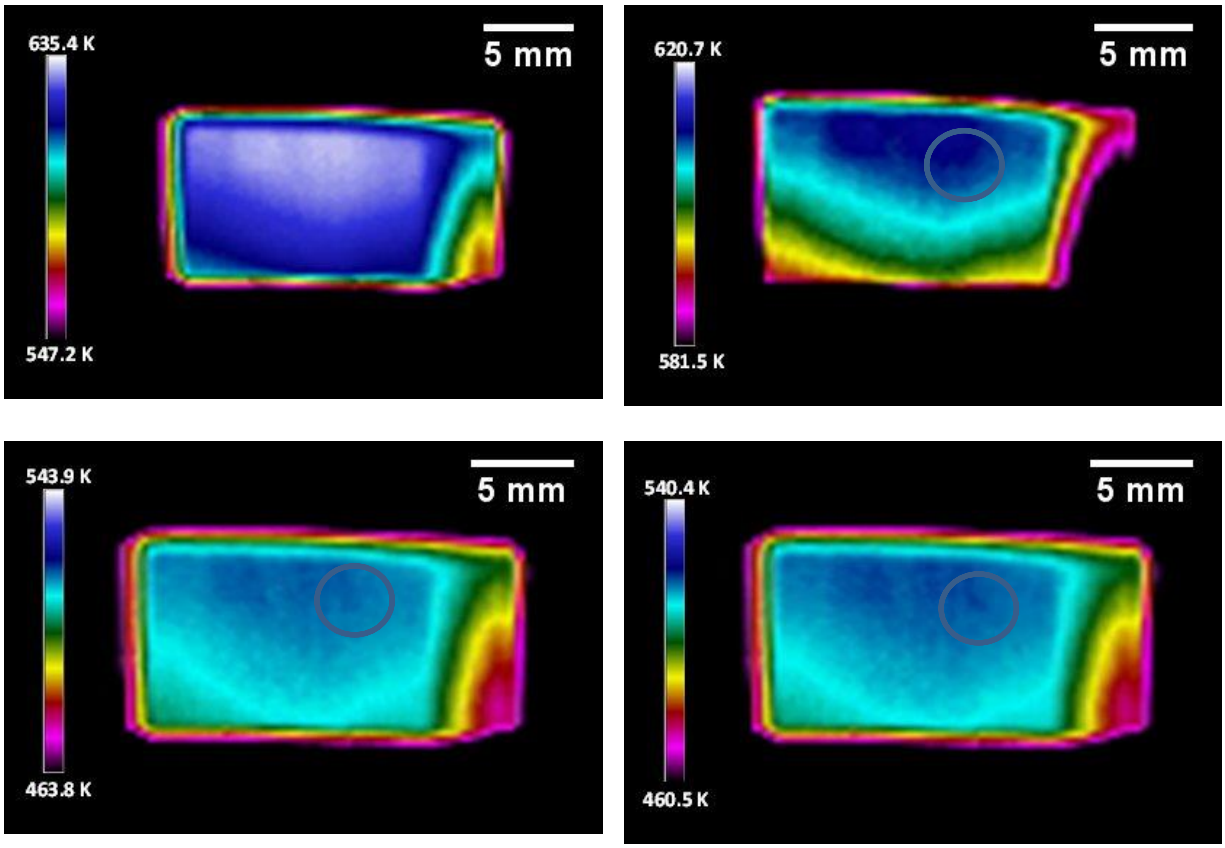

Figure 4-17 Thermographic images of the inner concave surface of TP347H FG during cooling after oxidation in air saturated steam at 923 K for 750 hours where (a) is 1 second prior to delamination, (b) is at the time of delamination, (c) is 1 second prior to complete localised spallation and (d) is at the time of spallation.

The radius of the localised spall site was measured and is shown in Figure 4-18 as a function of ΔT of the localised site. For this sample R was shown to increase gradually during cooling. Spallation occurred 45 seconds after the initial delamination event. Also included in the plot is the CSEC which assumes that a ΔT of 540.0 K would be required to release the strain energy built up in that localised site.

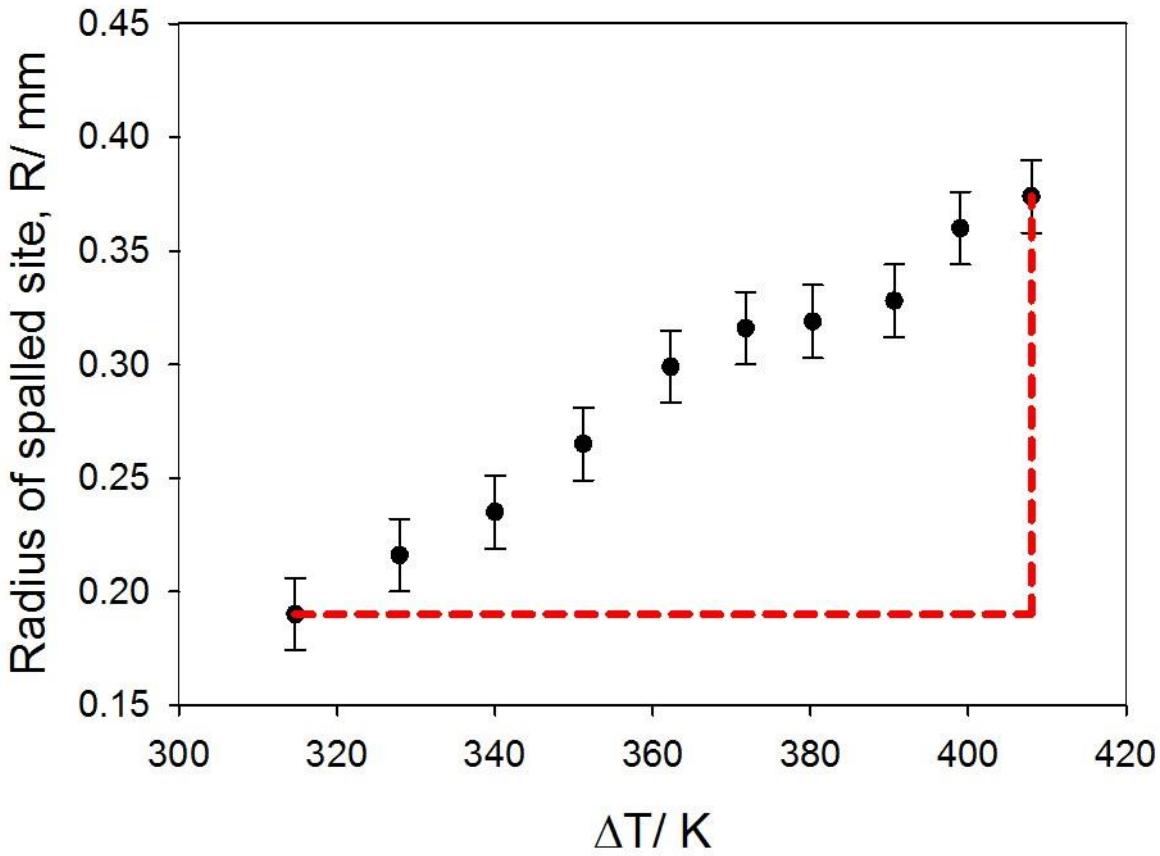

Figure 4-18 Radius of spalled site, R, highlighted in Figure 4-17 as a function of ΔT after 750 hours oxidation in air-saturated steam at 923 K. The error bars included in the figure are the error associated with the IR camera. Also included in this plot is the CSEC.

4.3.1.7 1000 hours isothermal oxidation

A localised spall site was identified using the STORME technique and the resulting thermographic images are shown in Figure 4-19 where (a) is 1 second prior to delamination, (b) is at the time of delamination, (c) is 1 second prior to complete localised spallation and (d) is at the time of complete localised spallation. This sample became more difficult to interpret than earlier oxidation times due to an increased number of localised delaminated regions of oxide resulting in some interference between adjacent spall sites.

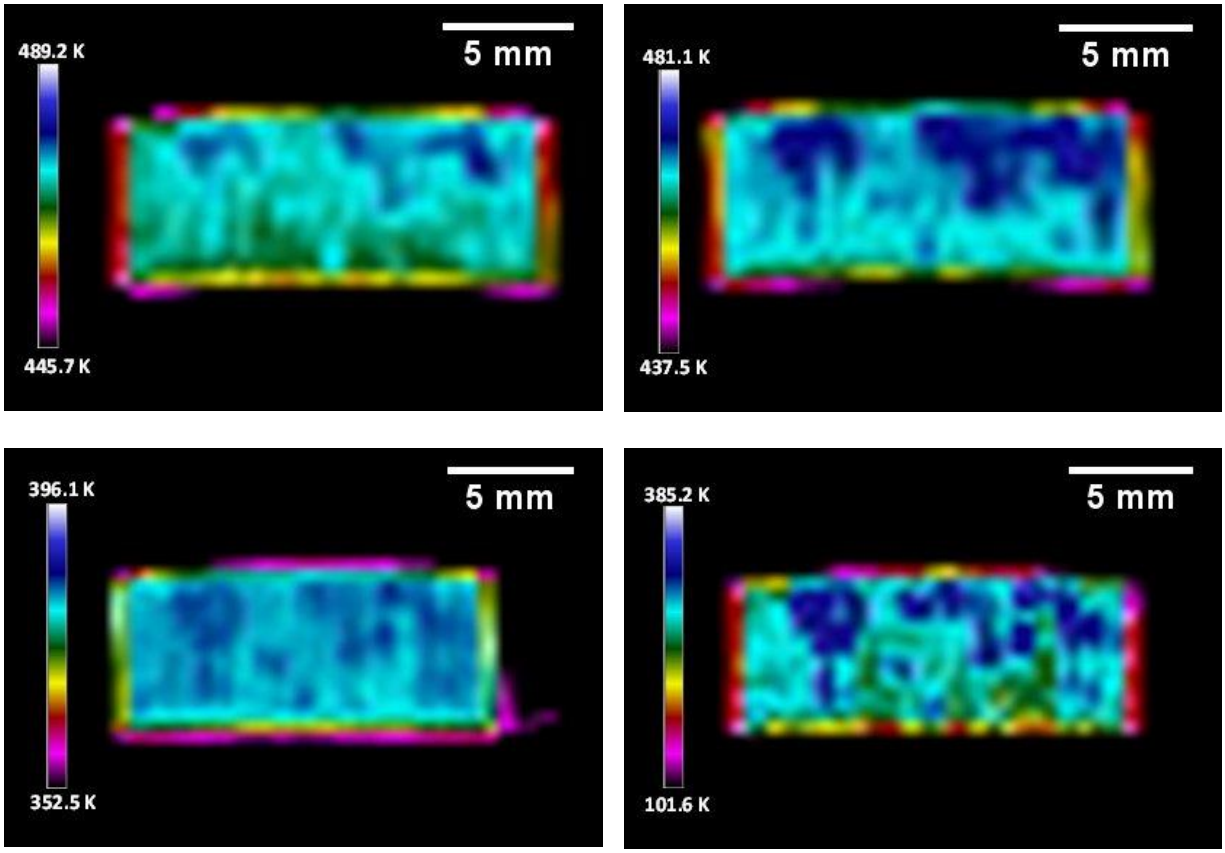

Figure 4-19 Thermographic images of the inner concave surface of TP347H FG during cooling after oxidation in air saturated steam at 923 K for 1000 hours where (a) is 1 second prior to delamination, (b) is at the time of delamination, (c) is 1 second prior to complete localised spallation and (d) is at the time of spallation.

The radius of the localised spall site identified with the STORME technique was measured and is shown in Figure 4-20. The localised site was shown to remain stable for the first 10 seconds after delamination but then generally increased until a ΔT of 540.0 K was achieved when the localised site completely spalled, 60 seconds after the initial delamination event. Also included in this plot is the CSEC which assumes that strain energy builds up from the time at which delamination occurred until a critical ΔT value of 540.0 was achieved. However, a gradual increase in R was observed indicating that strain energy was released gradually as ΔT increased.

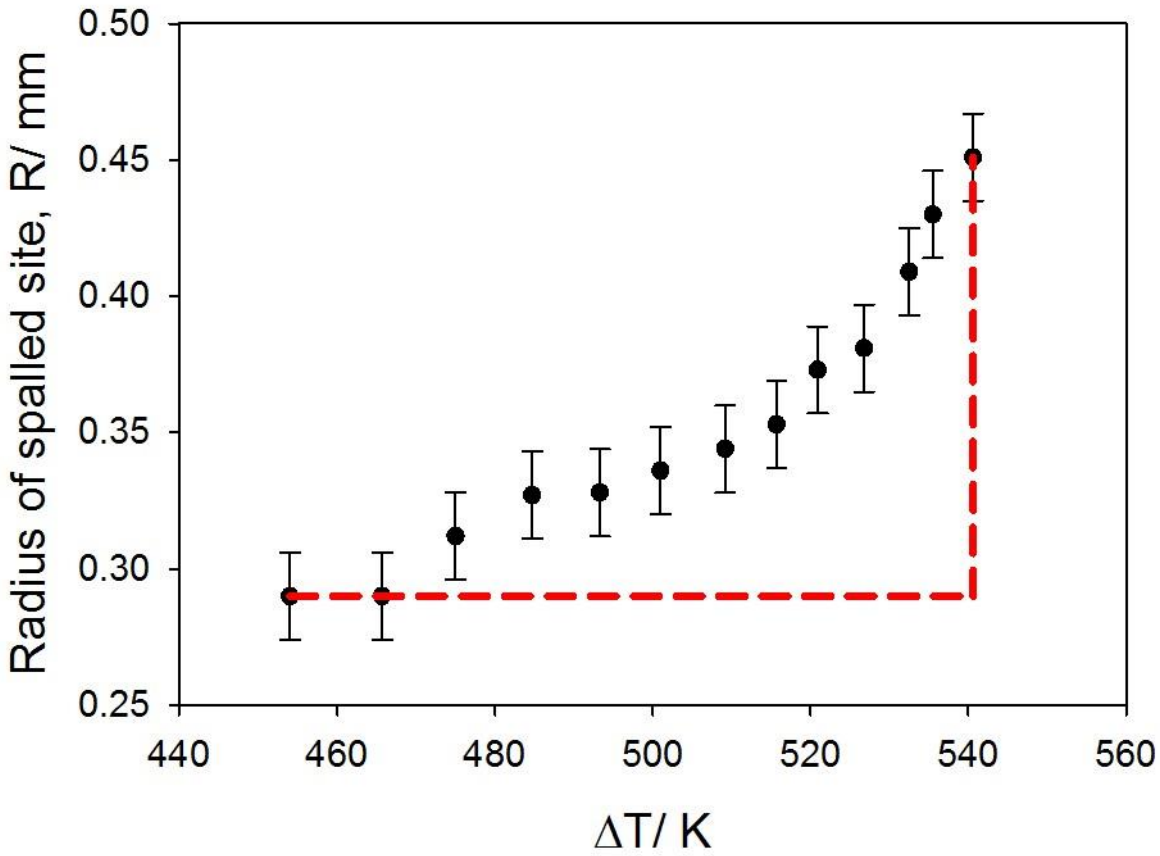

Figure 4-20 Radius of spalled site, R, highlighted in Figure 4-19 as a function of ΔT after 1000 hours oxidation in air-saturated steam at 923 K. The error bars included in the figure are the error associated with the IR camera. Also included in this plot is the CSEC.

4.3.2 Thickness of Spalled Oxide

Spalled oxide particles identified using the STORME technique were collected for SEM analysis and were shown to be approximately circular in planar section, Figure 4-21, suggesting that the concave geometry of the specimens did not affect the spallation behaviour of the oxide for the oxidation times tested. Micrographs of the spalled particles in cross section are shown in Figure 4-22. For the shorter oxidation exposures of 50 – 100 hours a single oxide morphology was observed. Images taken from the spall particles obtained after 300 hours showed an interface suggesting that two different oxides had spalled. Details of the spalled oxide morphology for each oxidation time studied are given in Table 4-3.

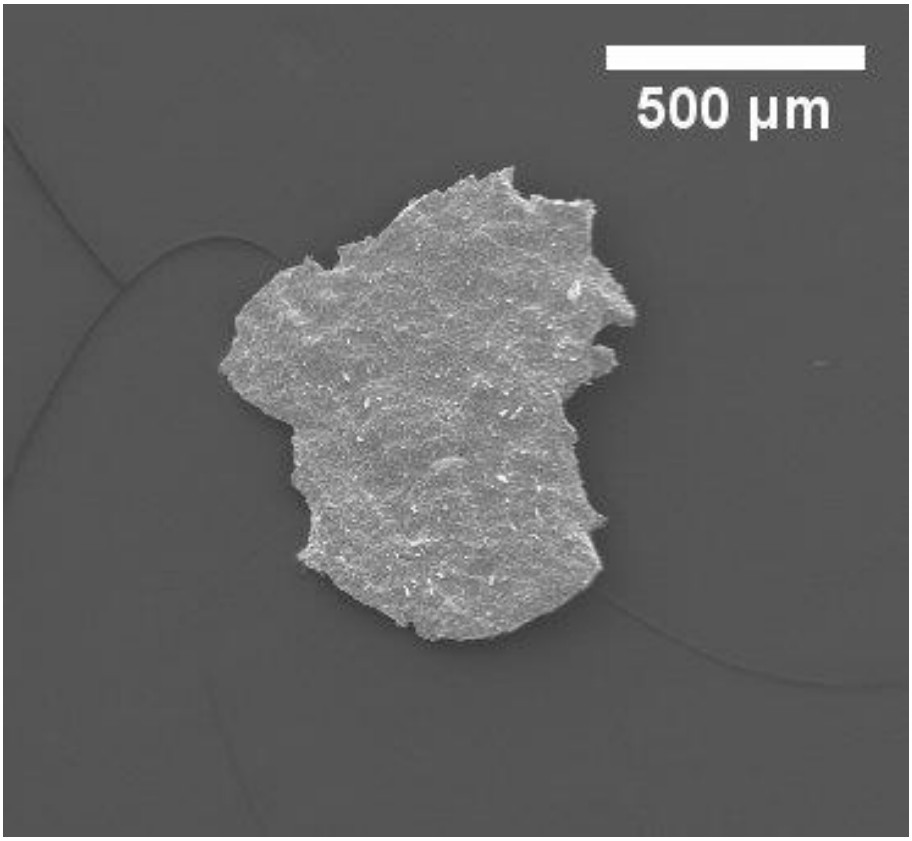

Figure 4-21 SE micrograph of surface of spalled oxide particle exposed to air saturated steam for 500 hours at 923 K.

Table 4-3 Spallation observations for TP347H FG exposed to air saturated steam at 923 K for 50 - 1000 hours.

Oxidation time (hours)	Observations	ΔT_d (K)	ΔT_p (K)	ΔT_{sp} (K)
50	Fe_2O_3 spallation.	352.4	370.7	557.8
100	Fe_2O_3 spallation.	341.9	370.3	487.9
300	Fe_2O_3 + Fe_3O_4 spallation.	335.1	335.1	555.3
500	Fe_2O_3 + Fe_3O_4 spallation.	277.0	329.9	394.5
750	Fe_2O_3 + Fe_3O_4 spallation.	292.2	327.9	540.0
1000	Fe_2O_3 + Fe_3O_4 spallation.	405.5	475.0	518.9

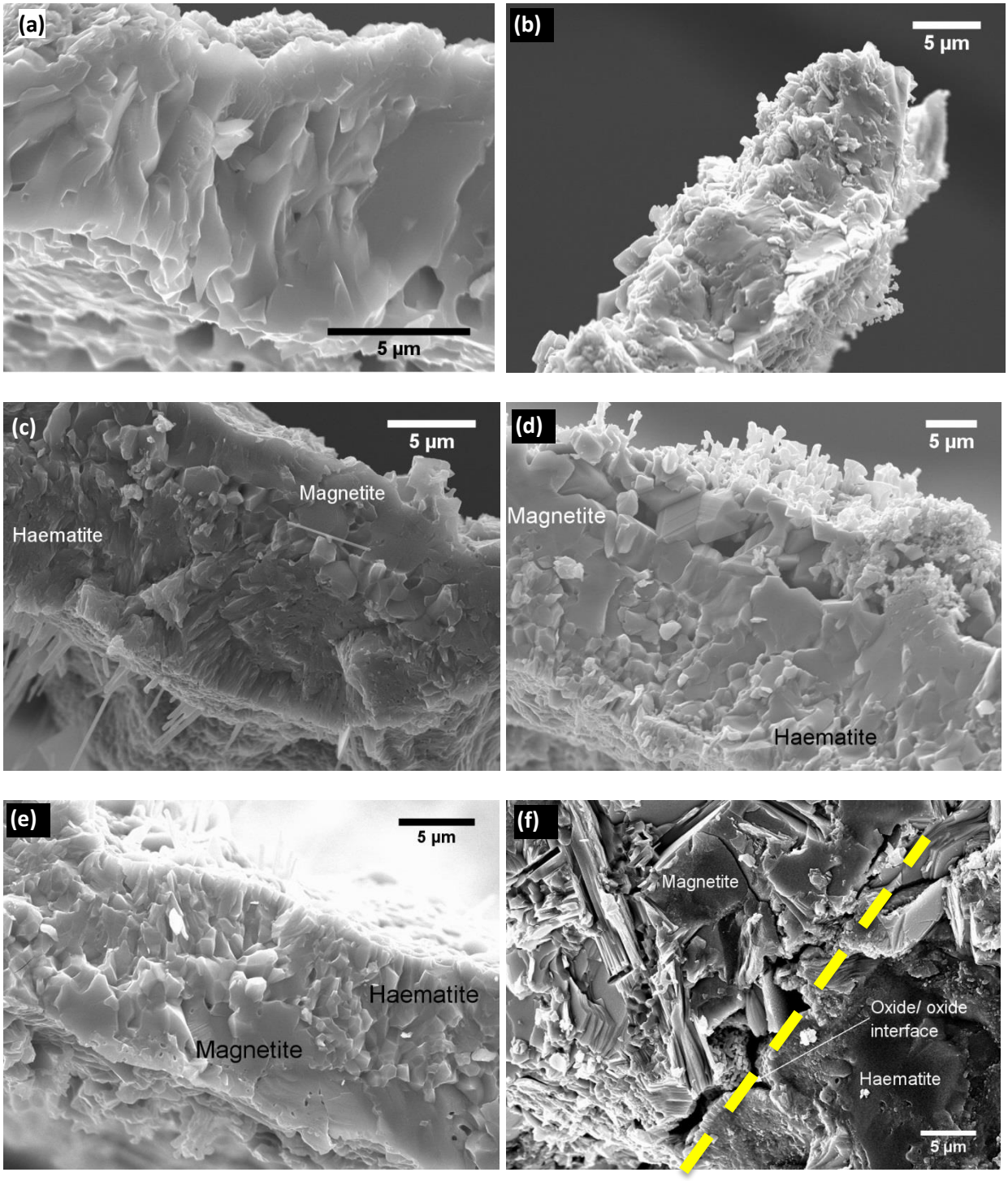

Figure 4-22 SEI micrograph of spall particle collected from TP347H FG post oxidation in air saturated steam at 923 K for (a) 50 hours, (b) 100 hours, (c) 300 hours, (d) 500 hours, (e) 750 hours and (f) 1000 hours.

The thickness of each spall particle was measured and plotted as a function of oxidation time and includes the standard deviations, Figure 4-23. As can be seen in the figure below, the thickness of haematite did not vary significantly for the duration

of the testing period with only a small increase between 50 and 1000 hours. It was mentioned earlier in the literature review, Section 2.3.7.3, that Gorman and Fry [41] suggested the formation of haematite under high oxygen partial pressures decreased the diffusion rate of oxygen and prevented further formation of haematite. The small increase in the thickness of haematite observed in this thesis provides some evidence for that theory. The main contribution to the increase in thickness of the spalled particles was from magnetite.

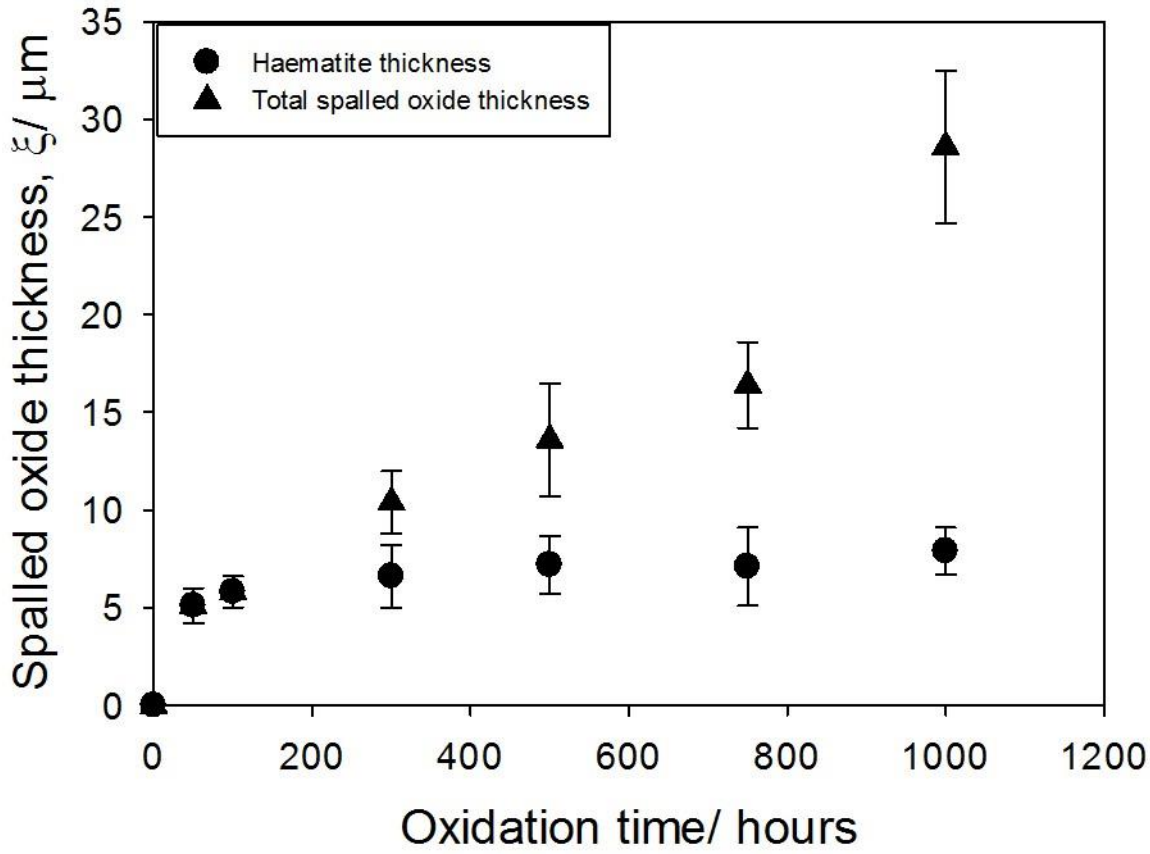

Figure 4-23 Haematite and total spalled oxide thickness as a function of oxidation time at 923 K.

4.4 Discussion

Previous work showed the oxides formed on TP347H FG to be that of haematite, magnetite, spinel, a Cr-rich oxide and Cr_2O_3 [2]. Other studies have also described the oxide at the base of the spinel to be Cr-rich [104], [162]. Further investigations into the Cr-rich oxide in this thesis have shown that the oxide chemistry is that of chromite, $FeCr_2O_4$. The initial stages of oxidation were investigated in this work and Figure 4-24 shows a proposed oxidation mechanism for TP347H FG exposed to air-saturated steam up to 1000 hours at 923 K. Chromite and chromia are shown to form along the grain boundaries whilst spinel is an inwardly growing oxide and haematite/ magnetite are outwardly growing oxides.

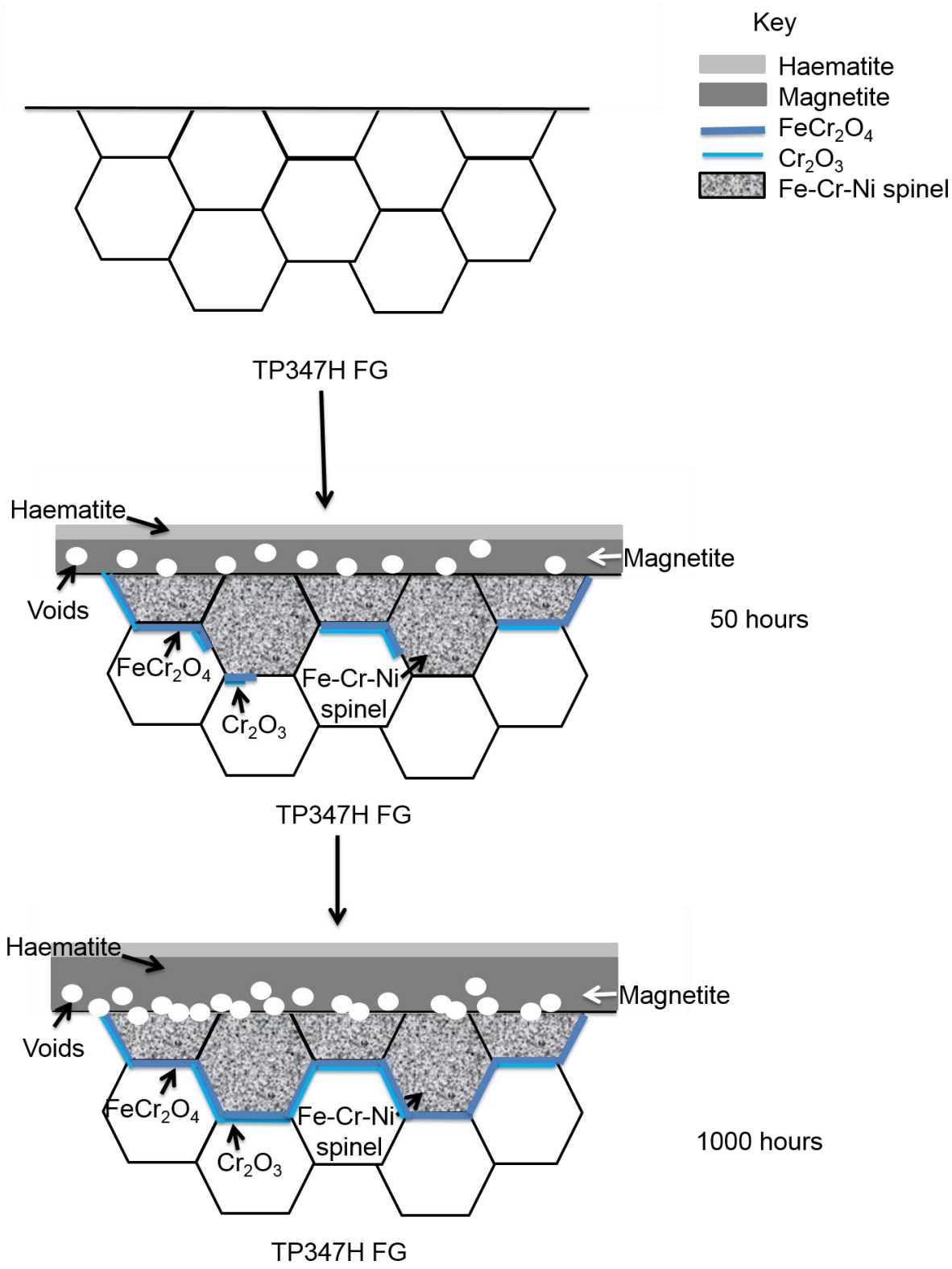

Figure 4-24 Proposed oxidation mechanism for TP347H FG exposed to air-saturated steam at 923 K.

Energy release by wedging was considered by H.E. Evans *et al.* [163] and buckling considered by A.G. Evans and J.W. Hutchinson [146] and C.H. Wells *et al*. [147]. These mechanisms can be modelled respectively by:

$$\Delta T_w = \left(\frac{\gamma_F}{\xi E_{ox}(\Delta\alpha)^2(1-\nu_{ox})}\right)^{1/2}$$ **Equation 4-4**

and:

$$\Delta T_b = \frac{1.22}{\Delta\alpha(1-\nu_{ox}{}^2)}\left(\frac{\xi}{R}\right)^2$$ **Equation 4-5**

where γ_F is fracture energy, J.m^{-2}, ξ is oxide thickness, m, E_{ox} is Young's modulus, Pa, $\Delta\alpha$ is the difference in thermal expansion coefficient between metal and oxide, K^{-1}, v is Poisson's ratio, R is the radius of decohesion, m, and ΔT_w and ΔT_b are the temperature drops to initiate spallation via wedging and buckling, respectively, K.

For some systems, spallation does not result from buckling, i.e. stable buckles form. Propagation of the crack is therefore necessary to result in spallation of the oxide, i.e. unstable buckling which can be described thus [147]:

$$\Delta T_{ub} = \left(\frac{1.052\xi^4}{R^4} + \frac{1.041\gamma_F}{E_{ox}\xi}\right)^{1/2} x\ \frac{1}{\Delta\alpha}$$ **Equation 4-6**

where ΔT_{ub} is the critical temperature drop required to initiate spallation via unstable buckling and all other parameters are as above.

This equation includes a term corresponding to the initiation of the buckle, i.e. Equation 4-5, and a term corresponding to the propagation of the buckle. However,

this mechanism is unable to occur without prior buckling. These mechanisms are shown schematically in Figure 4-25 and assume that the oxide is unstressed at temperature. On cooling, the oxide is under compression which introduces stresses.

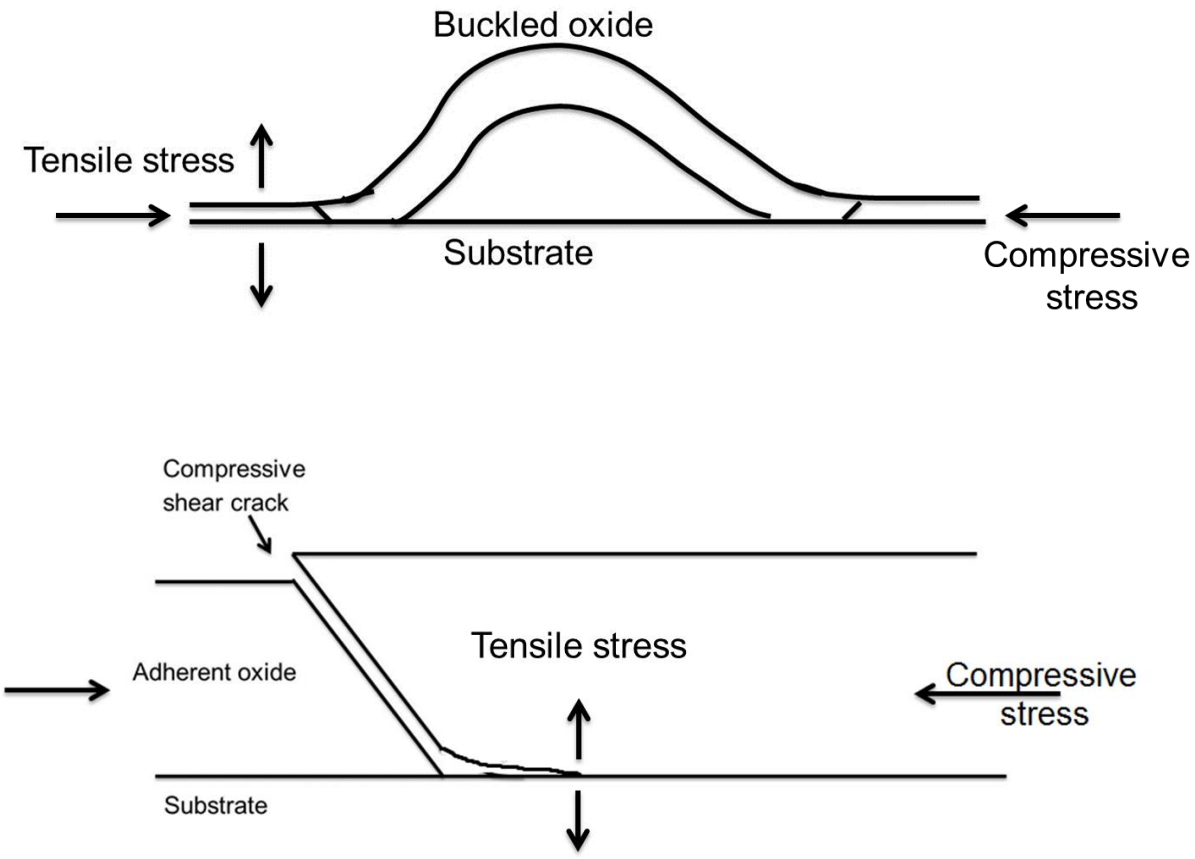

Figure 4-25 Buckling spallation mechanism (top) described by Equation4-3 and wedging spallation mechanism (bottom) described by Equation 4-2.

The release of strain energy derived from compressive stresses is the driving force for these processes. The system under consideration here undergoes these processes as a result of the difference in thermal expansion coefficient between the metal and oxide. If the spallation mechanism followed that of stable buckling, the radius of delamination would follow the red lines shown in Figure 4-10, Figure 4-12,

Figure 4-14, Figure 4-16, Figure 4-18, Figure 4-20, i.e. the critical strain energy criterion (CSEC).

Where the thermal expansion coefficient of the oxide is lower than that of the alloy, significant compressive stresses can develop during cooling, e.g. between haematite and TP347H FG. Thermal expansion coefficients have been studied in the literature and while the value for haematite is relatively constant with temperature, there is some debate over the correct value for magnetite. Gorton *et al*. [138] and Takeda *et al*. [135] have both proposed values for the thermal expansion coefficient of magnetite, the curves for which are shown in Figure 4-26 as a function of the temperature range the values were measured over. Gorton *et al*. measured the thermal expansion coefficient for natural magnetite in air from the temperature dependence of lattice parameters. Results from that work indicated that magnetite undergoes a transformation between 798 and 948 K from an inverse spinel structure to a normal spinel structure as indicated in Figure 4-26. Takeda *et al*. [135] on the other hand investigated the thermal expansion coefficient of synthetic oxides. The coefficients in that work were measured using a thermo mechanical analyser between room temperature and 1273 K. The measurements on magnetite were carried out in an inert atmosphere to prevent further oxidation to haematite and reduction to wüstite. Armitt *et al*. [136] also reported on the work carried out by Gorton *et al*. [138].

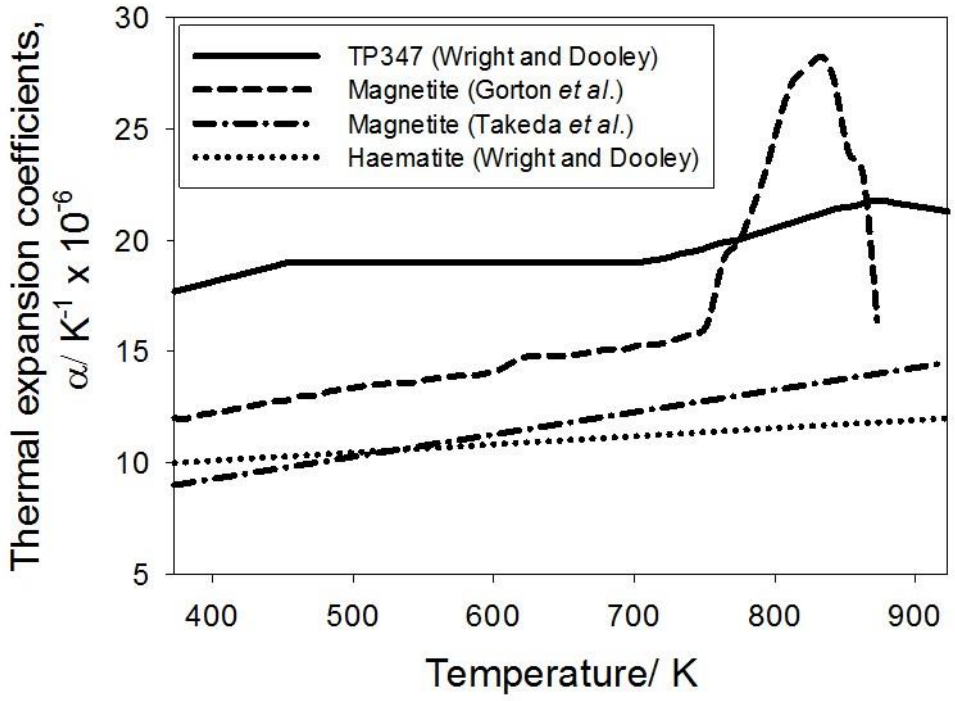

Figure 4-26 Thermal expansion coefficients for alloy TP347H [2] and its oxides haematite [2] and magnetite after [138] and [135].

The thermal expansion curves shown in Figure 4-26 were integrated between 373 K and 923 K to obtain an average thermal expansion coefficient, i.e. the oxidation temperature used in this thesis down to the lowest spallation temperature observed with STORME. Simpson's rule was used for the integration with a spacing of 10 K. The average values obtained for haematite, magnetite from both Takeda *et al*. [135] and Gorton *et al*. [138] and TP347H FG are shown in Table 4-4. In the case of magnetite, the average value obtained was higher when measurements were taken in air [138].

Table 4-4 Average thermal expansion coefficients obtained from integration.

Oxide/ Alloy	α x 10^{-6} (K^{-1})	Temperature range (K)
Fe_2O_3 [2]	12.2	373-923
Fe_3O_4 [138]	16.6	373-873
Fe_3O_4 [135]	12.0	373-923
TP347H FG [2]	19.9	373-923

Since the value obtained by Takeda *et al*. was for that of synthetic oxides, it was deemed more appropriate in this thesis to use the value for natural magnetite obtained by Gorton *et al*. [133].

Table 4-5 Parameters obtained from the literature for the Young's modulus and Poisson's ratios of haematite and magnetite.

	Haematite	Magnetite
E_{ox} (GPa)	230 [164]	210 [165]
v_{ox}	0.3 [142]	0.3 [142]

Spallation will occur when the strain energy contained within that part of the oxide is equal to the fracture energy required to form new surfaces at the oxide/ oxide or oxide/ metal interface [142]. For the thin layer approximation, the stored energy within the oxide layer, W*, can be determined from:

$$W^* = (\Delta\alpha)^2(\Delta T)^2(1-\nu_{ox})E_{ox}\xi \qquad \text{Equation 4-7}$$

where Δα is the difference in thermal expansion coefficients, K^{-1}, ΔT is the temperature drop, K, v is Poisson's ratio, E_{ox} is Young's modulus, Pa, and ξ is thickness, m.

Strain energy calculations were carried out using Equation 4-7 for both haematite and magnetite using the data shown in Table 4-5 and the temperature drop for

propagation to investigate which of the two oxides had the highest contributing factor. The results obtained from these calculations are shown in Table 4-6. Also included in this table is the total strain energy, W_t^*. Since magnetite did not spall after 50 and 100 hours isothermal oxidation it was not possible to determine the strain energy contribution. For all other oxidation times it can be seen that the largest contribution to the overall strain energy was haematite suggesting haematite is the main cause for spallation in the system considered in this thesis.

Table 4-6 Strain energy for haematite and magnetite calculated from Equation 4-7.

Oxidation time/ hours	W_h^* J.m^{-2}	W_m^* J.m^{-2}	W_t^* J.m^{-2}
50	6.7		6.7
100	7.6		7.6
300	7.1	1.2	8.3
500	7.5	1.2	8.7
750	7.3	1.5	8.8

Theoretical ΔT values were calculated using Equations 4-4, 4-5 and 4-6 based on experimentally determined values of spalled oxide thickness and radius of localised spall sites, the calculated Δα values obtained from Table 4-4 and literature values of E_{ox} and v_{ox}, Table 4-5.

The calculated values of ΔT from Equations 4-6, 4-5 and 4-6 were plotted as a function of the experimental values measured using STORME, Figure 4-27, Figure 4-28 and Figure 4-29, respectively. In the first instance only haematite thickness was taken into consideration since this was thought to be the main cause for spallation. Since spallation via wedging occurs via through thickness cracking of the oxide

followed by cracking at the oxide/ oxide, oxide/ alloy interface or within the oxide, theoretical ΔT_w values were plotted as a function of ΔT_{sp}, Equation 4-4, Figure 4-27. Buckling on the other hand occurs via delamination at an interface followed by through thickness cracking and so theoretical ΔT_b values were plotted as a function of experimental ΔT_d, Equation 4-5, Figure 4-28. Finally, Wells *et al*. [147] modelled unstable buckling and Equation 4-6 is based upon the start of the release of energy, i.e. the buckle propagation. Therefore theoretical ΔT_{ub} values calculated from Equation 4-6 were plotted as a function of experimental ΔT_p, the propagation temperature drop, measured using STORME, Figure 4-29. If the oxide system presented in this thesis was spalling via one of the aforementioned mechanisms the points on the ΔT vs ΔT graphs would be expected to cluster on a 45° line. These lines have been included in Figure 4-27, Figure 4-28 and Figure 4-29.

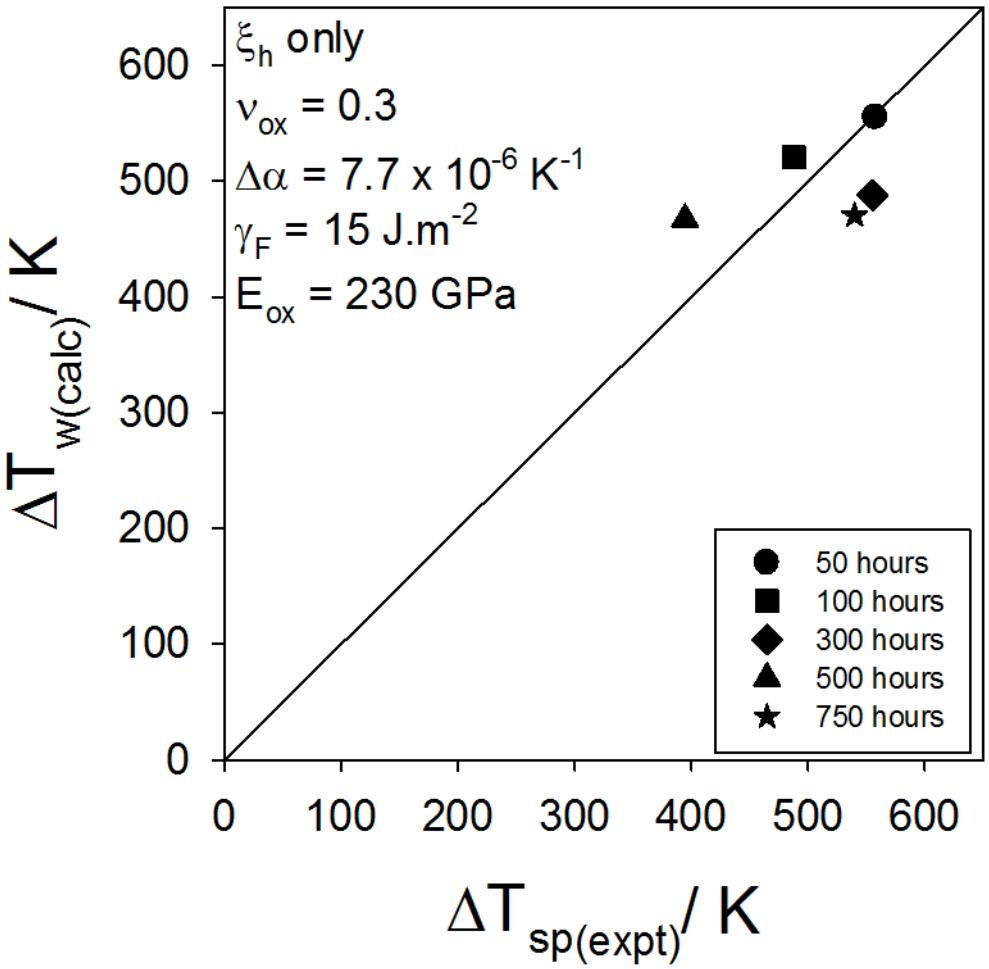

Figure 4-27 Plot of calculated ΔT_w from Equation 4-4 as a function of experimental ΔT_{sp} values measured using the STORME technique for each of the oxidation times tested.

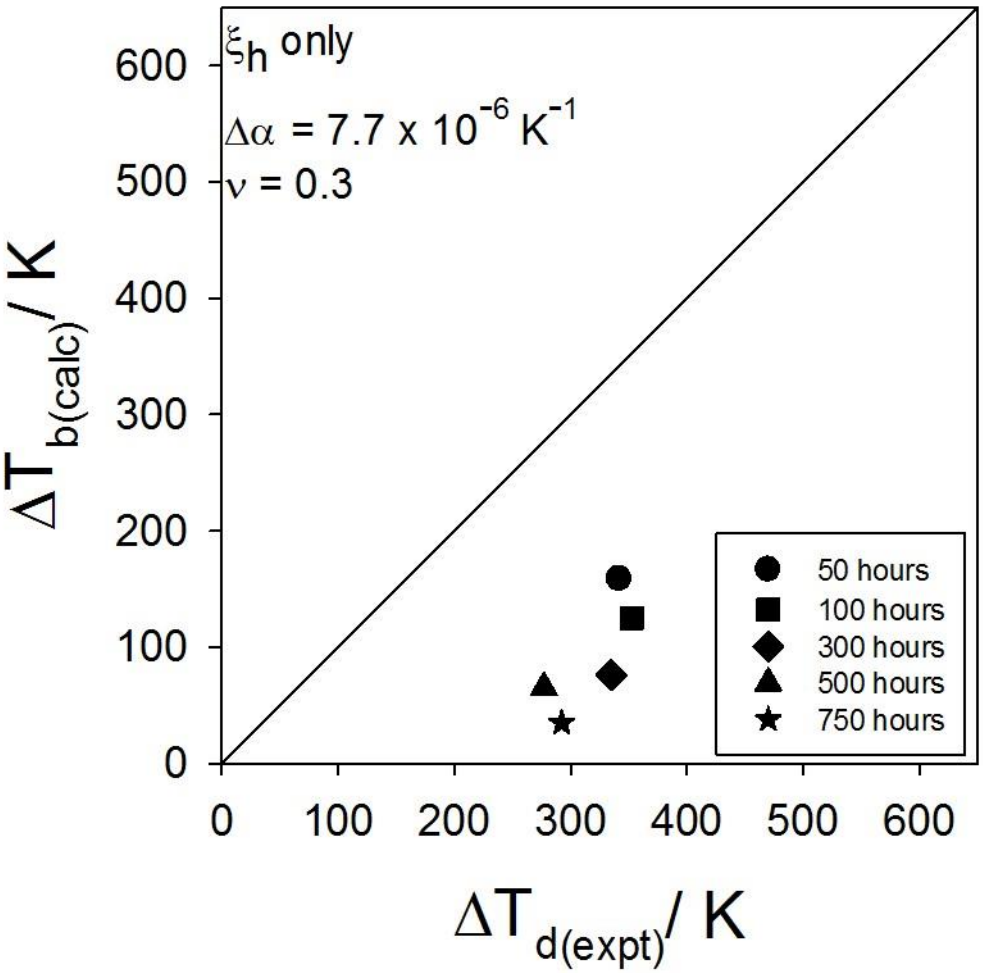

Figure 4-28 Plot of calculated ΔT_b from Equation 4-5 as a function of experimental ΔT_d values measured using the STORME technique for each of the oxidation times tested.

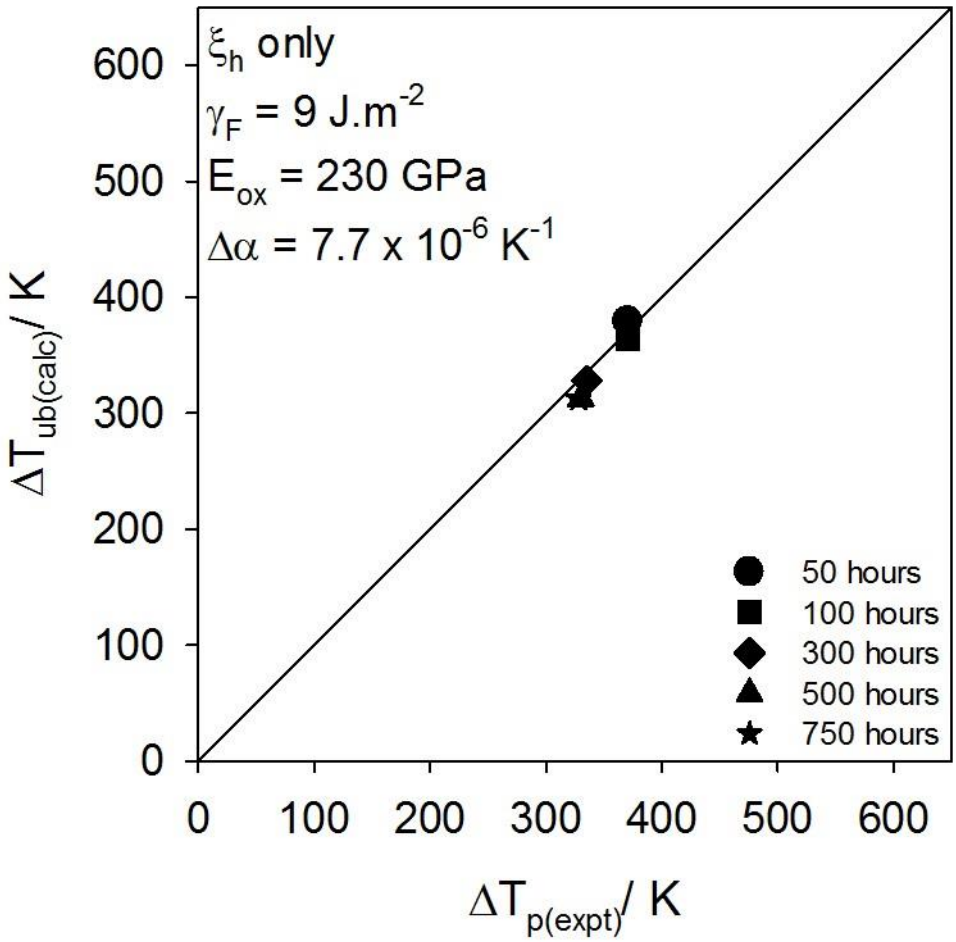

Figure 4-29 Plot of calculated ΔT_{ub} from Equation 4-6 as a function of experimental ΔT_p values measured using the STORME technique for each of the oxidation times tested.

Based on experimental observations such as the visible delamination in thermographic images and cross sectional analysis, initial thoughts were that spallation occurred via a buckling mechanism. It has also been suggested in the literature that the difference in thermal expansion coefficient between haematite and magnetite increases the buckling affinity of the outer oxides [166] therefore increasing the expectation of the buckling mechanism. It can be seen from Figure 4-27 and Figure 4-28, where the wedging and buckling equations were used respectively, to calculate theoretical values of ΔT, that the calculated values do not fit with the experimental values measured although the wedging approach shows an improved fit compared to buckling. Figure 4-29 gave the best fit of theoretical values

to experimental values of ΔT where the unstable buckling equation was used and a line of best fit was used to determine fracture energy, γ_F, 9 $J.m^{-2}$ for the haematite/ magnetite interface.

Further evidence for the unstable buckling mechanism was observed during cross sectional analysis where a region of oxide had appeared to buckle with some possible crack extension, Figure 4-3 (b), as mentioned earlier. There was no extensive experimental evidence to suggest spallation occurred via the wedging process. However, Figure 4-3(d) could suggest wedge cracking.

Data obtained from the literature indicated that no spallation occurred for samples that were exposed to deoxygenated steam where there was no haematite formation, [21], [167]. Other studies also showed that in air + Ar environments where haematite was observed spallation occurred. However, in H_2 + Ar environments there was no evidence of haematite growth or spallation [104]. In this thesis, where air saturated steam was used, haematite was formed and spallation was observed of both haematite and magnetite for longer term testing of more than 300 hours. It is therefore hypothesised that the cause for spallation in this system is the presence of haematite. The reason for magnetite spallation for tests of ≥ 300 hours is thought to be as a result of void coalescence. Other research available in the literature has also suggested that the formation of voids is the leading cause for spallation of steam grown oxides [80]. It was mentioned earlier in Section 4.2.3 that voids were observed within the magnetite layer over shorter term oxidation testing and at the magnetite/ spinel interface for longer term testing. Voids are thought to occur as a result of the Kirkendall effect whereby the difference in the diffusion coefficients between two species moving in counter directions within the oxide (or alloy) can result in the

formation of vacancies [168]. Where the vacancies coalesce pores form and grow. Diffusion coefficients of O and Fe are shown in Appendix D through the various oxides of relevance here. Diffusion coefficients of elements through spinel were not available in the literature but since magnetite possesses an inverse spinel structure it is thought that the diffusion coefficients will be of the same order of magnitude. In this study the diffusion of O inwards through the Fe oxides to the magnetite/ spinel interface is slower than that of Fe outwards through the spinel layer. For longer term oxidation testing spallation was observed to occur at the magnetite/ spinel interface and remnants of the void walls were visible in cross sectional analysis at the spallation interface. The area fraction of voids was shown to remain constant for shorter term oxidation testing of 50 – 100 hours but was more difficult to interpret when void coalescence resulted in a change of spallation interface, Table 4-2. Instead the diameter between void walls was measured and was shown to increase with increasing oxidation time, Table 4-2. Evidence for void coalescence was shown in Figure 4-3 (f).

Data gathered from the STORME technique and values obtained in the literature were then used to model the spallation behaviour using the wedging and buckling equations, 4-4 and 4-5, respectively, as boundary conditions, Figure 4-30. In this instance again only haematite spalled thickness was taken into consideration. The spallation map includes four regions separated by the two boundary conditions calculated using the buckling and wedging equations; buckling; unstable buckling or wedging; wedging and adherent oxide. Where only haematite was considered, the delamination events fall within the stable buckling region. However, once spallation occurred the points then fell within the unstable buckling or wedging region providing

further evidence for the unstable buckling regime. Haematite has been shown to play a significant part in the spallation process.

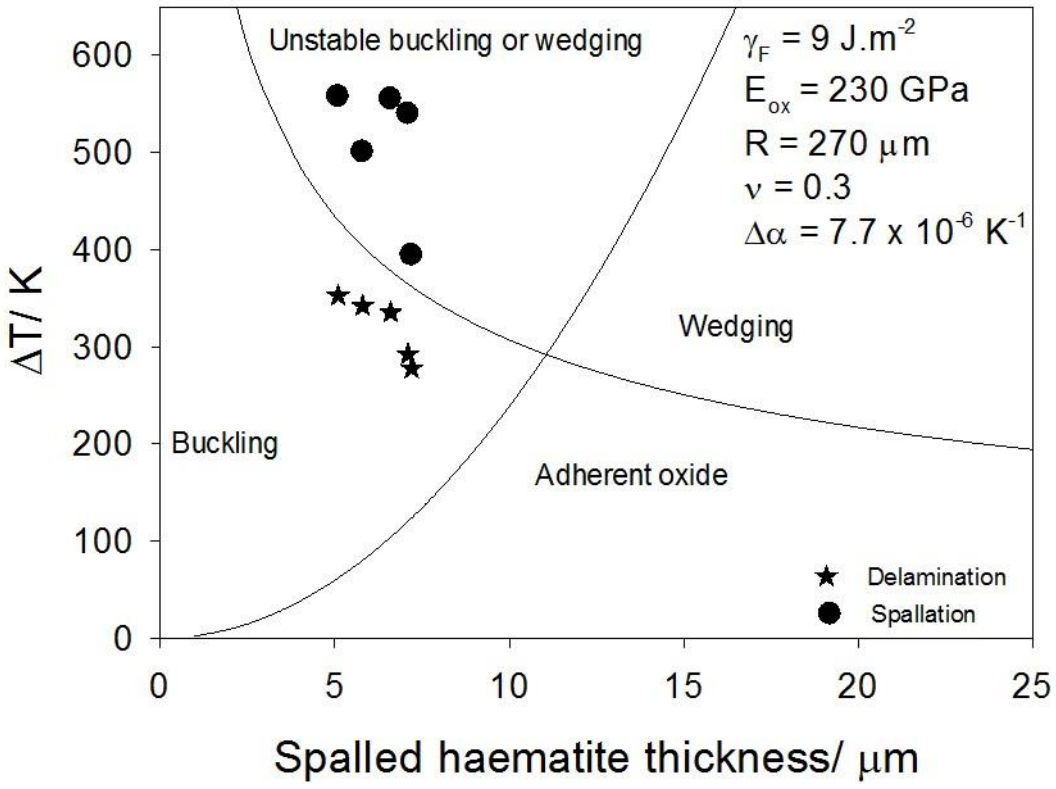

Figure 4-30 Spallation map constructed from the wedging and buckling equations showing experimental data for haematite spallation only.

Since magnetite did spall after 300 hours isothermal oxidation, the ΔT vs ΔT graphs for Equations 4-4, 4-5 and 4-6 were plotted taking only magnetite thickness into consideration, Figure 4-31, Figure 4-32 and Figure 4-33, respectively.

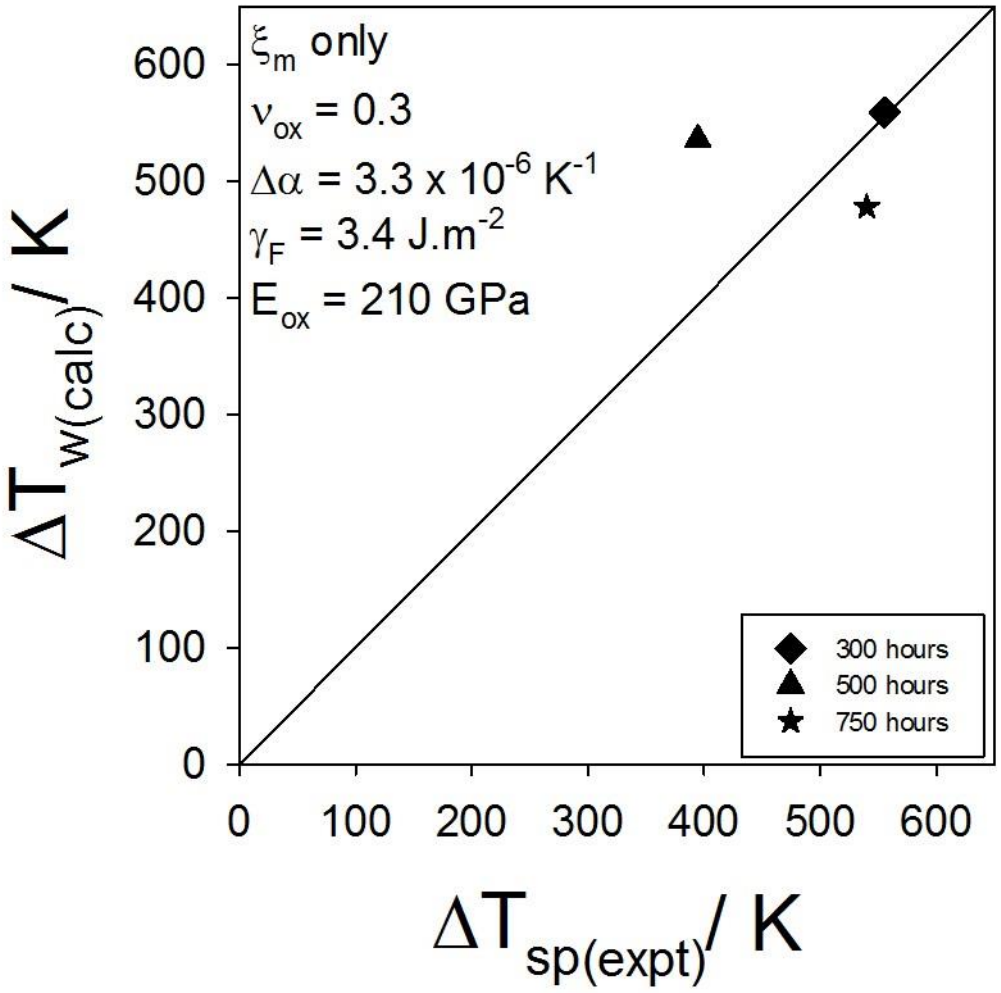

Figure 4-31 Plot of calculated ΔT_w from Equation 4-4 as a function of experimental ΔT_{sp} values measured using the STORME technique for each of the oxidation times tested.

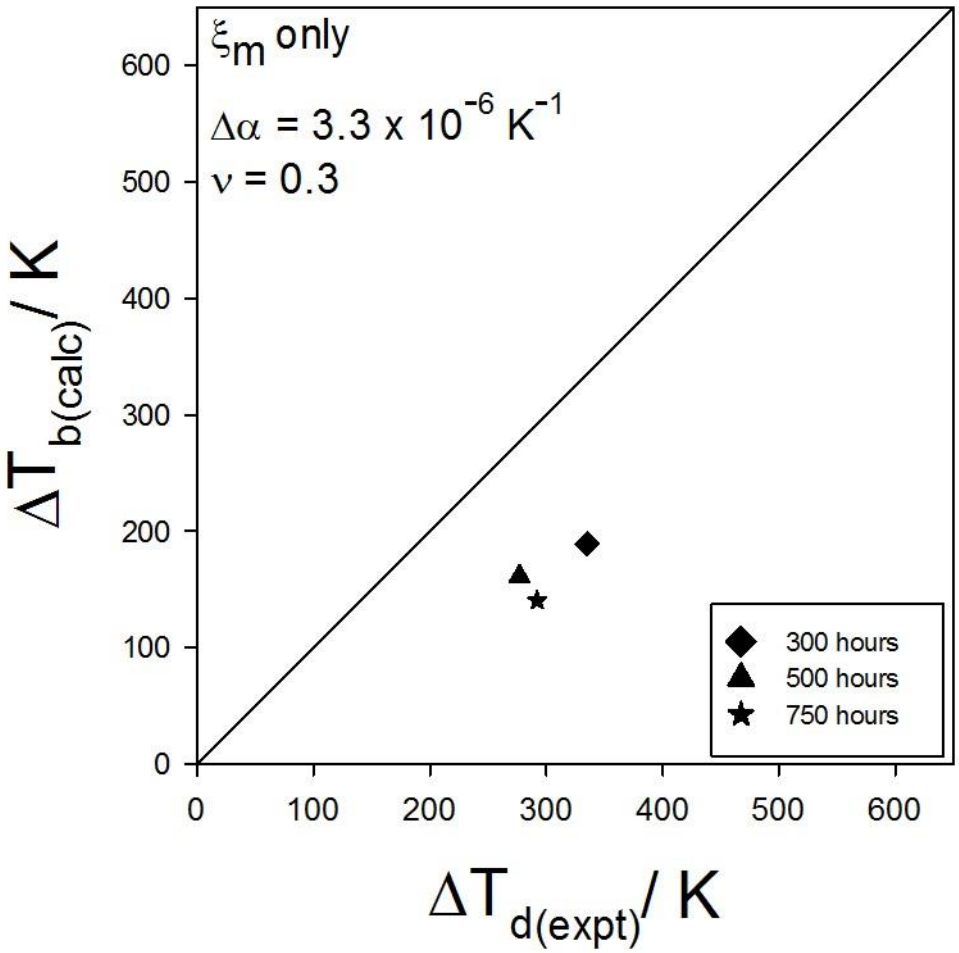

Figure 4-32 Plot of calculated ΔT_b from Equation 4-5 as a function of experimental ΔT_d values measured using the STORME technique for each of the oxidation times tested.

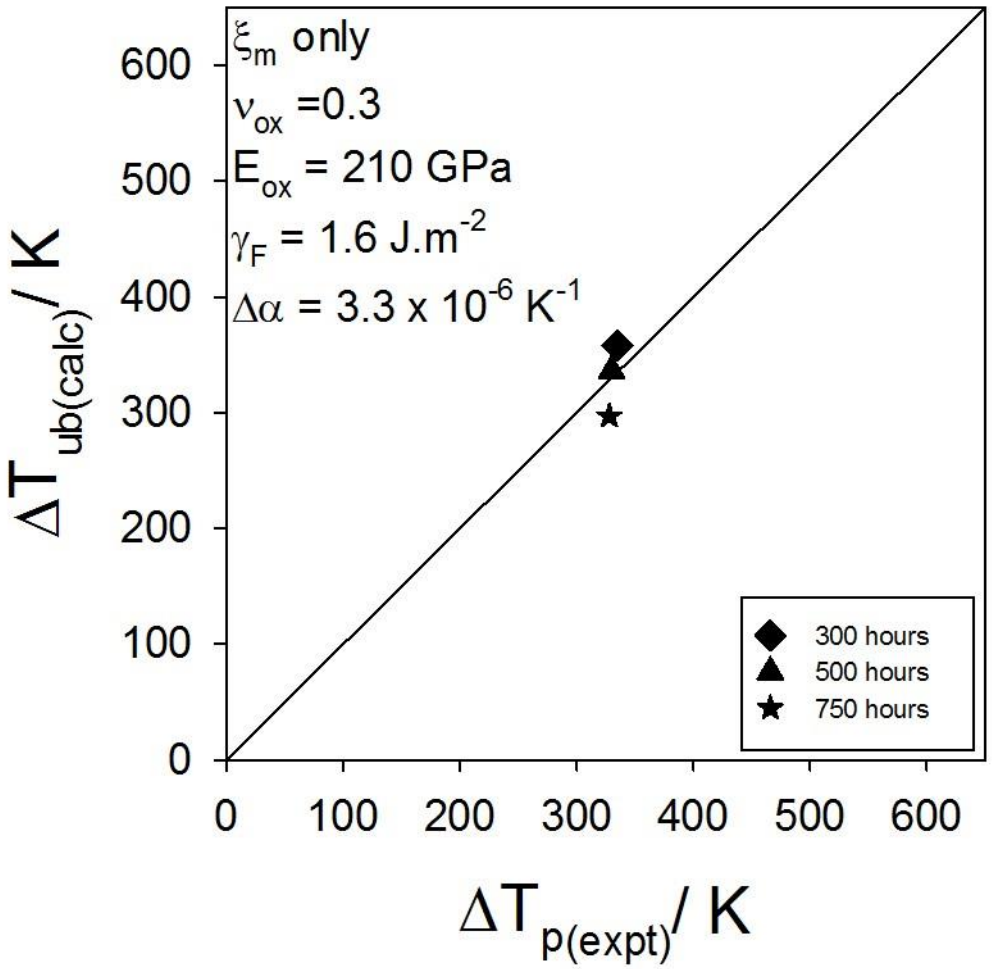

Figure 4-33 Plot of calculated ΔT_{ub} from Equation 4-6 as a function of experimental ΔT_p values measured using the STORME technique for each of the oxidation times tested.

The wedging and buckling equations did not show as good a fit as the unstable buckling equation, as was observed for haematite. Again a line of best fit was used for the unstable buckling plot to determine the fracture energy for spallation at the magnetite/ Fe-Cr-Ni spinel interface and was found to be 1.6 $J.m^{-2}$. This is significantly lower than the 9 $J.m^{-2}$ observed for the haematite/ magnetite interface calculated earlier, Figure 4-29, and is thought to be caused by the coalescence of voids indicated in cross sectional figures, Figure 4-3.

A spallation map was produced where only the thickness of magnetite was taken into consideration, Figure 4-34. In this instance, at the time of delamination two of the oxidation times tested would be expected to remain adherent and one fell in the buckling region of the map. In all cases where magnetite spallation was also observed the points fell in the unstable buckling or wedging regime.

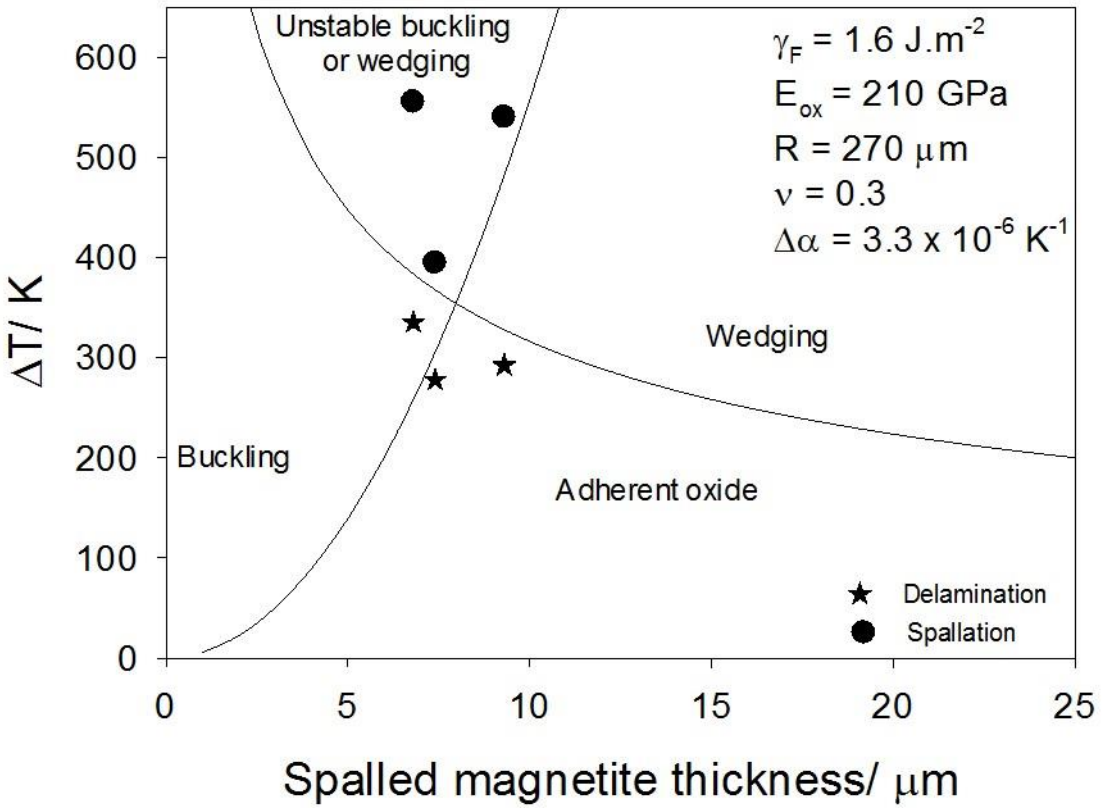

Figure 4-34 Spallation map where the boundaries were determined from buckling and wedging equations and only magnetite thickness was taken into consideration.

The spallation mechanism was then determined using the total spalled oxide thickness where both the haematite and magnetite contributions were included. An average value of Δα was obtained by determining individual Δα values based on total strain energy from Table 4-6 and then averaging these. Again the ΔT vs ΔT graphs were plotted to determine the best fit to the spallation mechanisms, Figure 4-35, Figure 4-36 and Figure 4-37.

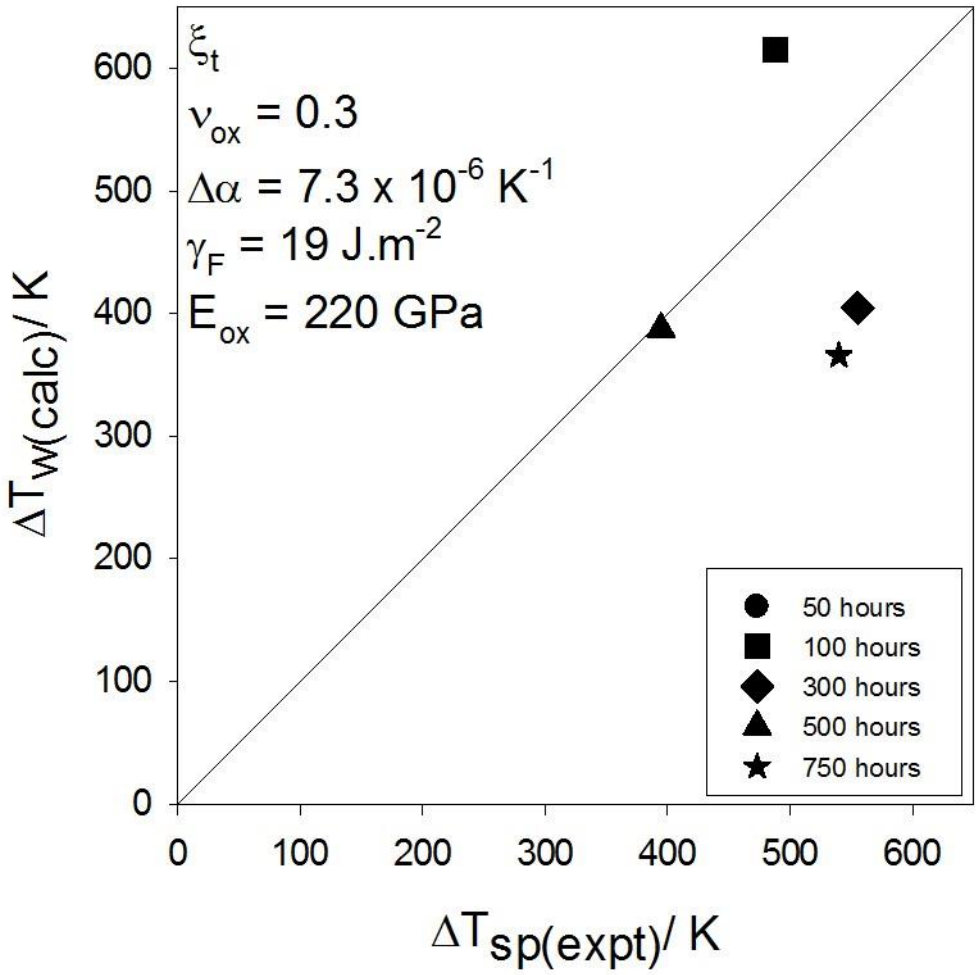

Figure 4-35 Plot of calculated ΔT_w from Equation 4-4 as a function of experimental ΔT_{sp} values measured using the STORME technique for each of the oxidation times tested.

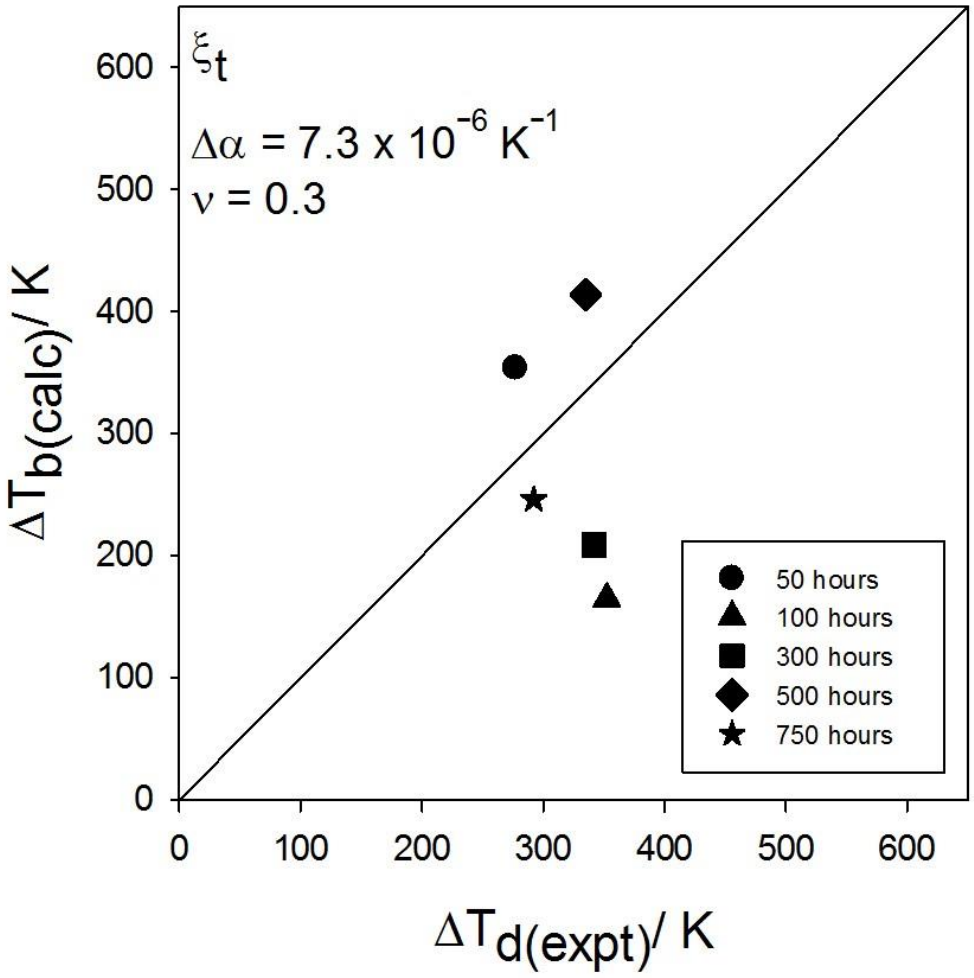

Figure 4-36 Plot of calculated ΔT_b from Equation 4-5 as a function of experimental ΔT_d values measured using the STORME technique for each of the oxidation times tested.

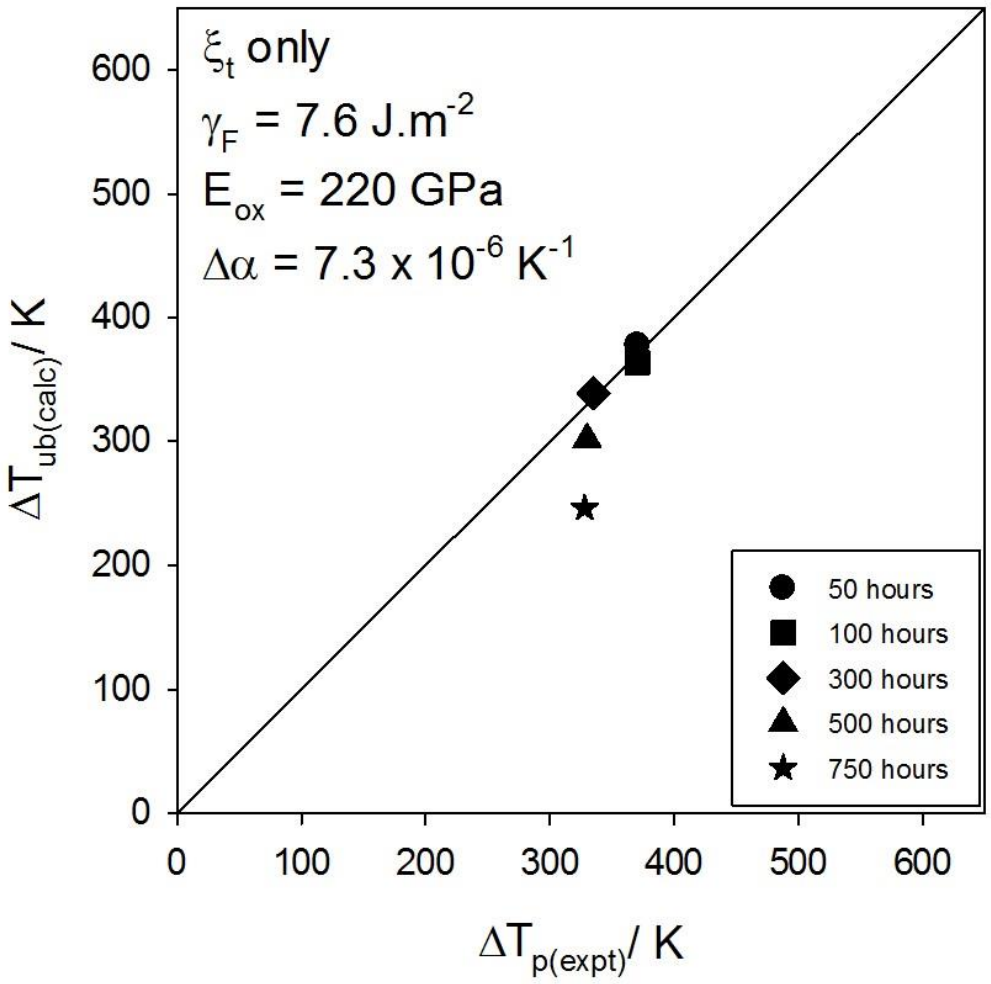

Figure 4-37 Plot of calculated ΔT_{ub} from Equation 4-6 as a function of experimental ΔT_p values measured using the STORME technique for each of the oxidation times tested.

Again, the best fit produced by the ΔT vs ΔT plots was obtained when the unstable buckling equation was used, Figure 4-37. The fracture energy in this case, determined from a line of best fit, was found to be 7.6 $J.m^{-2}$. A spallation map for total spalled oxide thickness was then plotted using the wedging and buckling equations, Equations 4-4 and 4-5, respectively, as the boundary conditions, Figure 4-38. In this instance, the delaminated points fall into 3 regions, buckling, wedging and unstable buckling but fall close to the boundary. All of the spallation points fall within the

unstable buckling regime, as was observed when haematite and magnetite thickness were considered separately, Figure 4-30 and Figure 4-34, respectively.

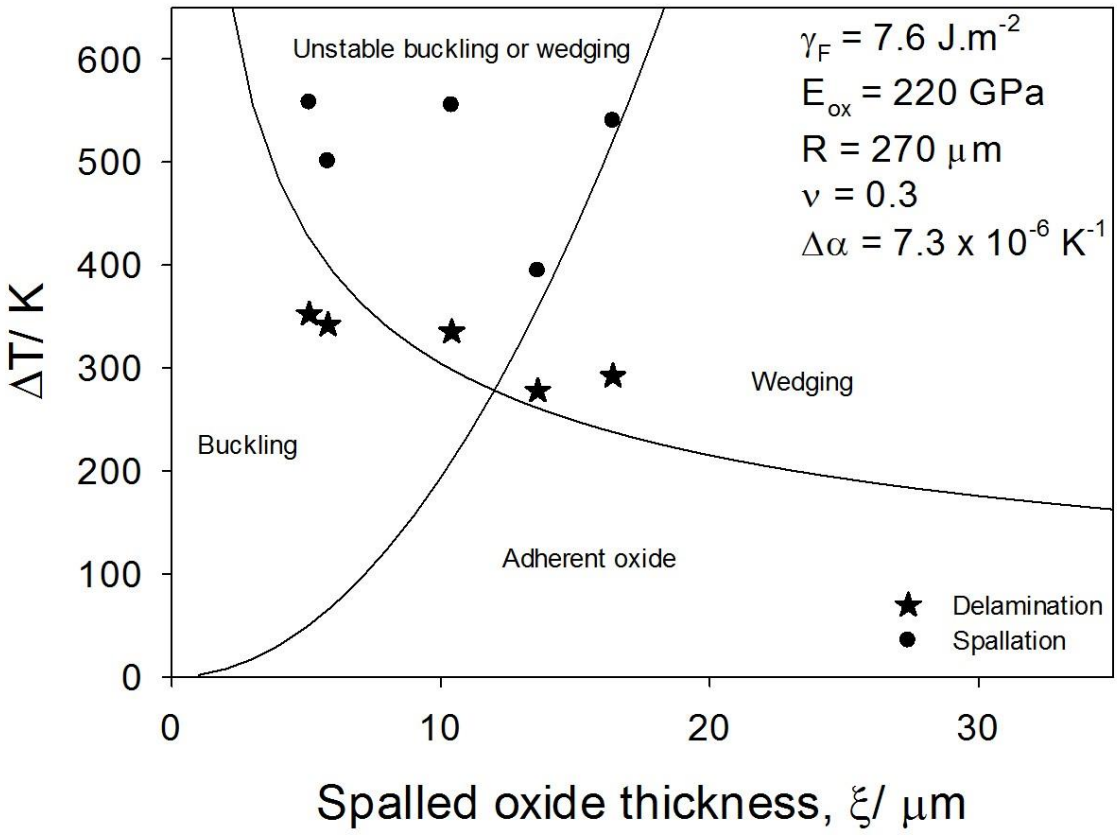

Figure 4-38 Spallation map where the boundaries were determined from buckling and wedging equations and the total spalled oxide thickness was taken into consideration.

4.5 Concluding Summary

The initial stages of oxidation of TP347H FG in air-saturated steam at 923 K were investigated in this chapter. Oxidation under these conditions resulted in the formation of layers of Fe-Cr-Ni spinel, magnetite and haematite. In this work it has also been shown that a Cr-rich oxide develops at the spinel/ alloy interface. This layer has been shown to be a double layer of the chromite $FeCr_2O_4$ and a thin Cr_2O_3 layer in contact with the alloy using TEM analysis. A mechanism for oxidation has

been suggested, Figure 4-24. Measurements of the thickness of the Cr_2O_3 agree well with that predicted from literature values [154]. Kinetic data for the Fe-Cr-Ni spinel was also included in this work and was shown to follow near-cubic behaviour. This behaviour could be as a result of the formation of the Cr_2O_3 layer reducing the growth rate. This was also shown with TEM/ EDS analysis where Fe enhancement was observed beneath the Cr-rich layers.

A significant contribution was made in the understanding of the processes leading to spallation in this system by the development of a technique, termed STORME. The novel STORME technique was developed throughout the course of this project and provided the ability to monitor the temperature of a surface during cooling and identify the temperature of initial delamination and spallation events. Meticulous collection of spalled particles enabled cross sectional SEM examination and enabled the oxide thickness to be measured and oxide chemistry to be identified through cross examination of morphologies. Haematite thickness was shown to increase slightly for the complete testing period whereas magnetite thickness increased substantially, especially after 1000 hours oxidation. Results obtained through the STORME technique and modelling of the spallation behaviour have shown that haematite is required to initiate spallation with a fracture energy of 9 $J.m^{-2}$ at the haematite/ magnetite interface. This was also apparent in the literature [21], [136], [167], where spallation was not observed in deoxygenated steam conditions that resulted in the growth of magnetite only. Magnetite was shown to spall after 300 hours in air-saturated steam which was postulated to be as a result of void formation. Evidence for void formation was found in the literature for Super 304 H, which has a similar composition to that of TP347H FG, exposed to deoxygenated steam at 973 K

for 100 hours [21]. The area fraction of voids in that work was measured to be around 1%, noticeably less than in air-saturated steam observed for this work, and there was no evidence for void coalescence. The coalescence of voids within the magnetite layer for shorter term testing and at the magnetite/ spinel interface for longer term testing in this thesis was shown to decrease the fracture energy to 1.6 $J.m^{-2}$ at the respective sites resulting in the spallation of magnetite. Investigations into the spallation mechanism showed that unstable buckling provided the most suitable fit for both haematite and magnetite individually and when considering the total oxide thickness. Spallation maps were plotted to model the oxidation behaviour and provide a basis for predicting the onset of spallation. In all of the maps produced in this work spallation was shown to fall within the unstable buckling domain of the map.

Chapter 5 Cyclic Steam Oxidation Behaviour of TP347H FG

5.1 Introduction

This chapter will compare the results seen when TP347H FG was exposed to different steam environments for the second thermal exposure to examine the effect of oxygen partial pressure on continued oxidation and spallation behaviour. The effect of oxide thickness from cycle 1 will also be considered and comparisons will be made to samples oxidised isothermally under constant steam conditions at 923 K. Where possible, thermographic snapshots of the inner concave surface during cooling have been included in the results to investigate the spallation behaviour subsequent to the first thermal exposure. On some occasions, the thermal imaging camera was unavailable.

Several cyclic oxidation experiments were carried out for various times in different steam atmospheres at 923 K, as described in Table 5-1. The results for cycle one of these exposures were discussed in Chapter 4.

Three series of experiments were carried out for this chapter of the work. The first consisted of two separate batches of experiments that were all thermally cycled for the same duration. The first batch consisted of thermal exposures where both cycles were carried out in air-saturated steam, labelled A1, B1, C1 and D1 in Table 5-1. The second batch of experiments in the first series of experiments involved the second thermal cycle being carried out in deoxygenated steam, labelled A2, B2, C2 and D2

in Table 5-1. The second series of experiments comprised thermal cycling exposures of various oxidation times of 50-1000 hours for the first thermal cycle followed by 1000 hours in deoxygenated steam for the second cycle, Section 5.2.2, labelled A3, B3, C3 and D2 in Table 5-1. Finally thermal cycling has been compared to isothermal oxidation for tests of the same duration under air-saturated steam conditions, Section 5.2.3.

Table 5-1 Experimental matrix for thermal cycling of TP347H FG in steam environments.

Test	Cycle one (air saturated steam)	Cycle two	Total oxidation time
A1	50 hours	50 hours: air-saturated steam	100 hours
A2	50 hours	50 hours: deoxygenated steam	100 hours
A3	50 hours	1000 hours: deoxygenated steam	1050 hours
B1	100 hours	100 hours: air-saturated steam	200 hours
B2	100 hours	100 hours: deoxygenated steam	200 hours
B3	100 hours	1000 hours: deoxygenated steam	1100 hours
C1	500 hours	500 hours: air-saturated steam	1000 hours
C2	500 hours	500 hours: deoxygenated steam	1000 hours
C3	500 hours	1000 hours: deoxygenated steam	1500 hours
D1	1000 hours	1000 hours: air-saturated steam	2000 hours
D2	1000 hours	1000 hours: deoxygenated steam	2000 hours

5.2 Results

5.2.1 Comparison of different environments for cycle 2

The first series of cyclic experiments investigated for this area of the work involved thermally cycling TP347H FG in steam and altering the oxygen partial pressure for the second thermal cycle. Deoxygenated steam with an oxygen partial pressure of 1×10^{-8} is more closely representative of the steam conditions seen in plant. The change in environment for the second cycle of some of the tests enabled an examination into the effect of oxygen partial pressure. Table 5-2 gives observational details on spallation behaviour for each of the experiments performed. For samples thermally cycled in air-saturated steam, spallation was observed on cooling from the second cycle. Deoxygenated steam cycles on the other hand showed no signs of visible spallation on cooling. Previous work in the literature where TP347H FG was thermally cycled in a steam environment with an oxygen content of 5 – 6 ppm at 893 K observed spallation on cooling reportedly after 400 hours where mass gain was shown to decrease [86]. Up until that point mass change was shown to increase for each cycle although results in this work as well as in the literature [21] have shown that mass change can be positive even when spallation of the outer Fe oxides has occurred. This was therefore not a true indication of whether a spallation event happened prior to 400 hours. Oxide chemistry and thickness measurements were not investigated between each cycle in that work making it difficult to interpret the actual oxidation and spallation behaviour. Dudziak *et al*. [169] on the other hand also exposed TP347H FG to steam for up to 1000 hours at 923 K and they observed an increase in mass gain at each 250 hour interval although the steam environment used in that study was deoxygenated. Spallation would therefore not be expected.

Table 5-2 Observations made for the second thermal cycle of TP347H FG in different steam environments at 923 K.

Test – cycle 2	Steam environment	Spallation observations	Area fraction of spallation (%)	Spalled oxide thickness (μm)
A1	Air-saturated	Spallation	2.6	5.5±1.3
A2	Deoxygenated	No spallation	0.0	-
B1	Air-saturated	Spallation	15.7	3.4±0.9
B2	Deoxygenated	No spallation	0.0	-
C1	Air-saturated	1 spall particle	0.8	7.1±1.1
C2	Deoxygenated	No spallation	0.0	-
D1	Air-saturated	No spallation	0.0	-
D2	Deoxygenated	No spallation	0.0	-

Chemical information of the Fe-Cr-Ni spinel oxide and oxide thickness measurements for each of the tests carried out are given in Table 5-3. These observations will be discussed in further detail throughout this section and experiments A1 and A2, B1 and B2, C1 and C2 and D1 and D2 will be discussed in turn in Subsections 5.2.1.1, 5.2.1.2, 5.2.1.3 and 5.2.1.4, respectively.

Table 5-3 Oxide thickness data and Fe concentrations of TP347H FG after oxidation in steam at 923 K for different durations.

Test	Cycle	Average Fe concentration in spinel (at.%)	Average spinel thickness (μm)	Maximum spinel thickness (μm)	Average Fe oxide thickness (μm)	Average Cr-rich oxide thickness (μm)
A1	1	23.1	7.6±2.5	13.7	5.4±2.4	0.0
	2	23.5	12.2±3.8	24.8	-	0.0
A2	1	30.4	6.6±2.3	11.5	7.5±1.4	0.0
	2	25.8	9.6±4.4	21.3	9.7±2.5	0.0
B1	1	23.0	9.7±3.6	20.4	12.8±3.9	0.0
	2	30.5	13.1±4.9	21.9	-	0.0
B2	1	29.9	10.2±3.4	17.5		0.0
	2	23.9	12.7±3.9	20.5	16.1±3.7	0.0
C1	1	25.3	12.2±3.6	19.7	-	1.1±0.4
	2	19.7	12.9±4.8	23.4	-	1.3±0.6
C2	1	30.4	13.4±4.8	25.4	-	1.1±0.5
	2	21.5	14.0±4.6	28.8	4.3±1.6	1.8±0.5
D1	1	28.6	18.4±9.1	31.6	-	1.5±1.0
	2	24.8	15.2±4.3	22.1	7.9±1.3	2.5±1.2
D2	1	24.7	15.2±5.3	29.5	-	1.5±0.8
	2	19.2	13.5±6.4	27.1	14.0±5.6	1.7±0.9

5.2.1.1 Experiment A1 versus A2

Secondary electron micrographs of the surface of TP347H FG for experiments A1 and A2 are shown in Figure 5-1. Both samples were oxidised for a total of 100 hours (2 x 50 hours) at 923 K where the first 50 hours was in air-saturated steam. In the case of experiment A1 the second 50 hour exposure was also in air-saturated steam whereas the second thermal exposure for A2 was in deoxygenated steam. On cooling after the first 50 hour cycle, both samples, shown in Figure 5-1(a) and (b), exhibited significant spallation with approximately 95% of the pickled concave surface spalling, mentioned earlier in Chapter 4. Adherent oxide was only observed around the edges of the samples. Further exposure resulted in further spallation of approximately 2.6% in A1 but no further spallation was observed in A2, as shown in Figures 5-1(c) and (d), respectively. SEM analysis of the surface of the samples further exposed to air-saturated steam, A1, showed areas of spallation and two distinguishable oxide morphologies. In regions of adherent oxide cracks were seen in the outer oxide layer. Where a deoxygenated environment was used, the surface of the sample had a uniform morphology and did not alter significantly between cycles.

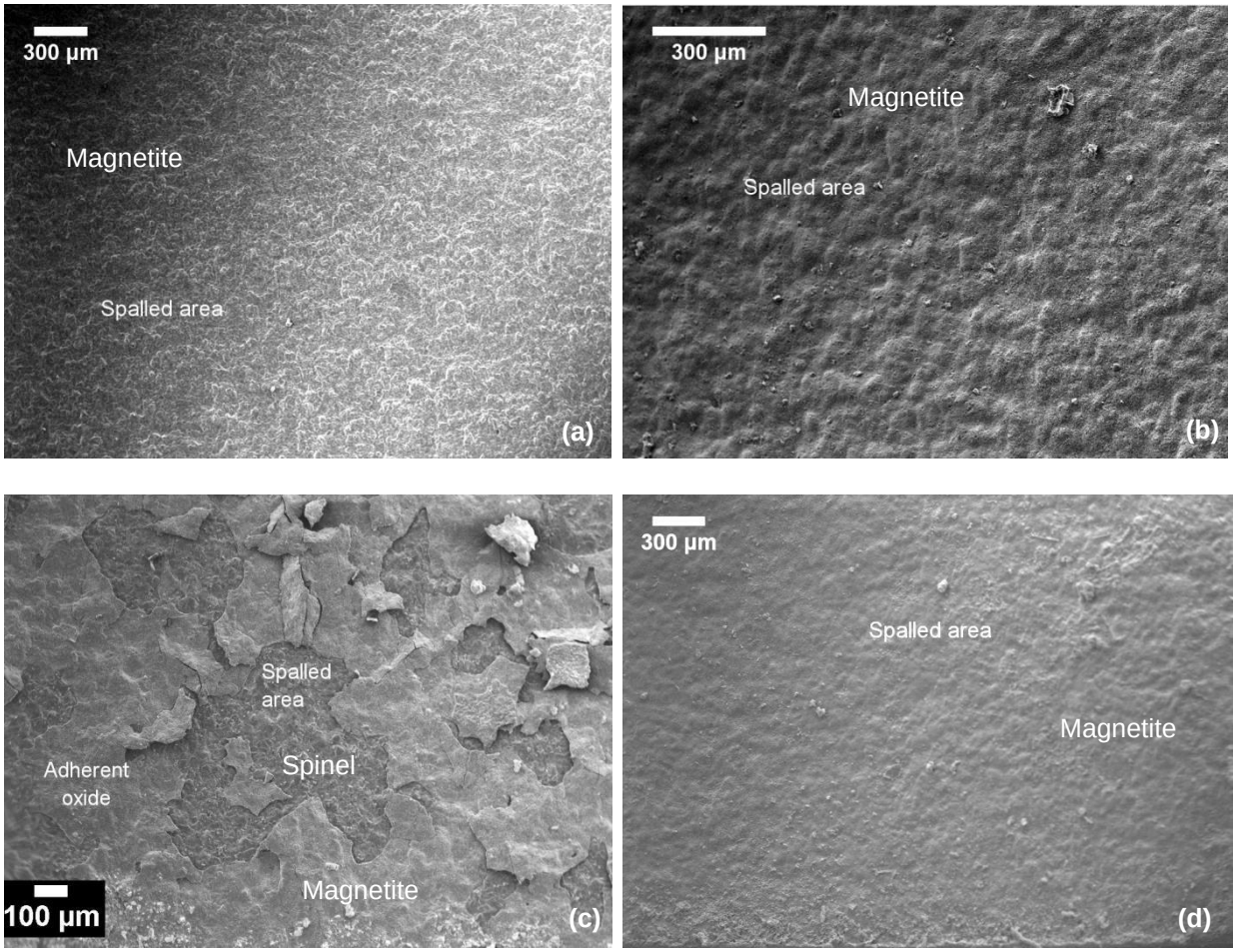

Figure 5-1 Secondary electron (SE) micrographs of the inner pickled surface of TP347H FG where (a) is cycle 1 of A1, (b) is cycle 1 of A2, (c) is cycle 2 of A1 and (d) is cycle 2 of A2. All exposures were for 50 hours at 923 K.

Spalled particles were collected after cycle 2 of experiment A1, Figure 5-2(a). The SEM images obtained of the spalled particles subsequent to the second exposure indicate two oxide morphologies suggesting spallation of both haematite and magnetite. Whiskers observed on spalled particles were used to help identify each oxide layer since whiskers were only observed on unspalled regions of the outer surface during SEM examination, i.e. from the haematite layer. Whisker morphology was also reported in the literature as occurring on haematite [79].

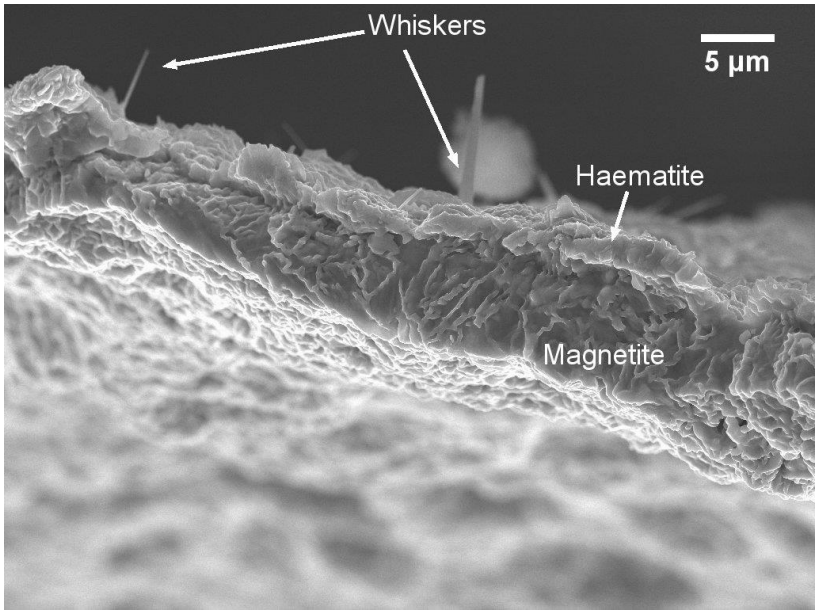

Figure 5-2 SE micrograph of spalled oxide from TP347H FG exposed to air-saturated steam for 2 x 50 hours at 923 K (experiment A1).

Optical microscopy allowed the difference in contrast between haematite and magnetite to be observed that was not otherwise seen with SEM examinations of polished cross sections. Haematite appears a marginally darker grey than magnetite, Figure 4-4. There was no evidence for haematite found in optical cross sectional analysis for cycle 2 of experiment A1 as indicated in Figure 5-3. Magnetite was observed at the outer surface and spinel was seen as an inwardly growing oxide adjacent to the alloy. A Cr-rich oxide found to be chromite with a thin layer of Cr_2O_3 at the interface but not resolvable in Figure 5-6 was also observed at the base of the spinel along the grain boundaries.

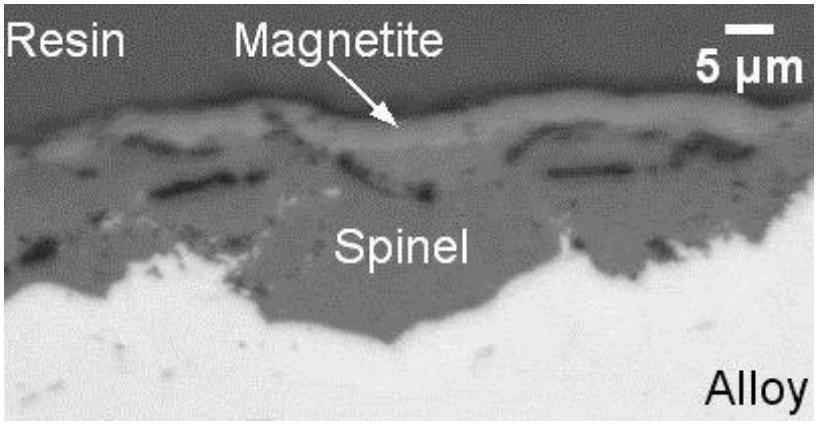

Figure 5-3 Optical cross sectional micrograph of TP347H FG exposed to air-saturated steam for 2 x 50 hours at 923 K, experiment A1.

The STORME technique was used to monitor the samples during cooling in laboratory air for these tests. Thermographic images were obtained for cycle 2 in both steam environments. A snapshot image is shown in Figure 5-4 where one spall site was identified and the thermal history was tracked. It was not possible to observe the delamination event for this site as it occurred during transition from the furnace to the heat proof surface, i.e. $\Delta T < 181.1$ K. The radius of the spalled site increased gradually over the 35 seconds it was measured, with a large increase within the last 5 seconds prior to complete spallation. Also included in the figure is the critical strain energy criterion (CSEC). The CSEC assumes that strain energy builds up during cooling from the time at which delamination occurred and is only released when the critical value of ΔT was reached which in this instance was 405.6 K. Observations from the thermal imaging camera however showed the strain energy to be released gradually with increasing radius of the buckled site suggesting unstable buckling as was observed during cycle one of Chapter 4.

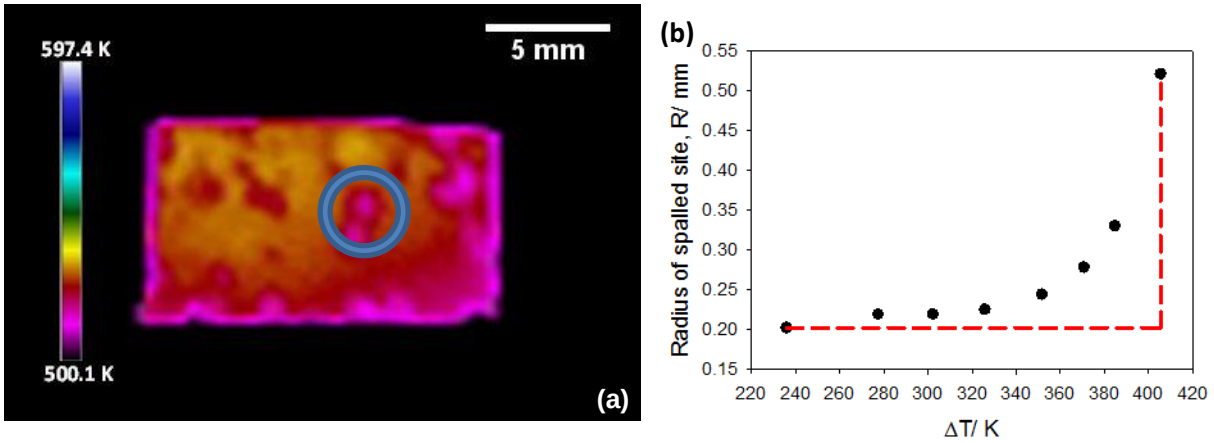

Figure 5-4 (a) Thermographic image of TP347H FG during cooling from the second cycle in air-saturated steam for 50 hours at 923 K and (b) the radius of the spalled site indicated in the thermographic image with cooling.

A thermographic snapshot image taken from a sample from experiment A2 is shown in Figure 5-5. The surface of the sample cooled more uniformly than the corresponding sample in experiment A1. There were some localised points for which the temperature was measured to be lower than the rest of the surface, as highlighted in the image, but no visible spallation occurred at these sites. The radius of the localised site indicated in Figure 5-5 was measured and was shown to remain constant during the cooling period.

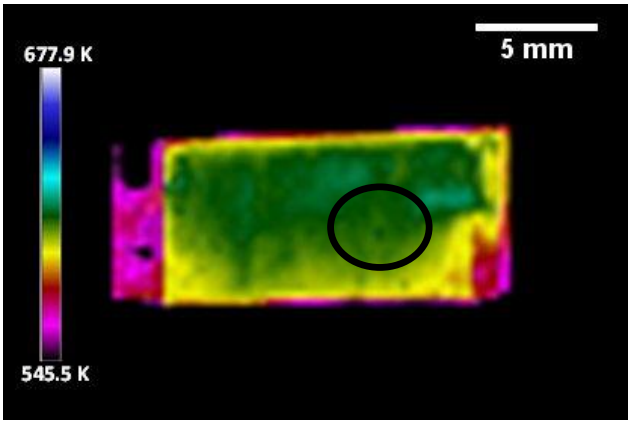

Figure 5-5 Thermographic snapshot of TP347H FG on cooling after the second thermal cycle in deoxygenated steam at 923 K for 50 hours.

Cross sectional micrographs of the second thermal exposure for experiments A1 and A2 are shown in Figure 5-6. For experiment A1 (Figure 5-6(a)) the cross sectional image indicated that spallation occurred at the magnetite/ spinel interface and the crack continued beneath the magnetite layer that did not completely spall. Cross sectional analysis of a sample from experiment A2 (Figure 5-6(b)) indicated cracking occurred in the outer Fe oxide. These cracks were observed sporadically during cross sectional examination. It is postulated that these cracks were the reason for the localised temperature drops seen in the thermographic image for experiment A2, Figure 5-5. A Cr rich oxide was also observed at the base of the spinel along the grain boundaries.

EDS analysis was carried out on each sample and showed that from cycle one to cycle two there was negligible change in the concentration of oxidising elements within the Fe-Cr-Ni spinel scale for experiment A1. For deoxygenated conditions on the other hand, there was a decrease in the Fe concentration within the spinel layer, Table 5-3.

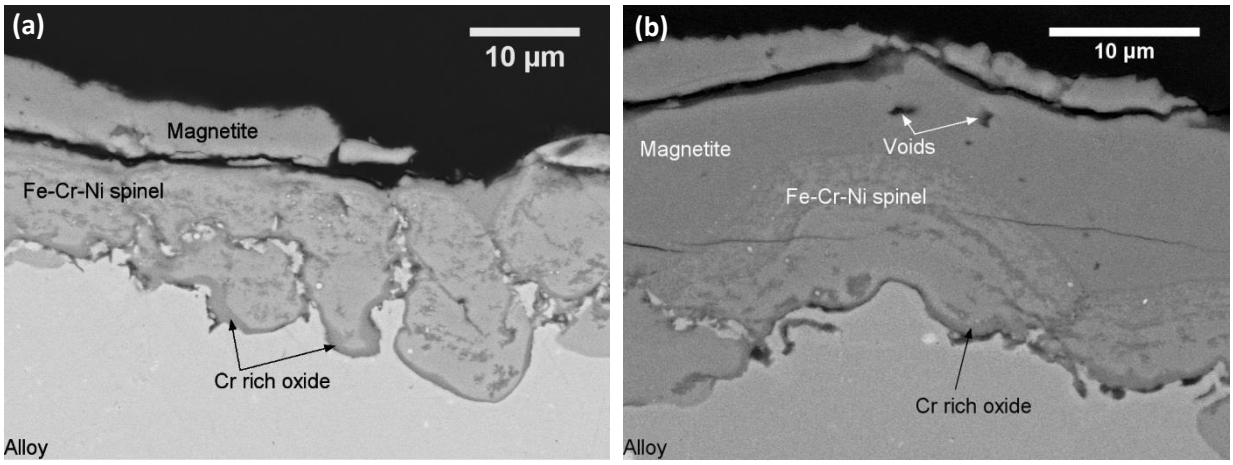

Figure 5-6 BSE images of TP347H FG where cycle 1 was carried out in an air-saturated environment at 923 K for 50 hours and cycle 2 was carried out for 50 hours at 923 K in (a) air-saturated steam and (b) deoxygenated steam.

Oxide thickness measurements were taken for both the Fe-Cr-Ni spinel and where possible, the outer Fe rich oxide, Table 5-3. As spallation of the outer Fe oxide occurred on cooling from the second cycle in experiment A1, the oxide thickness was difficult to interpret since it was unclear whether spallation always occurred at the spinel/ magnetite interface or within the magnetite layer where voids were observed. For this reason, Fe rich oxide thickness measurements were not taken for this experiment. Since spallation did not occur on cooling during cycle two of experiment A2 measurements were able to be made for the Fe oxide. Comparisons between the two steam environments indicated the Cr rich oxide, identified as predominantly chromite in Chapter 4 at the base of the spinel is not continuous under either circumstances but continued to grow during the second thermal cycle. Because the oxide layer was not continuous, oxide thickness measurements were not recorded.

For both experimental conditions considered the average Fe-Cr-Ni spinel oxide thickness increased from cycle one to cycle two. Figure 5-7 compares the Fe-Cr-Ni spinel oxide thickness measurements for air-saturated and deoxygenated steam after cycle two conditions and indicated that the spinel oxide grew to a greater extent under air-saturated conditions and increased by 60% compared to 45% for deoxygenated conditions. The increasing slope observed for both conditions is indicative of the wavy interface detected during cross sectional examination. This is similar to that seen by Osgerby *et al*. [36] for 9Cr-1Mo steel exposed to flowing steam at 823 K.

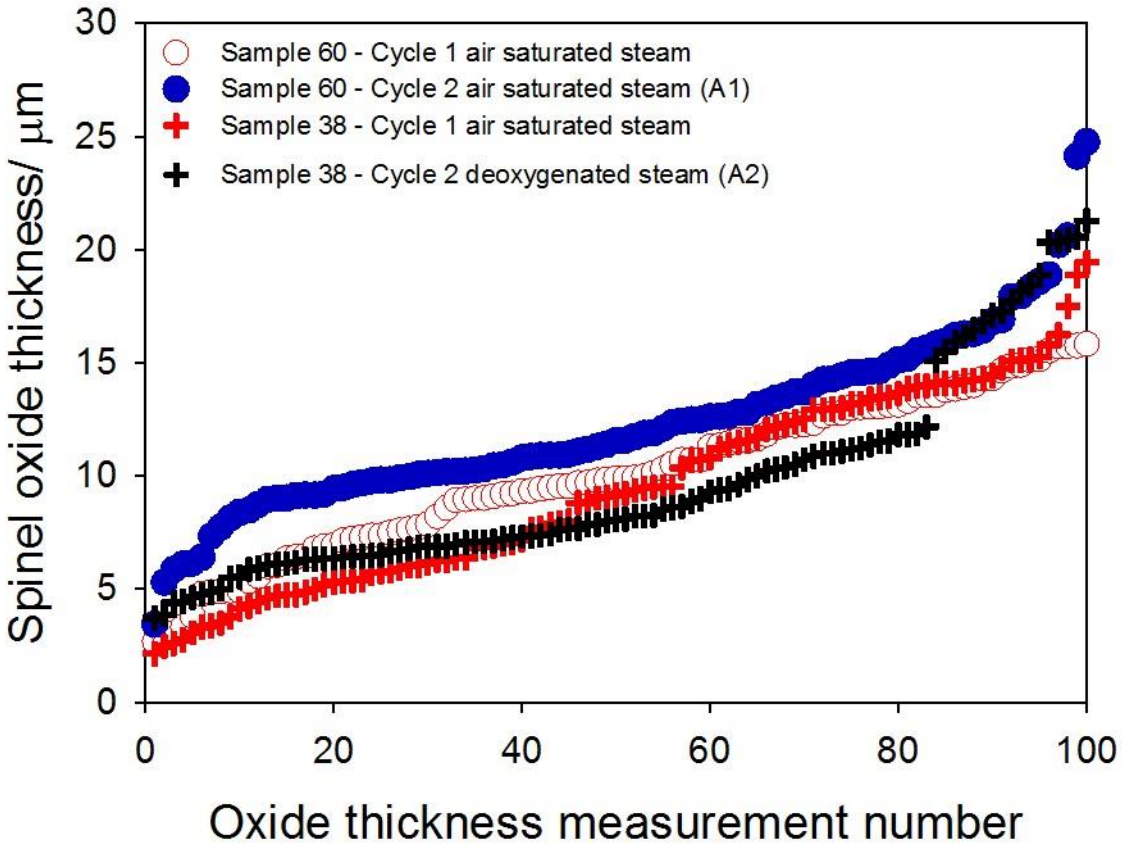

Figure 5-7 Oxide thickness measurements of Fe-Cr-Ni spinel as a function of the number of measurements taken for the oxide grown on TP347H FG in steam environments at 923 K for 50 hour cycles.

5.2.1.2 Experiment B1 versus B2

The surfaces of samples exposed for a total of 200 hours (2 x 100 hours) are shown in Figure 5-8. On cooling from the first 100 hour exposure a significant amount of spallation of the outer haematite layer from the inner concave surface occurred for both samples. Subsequent to the second exposure, spallation occurred in experiment B1 (Figure 5-8 (c)) but not in experiment B2 where deoxygenated steam was used. In the case of experiment B1 where both cycles were carried out under an air-saturated steam environment, the same location on the surface was identified between thermal cycles where a region of oxide remained adherent on cooling from the first cycle but

further exposure resulted in additional cracking both at the interface and within the oxide itself. The surface of the sample identified three oxide morphologies, i.e. haematite (1), magnetite (2) and Fe-Cr-Ni spinel (3) after the second thermal cycle suggesting magnetite spalled after cycle two. For experiment B2 where spallation did not occur during the second cycle on cooling, cracking of the outer oxide can be seen on the surface, Figure 5-8(d). The spalled region highlighted in that image is present from the first cycle and not as a result of spallation during the second exposure.

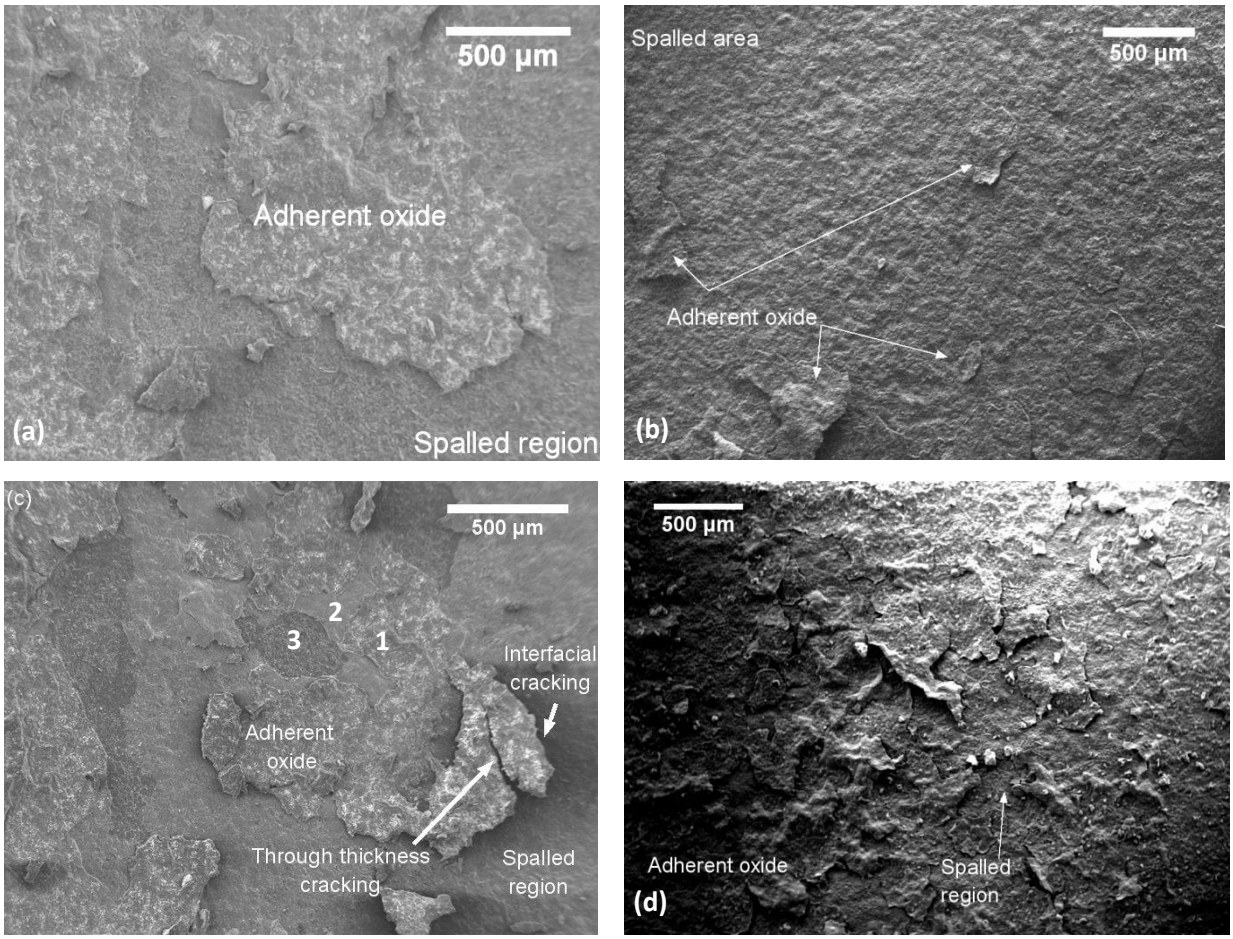

Figure 5-8 Secondary electron micrographs of the inner pickled surface of TP347H FG where (a) is cycle 1 of experiment B1, (b) is cycle 1 of experiment B2, (c) is cycle 2 of experiment B1 and (d) is cycle 2 of experiment B2. All cycles were carried out for 100 hours at 923 K.

The surface of a spall particle collected from the second thermal exposure of experiment B1 is shown in Figure 5-9(a). This secondary electron micrograph indicated two different oxide morphologies were present suggesting a mixture of both

haematite and magnetite. The morphology of the two oxides was comparable to that shown on the surface of the bulk sample in Figure 5-8(c). Examination of another spall particle from the same sample in cross section also indicated the presence of two oxides where an interface could clearly be seen between the two, Figure 5-9(b). The image shown here also provided evidence for buckling formation of haematite where decohesion at the oxide/ oxide interface had occurred. Further investigation of that spall particle indicated the presence of needles on one of the surfaces. Needles were identified on unspalled regions, as previously mentioned. The buckled side of the oxide particle shown in the figure was therefore identified as haematite whilst the remainder of the spalled particle was magnetite.

Further evidence for buckle formation of the haematite was found during examination of B1. The surface showed an area where the outer oxide had buckled on cooling, Figure 5-10. Cracking beneath the magnetite layer was also visible.

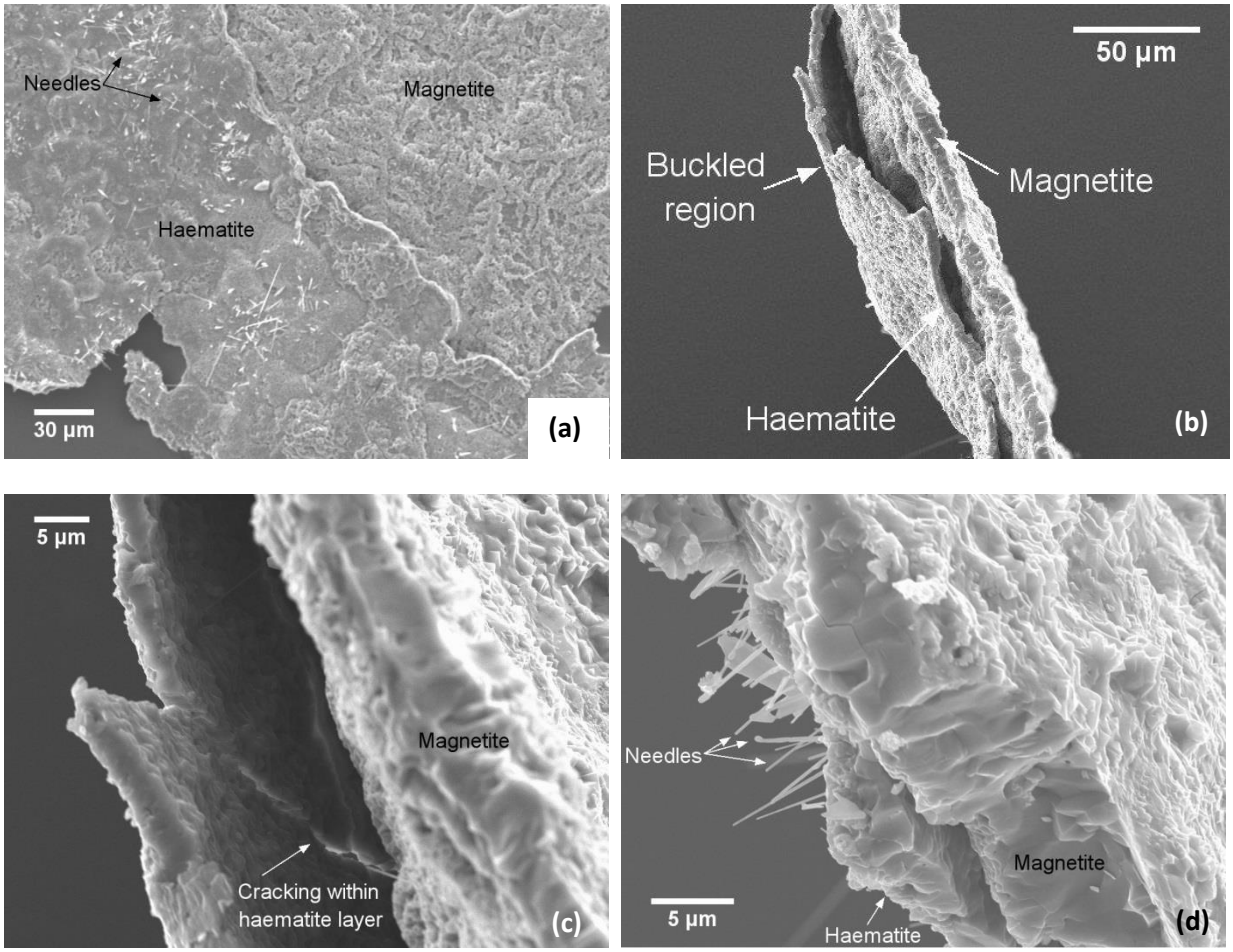

Figure 5-9 Secondary electron images of (a) the surface of oxide particle spalled from TP347H FG on cooling after the second exposure of experiment B1 and (b), (c) and (d) the cross section of another oxide particle from the same conditions.

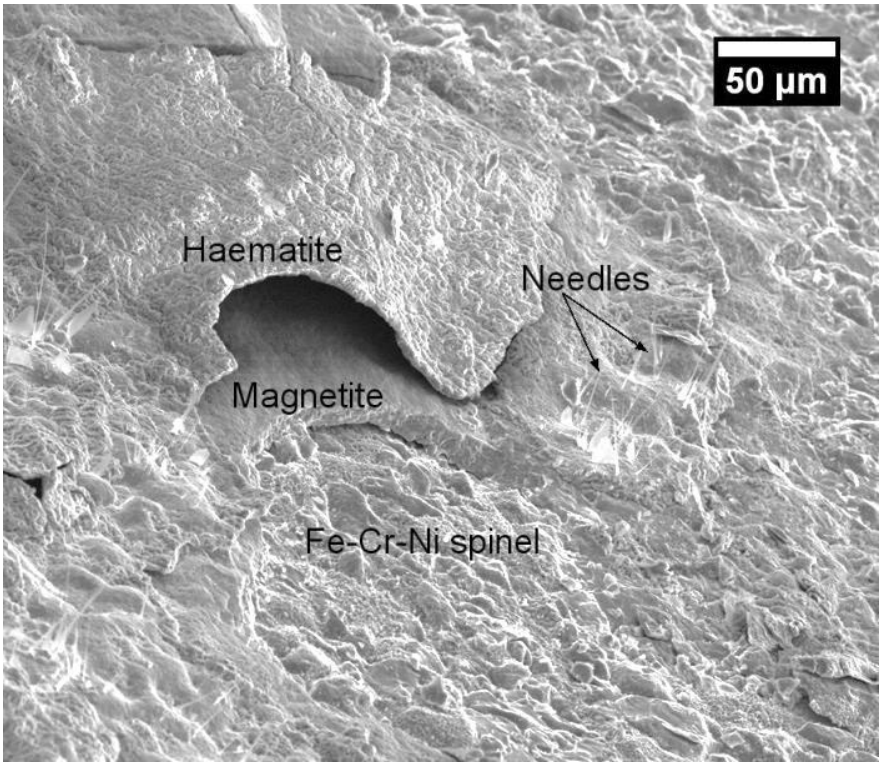

Figure 5-10 Secondary electron micrograph of the surface of TP347H FG exposed to air-saturated steam for 2 x 100 hours at 923 K.

The IR camera was unavailable for use during the second thermal cycle of experiment B1 in air-saturated steam and so the cooling behaviour of the sample is unknown. Since spallation occurred it is assumed that localised temperature drops would have been visible during the cooling period as was seen with other samples. Spallation was not observed during cooling after cycle 2 of experiment B2. However, thermographic images did indicate localised regions of temperature fluctuations suggesting some delamination, Figure 5-11. The radius of these localised regions was shown to remain stable in size during cooling, assumed to be stable buckling.

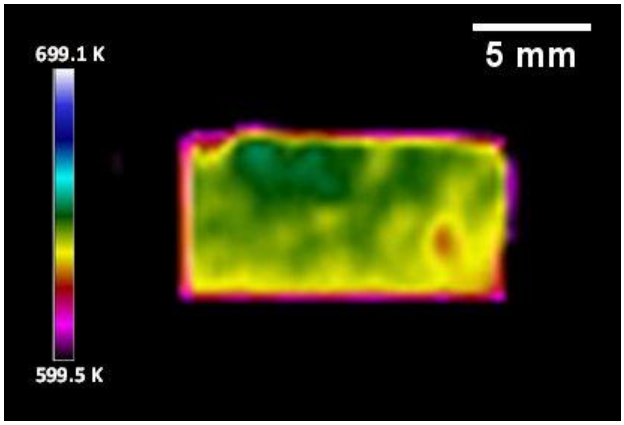

Figure 5-11 Thermographic image of TP347H FG during the second thermal exposure of 100 hours in deoxygenated steam at 923 K.

Cross sectional analysis of samples following the second thermal cycle of 100 hours indicated spallation occurred at the magnetite/ spinel interface when exposed to an air-saturated steam environment, experiment B1, as shown in Figure 5-12(a). In the case where deoxygenated steam was used for the second thermal exposure of 100 hours, experiment B2, cross sectional analysis showed cracking at the magnetite/ spinel interface which is suggested to be the cause of the localised temperature changes observed in the thermographic images, Figure 5-11.

There was no spallation subsequent to the second thermal cycle of 100 hours in deoxygenated steam, Table 5-2 but, as can be seen in the cross sectional image in Figure 5-12, the voids have coalesced and so a further exposure may result in spallation at the weakened interface.

Oxide chemistry investigations of these two experiments showed an increase in the Fe concentration within the Fe-Cr-Ni spinel oxide when the second thermal cycle was carried out in air-saturated steam, Table 5-3. For deoxygenated conditions a decrease in the Fe concentration was observed.

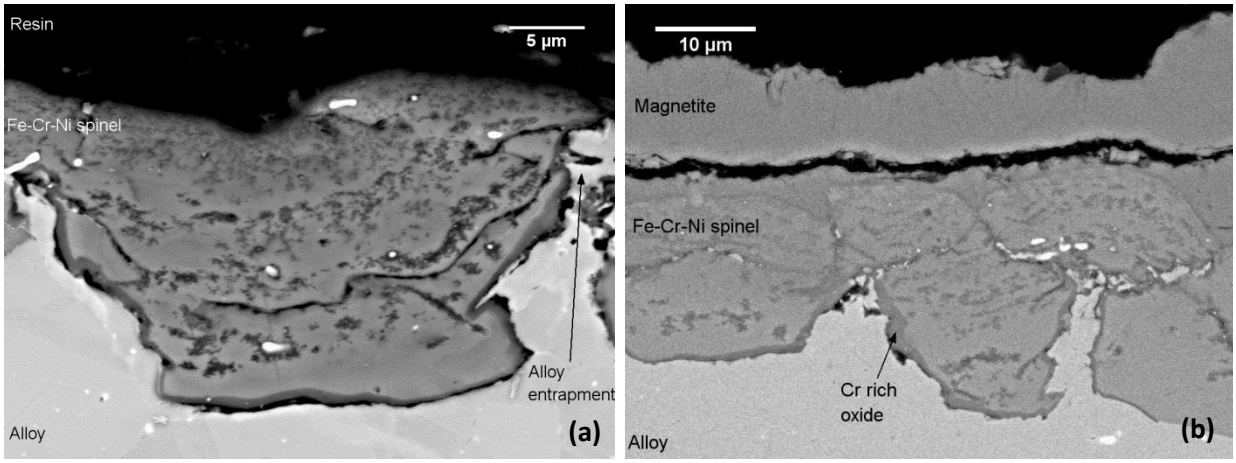

Figure 5-12 BSE cross section images of TP347H FG for cycle 2 of (a) experiment B1 and (b) experiment B2. All thermal cycles were carried out for 100 hours at 923 K.

Oxide thickness measurements of the Fe-Cr-Ni spinel were recorded for both conditions and increased in each case, Table 5-3. For cyclic oxidation totalling 200 hours there was no growth of the outer magnetite layer during the second thermal exposure under deoxygenated conditions. Because spallation occurred during the second thermal cycle of experiment B1 it is unknown whether the outer Fe oxide grew during the second cycle. It is postulated that the lack of magnetite growth seen during the second thermal cycle under deoxygenated conditions was as a result of voids that were formed during the first 100 hour exposure preventing diffusion of Fe ions outwards to continue the growth since it was previously suggested that pores mitigate solid state diffusion [163]. If this were the case then it would also be expected that the same observations would be seen under air-saturated conditions had spallation not occurred.

A plot of the Fe-Cr-Ni spinel oxide thickness measurements is shown in Figure 5-13. The average spinel thickness increased by 35% for air-saturated conditions but only 25% for deoxygenated conditions. Again an increase in spinel thickness was observed under both conditions, Table 5-3.

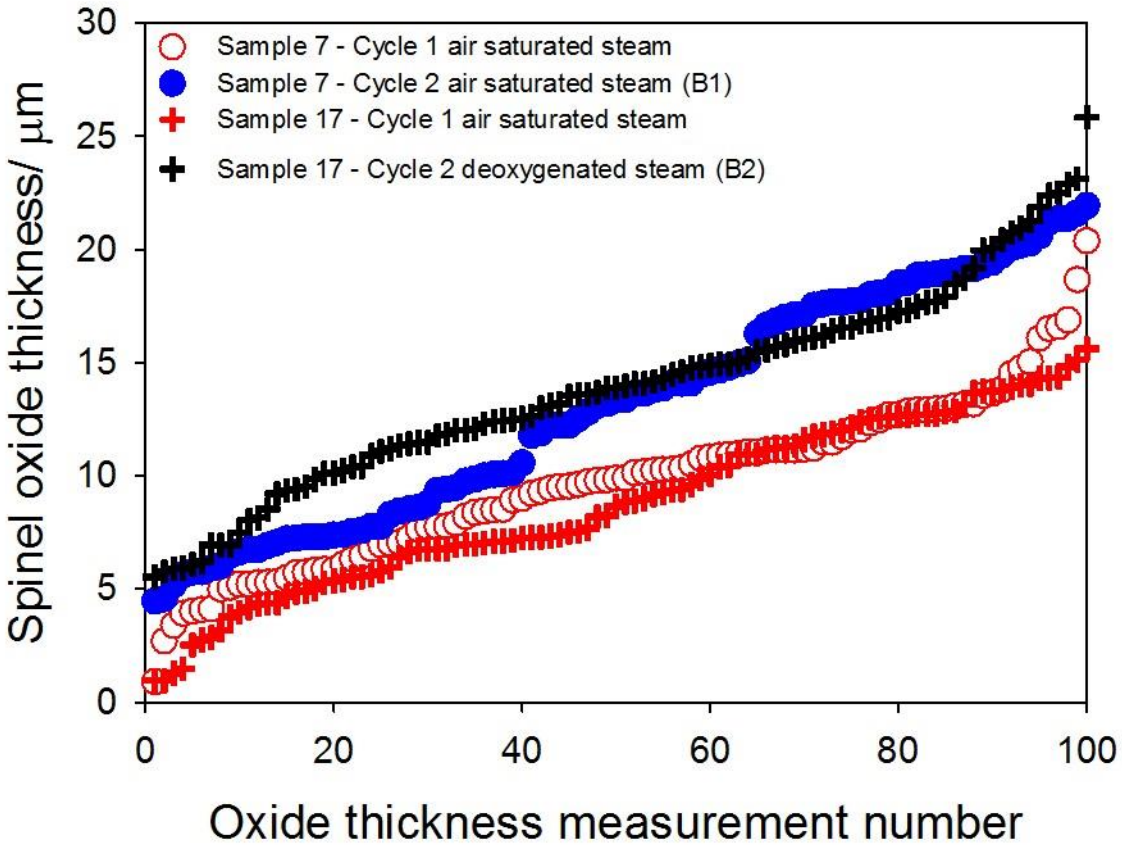

Figure 5-13 Oxide thickness measurements of Fe-Cr-Ni spinel as a function of the number of measurements taken for the oxide grown on TP347H FG in steam environments at 923 K for 100 hour cycles.

A change in slope was observed for cycle 2 of experiment B1 at approximately 12 µm suggesting the spinel oxide thickness was not normally distributed. A histogram was plotted to determine the distribution and is shown in Figure 5-14 confirming a bimodal distribution. The bimodal behaviour of the spinel oxide thickness will be discussed in further detail in Section 5.3.

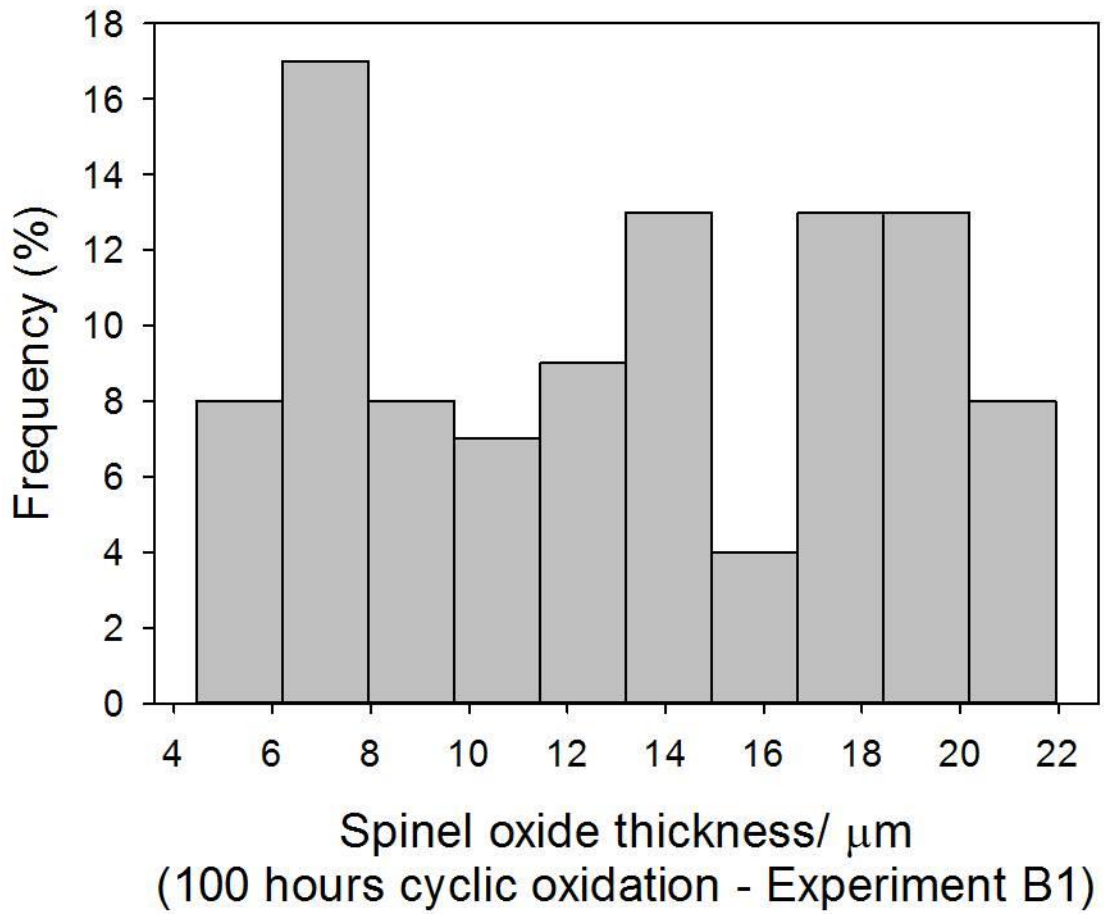

Figure 5-14 Histogram plot for Fe-Cr-Ni spinel oxide grown during cycle 2 of experiment B1 at 923 K.

5.2.1.3 Experiment C1 versus C2

SEM micrographs of the surface of samples from experiments C1 and C2 are shown in Figure 5-15. Further oxidation for 500 hours in air-saturated steam resulted in a small amount of additional spallation but where deoxygenated steam was used no visible spallation occurred, Table 5-2. Under both air-saturated and deoxygenated steam conditions the surface of the sample after the second thermal exposure is uniform with no apparent cracking within the surface oxide layer and no significant changes between thermal cycles, Figure 5-15. The surface of the samples

subsequent to the second thermal cycle indicated the presence of a single oxide morphology.

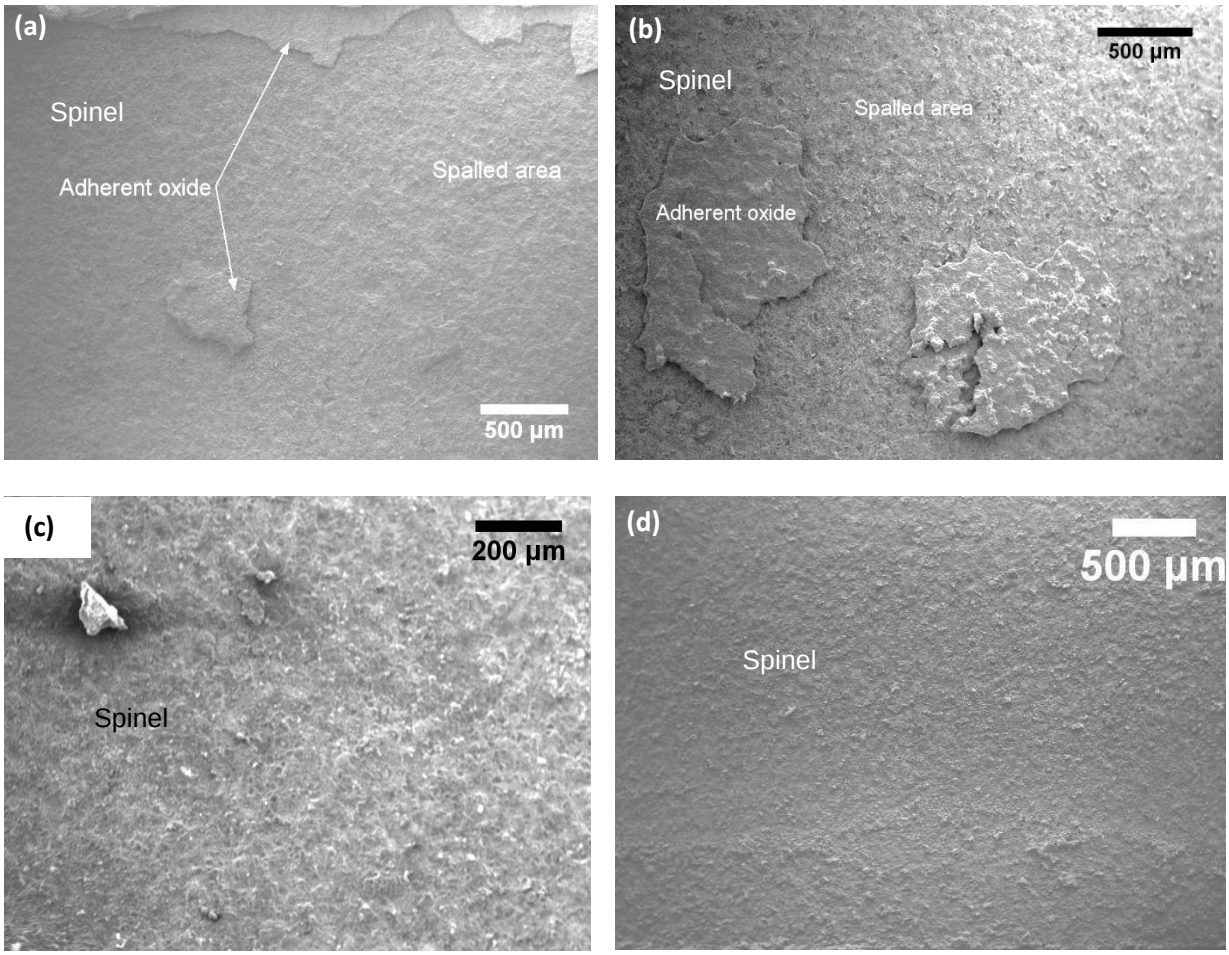

Figure 5-15 Secondary electron micrographs of the inner pickled surface of TP347H FG where (a) is cycle 1 of experiment C1, (b) is cycle 1 of experiment C2, (c) is cycle 1 of experiment C1 and (d) is cycle 2 of experiment C2. All cycles were carried out for 500 hours at 923 K.

Again, significant spallation of the inner pickled concave surface occurred on cooling from the first 500 hour thermal cycle and the spalled oxide consisted of both haematite and magnetite, Figure 5-16. It is thought therefore that a region of haematite remained adherent after the first thermal exposure, such as that shown in Figure 5-15(a), which then subsequently spalled on cooling from the second thermal exposure.

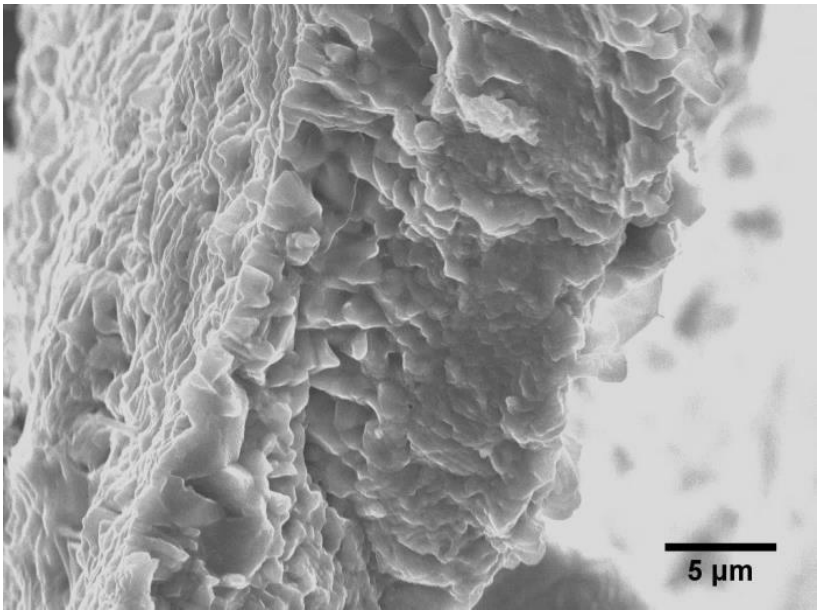

Figure 5-16 SE cross section micrograph of spalled oxide particle from experiment C1.

A thermographic image at the time at which spallation of the single spall particle occurred on cooling from experiment C1 is shown in Figure 5-17. The location of the spalled site is highlighted and a snapshot taken from the optical video camera 1 second prior to spallation is also shown.

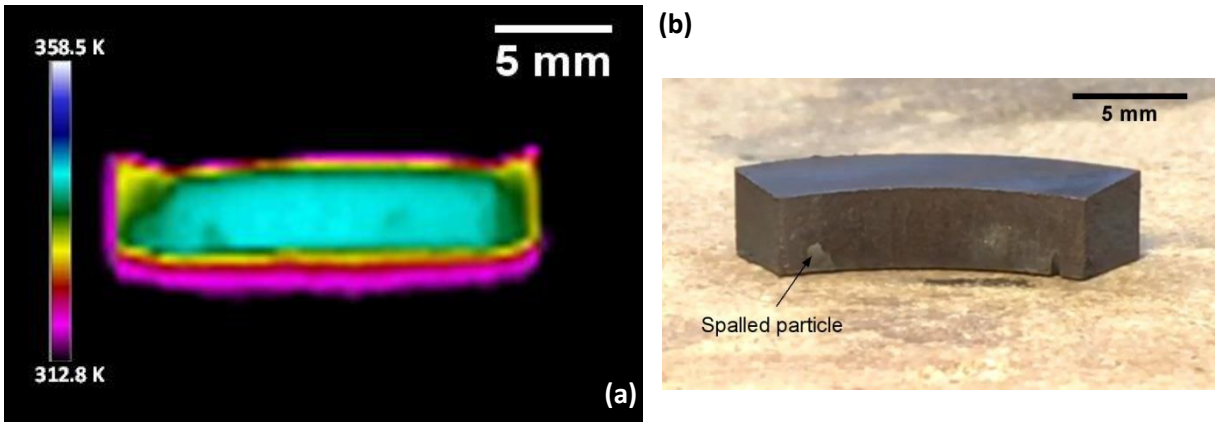

Figure 5-17 (a) Thermographic image at the time of spallation and (b) optical snapshot from the video camera 1 second prior to complete localised spallation for TP347H FG on cooling after the second thermal exposure at 923 K of experiment C1.

The radius of the spalled site was measured at 5 second intervals from the time at which delamination occurred to the time at which spallation occurred and was shown to increase with cooling time although there were periods of time where the localised

site remained constant in size, Figure 5-18. Also included in this plot is CSEC (red lines) which assumes strain energy would build up until a critical ΔT of 590.0 K was achieved to release the strain energy. What was actually observed for this experiment was a gradual release of strain energy with increasing ΔT, indicative of unstable buckling.

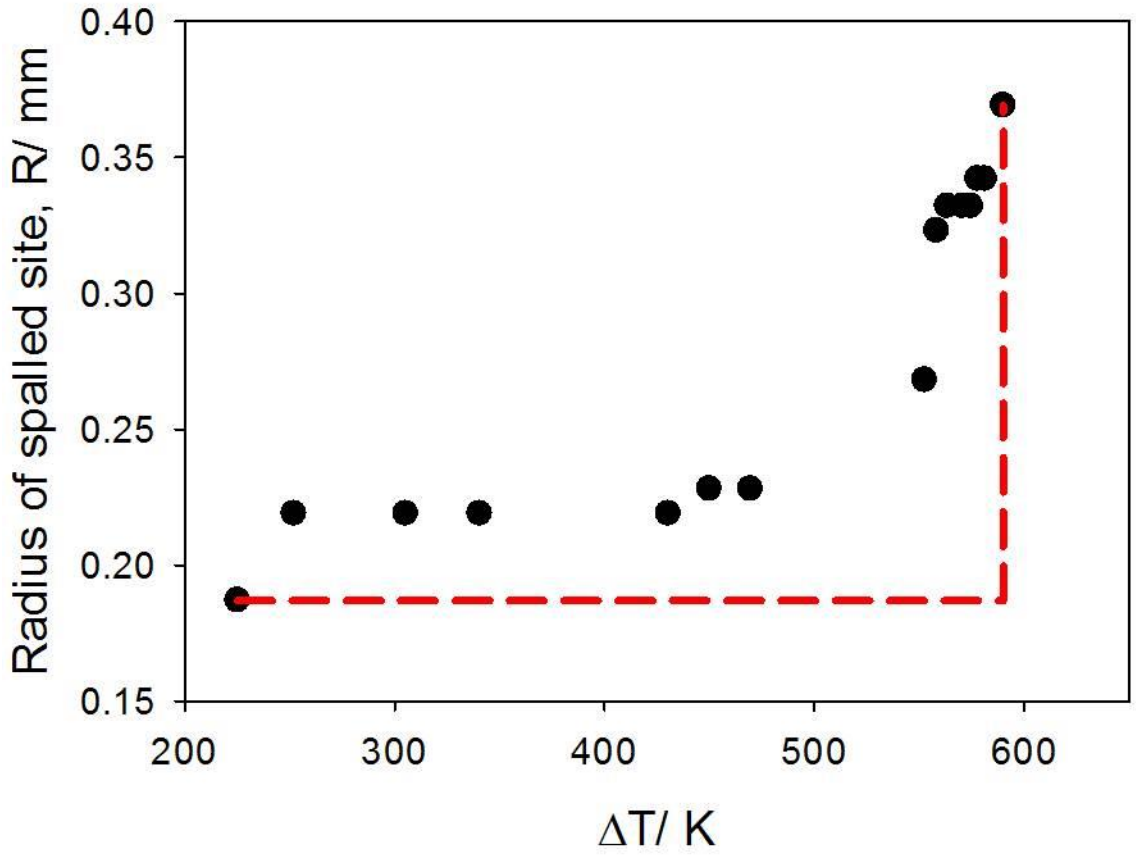

Figure 5-18 Radius of localised spalled site for TP347H FG for cycle 2 of experiment C1.

For experiment C2 the inner surface was shown to cool uniformly with a slight temperature gradient around the edges and where the sample was in contact with the heat proof surface, Figure 5-19. No spallation was observed during cooling and the uniformity of the surface suggested no delamination or cracking.

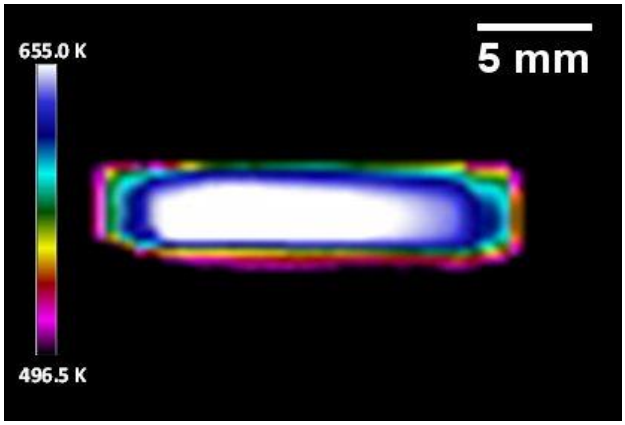

Figure 5-19 Thermographic image of TP347H FG during cooling after cycle 2 of experiment C2.

Cross sectional analysis of cycle 2 of experiment C1 and C2 indicated the samples behaved in a similar way independent of steam environment although the spinel oxide does appear to be more undulated for deoxygenated steam, Figure 5-20(b). The chromite oxide at the base of the Fe-Cr-Ni spinel oxide was seen to be continuous after the first 500 hour thermal exposure, Figure 4-3(d). Only a small amount of spallation was observed on cooling during the second cycle of experiment C1, Table 5-2, where both thermal cycles were carried out in air-saturated steam although cracking at the magnetite/ spinel interface was observed during cross sectional analysis, Figure 5-20. Since spallation within the magnetite layer had occurred during cycle 1 as a result of void coalescence, it is believed that the fracture energy required to produce a new surface at the magnetite/ spinel interface subsequent to the second thermal exposure is too high. Therefore no further spallation was seen at that interface. Evidence for void coalescence was seen during cross sectional examination where remnants of void walls were observed, Figure 5-20.

EDS studies of these two experiments indicated a decrease in the average Fe concentration within the Fe-Cr-Ni spinel in both air-saturated and deoxygenated conditions, Table 5-3.

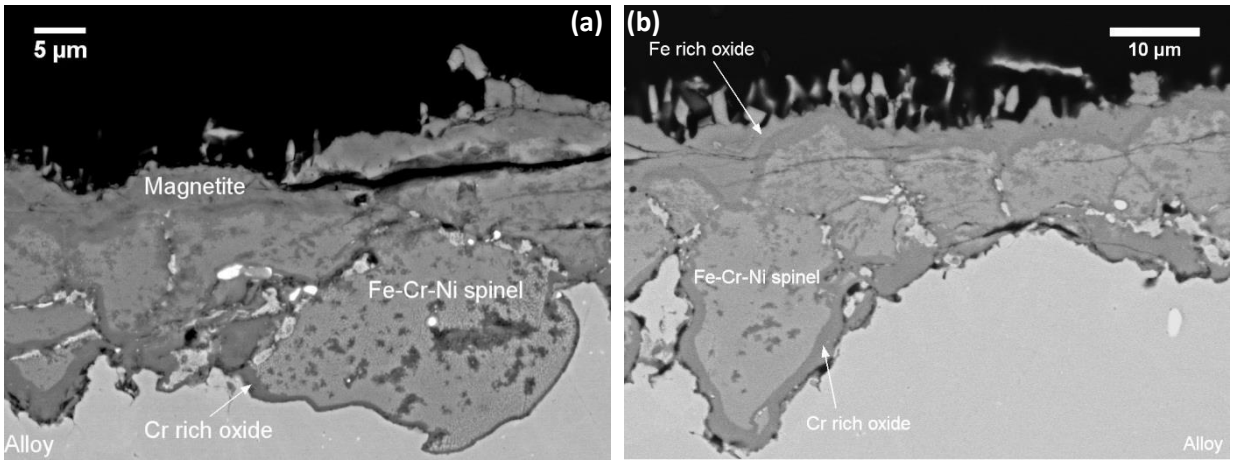

Figure 5-20 BSE images of TP347H FG where cycle 1 was carried out at 923 K for 500 hours in air-saturated steam and cycle 2 was carried out at 923 K for 500 hours in air-saturated steam (a) and deoxygenated steam (b).

Oxide thickness measurements of the Fe-Cr-Ni spinel were measured, Table 5-3, and plots of these measurements comparing cycles 1 and 2 and the different steam environments is shown in Figure 5-21. In each case the average spinel oxide thickness increased by around 5%. Cross sectional SEM analysis indicated an undulated thickness when the samples were exposed for a further 500 hours in deoxygenated steam which would suggest a bimodal distribution. The oxide thickness measurement plot also showed a change in slope indicative of a bimodal distribution. Histograms were plotted to confirm the distribution and it was shown that for cycle 2 of experiment C2 the distribution was bimodal, Figure 5-22. The development of a bimodal oxide thickness distribution, with increasing time at temperature, will be discussed in Section 5.3.

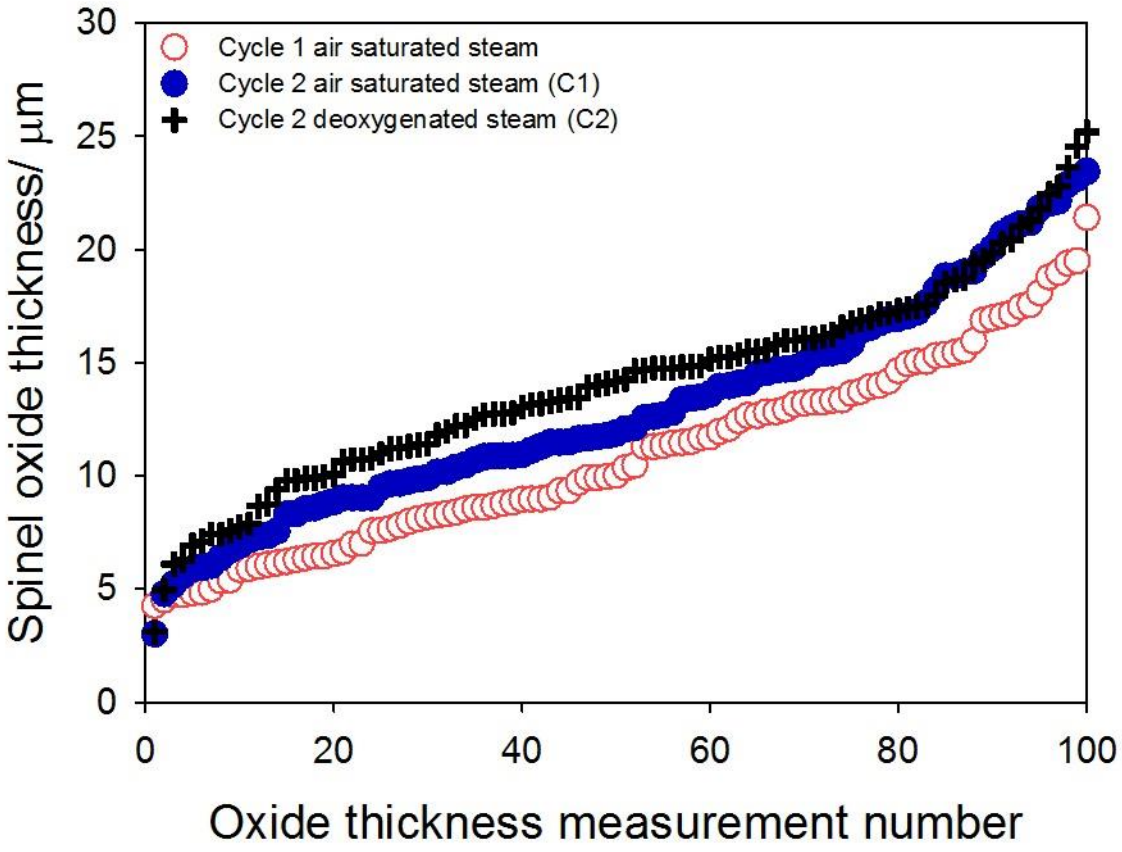

Figure 5-21 Oxide thickness measurements of Fe-Cr-Ni spinel as a function of the number of measurements taken for the oxide grown on TP347H FG in steam environments at 923 K for 500 hour cycles.

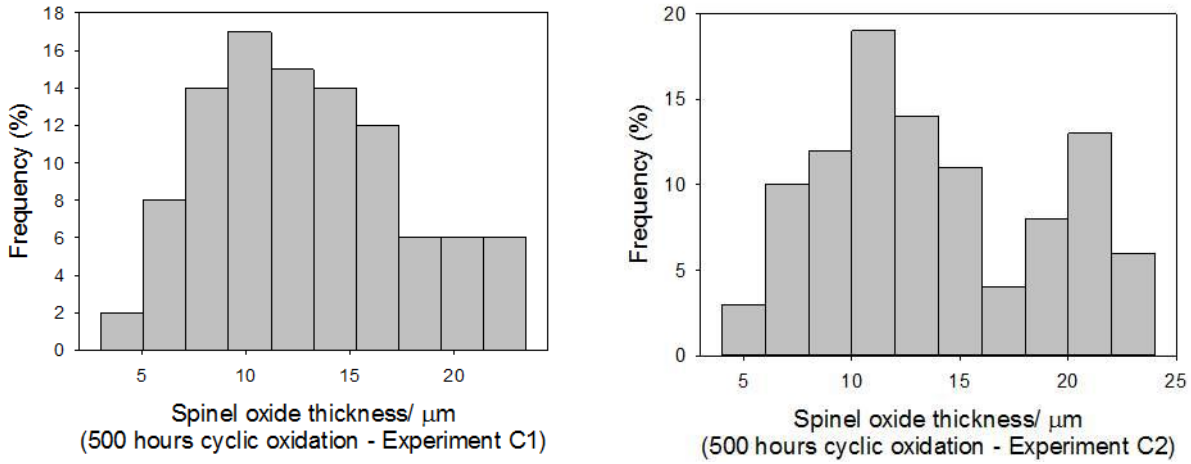

Figure 5-22 Histogram plots for Fe-Cr-Ni spinel oxide grown during cycle 2 of experiments C1 and C2 at 923 K showing the development of a bimodal distribution.

5.2.1.4 Experiment D1 versus D2

The final comparison for air-saturated and deoxygenated environments were exposures of 2000 hours (2 x 1000). Secondary electron images of the surfaces after each 1000 hour exposure are shown in Figure 5-23. Approximately 50% of the concaved pickled surface spalled on cooling subsequent to the initial thermal exposure of 1000 hours, Table 5-2. On cooling from the second exposure however, no spallation occurred in either atmosphere unlike the short term exposures where spallation was observed for samples exposed for a second time in air-saturated steam. Figure 5-23(c) and (d) indicated adherent oxide from the first exposure was still attached after the second exposure.

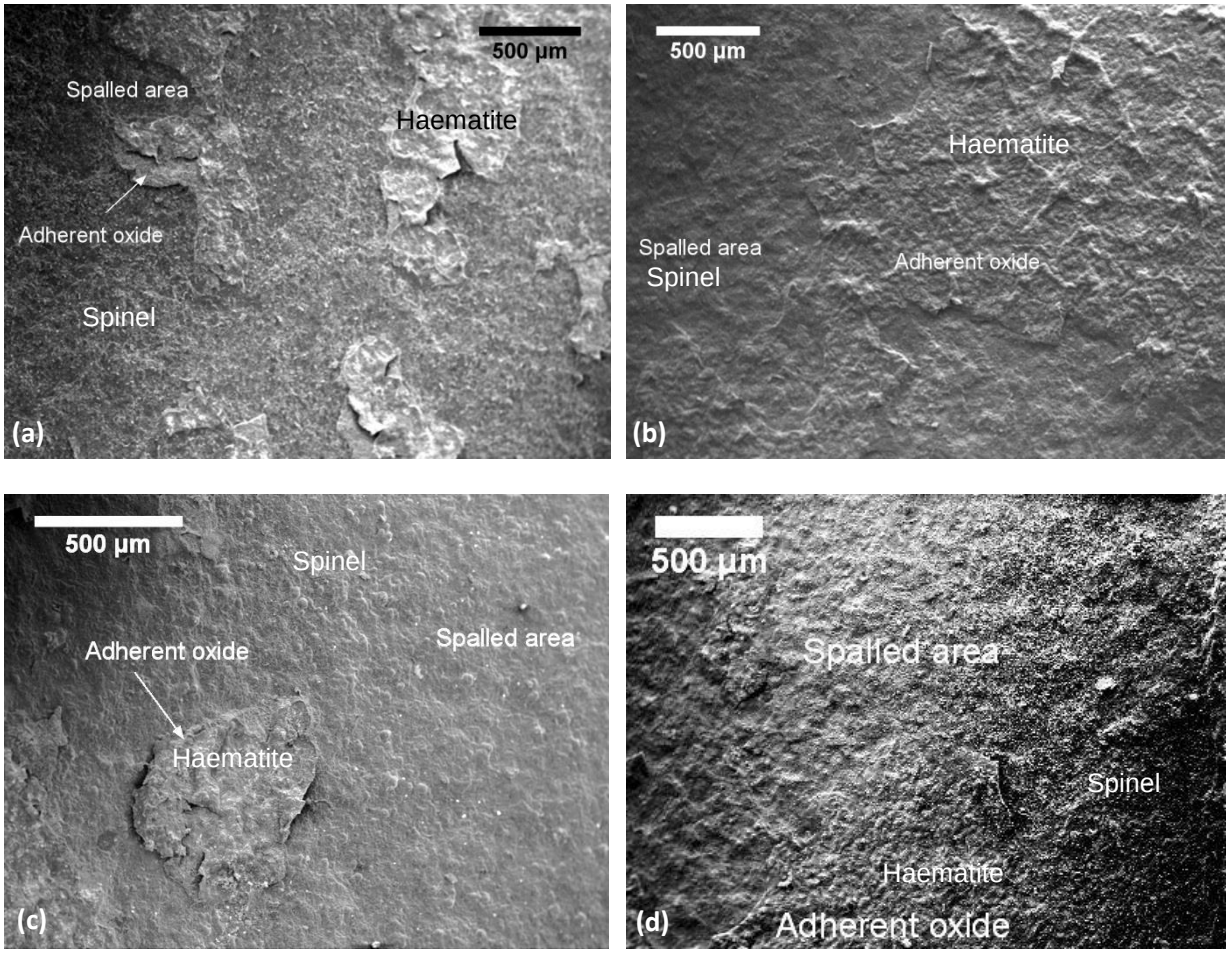

Figure 5-23 Secondary electron micrographs of the inner pickled surface of TP347H FG where (a) is cycle 1 of experiment D1, (b) is cycle 1 of experiment D2, (c) is cycle 2 of experiment D1 and (d) is cycle 2 of experiment D2. All cycles were carried out for 1000 hours at 923 K.

Figure 5-24(a) and (b) show the back scattered electron cross sectional images of TP347H FG after 2000 hours thermal cycling in air-saturated and deoxygenated steam environments, respectively. Initial observations from these micrographs found the Fe rich oxide had regrown during the second thermal cycle in both environments. Very few voids were observed where the Fe rich oxide had completely regrown during the second thermal cycle compared to that seen during cycle 1, Figure 4-3.

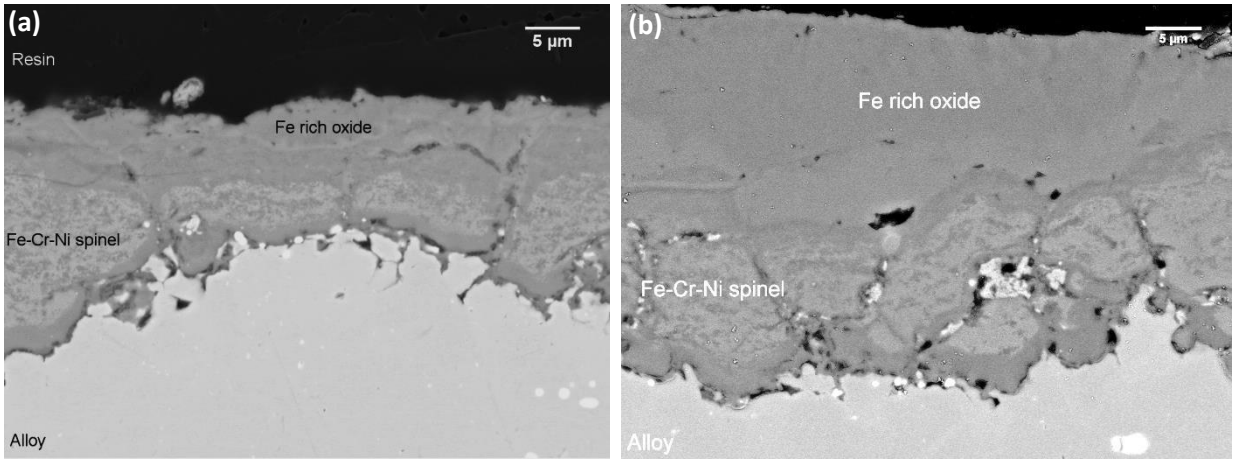

Figure 5-24 BSE images of TP347H FG where cycle 1 was carried out at 923 K for 1000 hours in air-saturated steam and cycle 2 was carried out at 923 K for 1000 hours in (a) air-saturated steam and (b) deoxygenated steam.

Oxide thickness measurements taken from these micrographs showed that the Fe rich oxide was thicker when the second thermal cycle was carried out in deoxygenated steam and the Cr rich oxide grew to a greater extent when thermally cycled in air-saturated steam compared to deoxygenated steam, Table 5-3. Further investigations into this showed the depth of Cr depletion was greater under air-saturated steam as shown in Figure 5-25 confirming that the Cr rich oxide was truly thicker when exposed to an oxygenated environment.

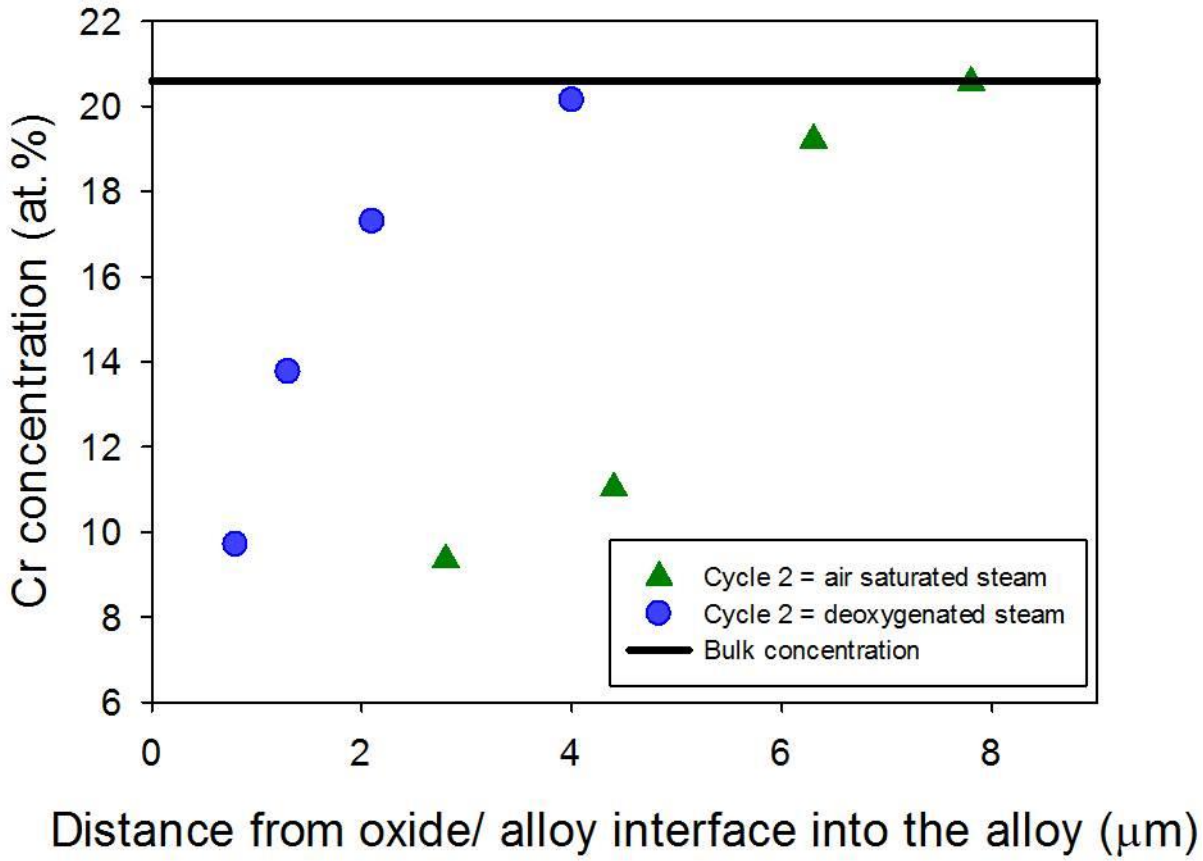

Figure 5-25 Cr concentration profiles measured by EDS for TP347H FG exposed to air-saturated steam for 1000 hours at 923 K followed by a further 1000 hours in air-saturated steam (green triangles) and deoxygenated steam (blue circles) at 923 K.

Similar observations to those seen for experiments C1 and C2 were observed here where EDS analysis showed a decrease in the average Fe concentration within the Fe-Cr-Ni spinel oxide under both oxidising environments, Table 5-3.

Plots for Fe-Cr-Ni spinel oxide thickness are shown in Figure 5-26. In both environments it is clear to see that the thickness of spinel decreased during the second thermal exposure of 1000 hours but decreased to a greater extent under deoxygenated steam.

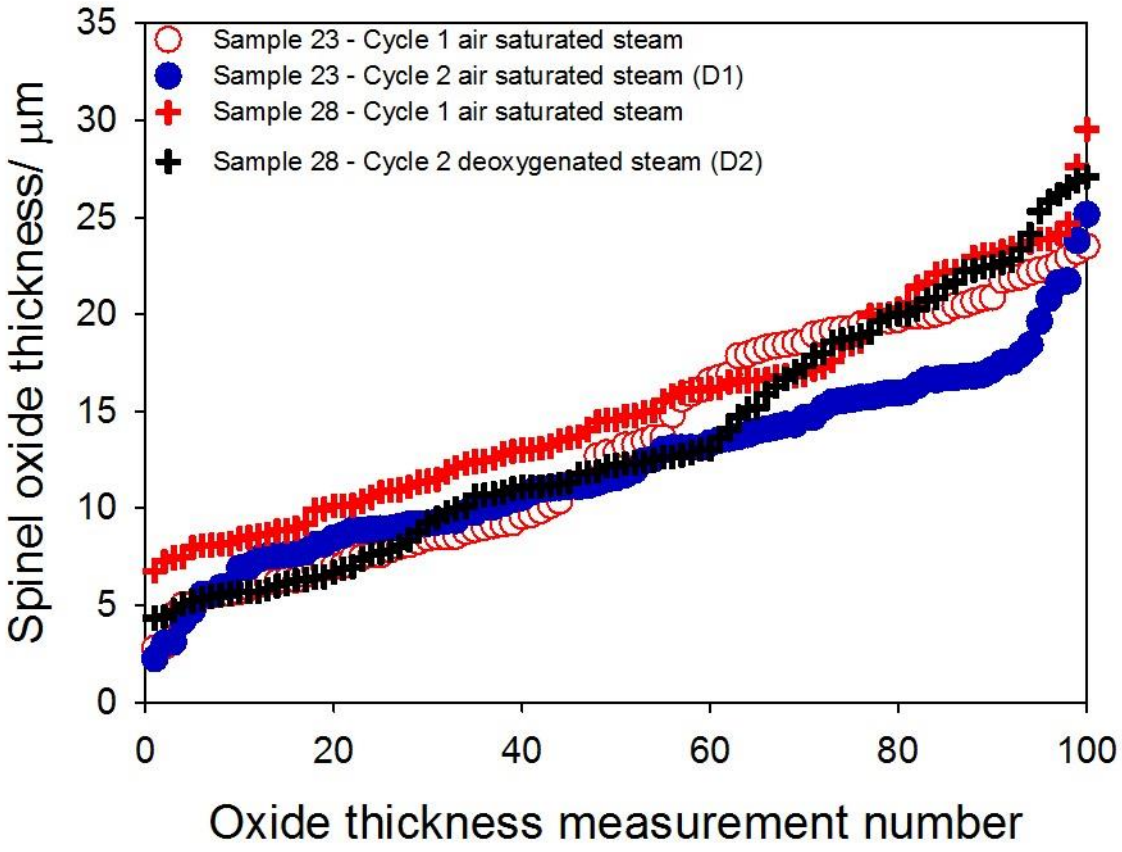

Figure 5-26 Oxide thickness measurements of Fe-Cr-Ni spinel as a function of the number of measurements taken for the oxide grown on TP347H FG in steam environments at 923 K for 1000 hour cycles.

A change in slope was observed for the second thermal cycle of experiment D2 indicative of a bimodally distributed oxide thickness. This was confirmed through the use of histograms as shown in Figure 5-27. The cause for a bimodal distribution in oxide thicknesses will be discussed further in Section 5.3.

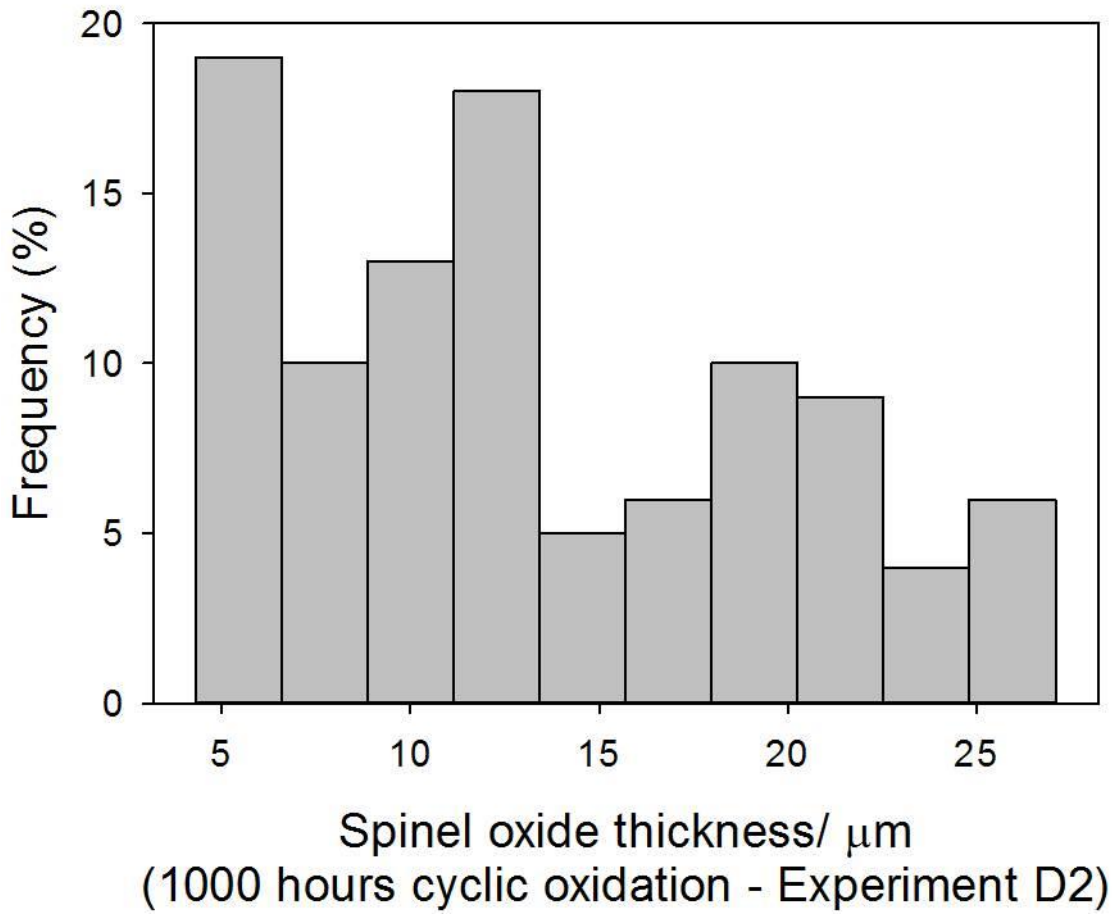

Figure 5-27 Histogram plot for Fe-Cr-Ni spinel oxide grown during cycle 2 of experiment D2 at 923 K.

5.2.1.5 Summary

In all of the experiments where a comparison was made for cycle 2, no spallation was observed during cooling when deoxygenated steam was used. As oxidation time increased, spallation from samples exposed to air-saturated steam for the second thermal cycle also became less noticeable until 1000 hours when no spallation was observed in either atmosphere.

An increase in the Fe-Cr-Ni spinel oxide thickness was observed for cycles of 50-500 hours in both air saturated and deoxygenated steam but increased to a greater

extent when the experiments were conducted in an air-saturated environment. However, for 1000 hours the spinel oxide thickness decreased during the second thermal cycle and again, decreased to a greater extent in air-saturated steam than in deoxygenated steam. The mechanism for oxidation will be discussed in Section 5.3.

5.2.2 Deoxygenated steam cycles

For industrial applications cycle times are unlikely to be equivalent for each exposure period. Investigations were therefore carried out to determine the spallation behaviour of samples exposed for various oxidation times for the first cycle followed by a 1000 hour exposure in deoxygenated steam, i.e. experiments A3, B3, C3 and D2 in Table 5-1. All cycles were carried out at 923 K. Again air-saturated steam was used for the first cycle to initiate spallation as discussed in Chapter 4. Deoxygenated steam environments were used for the second cycle to more closely replicate the atmosphere seen in power plants.

Spallation observations for this series of experiments are given in Table 5-4. For experiments A3, B3 and C3 a small amount of spallation was observed on cooling from cycle 2. No visible spallation was observed on cooling from cycle 2 for experiment D2. Spallation observations for the first cycle were shown earlier in Table 4-1.

Table 5-4 Spallation observations for TP347H FG during the second thermal cycle of 1000 hours in deoxygenated steam at 923 K.

Test – Cycle 2 (1000 hours)	Total oxidation time (hours)	Spallation observations	Area fraction of spallation (%)
A3	1050	1 spall particle	0.6
B3	1100	2 spall particles	2.6
C3	1500	3 spall particles	2.8
D2	2000	No spallation	0.0

Spalled oxide from cycle 2 of test A3 and C3 was collected after cooling, Figure 5-28(a) and (b), respectively. A single oxide morphology was seen for cycle 2 of experiment A3. Based on the morphology of the oxide shown in the micrograph and comparisons to spalled particles collected from cycle 1 it is believed that the oxide is haematite. Two oxide morphologies were identified in the spalled particle collected from cycle 2 of experiment C3 suggesting that both haematite and magnetite spalled on cooling.

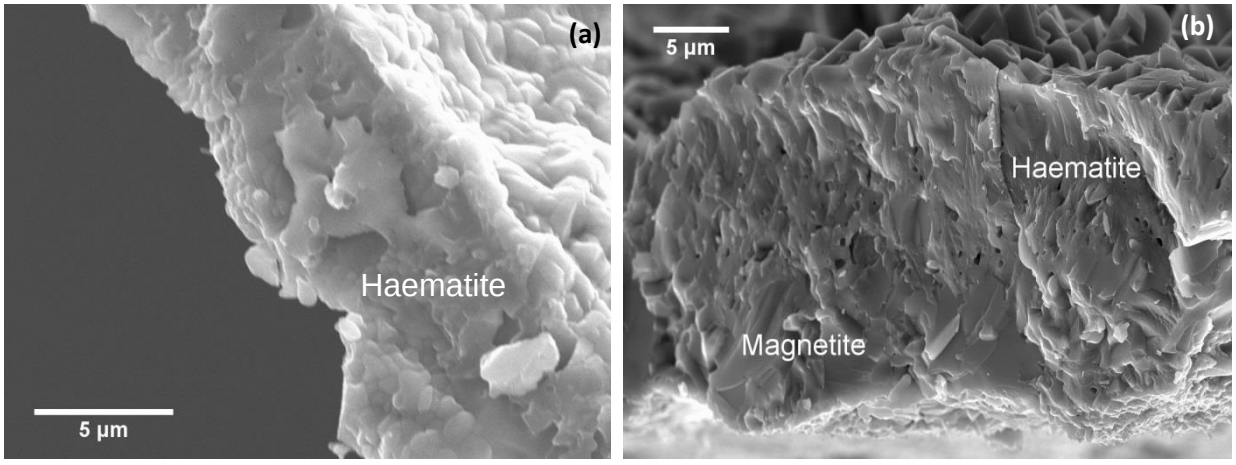

Figure 5-28 Secondary electron micrographs of spalled oxide from cycle 2 in deoxygenated steam at 923 K for 1000 hours where cycle 1 was carried out for (a) 50 hours and (b) 500 hours in air-saturated steam at 923 K.

Thermographic images of the concave surface for the second cycle of experiments A3, B3 and C3 are shown in Figure 5-29 where spallation sites of interest are highlighted. In each of the experiments, the history of the localised spalled site was examined using the STORME technique to determine the point at which delamination of the site occurred. At the start of the thermographic recording when the samples were set down on the heat proof mat, each of the localised spalled sites identified in the figure below were visible. The exact temperature drop at which delamination occurred was therefore not recorded but occurred at $\Delta T_d \leq 221.3$, 119.5 and 185.7 K for A3, B3 and C3, respectively. Investigations into the radius of the spalled site from the time at which the samples were positioned to the complete local spallation were recorded. It was shown that the radius did not increase on any of the samples exposed to deoxygenated steam for 1000 hours and were measured to be 431, 519 and 528 µm for experiment A3, B3 and C3, respectively.

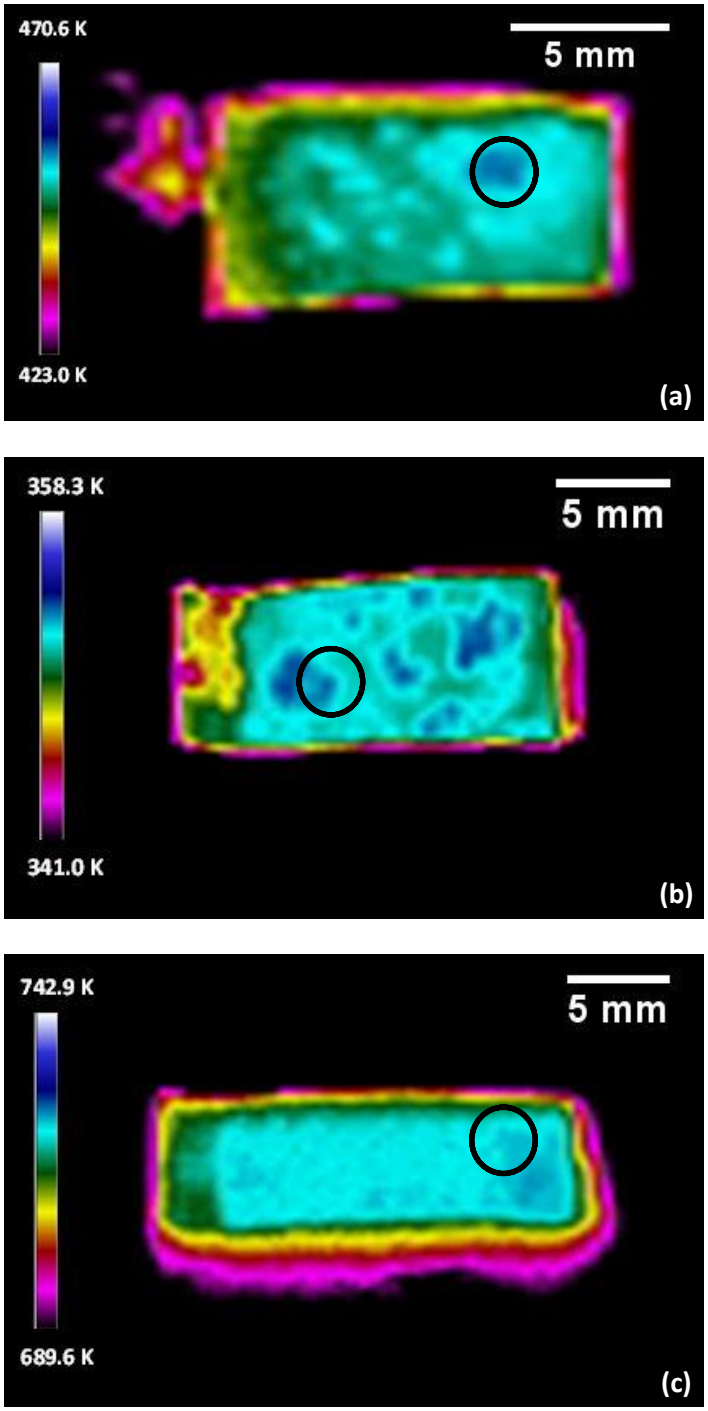

Figure 5-29 Thermographic images of the inner concave surface of TP347H FG for (a) experiment A3, (b) experiment B3 and (c) experiment C3 where the circles indicate the spallation site of interest.

No evidence was found for haematite reformation during the second thermal exposure. However, images of the spalled particles indicated the presence of haematite. Therefore, the spalled oxide must be that of haematite that had grown

during the first thermal cycle but did not spall on cooling subsequent to that cycle. Evidence for this was also shown in Figure 5-8 where the same site was identified subsequent to the first and second thermal exposure. On cooling from cycle one, strain energy is released through the delamination and spallation of the outer haematite layer. Since there was significantly less spallation on cooling for cycle two, the strain energy must also be less and occurred only at an already weakened interface with pre-existing cracks. It has previously been suggested that over time, magnetite will further oxidise to haematite [170], [171]. Since there was no evidence of haematite regrowth during cycle two for this thesis, much longer oxidation times would be expected to be needed to lead to such a transformation. Continued spallation with increasing cycle time would therefore only be significant when haematite has been able to reform.

Back scattered electron images of cross sections for each test are shown in Figure 5-30. Initial observations showed that the outer magnetite oxide regrew during the second thermal cycle of 1000 hours in deoxygenated steam. Voids were also identified within this oxide scale. A general trend of an increase in the thickness of the magnetite oxide and chromite oxide at the base of the spinel was observed in all instances whereas the average concentration of Fe within the spinel oxide layer decreased compared to the first thermal exposure, Table 5-3.

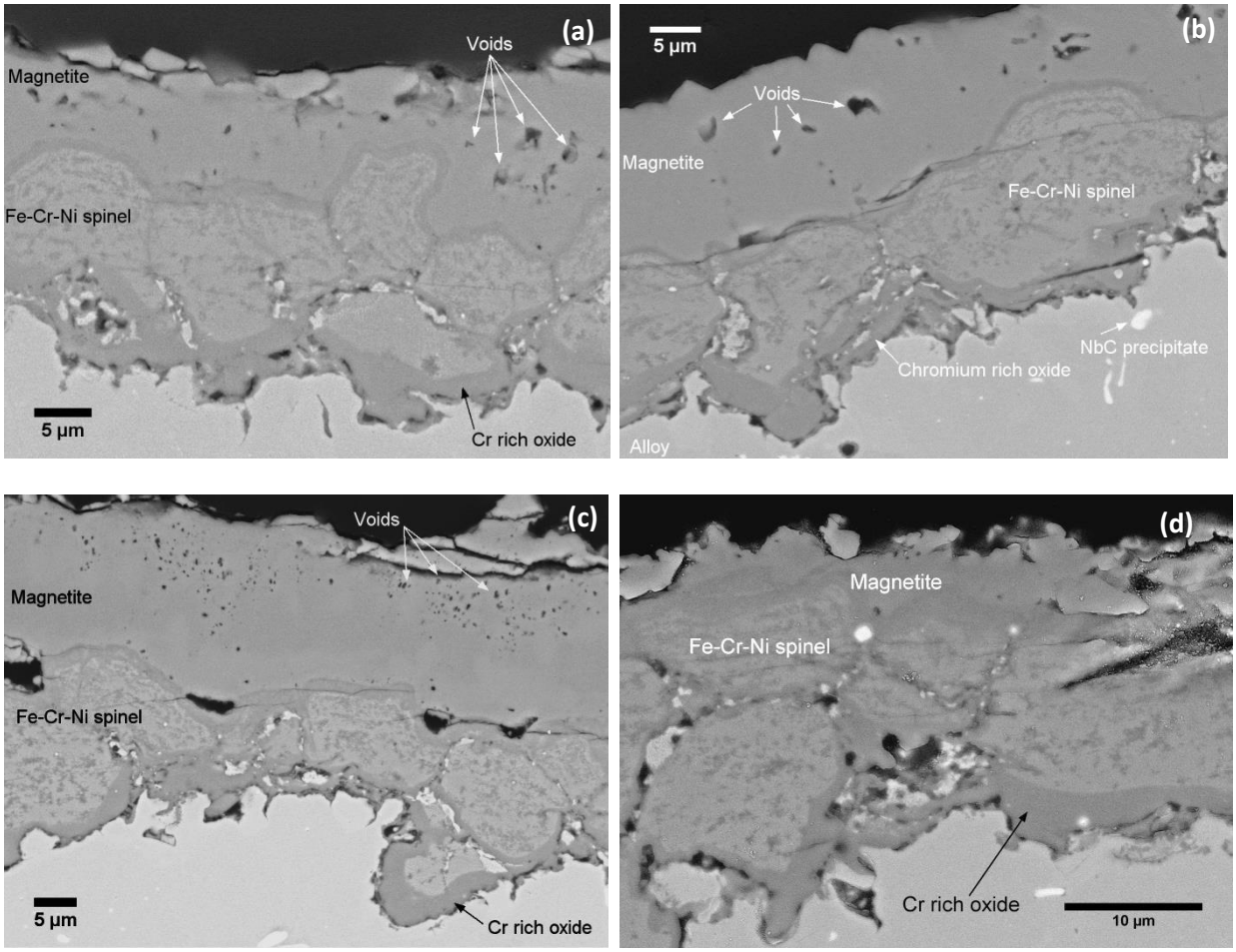

Figure 5-30 BSE image of TP347H FG after oxidation at 923 K for cycle 2 of (a) experiment A3, (b) experiment B3, (c) experiment C3 and (d) experiment D2. All cycles were carried out at 923 K.

In each of the samples shown in Figure 5-30, the chromite layer at the base of the spinel was continuous. For experiments A3 and B3 this layer was not continuous after the first thermal cycle, Figure 4-3(a) and (b). Thickness measurements of this scale for longer term testing showed an increase compared to the first thermal cycle as indicated in Table 5-5.

Table 5-5 Cross sectional observations from experiments carried out for various oxidation times for cycle 1 followed by 1000 hours in deoxygenated steam at 923 K. Oxide thickness measurements are the mean values ± standard deviations.

Test	Cycle	Average Fe concentration in spinel (at.%)	Average spinel thickness (μm)	Maximum spinel thickness (μm)	Average Fe oxide thickness (μm)	Average Cr oxide thickness (μm)
A3	1	27.2	9.4±3.3	15.5	4.7±2.1	0.0
	2	20.3	13.7±5.4	27.4	16.2±6.0	1.3±0.5
B3	1	28.0	11.2±4.9	23.1	8.1±2.2	0.0
	2	27.7	10.4±4.0	30.2	27.9±2.0	1.7±0.5
C3	1	22.6	14.2±5.6	29.7	-	0.9±0.5
	2	19.7	17.4±5.8	30.4	27.4±6.4	1.3±0.4
D2	1	24.7	15.2±5.3	29.5	-	1.5±0.8
	2	19.2	13.5±6.4	27.1	14.0±5.6	1.7±0.9

5.2.3 Cyclic versus isothermal exposures

Comparisons were made between oxide chemistry and oxidation kinetics for a series of cyclic exposures relative to isothermal tests of the same duration. All oxidation exposures in this section were performed in an air-saturated steam environment at 923 K.

Table 5-6 gives details of the results obtained from SEM and quantitative oxide chemistry analysis. Each of the tests will be discussed in turn below.

Table 5-6 SEM/ EDS results observed for TP347H FG thermally cycled in air-saturated steam for various oxidation times at 923 K. Oxide thickness measurements are mean values ± standard deviations.

Test	Oxidation time (hours)	Average Fe concentration in spinel (at.%)	Average spinel thickness (µm)	Thickest measured spinel (µm)	Fe rich oxide thickness (µm)	Cr rich oxide thickness (µm)
	1 x 50	23.1	7.6±2.5	13.7	5.4±2.4	-
A1	2 x 50	23.5	12.2±3.8	24.8	-	-
	1 x 100	23.0	9.7±3.6	20.3	3.2±1.2	-
B4	2 x 100	30.5	13.1±5.1	21.9	-	-
	3 x 100	33.9	16.4±5.9	24.0	5.4±2.4	-
I3	1 x 300	26.3	13.8±4.1	23.4	15.6±3.0	1.3±1.0
	1 x 500	25.3	10.9±5.0	21.4	-	1.7±1.0
C1	2 x 500	19.7	12.9±4.8	23.6	-	1.3±0.6
I6	1 x 1000	28.6	18.4±5.9	31.6	-	1.5±1.0

5.2.3.1 2 x 50 hours versus 1 x 100 hours

Secondary electron micrographs of the inner pickled concave surface of TP347H FG exposed for a total of 100 hours in air-saturated steam are shown in Figure 5-31. Both cyclic and isothermal exposures were similar in appearance with adherent oxide visible as well as regions where the outer oxide had spalled. Spallation occurred subsequent to the second cycle of 50 hours and it was shown to be a mixture of haematite and magnetite that had spalled, Figure 5-2. Isothermal exposures of 100 hours on the other hand resulted in only the spallation of haematite as discussed in Chapter 4.

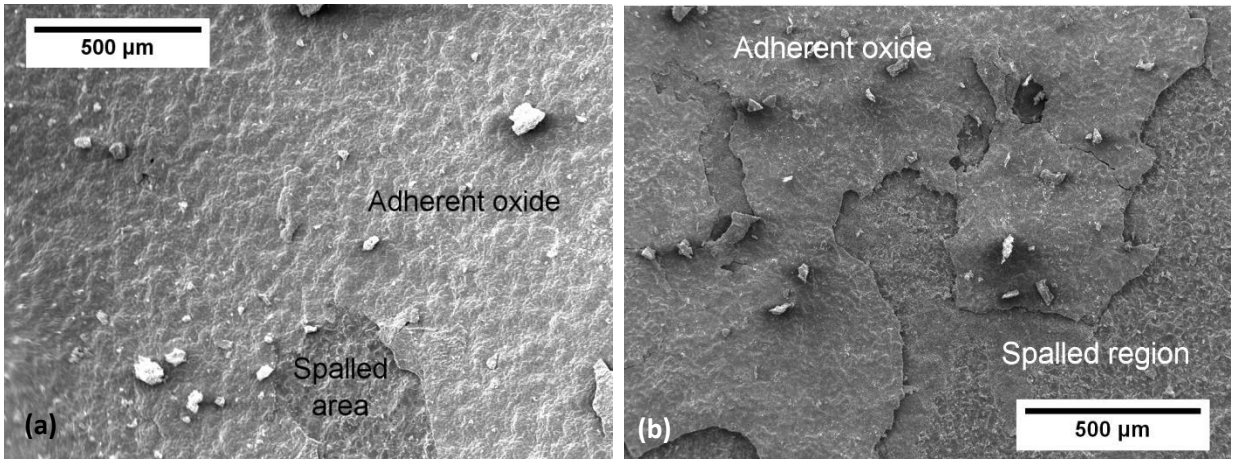

Figure 5-31 SE micrographs of the inner pickled concave surface of TP347H FG subsequent to (a) thermal cycling for a total of 100 hours (two 50 hour cycles) and (b) isothermal oxidation for 100 hours both in air-saturated steam at 923 K.

Cross sectional analysis indicated the presence of voids in the case of cyclic oxidation but where oxidation is isothermal for the same duration void formation was less apparent and was observed to be more sporadic in isothermal exposures, Figure 5-32. For cyclic oxidation the voids were seen within the magnetite layer. Both exposure types resulted in a duplex oxide formation with an outer decoration of haematite. Under both exposure types the Cr-rich oxide at the base of the spinel was not continuous but had started to form.

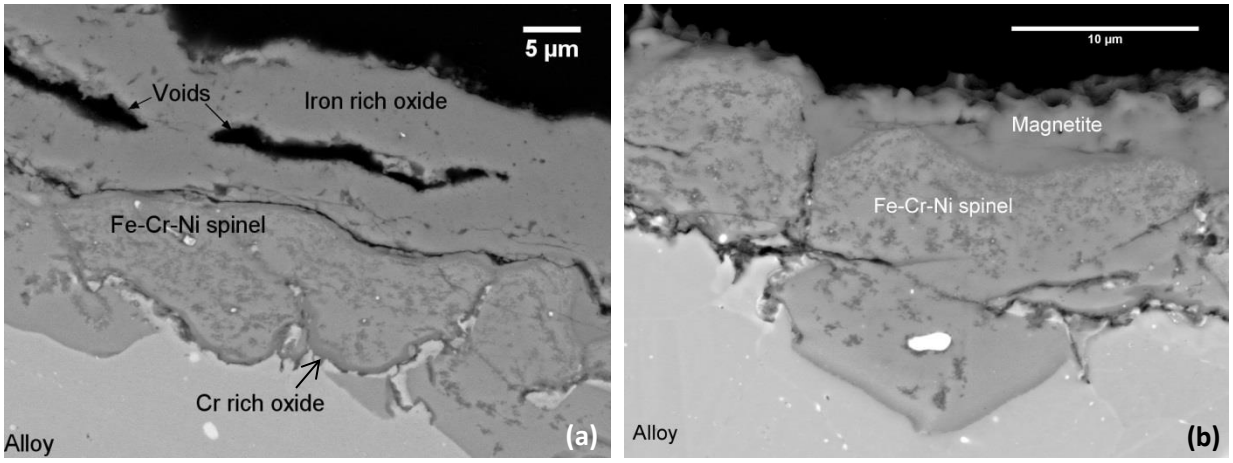

Figure 5-32 BSE images of TP347H FG after (a) 100 hour cyclic oxidation (2 x 50 hours) in air-saturated steam at 923 K and (b) 100 hours isothermal oxidation in air-saturated steam at 923 K.

EDS analysis showed the average Fe concentration within the spinel oxide layer was the same under both isothermal and cyclic conditions where total exposure time equalled 100 hours, Table 5-6.

Oxide thickness measurements for Fe-Cr-Ni spinel oxide were investigated and are plotted as a function of the number of measuements for each exposure type, shown in Figure 5-33. The same trend was followed in both cases but the spinel oxide was shown to be thicker under cyclic oxidation conditions compared to isothermal exposures.

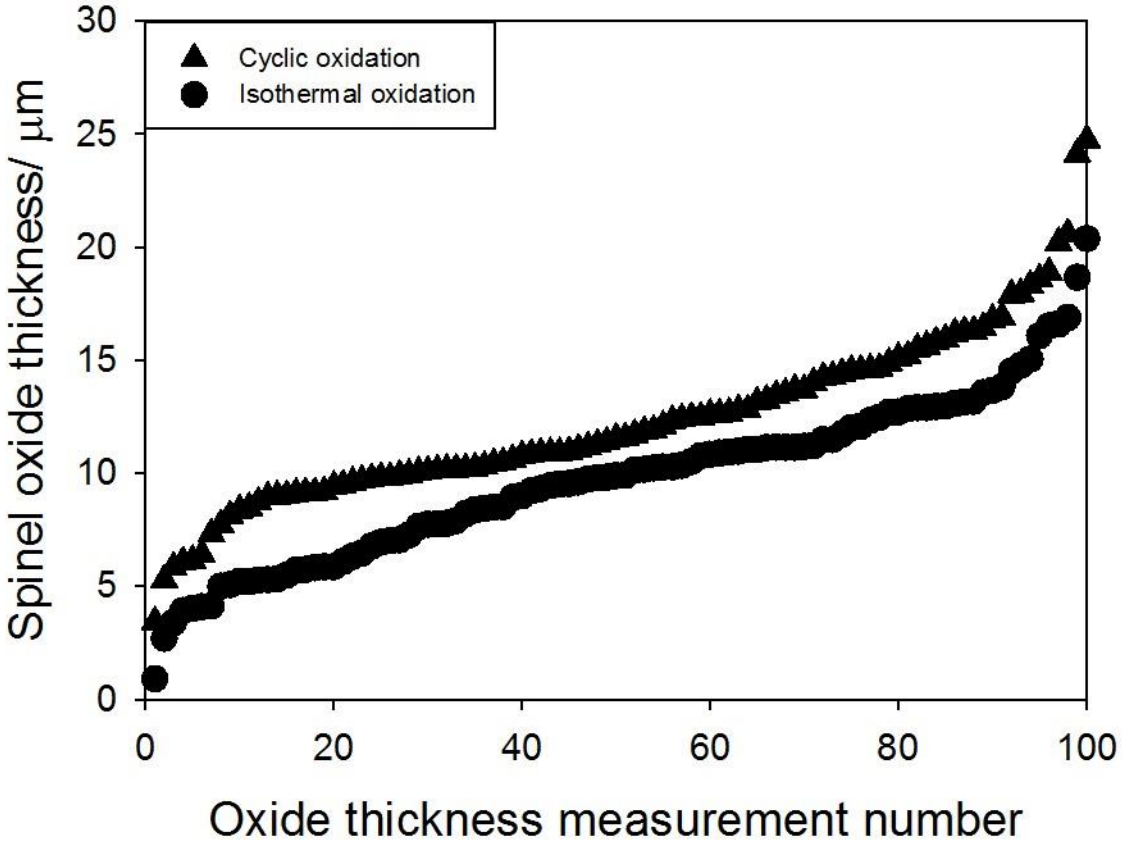

Figure 5-33 Oxide thickness measurements of Fe-Cr-Ni spinel as a function of the number of measurements taken for the oxide grown on TP347H FG in steam environments at 923 K for a total of 100 hours.

5.2.3.2 3 x 100 hours versus 1 x 300 hours

The second set of experiments for comparison was a 300 hour cyclic exposure with an isothermal 300 hour test. Secondary electron micrographs of the surface are shown in Figure 5-34. As previously mentioned, significant spallation occurred on cooling from the first thermal exposure where, approximately 80% of the surface spalled, Table 4-1. On cooling from the second thermal exposure, spallation did occur but only 15% of the surface spalled. After the third thermal exposure of 100 hours in air-saturated steam no visible spallation occurred and the surface of the sample was relatively uniform. Observations for the second cycle of this test were discussed in Section 5.2.1. Isothermal exposures on the other hand resulted in significant spallation on cooling from a 300 hour exposure as shown in Figure 5-34.

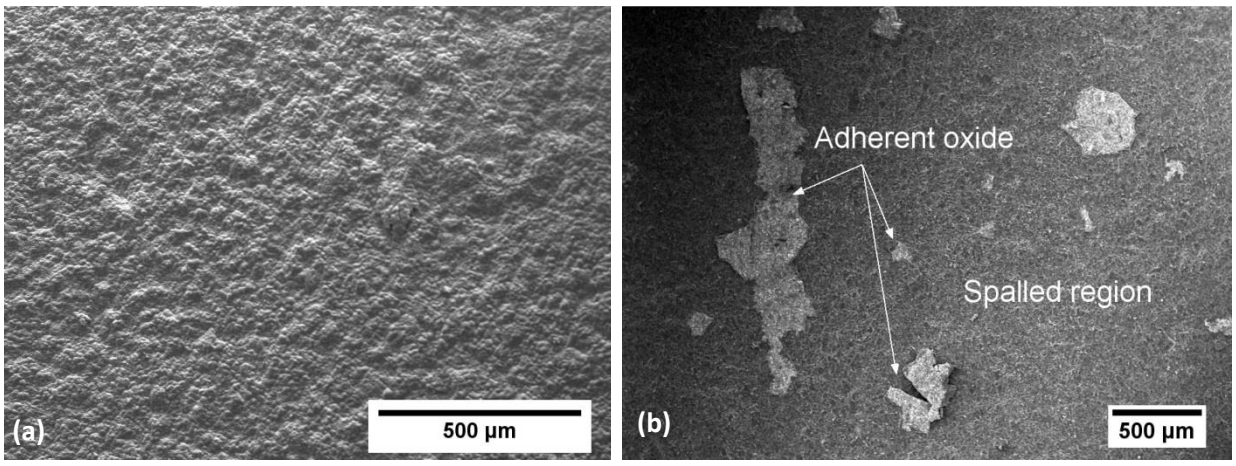

Figure 5-34 SE micrographs of the inner pickled concave surface of TP347H FG subsequent to (a) thermal cycling for a total of 300 hours (three 100 hour cycles) and (b) isothermal oxidation for 300 hours both in air-saturated steam at 923 K.

The second cyclic exposure of this test resulted in spallation of magnetite as well as haematite, Figure 5-9. Spallation from the isothermal exposure resulted in spallation of a mixture of haematite and magnetite. Further evidence for this was found using FIB microscopy to examine the surface, Figure 5-10. Three layers of oxide were

observed where the outer haematite layer had buckled and cracking beneath the magnetite layer was seen. It is thought that all haematite associated spallation had already occurred on cooling from cycles one and two, hence no further spallation was seen on cooling from cycle three.

Cross sectional analysis indicated the regrowth of the outer Fe oxide during the third 100 hour exposure, Figure 5-35(a). For 300 hours isothermal exposure a significant number of voids were observed in cross section at the magnetite/ spinel interface.

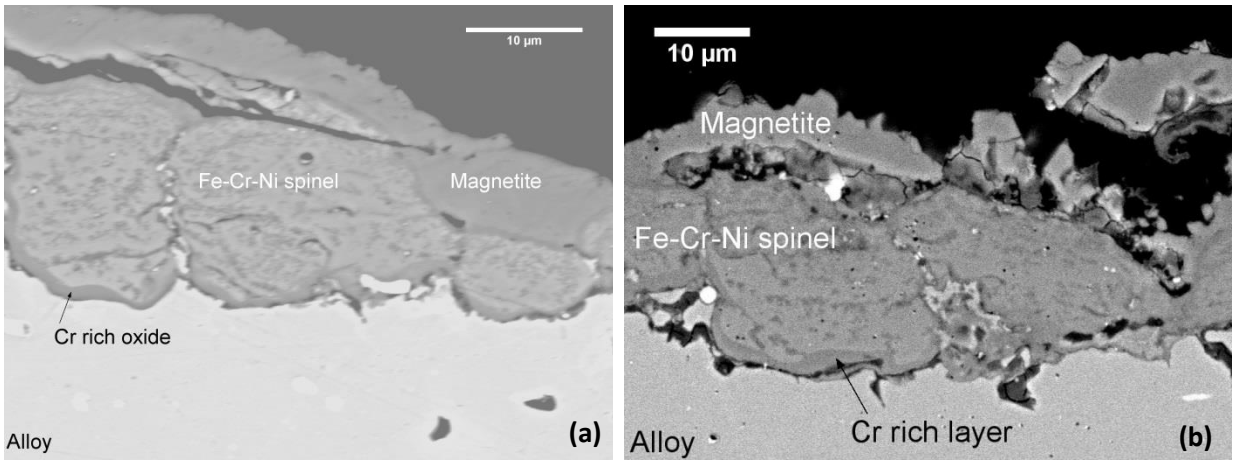

Figure 5-35 BSE images of TP347H FG after (a) 300 hour cyclic oxidation (3 x 100 hours) in air-saturated steam at 923 K and (b) 300 hours isothermal oxidation in air-saturated steam at 923 K.

Under these experimental conditions, the average Fe concentration in the spinel was shown to increase with each 100 hour thermal cycle, Table 5-6. Figure 5-35 compares samples of TP347H FG exposed (a) cyclically and (b) isothermally for a total of 300 hours. In both cases the chromite oxide was continuous at the base of the spinel and there was a layer of magnetite at the gas/ oxide interface. After 100 hours isothermal oxidation the chromite oxide at the base of the Fe-Cr-Ni spinel oxide was not continuous.

Oxide thickness measurements for Fe-Cr-Ni spinel oxide as a function of the number of measurements are shown in Figure 5-36. As was observed in the case of 100 hours total exposure, the oxide is thicker under cyclic conditions compared to isothermal exposures. The change in slope observed for cyclic conditions suggested the oxide thickness was not normally distributed. Histograms were plotted to identify the distribution, Figure 5-37. It was shown in the histogram that spinel thickness is not normally distributed confirming the change in slope on the probability plot. Bimodal behaviour was observed and will be discussed in further detail in Section 5.3.

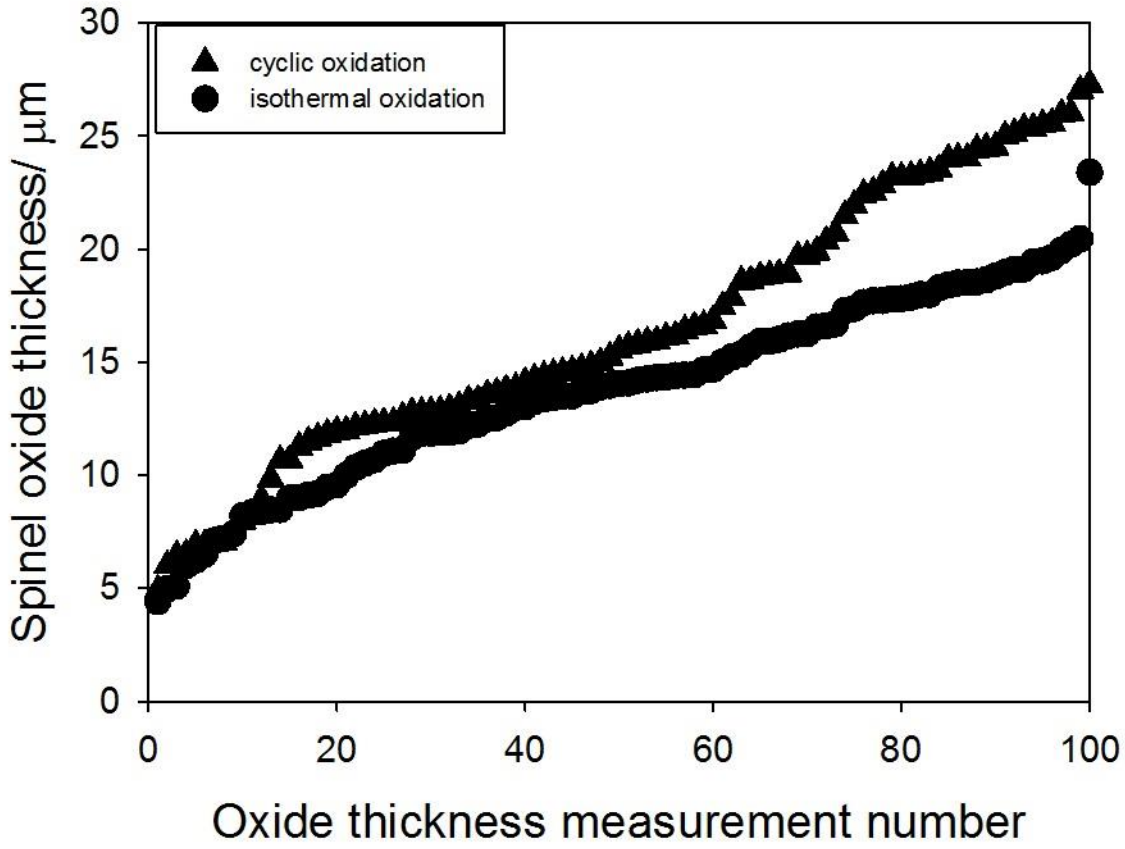

Figure 5-36 Oxide thickness measurements of Fe-Cr-Ni spinel as a function of the number of measurements taken for the oxide grown on TP347H FG in steam environments at 923 K for a total of 300 hours.

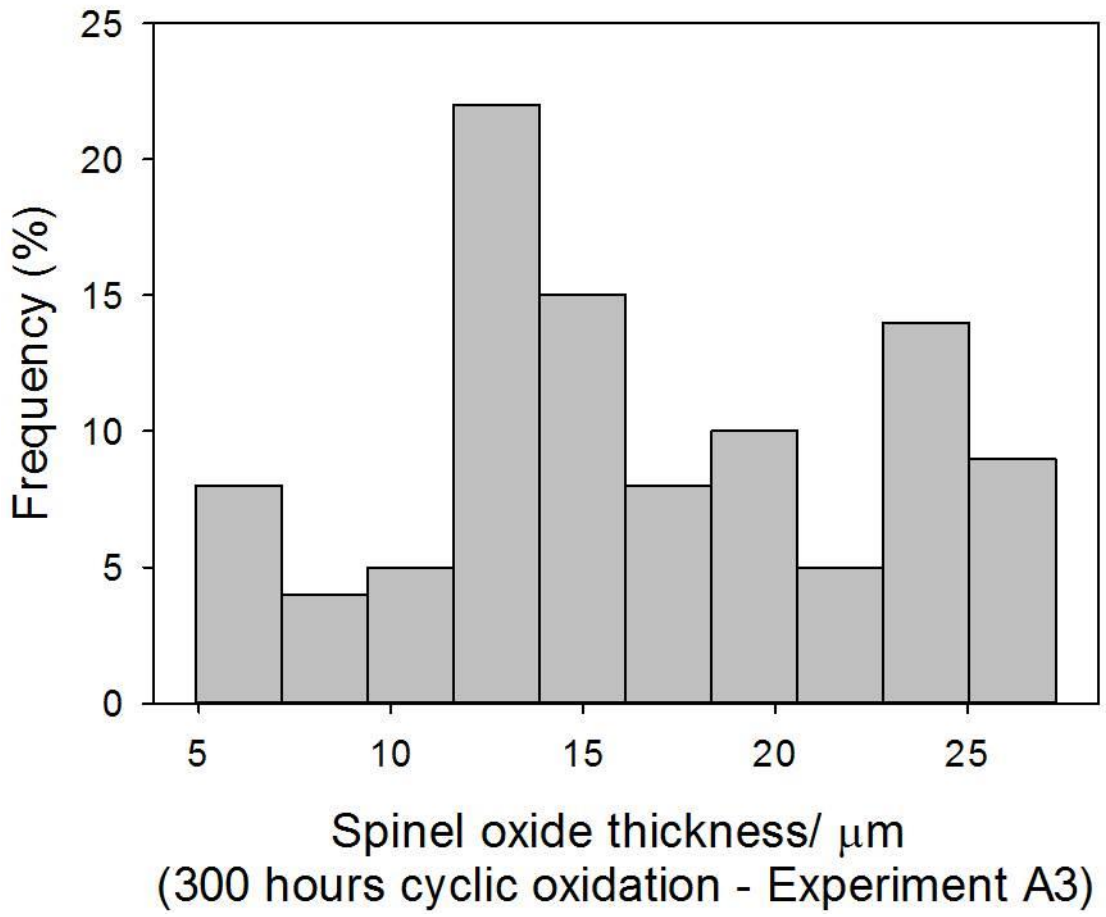

Figure 5-37 Histogram for 300 hours cyclic steam oxidation in air saturated steam at 923 K (3 x 100 hours).

Oxide thickness measurements of Fe-Cr-Ni spinel oxide were used to calculate a rate constant for the 300 hour cyclic exposure. A plot of oxide thickness as a function of oxidation time was plotted, Figure 5-38, and used to calculate oxidation kinetics according to the following equation:

$$\xi = (k_n t)^{1/n} \qquad \text{Equation 5-1}$$

where ξ is spinel oxide thickness, m, k_n is rate constant, $m^n.s^{-1}$ and t is time, s.

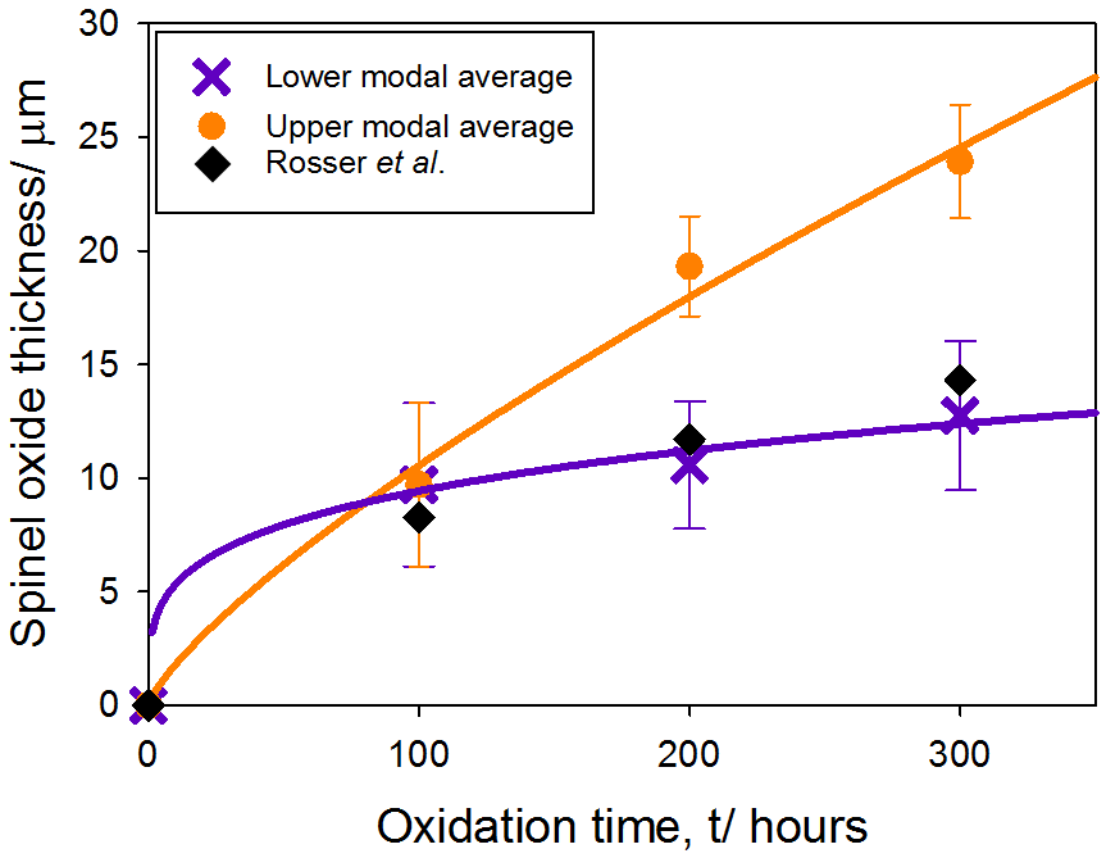

Figure 5-38 Cyclic oxidation kinetics for TP347H FG thermally cycled for 300 hours in air-saturated steam at 923 K.

Since the oxide thickness distribution was shown to be bimodal when histograms were plotted for the second and third thermal cycles, Figure 5-14 and Figure 5-37, respectively, an average value for that data would be meaningless. The bimodal distribution is the beginning of a more complex kinetic behaviour, therefore simple parabolic kinetics was not appropriate. Instead, the averages were obtained for each mode of these two cycles and kinetics were then determined using the above equation for each mode to obtain more realistic kinetics.

The value of n was determined using Equation 5-1. This produced a value for n of 4 for the lower mode and 1.3 for the upper mode. Values for k_n were calculated to be 7.2×10^{-18} $m^4.s^{-1}$ and 2.16×10^{-6} $m^{1.3}.s^{-1}$ for the lower and upper modes, respectively.

The rate of oxidation for a similar alloy exposed to deoxygenated steam in the literature was found to be 1.9 x 10^{-16} $m^2.s^{-1}$ [21] and is also included in Figure 5-38. This k_p value was in good agreement with the lower modal results observed for this thesis. TP347H FG could be slightly more protective than Super 304H shown in Figure 5-38 because of its slightly higher Cr concentration.

5.2.3.3 2 x 500 hours versus 1 x 1000 hours

Micrographs of the surface of samples exposed for a total of 1000 hours are shown in Figure 5-39. Where the oxidation exposure was cyclic, Figure 5-39(a), the surface of the sample was relatively uniform. A small amount of spallation was observed on cooling, as mentioned earlier in Section 5.3.2 and spalled particles were shown to contain both haematite and magnetite. In the case of the isothermal exposure, significantly more spallation was observed compared to the second cyclic exposure and again the spalled oxide particles contained both Fe oxides. A number of spalled regions were able to be identified on the surface for isothermal oxidation of 1000 hours.

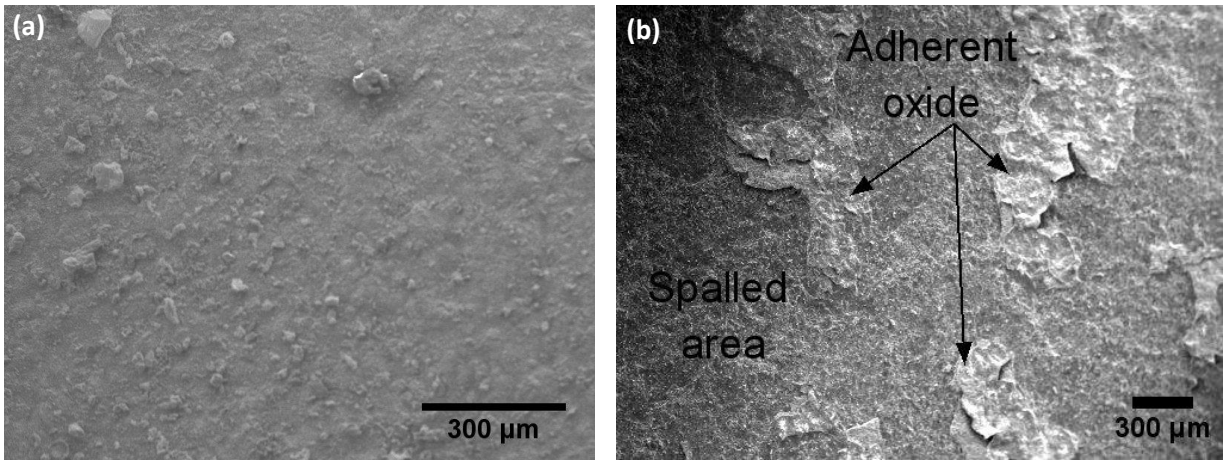

Figure 5-39 SE micrographs of the inner pickled concave surface of TP347H FG subsequent to (a) thermal cycling for a total of 1000 hours (two 500 hour cycles) and (b) isothermal oxidation for 1000 hours both in air-saturated steam at 923 K.

Cross sectional examination indicated that for cyclic oxidation totalling 1000 hours, magnetite was still adherent at the outer surface and remnants of the void walls could be seen, Figure 5-40(a). Isothermal oxidation on the other hand showed that spallation had occurred predominantly at the magnetite/ spinel interface rather than within the magnetite scale and no voids were visible. Both oxidation conditions showed the presence of a continuous Cr rich oxide at the base of the spinel.

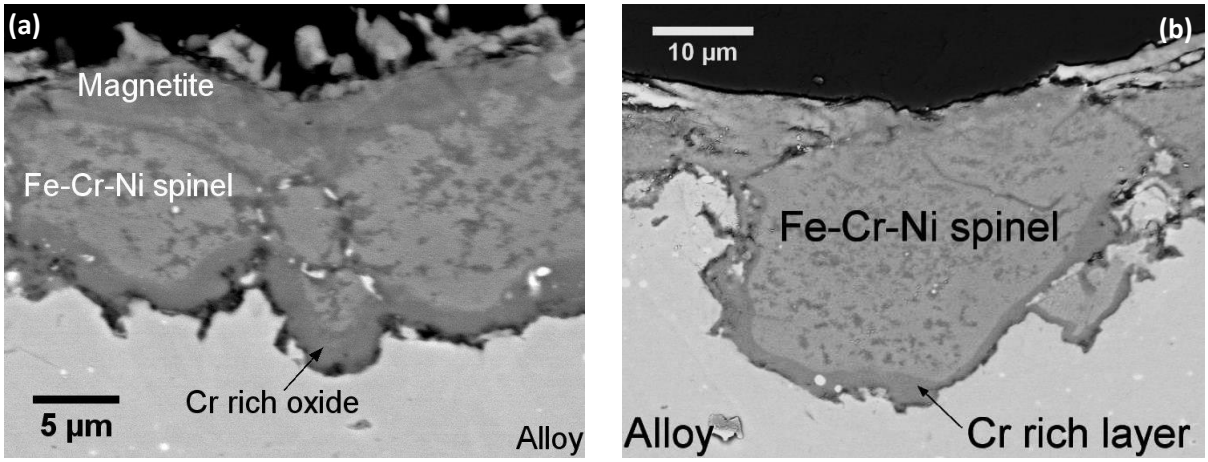

Figure 5-40 BSE images of TP347H FG after (a) 1000 hour cyclic oxidation (2 x 500 hours) in air-saturated steam at 923 K and (b) 1000 hours isothermal oxidation in air-saturated steam at 923 K.

EDS analysis showed the average Fe concentration within the Fe-Cr-Ni spinel was significantly lower under cyclic conditions compared to isothermal conditions.

Oxide thickness measurements for the Fe-Cr-Ni spinel oxide as a function of the number of measurements under both oxidation exposures are shown in Figure 5-41. For these longer term exposures the reverse trend was observed compared to short term cyclic and isothermal exposures and the average spinel oxide thickness was not thicker under cyclic conditions.

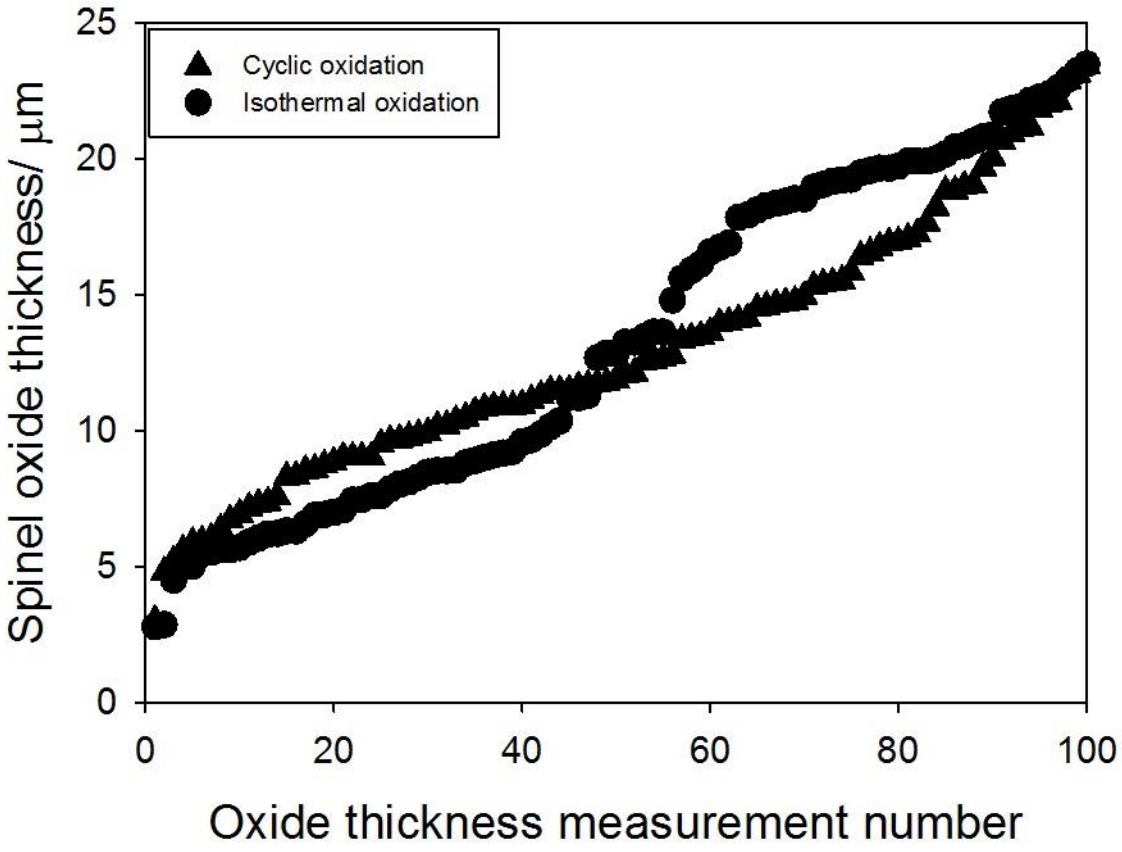

Figure 5-41 Oxide thickness measurements of Fe-Cr-Ni spinel as a function of the number of measurements taken for the oxide grown on TP347H FG in steam environments at 923 K for a total of 1000 hours.

A plot of Fe-Cr-Ni spinel oxide thickness as a function of the number of measurements for cyclic oxidation shown in Figure 5-41 indicated a change in slope at 12-13 µm which would suggest a bimodal distribution. Histograms of oxide thickness were plotted to determine the distribution, Figure 5-42. Where oxidation was carried out under cyclic conditions the distribution was shown to be normal. The same style distribution was also shown for isothermal oxidation under the same conditions although the normal distribution is more skewed under those conditions than under cyclic conditions.

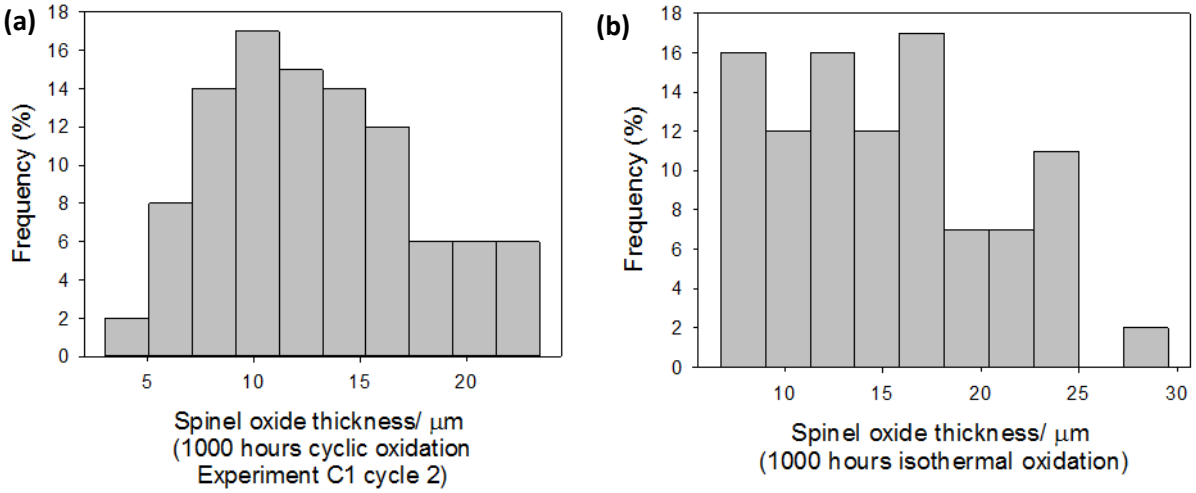

Figure 5-42 Oxide thickness histograms for a) 1000 hours cyclic oxidation (2 x 500 hours) and (b) 1000 hours isothermal oxidation where all cycles were carried out in air saturated steam at 923 K.

5.3 Discussion

For all tests, an outer layer of haematite formed during the initial exposure. The presence of this haematite results in significant spallation on cooling as a result of the large mismatch in thermal expansion coefficient between haematite and TP347H FG. Subsequent thermal exposures did not result in reformation of the outer haematite layer and there was a noticeable reduction in spallation with no spallation occurring in deoxygenated steam environments or long term thermal cycling in either environment studied. Haematite reformation during cyclic oxidation was reported to occur for samples of ferritic T91 exposed to Ar + steam environments at 923 K [57]. In that study, haematite and magnetite were removed through polishing subsequent to the initial exposure. In all but experiment A3, any further spallation on cooling from the second cycle was found to be that of both haematite and magnetite. It is postulated that the cause for this continued spallation is due to adherent haematite that did not spall on cooling from the first cycle. Evidence for this was found through SEM analysis of the surface of samples where the same site was located in both cycles.

The oxide that remained adherent subsequent to cycle 1 had cracked and spalled on cooling from cycle 2. Further evidence was found in SEM analysis of spalled particles where an interface could clearly be seen between haematite and magnetite where the former had buckled. Finally, the decrease in the amount of adherent haematite during cycle 2 would result in less being available for spallation, hence the noticeable decrease in the number of spallation events.

A protective Cr rich oxide developed at the base of the spinel but was not seen to be continuous until 300 hours, as mentioned earlier in Chapter 4. Short term thermal cycling of 50 and 100 hours in air saturated steam environments resulted in an increase in the average Fe concentration within the spinel with each cycle, Table 5-3. It is thought that the formation of the Cr rich oxide during that time restricted the amount of Cr diffusion into the spinel, hence increasing the relative concentration of Fe. The Fe-Cr-Ni spinel oxide was also shown to be bimodally distributed for cycles 2 of experiments A1 and B1, i.e. 50 and 100 hour cycles. For 500 and 1000 hour cycles in air saturated steam though, the spinel thickness was shown to be normally distributed. However, when the second thermal cycle was carried out in deoxygenated steam for 500 and 1000 hours, the spinel oxide thickness was shown to possess a bimodal distribution. The cause for the bimodal distribution is thought to be as a result of the Cr rich oxide formation at the base of the Fe-Cr-Ni spinel oxide around the grains and along the grain boundaries. The formation of this protective oxide reduces the rate of diffusion of O inwards and therefore slows down the rate of further oxidation. Therefore, the first peak of the bimodal distribution represents the formation of a continuous Cr rich layer and the second peak forms as a result of the Cr rich layer not being continuous around the grain therefore allowing oxidation to

continue at the same rate. Since this Cr rich layer was continuous after 300 isothermal hours of oxidation, further cyclic oxidation where cycle times are higher than this would lead to a normal distribution since all grains will be behaving in the same way. However, for cycle 2 of experiments C2 and D2 in a deoxygenated steam environment, the Fe-Cr-Ni spinel thickness was shown to have a bimodal distribution. This is thought to be as a result of the oxygen partial pressure. The lower oxygen partial pressure of 1×10^{-8} in deoxygenated steam compared to 1×10^{-5} in air-saturated steam means that there is less oxygen available for oxidation in deoxygenated steam. Therefore, whilst oxidation does continue beneath the Cr rich oxide, such as that shown in Figure 5-20 and Figure 5-24, in both environments, the lower oxygen partial pressure in deoxygenated steam results in a more undulated growth and therefore a bimodal distribution of the oxide thickness.

The bimodal nature of the Fe-Cr-Ni spinel oxide would also affect the oxidation kinetics, as mentioned earlier in Section 5.2.3.2. Figure 5-43 indicates the predicted oxidation kinetics based on the bimodal behaviour of the Fe-Cr-Ni spinel and compares it to the isothermal kinetic behaviour determined in Chapter 4. For the upper modal average of 100 hour cycles where the Cr rich oxide would not be continuous, the oxidation kinetics would be expected to be significantly faster than those under isothermal conditions. The lower average however, predicts the thickness would be reduced compared to that seen for isothermal conditions. The lower modal averages of experiment C2 and D2 were lower than the mean obtained for cycle 1 of those experiments and so kinetics under those conditions were not included. The oxide would be expected to grow at a faster rate than isothermal conditions for the upper modal average of 500 hour cycles and would be expected to

be thinner under 1000 hour cycles. Sureau *et al*. [172] proposed a model to predict cyclic oxidation kinetics. The model suggested in that work takes into consideration the probability of spallation with increasing oxide thickness and/ or time. The kinetic data shown in Figure 5-43 is based on experimental data rather than a numerical fit as this was not within the scope of this work.

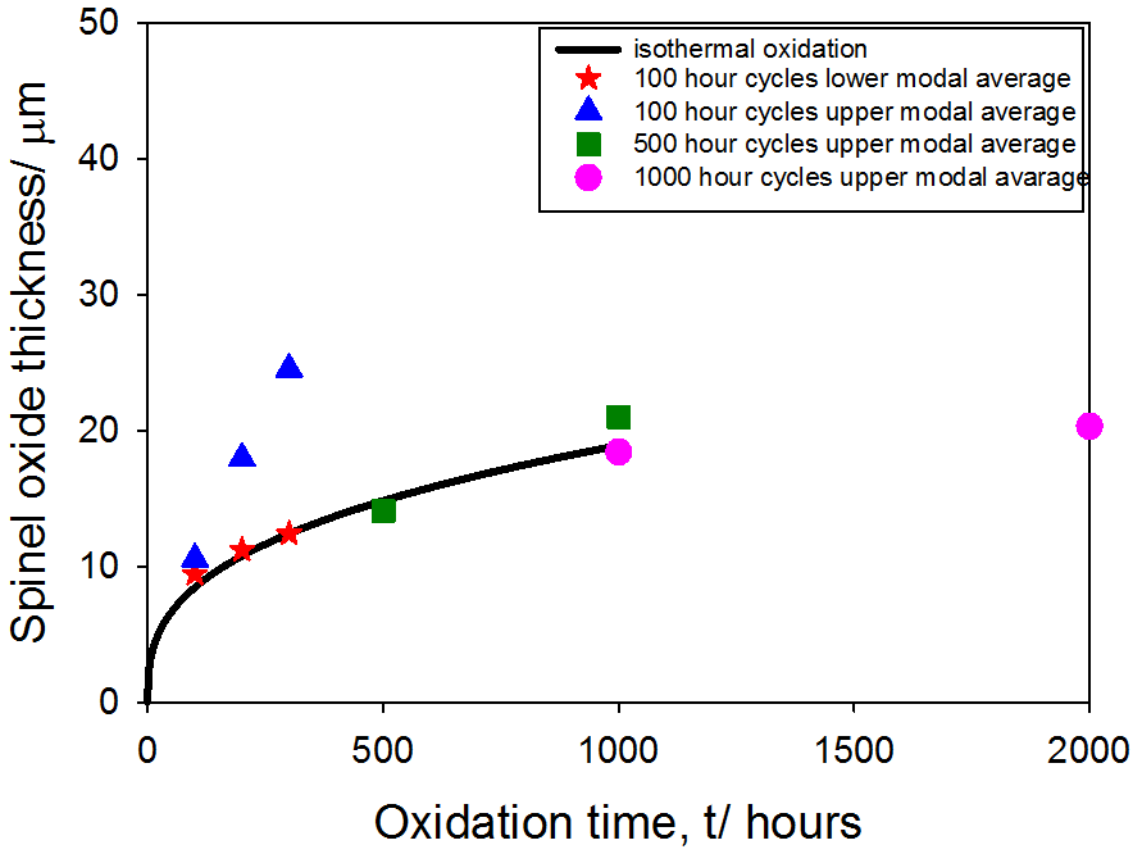

Figure 5-43 Oxidation kinetics taking into consideration the bimodal behaviour of the Fe-Cr-Ni spinel under cyclic conditions.

There was a general trend observed for Fe concentrations for each experiment although there were some differences between like for like samples. For instance cycle 1 of experiments A1 and A2 were carried out under the same conditions for the same testing period and the Fe concentration differed between the two samples. Likewise for cycle 1 of B1 and B2, C1 and C2 and D1 and D2. Therefore the

observations discussed here are based on a qualitative trend. Short term thermal cycles in deoxygenated steam and longer thermal cycles in both conditions studied however, resulted in a decrease in the average amount of Fe observed within the spinel. In the former case, the Cr rich oxide was still not continuous and so it was predicted that the Fe concentration should also increase.

For long term thermal cycling the Cr rich scale was continuous prior to the initial spallation event. It is therefore postulated that the decrease in Fe concentration and spinel thickness for 1000 hour cycles is as a result of decreased rates of diffusion through the protective Cr rich scale. The diffusion of Fe through thin films of chromia is two orders of magnitude slower than through the alloy lattice[2] and four orders of magnitude slower than through magnetite. Since magnetite possesses an inverted spinel structure it is expected that rates of Fe diffusion through spinel will be equivalent to those seen for magnetite. Consequently, on further oxidation where the Cr rich oxide is present, there is a reduced supply of Fe into the spinel. During the second thermal cycle magnetite continued to grow. The decrease in Fe concentration and spinel thickness was therefore thought to be as a result of Fe diffusing outwards from within the spinel and oxidising at the oxide/ gas interface to magnetite. This also resulted in a decrease in the thickness of Fe-Cr-Ni spinel. Other interesting observations to note for long term thermal cycling in different environments was that magnetite grew to a greater extent under deoxygenated conditions, the growth rate of the Cr rich scale was greater under air-saturated conditions and finally the thickness of spinel reduced in both instances but to a greater extent under air-saturated steam. Oxygen partial pressure differences between the two environments must be the

[2] A table of diffusion coefficients is given in Appendix D.

cause of these differences. The higher amount of O in air-saturated steam, where $pO_2 = 1 \times 10^{-5}$, compared to deoxygenated steam, where $pO_2 = 1 \times 10^{-8}$, means there is more O available for oxidation. Previous studies have suggested that with increasing oxidation time spinel becomes more protective in nature and hence reducing the rate of Fe diffusion. Further oxidative attack then leads to oxidation of magnetite to haematite because of the reduced supply of Fe ions [170], [171]. No evidence was found to suggest haematite regrows during re-oxidation and so if this is the case then longer oxidation times would be required to form haematite.

For short term oxidation times, 50 – 300 hours, the Fe-Cr-Ni spinel oxide was thicker under cyclic conditions compared to isothermal conditions. This is thought to be as a result of spallation of the outer Fe rich oxides. Spallation of haematite on cooling from the first cycle reduces the distance through which O has to diffuse inwardly to form spinel at the oxide/ alloy interface. For isothermal oxidation where the outer Fe oxide is adherent, O diffusion will be reduced hence restricting the extent of spinel growth. In the case of long term thermal cycles where the Cr rich scale is continuous at the base of the spinel prior to the initial spallation event, spinel is thicker under isothermal conditions. The protective nature of the Cr rich oxide restricts spinel formation during the second thermal cycle.

A mechanism for short term oxidation and spallation has been proposed and is shown schematically in Figure 5-44. Details of each stage of the thermal cycling process are:

1. Initial oxidation of TP347H FG. Outward diffusion of Fe ions and inward diffusion of O^{2-} results in the formation of the outer Fe oxides, haematite and

magnetite, and the inner Fe-Cr-Ni spinel, respectively. A Cr rich oxide at the base of the spinel scale has started to form but is not continuous.

2. Samples are removed from the furnace at temperature and cooled in laboratory air. Significant spallation of the outer haematite layer occurs.
3. Samples are exposed to steam for a second cycle of 50-100 hours at 923 K. The Cr rich oxide continues to grow but is still not continuous and the Fe-Cr-Ni spinel thickness also increases.
4. Spallation of any remaining haematite from cycle 1 and magnetite occurs on cooling.
5. Samples exposed for a total of 200 hours are inserted in to the furnace for a final time. Magnetite reforms and there is no evidence of haematite. The thickness of the Fe-Cr-Ni spinel continues to increase again.
6. No visible spallation on cooling. The Cr rich oxide at the base of the spinel is now continuous.

During the initial stages of oxidation, a Cr rich oxide at the base of the Fe-Cr-Ni spinel layer started to develop but was not continuous. As a result of this, further oxidation subsequent to the initial spallation event resulted in an increase in the Fe-Cr-Ni spinel because the Cr rich layer was not fully protective and therefore could not reduce the rate of diffusion of oxidising elements from within the alloy.

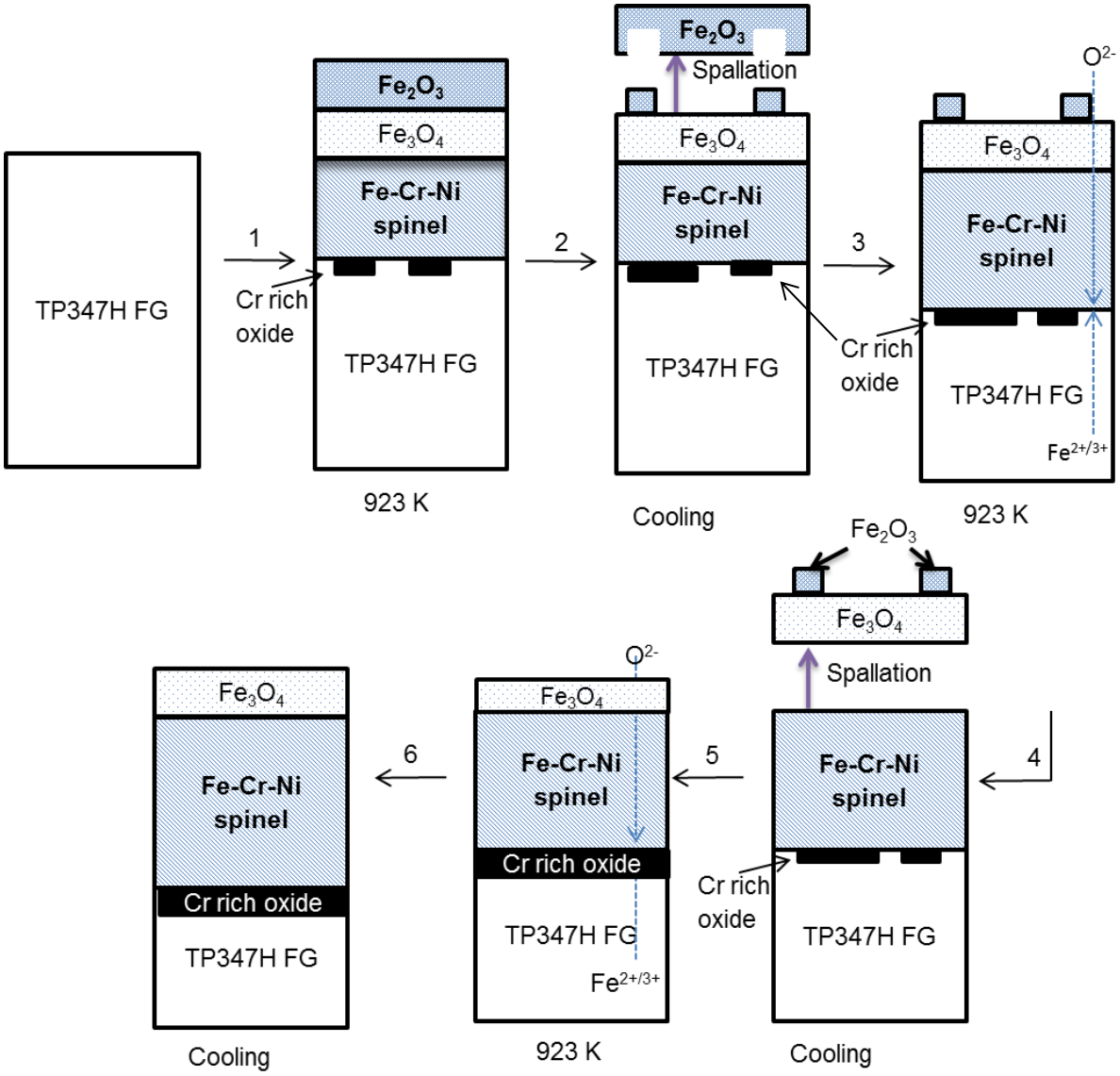

Figure 5-44 Oxidation mechanism for short term thermal cycling in air-saturated steam at 923 K.

A mechanism for long term thermal cycling has been proposed and is shown schematically in Figure 5-45. Each stage of the oxidation process can be described as:

1. Initial oxidation exposure of 500-1000 hours in air-saturated steam at 923 K. Formation of a duplex oxide scale with an outer decoration of haematite. A Cr rich oxide also formed at the base of the Fe-Cr-Ni spinel.
2. Cooling of the sample led to significant spallation where two oxide morphologies were observed believed to be that of haematite and magnetite.
3. The samples were exposed for a further 500-1000 hours in either an air-saturated or deoxygenated environment. The thickness of the Fe-Cr-Ni spinel decreased and Cr rich oxide scales increased during this thermal exposure.
4. The samples were again removed from the furnace at temperature and cooled in laboratory air. For air-saturated conditions spallation occurred where the second thermal cycle was for 500 hours and two oxide morphologies were observed, again believed to be that of haematite and magnetite.

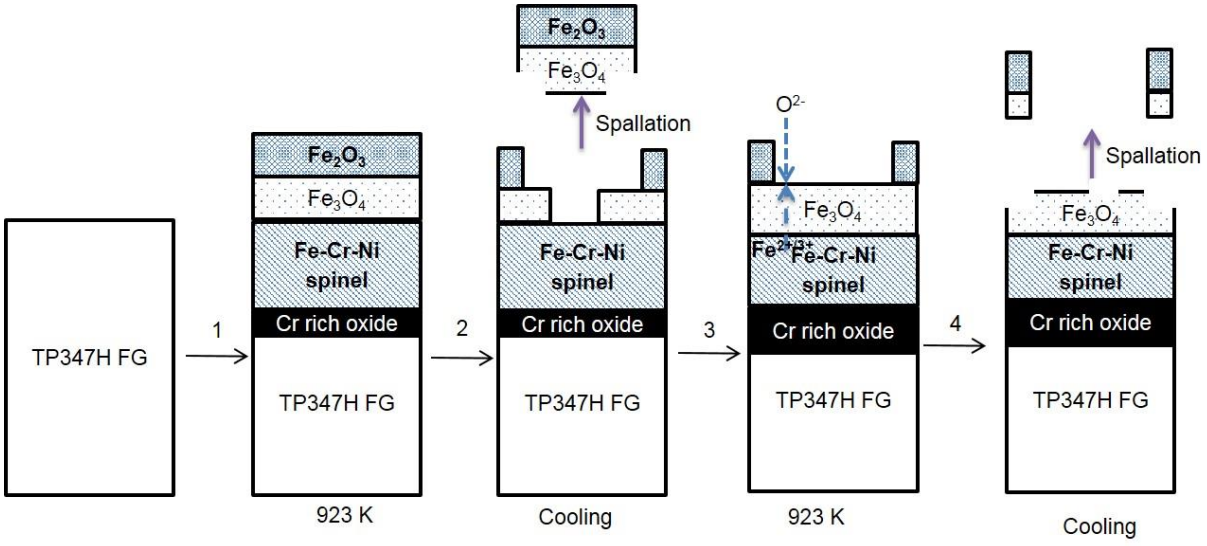

Figure 5-45 Oxidation mechanism for TP347H FG exposed steam environments at 923 K for 500-1000 hours.

5.4 Concluding Summary

Haematite was found to be essential for spallation on cooling from the first cycle, as discussed in Chapter 4. The significant amount of spallation of the outer oxide on cooling from the first thermal exposure is likely to reduce the stress in the residual haematite islands during cooling after the first thermal exposure. The stress reduction in the remaining adherent haematite causes the amount of visible spallation on cooling from subsequent thermal cycles to decrease. No evidence was observed for haematite reformation during the second thermal cycle and it is thought that longer exposure times were required to oxidise magnetite to haematite.

When exposure times remain the same between each cycle it is only when the environment is air-saturated that spallation occurs after the second exposure. Spallation was not observed for thermal cycles that were carried out in deoxygenated steam.

The Cr rich oxide at the base of the Fe-Cr-Ni spinel oxide, refined as $FeCr_2O_4$ and Cr_2O_3 in Chapter 4, dictated the oxidation behaviour in subsequent thermal cycles. When fully continuous, the growth of spinel oxide was reduced because of the protective nature of the Cr rich oxide. Where the Cr rich layer was not entirely continuous, a bimodal distribution was observed for the Fe-Cr-Ni spinel oxide thickness and more appropriate oxidation kinetics were suggested which were in good agreement with values available in the literature.

The STORME technique showed buckles formed on cooling. Without this technique it would be unknown whether the buckled oxide was present from the first cycle, if it had formed at temperature or during the cooling process. In cases where deoxygenated steam was used, the buckles formed were shown to be stable and the radius did not grow on cooling.

Chapter 6 Determination of the Critical Cr Concentration Required for Healing Layer Formation

6.1. Introduction

The method of vacuum annealing in order to evaporate elements from stainless steels was used previously by other researchers [112], [113]. It was suggested that the vaporisation of Cr using this technique is analogous to that of the selective oxidation of Cr [114] which results in the bulk alloy becoming depleted of Cr and as such creating a profile through the bulk. Cracking, spalling or erosion of the Cr containing oxides can therefore lead to a depleted metal surface exposed to the oxidising atmosphere. Section 2.3.7.4 of the literature review discussed the effects of Cr concentration on oxidation kinetics and it was shown that lower Cr containing alloys have faster growth kinetics of non-protective oxides. An exposed metal surface depleted of Cr can therefore form rapidly growing non-protective Fe rich oxides and can result in breakaway oxidation. The vacuum annealing technique therefore allowed controlled investigations into the surface concentration and Cr depletion profiles without the interference of complex oxides.

In this work, vacuum annealing was used to simulate the effect of Cr depletion on secondary spallation events and also to determine the critical Cr concentration required to form a healing layer.

This chapter presents and discusses the results obtained for both the vacuum annealing experiments and subsequent steam oxidation experiments for TP347H FG.

6.2. Vacuum annealing

6.2.1. Introduction

Vacuum annealing experiments were carried out for 16-1000 hours at 1273 K and 0.01 Pa to evaporate Cr from the surface of the alloy. The following section will discuss the results obtained for vacuum annealed specimens of TP347H FG through the use of SEM/ EDS analysis. The Cr concentration profiles were investigated and curve fitting was used to determine the diffusion coefficients and transfer coefficients of Cr evaporated from the pickled concave surface of the alloy.

6.2.2. Results

6.2.2.1. Observations

Prior to exposure, the alloy possessed a dull grey colour. After the samples were vacuum annealed at 1273 K the samples were shiny and light grey in colour.

Each specimen was weighed both before and after vacuum annealing to monitor the weight change. This was expected to correlate with the level of Cr evaporation observed. As can be seen from Figure 6-1 the weight loss generally increased with increasing annealing time, as would be expected. The weight change for 1000 hours was not as great as that seen for 500 and 750 hours which was not what would be expected. However, it is postulated that this anomaly was as a result of a change in vacuum furnace used. During the course of the EngD there was a change in the furnace used for vacuum annealing. Results discussed from this point refer to the

original furnace used as Furnace 1 and the furnace used for later testing as Furnace 2. Experiments carried out in Furnace 1 were performed by technical staff authorised to operate the equipment and so the furnace was not calibrated prior to testing. The cause for such a significant weight loss for 500 and 750 hours (Furnace 2) compared to 1000 hours (Furnace 1) could therefore be related to the temperature of the furnace. Either Furnace 1 was not at as high a temperature as the calibrated Furnace 2 and so the vapour pressure of alloying elements would be lower or the 1000 hour specimen was not in the hot zone of the furnace. Comparisons were carried out between samples exposed for 16 hours in both furnaces and this showed there was a greater mass loss in Furnace 2 compared to Furnace 1. Therefore, it is more likely that the cause in difference was probably the lower temperature in Furnace 1. Results from Furnace 1 for 16 hours vacuum annealing were discounted for further analysis. Longer times at temperature (1000 hours) were not able to be repeated in Furnace 2 due to time constraints and results from Furnace 1 experiments were analysed. It can also be noted from Figure 6-1 that the position of the sample within Furnace 2 also had an effect on the mass loss. The length of the hot zone of Furnace 2 was measured to be 4 cm. Two samples were inserted into the furnace at any one time using one alumina boat 6 cm in length. The difference in mass loss between two samples annealed at the same time therefore must be due to a temperature gradient along the tube. Samples with similar mass differences, for example 500 hours vacuum annealing, had a smaller temperature difference compared to samples exposed for 750 hours where there was a noticeable difference between the mass changes. The effect of temperature differences will be discussed in further detail in

Section 6.2.2.2. Also included in Figure 6-1 is the theoretical mass loss, M_t, based on Cr evaporation. This value will be discussed in further detail in Section 6.2.2.3.

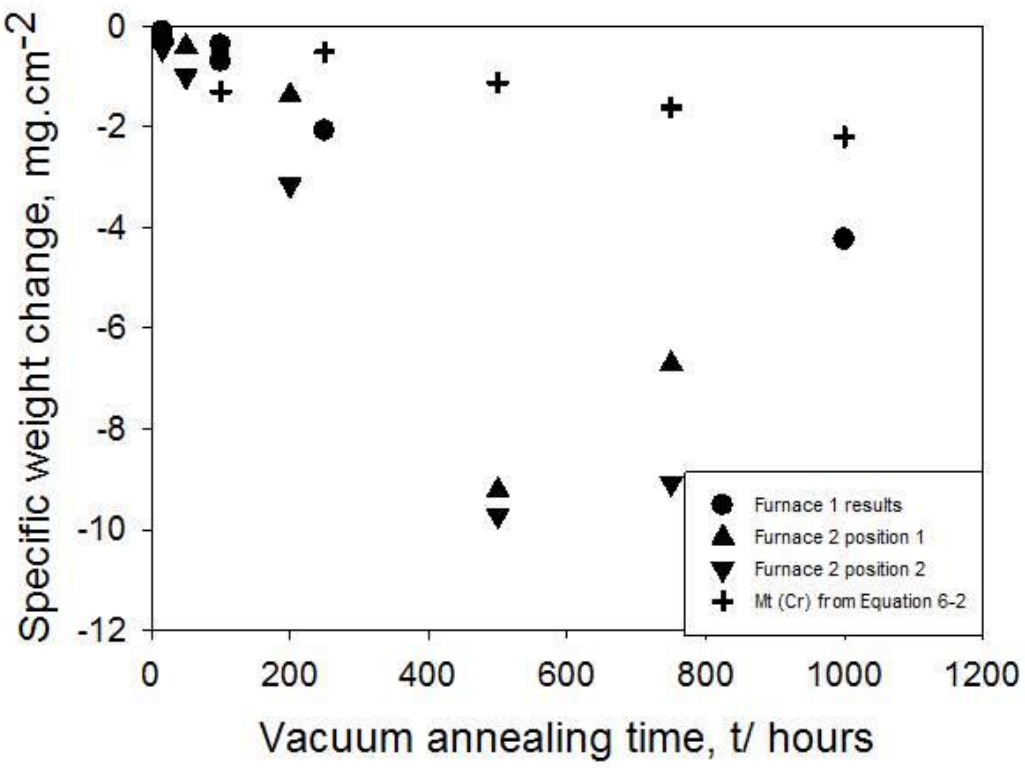

Figure 6-1 Specific weight change of TP347H FG as a function of annealing time.

6.2.2.2. Microscopy

The surface of the specimens was examined using SEM both prior to and post vacuum annealing. Figure 6-2 shows secondary electron (SE) micrographs of the surfaces of TP347H FG in the as-received condition (Figure 6-2 (a) and (b)), after 16 hours vacuum annealing at 1273 K and 0.01 Pa (Figure 6-2 (c) and (d)) and subsequent to 500 hours vacuum annealing with the same conditions (Figure 6-2 (e) and (f)).

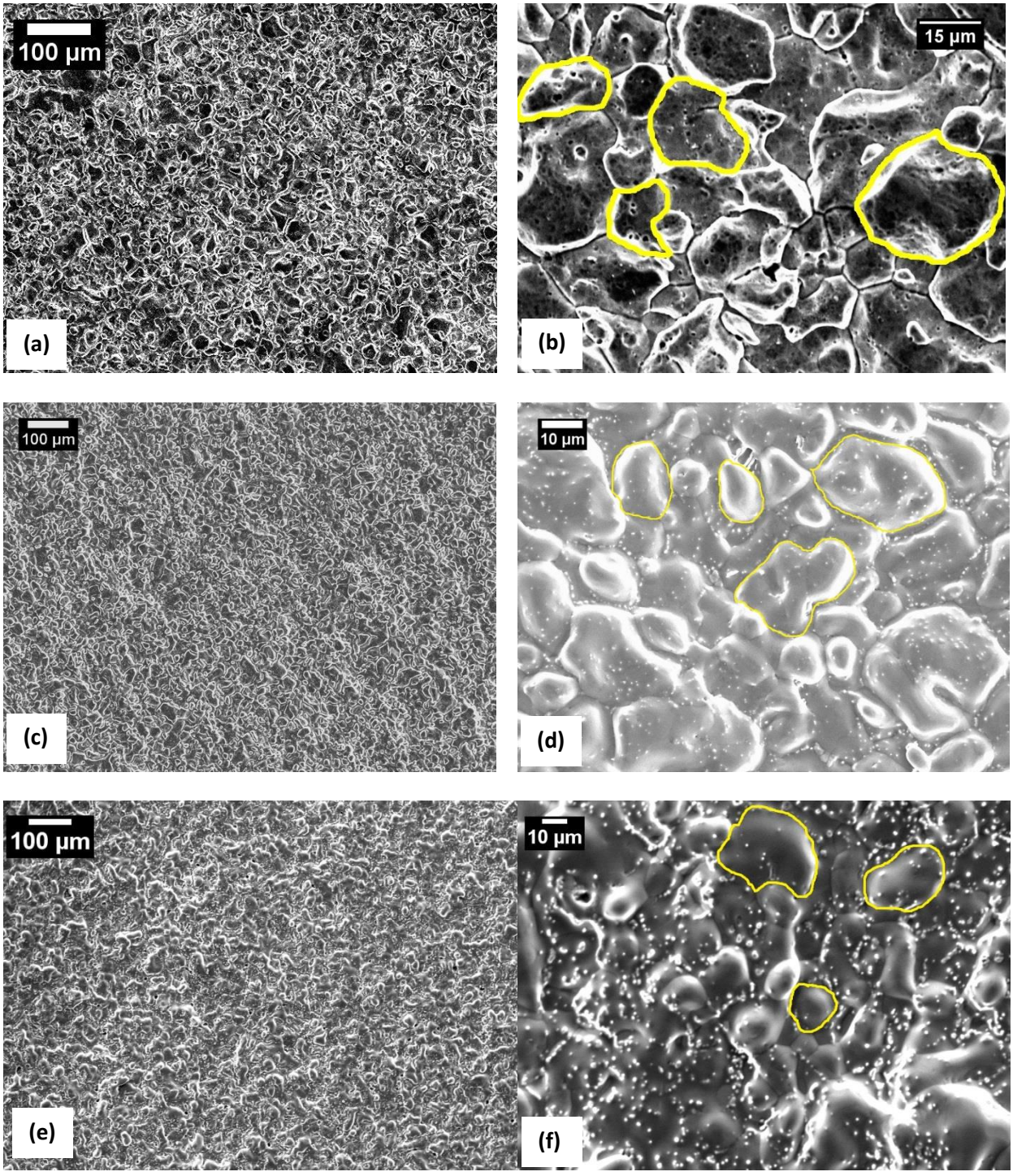

Figure 6-2 Secondary electron (SE) images of the surface of TP347H FG where (a) and (b) are pre annealed specimens, (c) and (d) subsequent to annealing for 16 hours at 1273 K and (e) and (f) are the surface subsequent to annealing for 500 hours at 1273 K.

Because the pickling process etches the grain boundaries, it was possible to see individual grains as highlighted by the yellow lines in the micrographs. These images indicated the surface was convoluted but uniform. Increasing vacuum annealing time

also made the definition of the grains less clear. Some speckling was observed once vacuum annealing had been carried out, Figure 6-2 (d) and (f). These speckles could be indicative of carbide formation.

Post vacuum annealing the specimens were sectioned and mounted for cross sectional analysis. An initial observation of the as-received alloy was the undulated surface profile. The second noticeable observation from the cross sections was grooving across the inner concave surface as shown in Figure 6-3(f). Overall the cross sections showed the alloy to be featureless. Finally, speckling was observed near the surface of the alloy subsequent to vacuum annealing.

Oxalic acid was used to etch and highlight the grain boundaries in the sample, Figure 6-4. This also revealed that the grooving observed during cross sectional analysis occurred at grain boundaries as shown in Figure 6-3(b-f) suggesting that Cr preferentially evaporates from grain boundaries rather than uniformly across the surface. Twinning was also observed for this sample as shown in Figure 6-4.

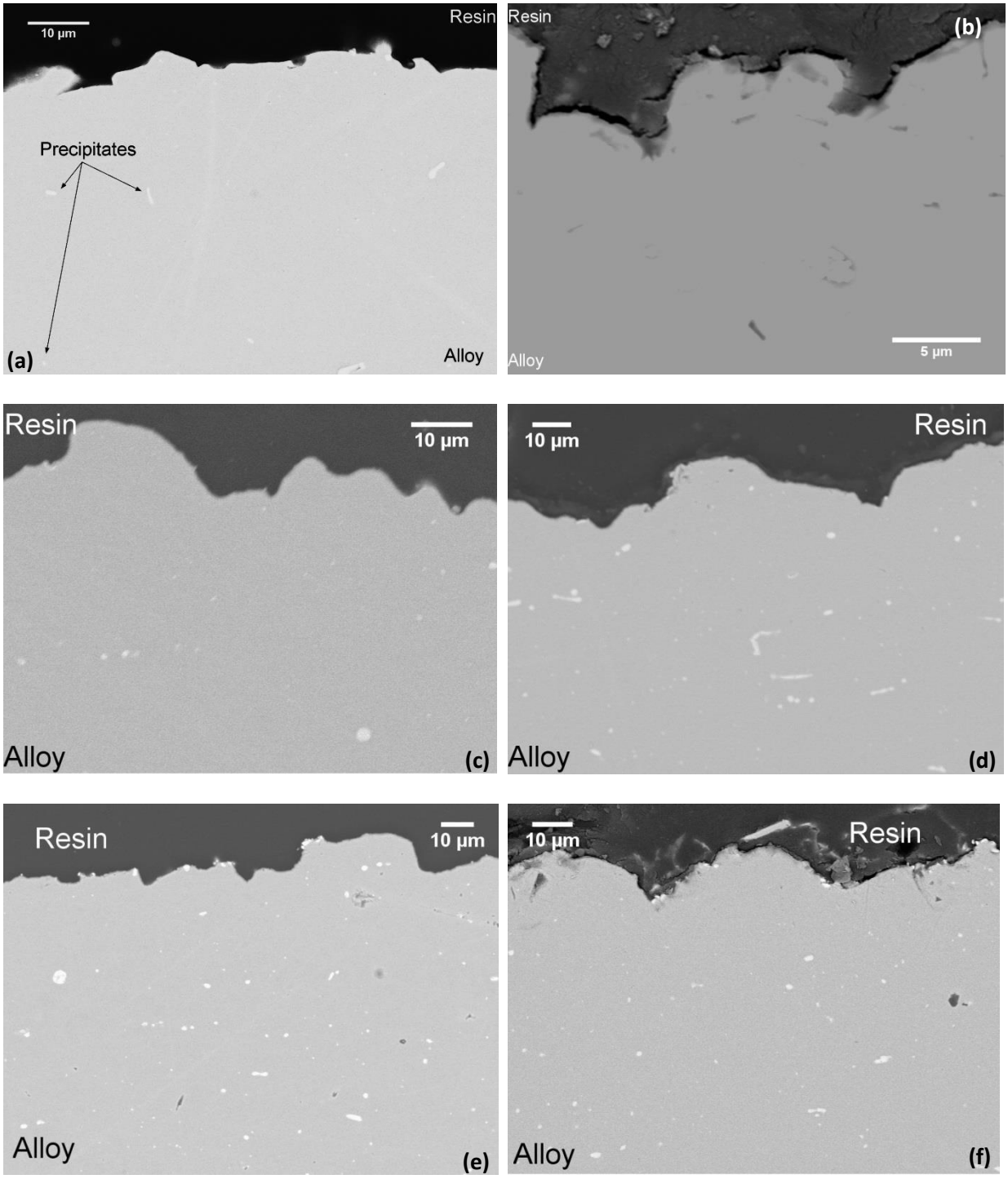

Figure 6-3 BSE micrographs of TP347H FG after vacuum annealing at 1273 K and 0.01 Pa for (a) 0 hours, (b) 16 hours, (c) 100 hours, (d) 500 hours, (e) 750 hours and (f) 1000 hours.

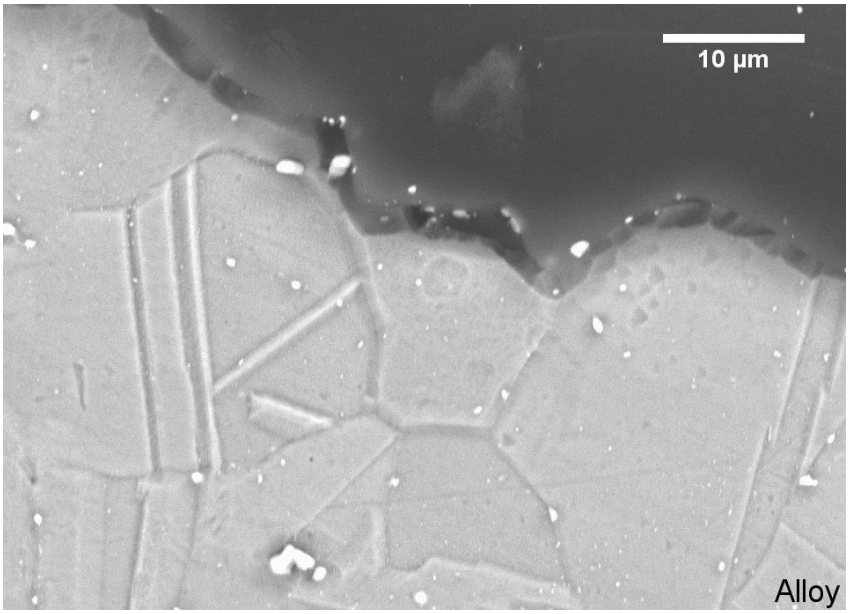

Figure 6-4 BSE cross sectional micrograph of TP347H FG vacuum annealed for 250 hours at 1273 K and 0.01 Pa indicating grain boundary grooving.

Grain size measurements were taken on back scattered electron micrographs of etched cross sections. The original grain size of the alloy surface is 6 µm and measurements showed an initial increase in the mean grain size with increasing vacuum annealing time, Figure 6-5, but an insignificant difference for longer annealing times. Also included in the figure are the standard deviations for the grain size measurements.

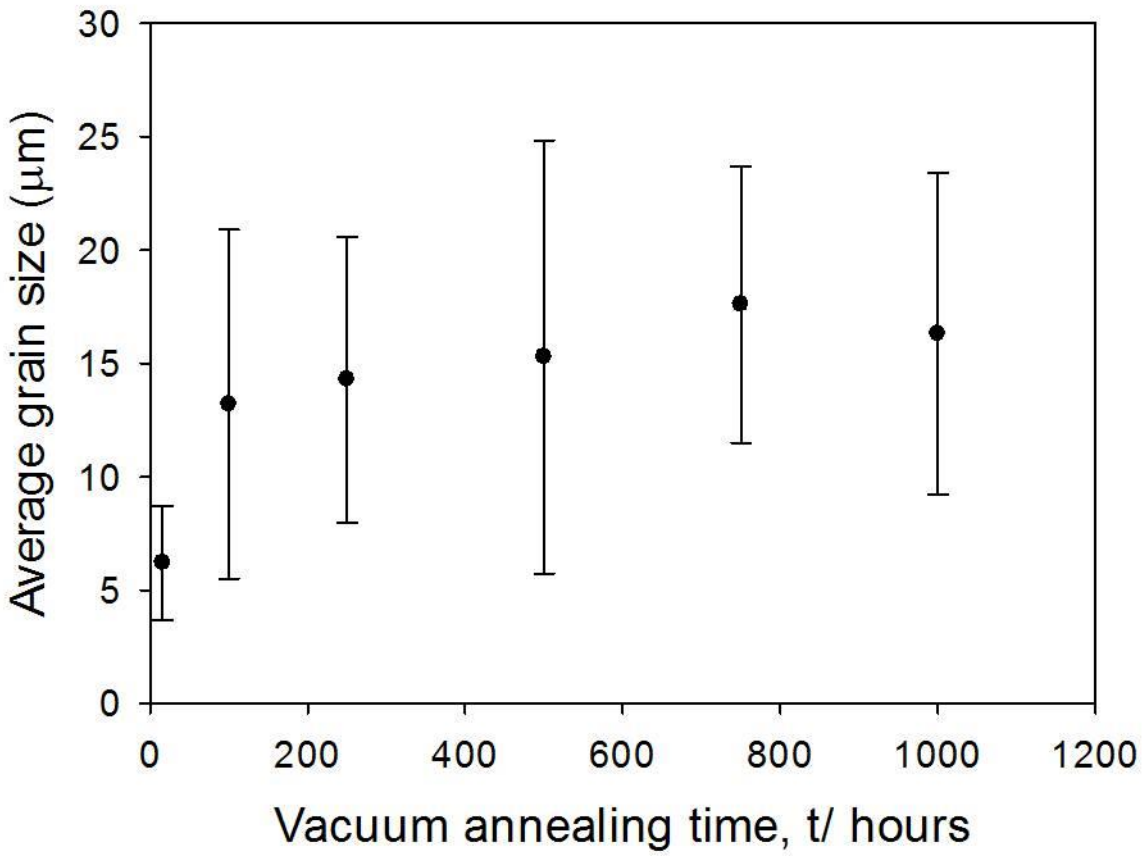

Figure 6-5 Grain size as a function of annealing time for TP347H FG vacuum annealed for 16-1000 hours at 1273 K and 0.01 Pa and the standard deviations.

Cr concentration profiles for each of the vacuum annealing times tested are shown in Figure 6-6. Concentration profiles were obtained perpendicular to the surface at the base of a groove and measurements will include a mixture of grain boundary and bulk concentration. These plots indicated the Cr concentration at the surface decreased with increasing vacuum annealing time and the gradient of the curves also increased with time at temperature. The concentration of Cr at the surface, C_S, as a function of annealing time is shown in Figure 6-7. The EDS point analysis of C_S was carried out as close to the surface as possible but the interaction volume was 3 µm therefore the concentration detected will have also included Cr further into the alloy.

The extent of Cr evaporation steadily decreased and despite the anomalous mass change behaviour for longer times at temperature the trend for C_S was as expected.

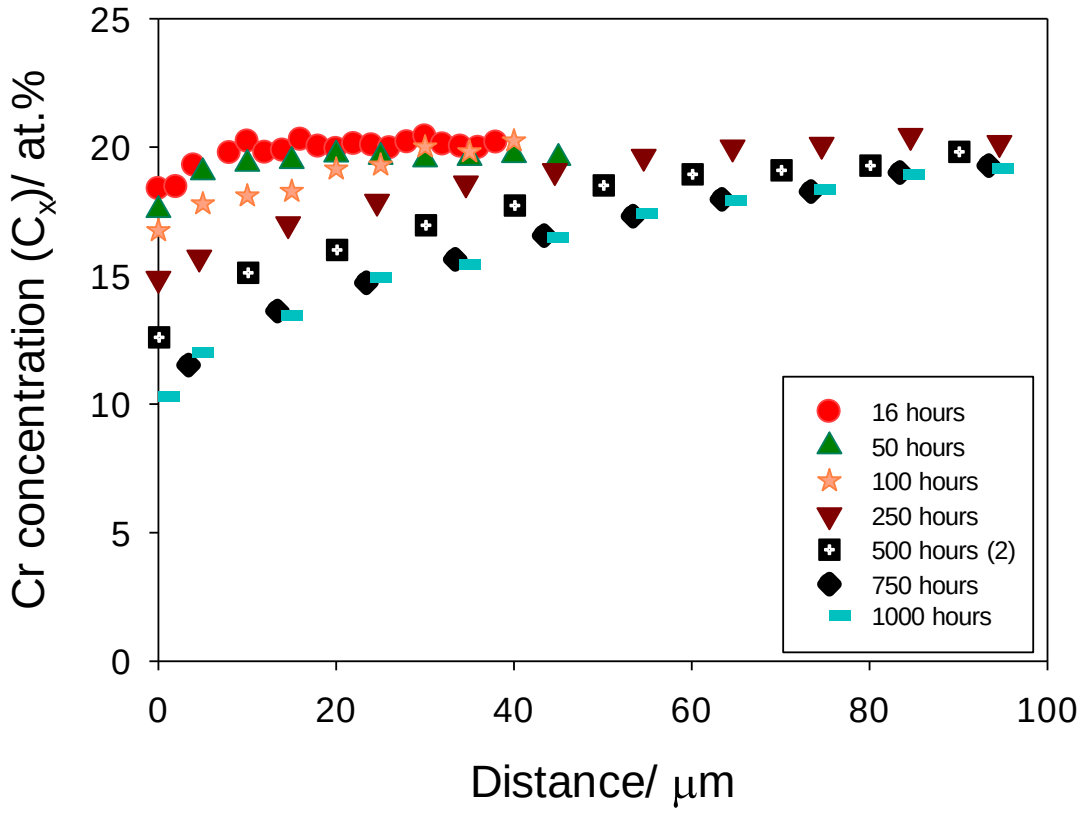

Figure 6-6 EDS plot of experimental Cr concentration as a function of distance from the surface for samples of TP347H FG vacuum annealed at 1273 K for 16-1000 hours in a vacuum of less than 0.01 Pa.

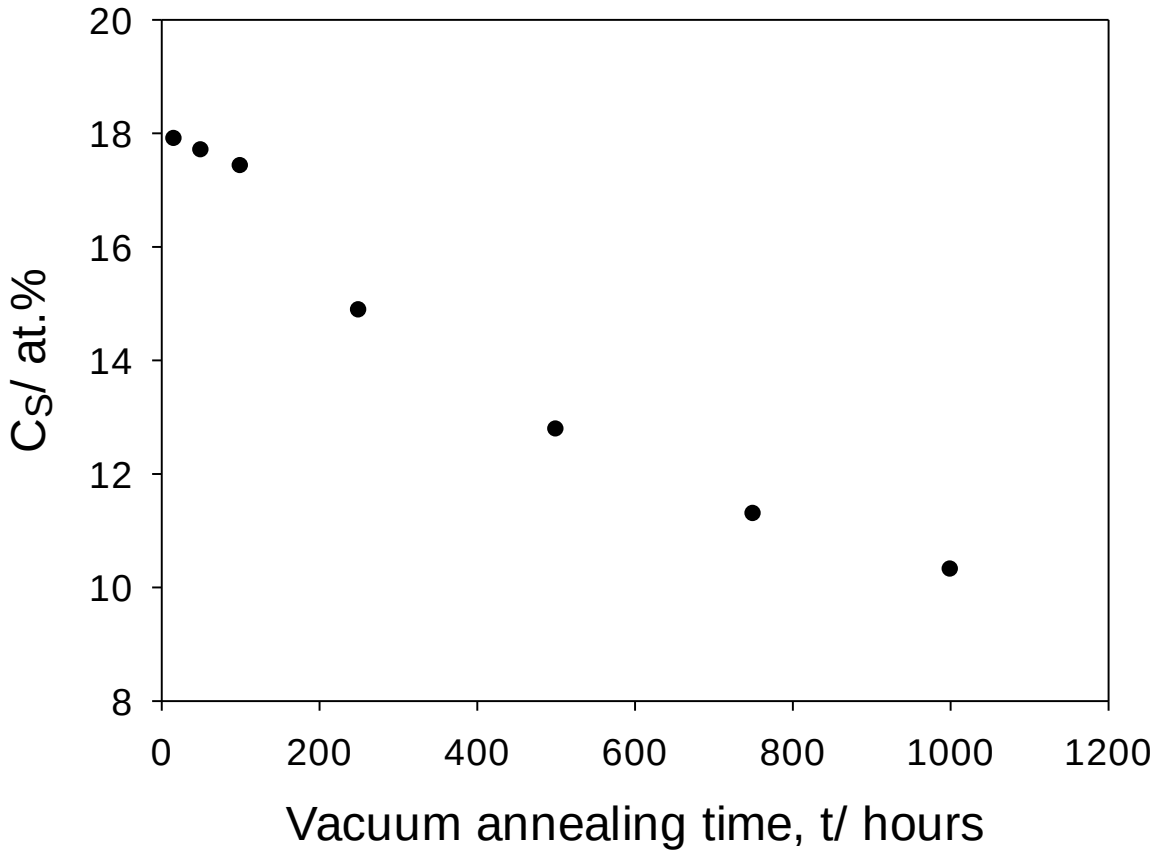

Figure 6-7 A plot of the surface Cr concentration, (Cs), as a function of vacuum annealing time, (t).

Mn depletion was also observed from cross sectional EDS analysis of the surface of specimens, Figure 6-8. There was a general trend of a depletion profile observed for Mn. Initial observations also indicated the surface concentration of Mn decreased with increasing annealing time. However, the error in the EDS measurements of ±0.2% suggests the difference in surface concentration is probably negligible. The interaction volume of 3 μm for EDS means there will also be some measurements from further into the alloy included in the reading. It is therefore more likely that the surface is completely depleted of Mn and the depth of depletion increases with increasing annealing time hence the decrease in the observed Mn concentration at the surface. The vapour pressure of Mn at 1253 K is 1.3 Pa compared to 13 Pa at

1293 K [173]. As was mentioned earlier in Section 6.2.2.1, it was believed that there was a temperature difference between Furnace 1 and Furnace 2. This significant increase in vapour pressure is postulated to be the cause for the greater mass change observed for 500 and 750 hours compared to 1000 hours vacuum annealing with a greater amount of Mn being evaporated from the alloy at the higher temperature.

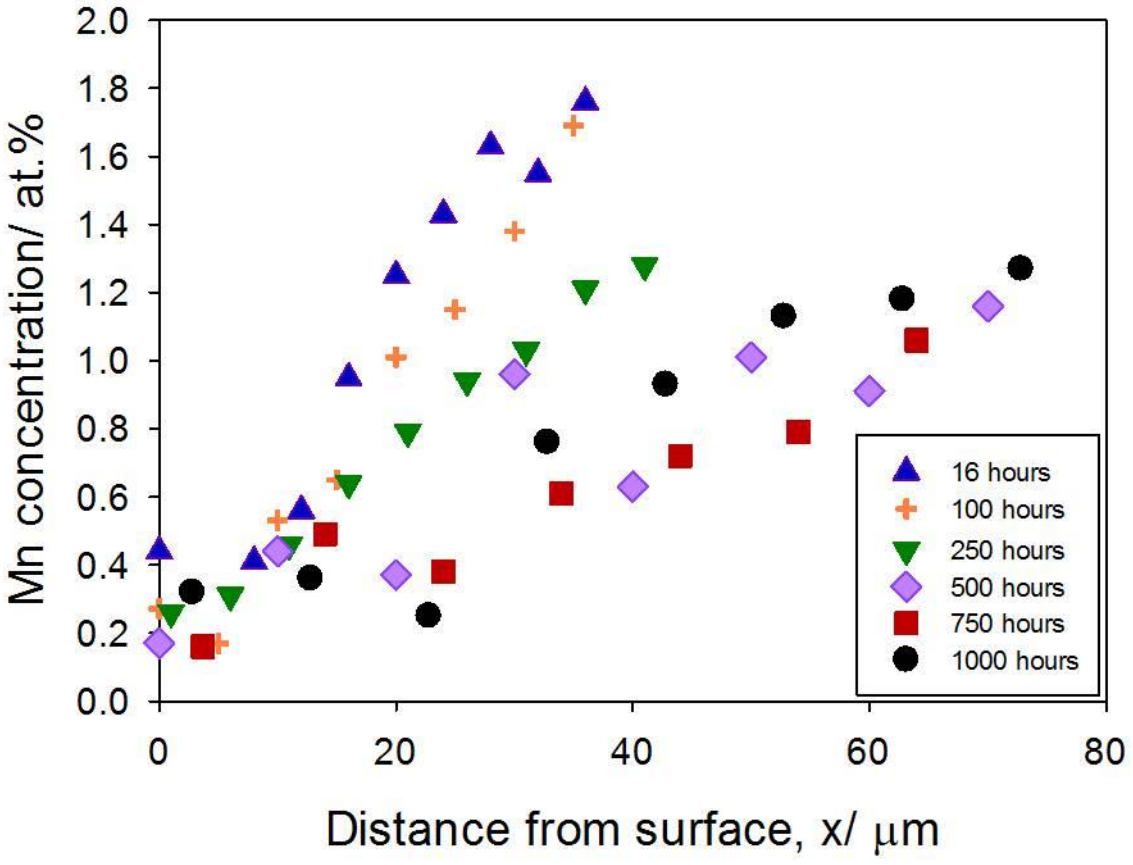

Figure 6-8 A plot of experimental Mn concentration as a function of distance from the surface for samples of TP347H FG vacuum annealed at 1273 K for 16-1000 hours in a vacuum of less than 0.01 Pa.

The depth of Cr depletion was also measured and is shown in Figure 6-9. Longer vacuum annealing times result in an increased depth of depletion as was previously shown in Figure 6-6.

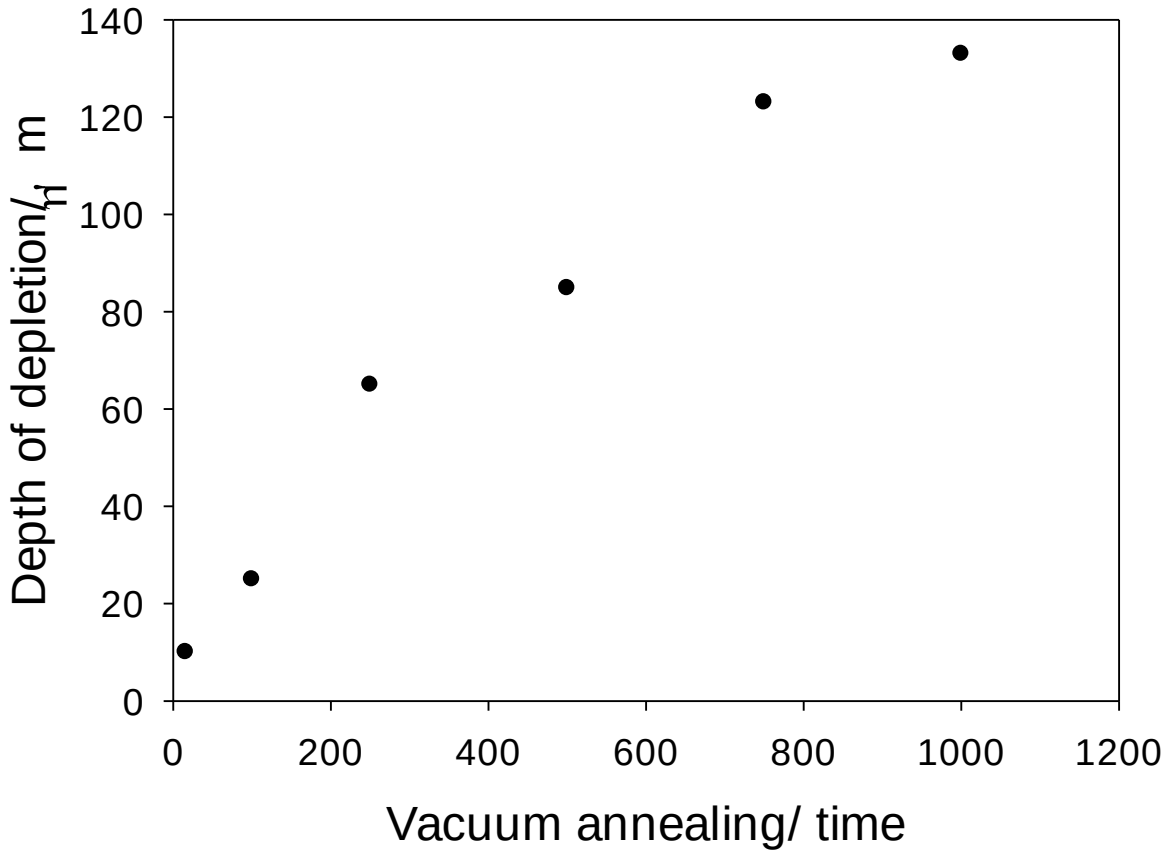

Figure 6-9 Depth of Cr depletion measured by EDS as a function of vacuum annealing time at 1273 K and less than 0.01 Pa.

A graph of depth of depletion squared as a function of time was plotted to determine whether the depth of depletion increased parabolically with time and is shown in Figure 6-10. The straight line produced suggests parabolic behaviour for depletion.

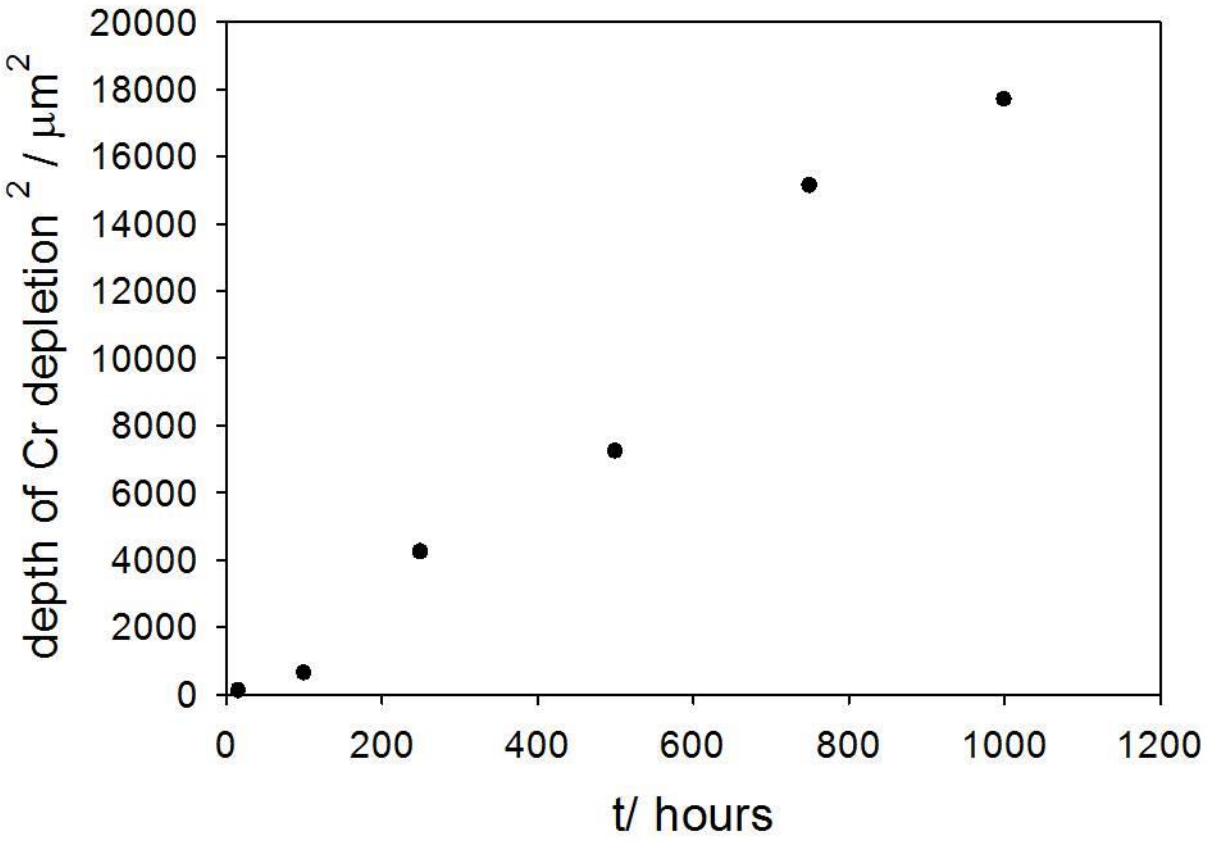

Figure 6-10 depth of depletion squared as a function of time squared.

Depletion profiles of the samples vacuum annealed for the same time in different furnaces revealed that the surface Cr concentration was less for Furnace 2 and that there was also a slightly greater depth of depletion, Figure 6-11. The cause for this variation in depletion profile is thought to be as a result of temperature variations between the furnaces resulting in a lower vapour pressure of alloying elements at lower temperature as already mentioned for Mn. The vapour pressure of Cr does not vary as significantly as Mn over a small temperature range, hence the evaporation rate of Cr does not vary but Mn does. This confirms the slightly lower temperature of Furnace 1 and hence confirms the results for mass change in Figure 6-1.

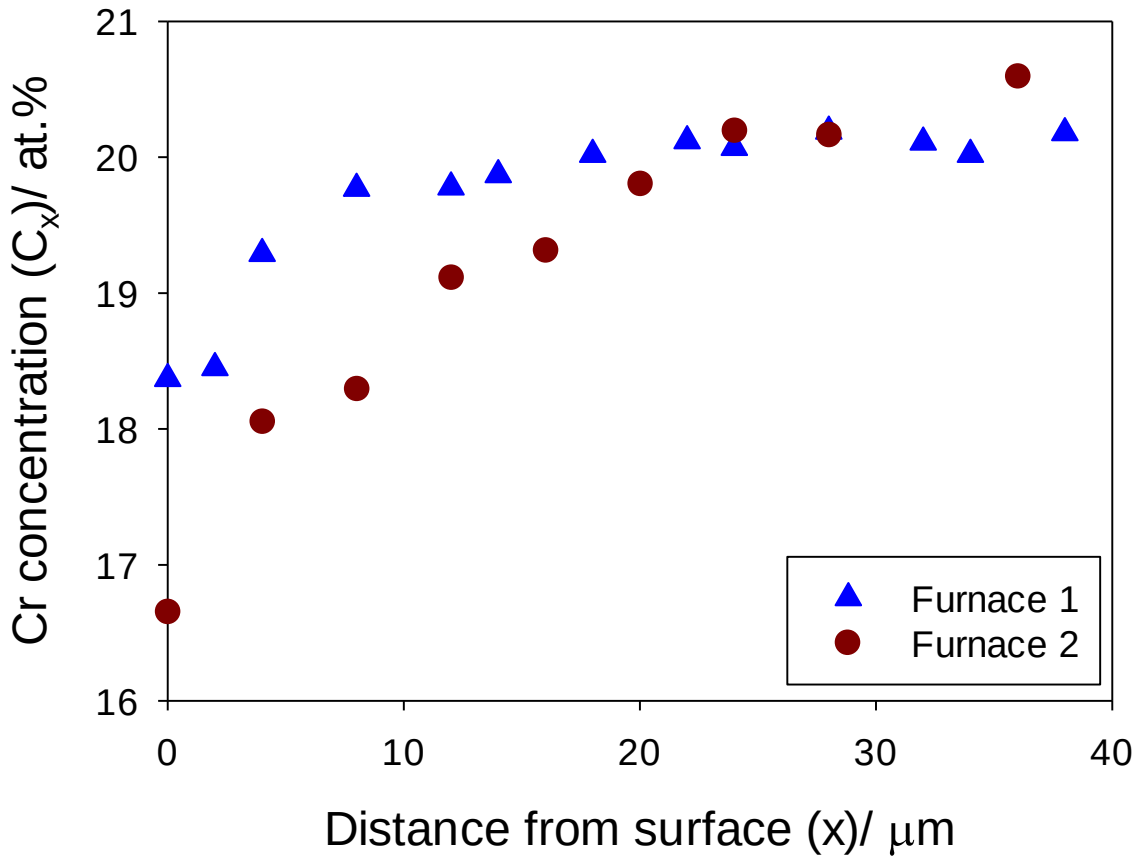

Figure 6-11 A comparison of Cr depletion profiles for samples vacuum annealed in different furnaces for 16 hours at 1273 K.

The Cr concentration profiles measured for two samples vacuum annealed at the same time in the same furnace were measured using EDS analysis and are shown in Figure 6-12. The hot zone in Furnace 2 was narrow and so there was some difference in the weight change between samples. Because of this slight difference in temperature the rate of diffusion between the two samples also varied and one sample had a smaller concentration of Cr at the surface compared to the other. This was most significant for the example shown in Figure 6-12 where two samples were vacuum annealed for 500 hours.

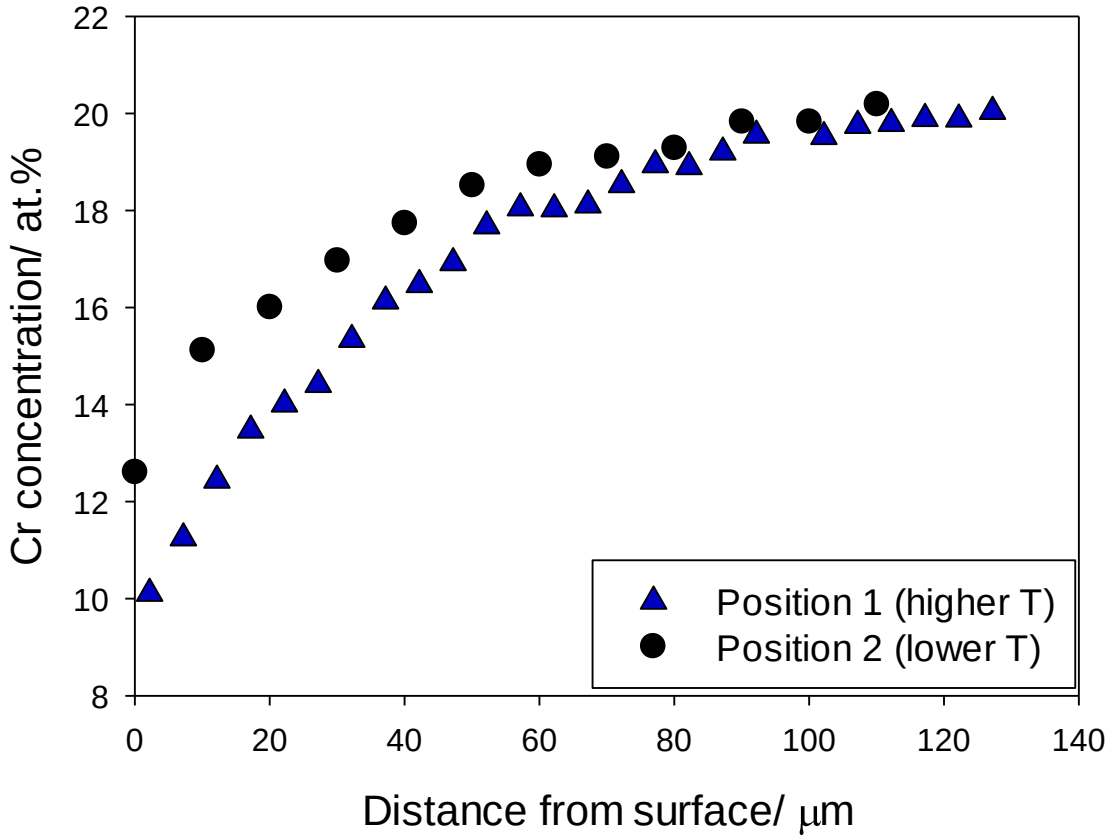

Figure 6-12 A comparison of two samples vacuum annealed in the same furnace at the same time for 500 hours at '1273 K'[3]).

Of the two samples shown in Figure 6-12, the sample in position 2 was used for further analysis based on C_S and mass change following the same trend as other samples used in this study.

6.2.2.3. Curve fitting

The Cr concentration profiles shown in Figure 6-6 were determined using SEM/ EDS analysis of cross sections as shown previously. Previous work using vacuum annealing experiments to evaporate Cr from the surface of an alloy assumed the flux of Cr ions leaving the metal surface was proportional to the concentration of Cr in

[3] '1273 K' is the temperature the furnace was set to once calibrated but the hot zone was narrow and so there was a temperature difference between the two samples in the boat.

equilibrium with the vapour pressure, C_0, minus the concentration of Cr at the surface of the alloy, C_S, i.e. $D \alpha (C_0 - C_S)$ [112], [113]:

$$-D\left(\frac{dc}{dx}\right) = \alpha(C_0 - C_S) \quad \text{Equation 6-1}$$

where D is diffusion coefficient of Cr in the alloy, $m^2.s^{-1}$, C is the concentration, at.%, x is the distance into the alloy where the surface is 0, m, α is the transfer coefficient of Cr leaving the surface, $m.s^{-1}$ and C_0 is the concentration in equilibrium with the vapour pressure, at.%. The transfer coefficient defines the evaporative mass loss.

The variation of Cr within the metal was given by Crank [116] as:

$$\frac{C_B - C}{C_B - C_0} = \boldsymbol{erfc}\left\{\frac{x}{2\sqrt{Dt}}\right\} - \boldsymbol{exp}\{\boldsymbol{hx} + \boldsymbol{h^2 Dt}\}.\boldsymbol{erfc}\left\{\frac{x}{2\sqrt{Dt}} + \boldsymbol{h}\sqrt{\boldsymbol{Dt}}\right\} \quad \text{Equation 6-2}$$

where C_B is the bulk concentration of Cr, 20.1 at.%, erfc is the error function complement, t is time, s, and h=α/D.

Since $C_0 << C_B, C_S$, Appendix A, Equation 6-2 can be rearranged to give:

$$\boldsymbol{C_x = C_B}\left[\boldsymbol{1 - erfc}\left\{\frac{\boldsymbol{x}}{\boldsymbol{2\sqrt{Dt}}}\right\} - \boldsymbol{exp}\{\boldsymbol{hx} + \boldsymbol{h^2 Dt}\}\,.\boldsymbol{erfc}\left\{\frac{\boldsymbol{x}}{\boldsymbol{2\sqrt{Dt}}} + \boldsymbol{h}\sqrt{\boldsymbol{Dt}}\right\}\right] \quad \text{Equation 6-3}$$

where C_x is the concentration of Cr, at.%, at a distance, x, away from the surface, m. This Equation is the solution to a specific diffusion controlled process.

The concentration profiles obtained were shown to fit Equation 6-3 which was then used to fit a curve to the data obtained from the EDS analysis to give values of the diffusion coefficient, D, and the transfer coefficient, α.

The number of Cr ions, M_t, leaving the sample can then be calculated using the following equation:

$$M_t = \frac{C_B}{h}\left\{1 - \frac{2}{\sqrt{\pi}} h\sqrt{Dt} - exp(\, h^2 Dt)\; erfc\left(h\sqrt{Dt}\right)\right\} \qquad \text{Equation 6-4}$$

The MATLAB script used for determining the values of h and D is attached in Appendix C and the results obtained from the curve fitting are shown in Table 6-1.

Table 6-1 Results obtained from curve fitting.

Vacuum annealing time, t (s)	C_s (at.%)	$\frac{C_S}{C_B}$ (experimental)	$\frac{C_S}{C_B}$ (curve fit)	D ($m^2\ s^{-1}$)	α = h/D ($m\ s^{-1}$)	M_t ($mg\ cm^{-2}$)
57,600	17.9	0.90	0.90	$4.20x10^{-15}$	$2.78x10^{-11}$	0.16
360,000	17.4	0.84	0.88	$1.43x10^{-15}$	$7.65x10^{-12}$	1.31
900,000	14.9	0.74	0.74	$8.40x10^{-16}$	$8.72x10^{-12}$	0.53
1,800,000	12.8	0.64	0.63	$5.33x10^{-16}$	$8.25x10^{-12}$	1.13
2,700,000	11.3	0.56	0.57	$4.53x10^{-16}$	$7.70x10^{-12}$	1.62
3,600,000	10.3	0.51	0.46	$4.31x10^{-16}$	$9.72x10^{-12}$	2.20

Plots for diffusion coefficient and transfer coefficient as a function of annealing time are given in Figure 6-13 and Figure 6-14, respectively. Diffusion coefficients were shown to decrease with increasing vacuum annealing times from 16 – 500 hours but remain relatively constant thereafter.

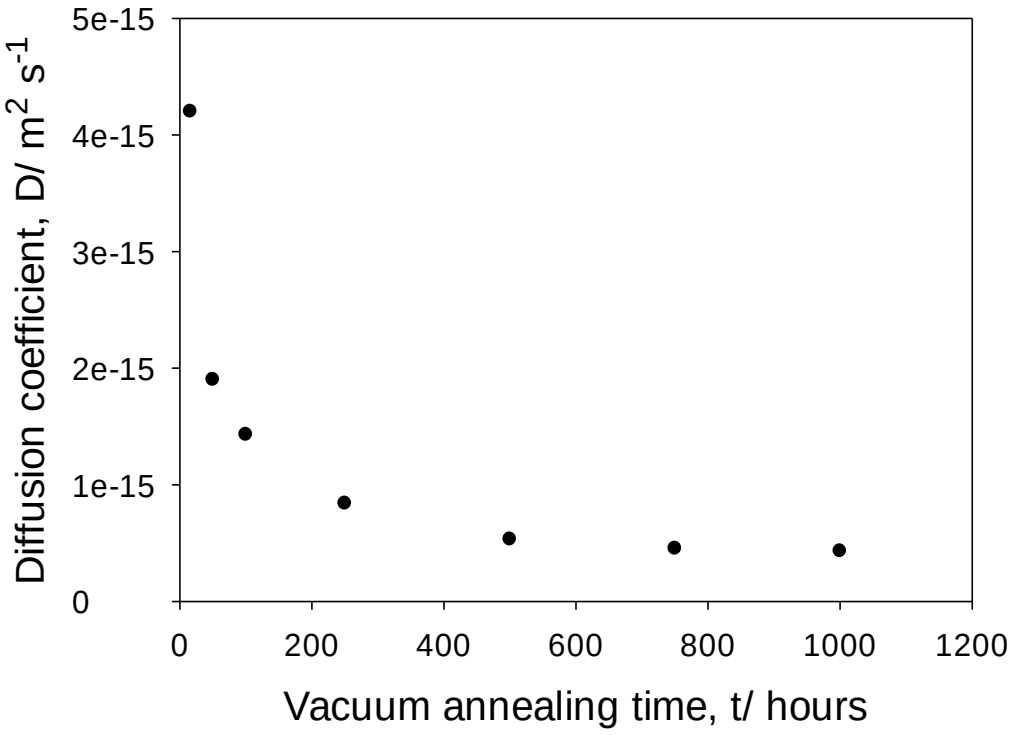

Figure 6-13 Cr diffusion coefficients calculated for TP347H FG during vacuum annealing at 1273 K and 0.01 Pa for 16-1000 hours.

Since Cr depletion profiles were obtained from a mixture of the grain boundary and the grain bulk, as mentioned earlier, it is more appropriate to calculate an effective diffusion coefficient that is a combination of both lattice and grain boundary diffusion parameters. The lattice diffusion coefficient, D_L, can be calculated using the following equation [174]:

$$D_L = D_{L,0} exp\left(\frac{Q_L}{RT}\right) \quad \text{Equation 6-5}$$

where $D_{L,0}$ is the frequency factor, $m^2.s^{-1}$, Q_L is the activation energy, $J.mol^{-1}$, R is the gas constant, $J.K^{-1}.mol^{-1}$ and T is temperature, K.

Grain boundary diffusion coefficients, δD_g, can be calculated using Equation 6-6 [174]:

$$\delta D_g = \delta D_{B,_0} exp\left(\frac{-Q_B}{RT}\right) \quad \text{Equation 6-6}$$

where $\delta D_{B,0}$ is the frequency factor, $m^2.s^{-1}$, Q_B is the activation energy, $J.mol^{-1}$, R is the gas constant, $J.K^{-1}.mol^{-1}$, and T is temperature, K.

The effective diffusion coefficient, D_{eff}, can then be calculated from the following equation:

$$D_{eff} = D_L + \left[\frac{2(\delta D_g)}{g}\right] \quad \text{Equation 6-7}$$

where g is grain size, m.

Lattice diffusion and grain boundary diffusion parameters were taken from the literature for 20Cr25NiNb stainless steel which has a similar composition to TP347H FG and were used to calculate the individual contribution of the bulk and grain boundaries, Table 6-2 [174].

Table 6-2 Cr lattice and grain boundary diffusion parameters for 20Cr25NiNb stainless steel [174].

Cr lattice diffusion parameters for 20Cr25NiNb stainless steel		Cr grain boundary diffusion parameters for 20Cr25NiNb stainless steel	
Q_L/ kcal mol^{-1}	D_{L0}/ $cm^2.s^{-1}$	Q_B/ kcal mol^{-1}	δD_B/ $cm^2.s^{-1}$
58.8 ± 3.7	0.19	44.7 ± 2.8	2.5×10^{-7}

D_L and δD_g were calculated to be 1.52×10^{-11} $cm^2.s^{-1}$ and 5.29×10^{-15} $cm^3.s^{-1}$, respectively, at 1273 K. Using the grain size measured earlier it was then possible to calculate D_{eff} for each of the vacuum annealing times and the results are shown in

Table 6-3. The results obtained indicate that the effective diffusion coefficient, i.e. the combination of bulk and grain boundary diffusion, makes a contribution but cannot fully explain the variation with annealing time of the calculated diffusion coefficient.

Table 6-3 Effective diffusion coefficients calculated using the data from Smith and Gibbs.

Vacuum annealing time, t/ hours (s)	D from curve fit/ $m^2.s^{-1}$	Grain size/ μm	D_{eff}/ $m^2.s^{-1}$
16 (57,600)	4.20×10^{-15}	6.2±2.5	3.23×10^{-15}
100 (360,000)	1.43×10^{-15}	13.2±7.7	2.32×10^{-15}
250 (900,000)	8.40×10^{-15}	14.3±6.3	2.26×10^{-15}
500 (1,800,000)	5.33×10^{-16}	15.3±9.6	2.21×10^{-15}
750 (2,700,000)	4.53×10^{-16}	17.6±6.1	2.12×10^{-15}
1000 (3,600,000)	4.31×10^{-16}	16.3±7.1	2.17×10^{-15}

The transfer coefficient can be defined as the amount of Cr evaporating from the surface of the alloy and was shown to decrease rapidly initially with increasing annealing time, Figure 6-14. This was similar to the results observed by Lobb and Evans [113] for 20Cr-25Ni-Nb stabilised stainless steel vacuum annealed under the same conditions. Equation 6-1 indicates the proportionality of the transfer coefficient, α, to the flux of Cr ions leaving the metal surface, D. Therefore, for lower annealing times of 16 hours where the flux of Cr is higher, the transfer coefficient is also higher. Hence the rapid initial decrease in α observed.

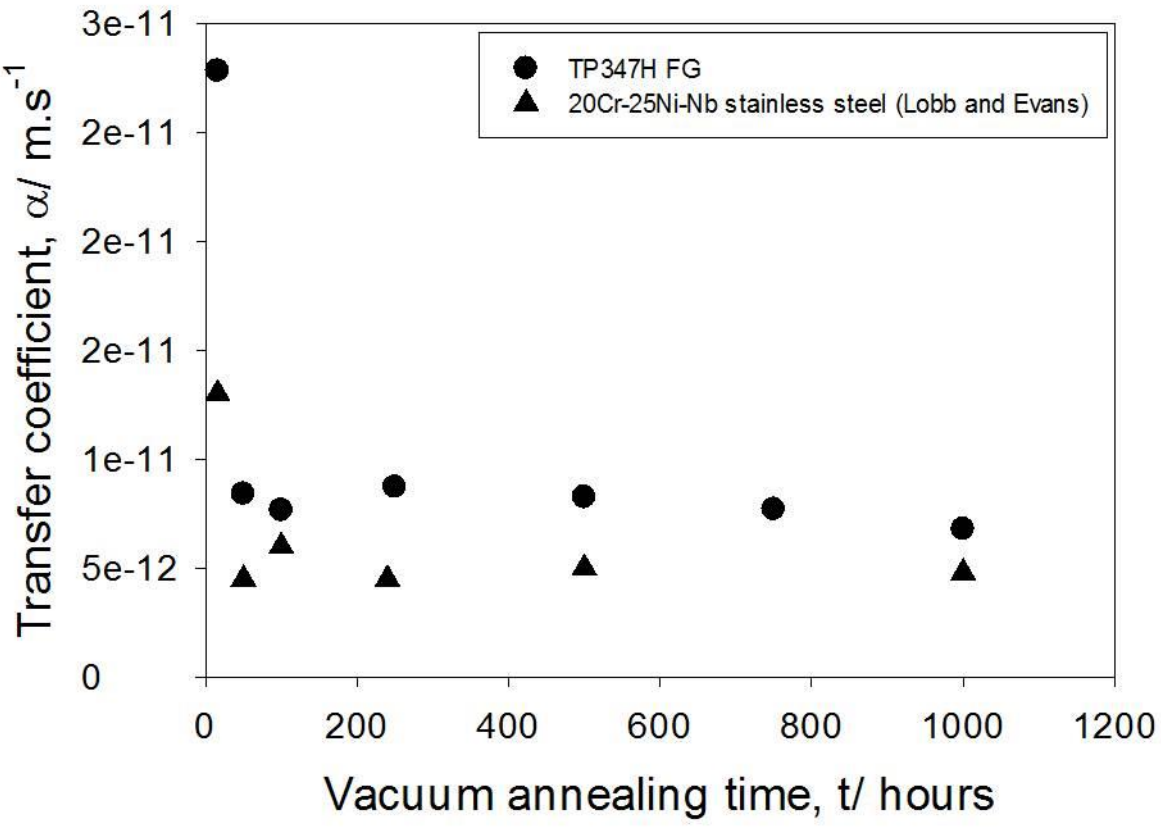

Figure 6-14 Transfer coefficient of Cr calculated for TP347H FG vacuum annealed at 1273 K and 0.01 Pa for 16-1000 hours.

Figure 6-15 shows the concentration profile obtained both experimentally and through curve fitting using MATLAB for a sample of TP347H FG vacuum annealed for 250 hours at 1273 K and 0.01 Pa. There is good agreement between the two sets of data where the curve had a mean square error of 0.0319.

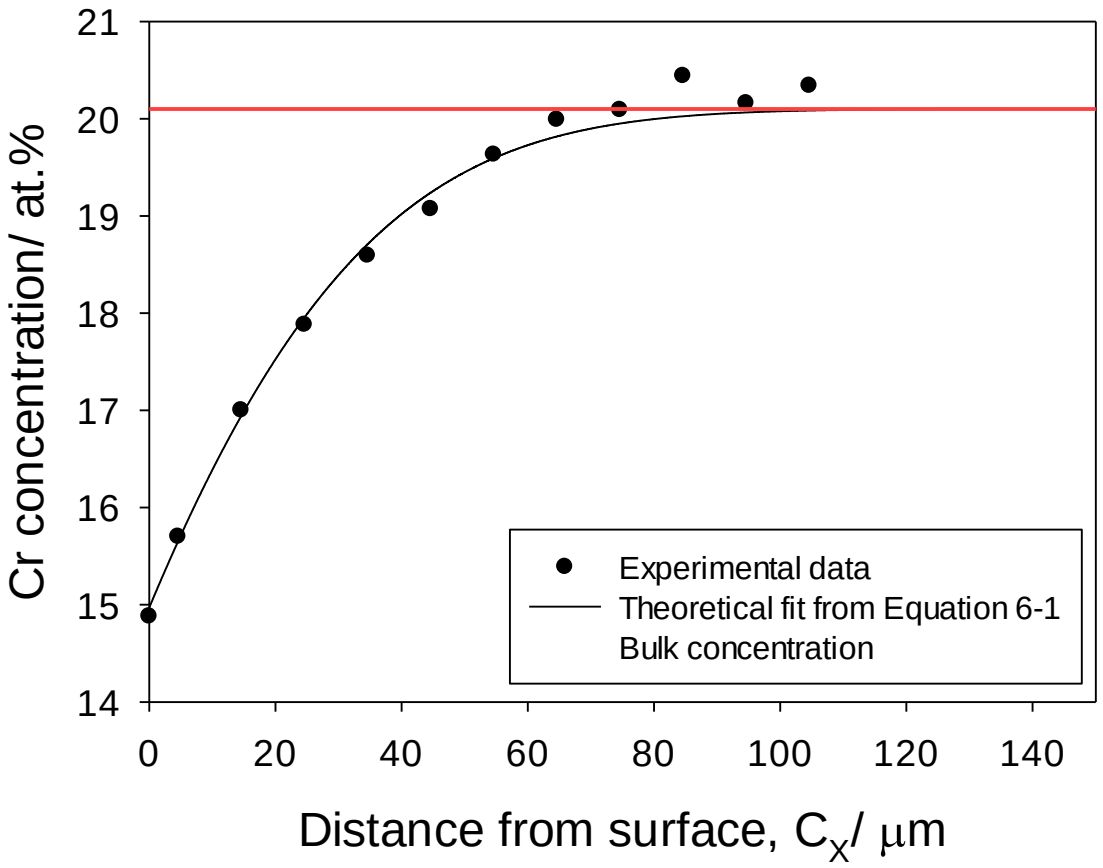

Figure 6-15 Cr concentration profile for a sample of TP347H FG vacuum annealed for 250 hours at 1273 K and 0.01 Pa.

The diffusion coefficients calculated for this work using the curve fitting in MATLAB were compared to those found in the literature, Figure 6-16. The diffusion coefficients obtained here showed a general decrease with vacuum annealing time. Work shown by Lobb and Evans for 20Cr-25Ni-Nb stabilised stainless steel [113] however shows that the diffusion coefficient was reasonably constant with only a slight decrease with increasing annealing time. Smith and Hales also showed there to be a constant diffusion coefficient for other austenitic stainless steels with similar composition to the alloy studied here [174]. The effective diffusion coefficient calculated in this work, using Smith and Gibbs' data on 20Cr25NiNb steel [174] are also included in the plot and are shown to be higher than those from the literature for other alloys. The results

presented for 20Cr-25Ni-Nb stabilised stainless steel by Lobb and Evans [113] indicated a significant change in grain size increasing from 6 μm to approximately 130 μm after just 250 hours. Such a significant change was not observed for TP347H FG in this work which could be the reason for the higher diffusion coefficients observed.

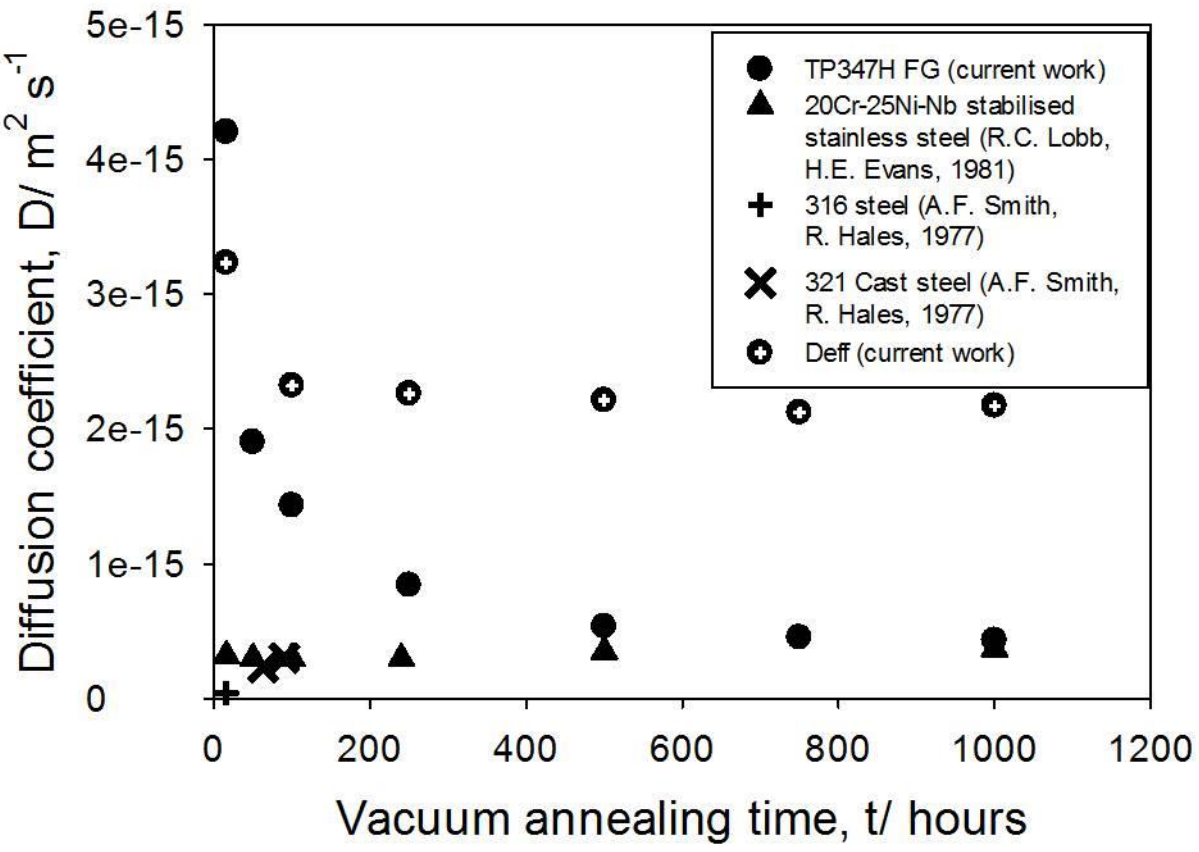

Figure 6-16 Comparison of diffusion coefficients obtained for Cr from this work in TP347H FG at 1273 K, 20Cr-25Ni-Nb stabilised stainless steel at 1273 K, 321 cast steel and 316 steel with a 180 grit surface finish.

A plot of the surface Cr concentration/ bulk Cr concentration (C_S/ C_B) as a function of annealing time is shown in Figure 6-17. Overall, there was a general decrease in the ratio C_S:C_B with increasing annealing time. There was a reasonable fit between the experimental data obtained and the results produced from curve fitting using

Equation 6-1. There was a slight discrepancy between the experimental values and curve fit values obtained for 50 and 100 hours and in both cases the curve fit values were higher than the experimental values observed.

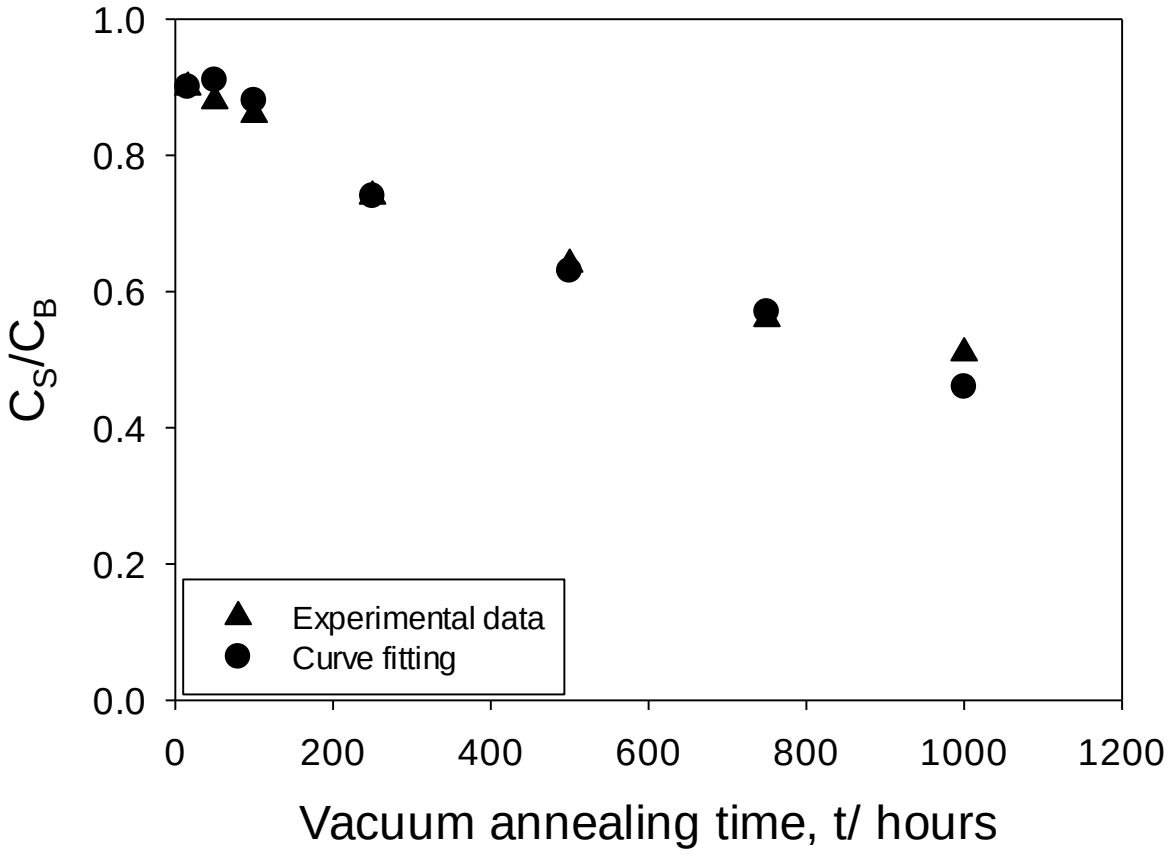

Figure 6-17 A plot of surface Cr concentration/ bulk concentration (C_s/C_B) as a function of vacuum annealing time (t) for experimentally measured EDS values and curve fitting values of C_s obtained from MATLAB curve fitting function.

6.2.3. Discussion

The theory outlined by Lobb and Evans [113] and used in this work assumed the transfer coefficient, α, to be invariant with time. Results from the Lobb and Evans paper however showed some discrepancy between the theory and experimental data which showed a decrease in α with increasing annealing time and it was suggested

that the theory was deficient in its ability to accurately model the evaporation process. However, it was concluded in that work by Lobb and Evans that since the theory was able to determine overall trends, the observation must be real and not a deficiency in the ability of the model. In this work α was also shown to decrease with increasing annealing time with a significantly higher transfer coefficient for 16 hours compared to longer annealing times similar to that seen in [113]. The reason for the higher value observed could be as a result of the number of grain boundaries. It is suggested in this work that grain boundary grooving was as a result of preferential Cr evaporation from grain boundaries. If grain size increased with increasing annealing time there would be fewer evaporation sites hence a decrease in the transfer coefficient. As was also mentioned earlier, the grain size increased initially but does not vary greatly for longer annealing times unlike 20Cr25NiNb stabilised stainless steel where the grain size increased by an order of magnitude. Hence the transfer coefficient value being higher for shorter annealing times. C_0 can be described as the Cr concentration in equilibrium with the vapour pressure and as was shown in Equation 6-1 is proportional to the flux of Cr ions leaving the metal surface when the surface concentration has been subtracted. For short term vacuum annealing times, the system will not be in equilibrium. There will therefore be a greater amount of Cr at the surface of the alloy than in the gas and so the transfer coefficient will be higher for these shorter annealing times where the flux is higher. Alternatively, the decrease in transfer coefficient with increasing annealing time could also be a result of the development of a zone at the surface of the alloy. Cross sectional examination indicated speckling subsequent to vacuum annealing possibly indicative of a phase transformation. Results from this work have shown there were compositional

changes at the surface of the alloy when it had undergone vacuum annealing. However, West *et al*. [169] predicted the phases present for 347H FG stainless steel at various temperatures using Thermo-calc software and showed that between 1023 and 1523 K only an austenitic phase would be expected. Therefore, no phase changes would be expected during vacuum annealing at 1273 K. It is therefore more likely that the speckling observed during cross sectional examination was as a result of carbide formation.

Table 6-4 Diffusion coefficients for various alloys.

Alloy	Diffusion coefficient, $m^2\ s^{-1}$	Temperature, K	Method	Reference
20Cr25NiNb	$1.5x10^{-15}$	1273	Tracer	[168]
316	$1.9x10^{-16}$	1273	Tracer	[170]
1-27Cr	$2.8x10^{-16}$	1273	Interdiffusion	[171]
316 and 321	$3.0x10^{-16}$	1273	Interdiffusion	[107]
TP347H FG	$4.3x10^{-16}$	1273	Curve fit	Thesis
α-Fe	$4.2x10^{-14}$	1273		[172]
γ-Fe	$3.7x10^{-16}$	1273		[172]

There is satisfactory agreement between the diffusion coefficient for other austenitic alloys with similar composition to TP347H FG reported by Smith and Gibbs [112] of $1.50 \times 10^{-15}\ m^2\ s^{-1}$ and the range of effective diffusion coefficients found for this work, $2.17 \times 10^{-15} – 3.23 \times 10^{-15}\ m^2\ s^{-1}$.

Theoretical weight change calculated from Equation 6-2 underestimated the experimental values, shown in Figure 6-1, and for times greater than 250 hours the

difference was significant. However, the calculated values only took Cr evaporation into consideration but Mn was also observed to be depleted at the surface. Grain boundary grooving was also not taken into consideration in this calculation. A mass contribution from the grooving was calculated for each vacuum anneal time tested by taking the depth of the groove and assuming the same width at the surface to give a metal volume loss for the length of a grain boundary. The density of the sample was calculated and the grain size of each specimen measured, as shown earlier, and since density = mass / volume the mass contribution could then be calculated, shown in Table 6-5. Although there was an increase in the mass contribution from grain boundary grooving, for longer vacuum annealing times the total calculated mass contribution was still not equal to the gravimetric weight loss measured experimentally. It is assumed that Mn will have some contribution to the mass loss observed but since it is present in such a small amount it is unlikely that it will account for the significant difference observed.

Table 6-5 Mass contributions

Vacuum annealing time, t (hours)	Gravimetric weight loss (mg cm^{-2})	M_t (mg cm^{-2})	Grain boundary grooving contribution (mg cm^{-2})
16	0.11	0.16	0.74
100	0.38	1.31	0.37
250	2.1	0.53	0.60
500	9.2	1.1	0.01
750	9.1	1.62	0.01
1000	4.2	2.20	0.02

6.2.4. Concluding remarks

Evaporation of Cr and Mn was observed when TP347H FG was vacuum annealed at 0.01 Pa and 1273 K for 16-1000 hours. Crank's mathematical approach to diffusion outlined in this section of the chapter [116] showed that the diffusion and transfer coefficient of Cr could be reasonably approximated with effective diffusion coefficients in the range of $2.17x10^{-15} – 3.23x10^{-15}$ $m^2.s^{-1}$.

Mass loss was not successfully predicted for any of the times tested and it is thought that other minor alloying elements such as Mn will contribute to the overall value.

A range of samples were successfully produced with a range of Cr surface concentrations to be used for subsequent steam oxidation experiments.

6.3. The Effect of Cr Concentration on the Oxidation Behaviour in Steam

6.3.1. The effect of surface Cr concentration on oxidation and spallation behaviour

6.3.1.1. Introduction

Cr evaporation through vacuum annealing is thought to be analogous to the selective oxidation of Cr. Subsequent steam oxidation of Cr depleted samples is therefore thought to give some indication into the oxidation and spallation behaviour during cyclic oxidation without the interference of complex oxides.

For this area of the work, the subsequent oxidation experiments in deoxygenated steam were used to identify the effect of the various Cr surface concentrations on the oxidation and spallation behaviour of TP347H FG. The experiments carried out

involved various vacuum annealing times to deplete the samples of Cr in various amounts followed by exposure to deoxygenated steam for 100 hours at 923 K. This environment was chosen to more closely replicate the steam conditions seen in plant. The oxide chemistry and oxidation kinetics were also the main interest for this area of the thesis and so it was important that oxidation did not result in spallation of the outer oxide.

6.3.1.2. Results and discussion

The various surface Cr concentrations observed for each vacuum annealing time studied are shown in Table 6-6. As was discussed earlier, C_S decreases with increasing annealing time and the depth of depletion increases with increasing annealing time.

Table 6-6 Concentration of Cr at the surface and depth of Cr depletion for various samples vacuum annealed at 1273 K and subsequently exposed to deoxygenated steam.

Vacuum annealing time (t) / s (hours)	Surface Cr concentration (C_s) / at.%	Depth of Cr depletion (μm)
57,600 (16)	17.9	10.0
360,000 (100)	17.7	25.0
900,000 (250)	14.9	65.0
1,800,000 (500)	12.8	84.8
2,700,000 (750)	11.3	123.0
3,600,000 (1000)	10.3	133.0

On removal from the furnace subsequent to 100 hours oxidation in deoxygenated steam at 923 K the STORME technique was used to record the cooling curve of the samples and any spallation events. Results from the IR recordings showed the

samples cooled uniformly with only a small gradient across the surface where the bottom edge of the sample surface was in contact with the heat proof surface and thus, cooled more quickly. Figure 6-18(a) shows two localised regions where there was a temperature fluctuation. This occurred on the cut edge of the sample rather than the inner pickled concave surface that was of interest for this work. The otherwise uniform cooling suggests no delamination of the outer oxide occurred and no spallation was observed.

The surface of the samples exposed to deoxygenated steam for 100 hours are shown in Figure 6-19 with a higher magnification image presented in Figure 6-20. The micrographs indicated no evidence of delamination or spallation of the outer oxide.

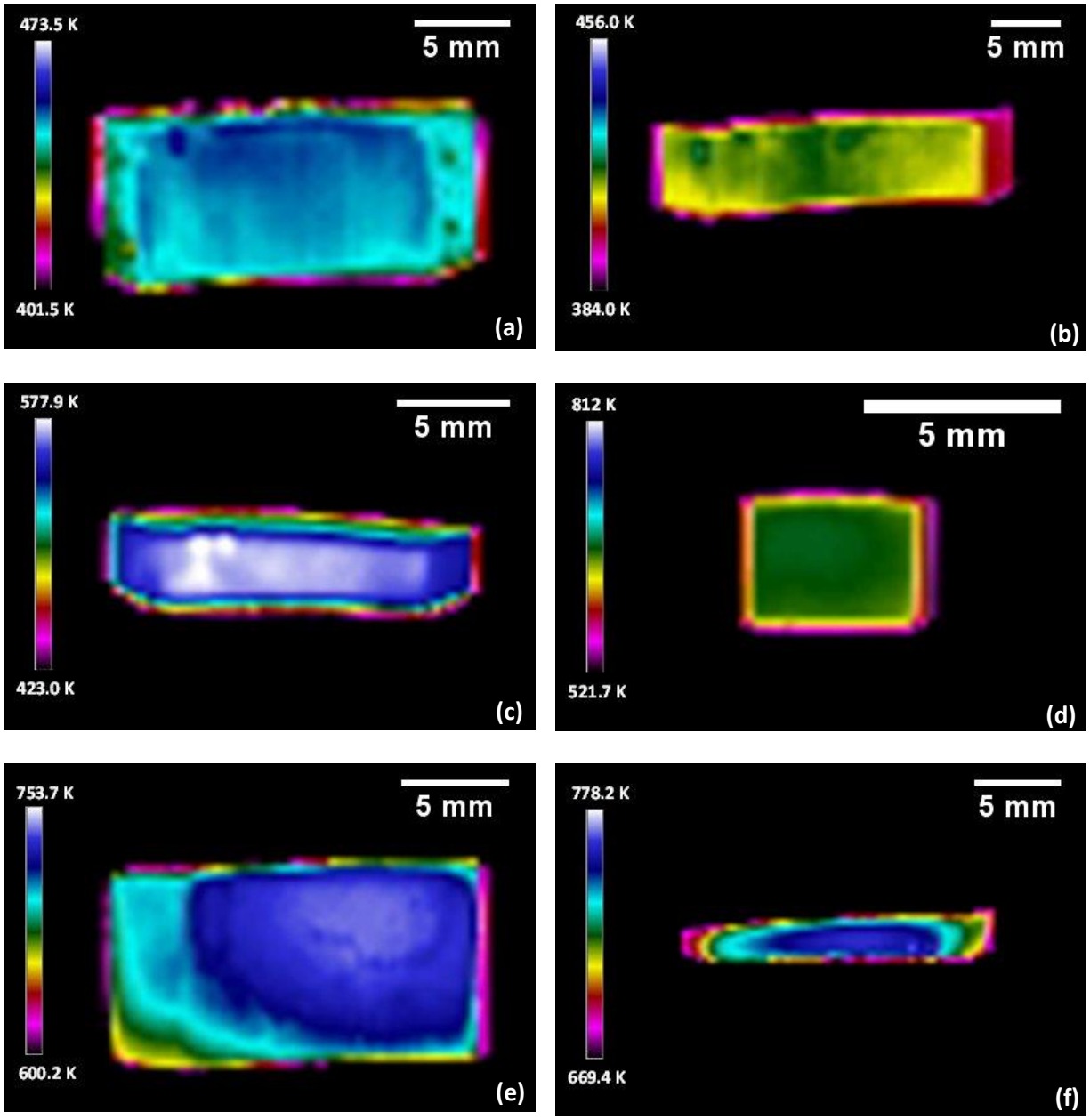

Figure 6-18 Thermographic images of TP347H FG vacuum annealed for a) 16 hours, b) 100 hours, c) 250 hours, d) 500 hours, e) 750 hours and f) 1000 hours all followed by oxidation in deoxygenated steam at 923 K for 100 hours.

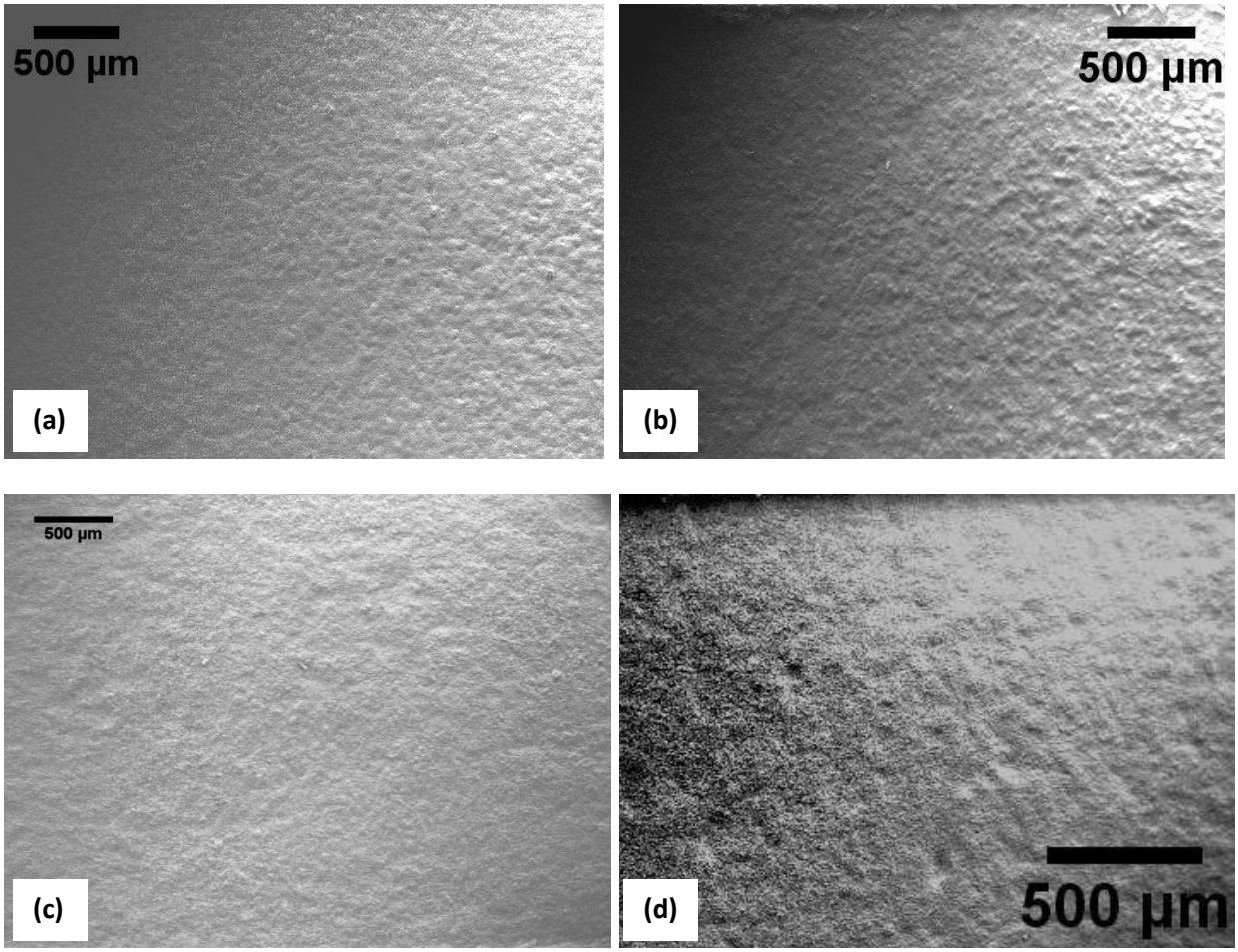

Figure 6-19 SE micrograph of TP347H FG vacuum annealed at 1273 K and 0.01 Pa for (a) 16 hours, (b) 500 hours, (c) 750 hours and (d) 1000 hours followed by subsequent oxidation in deoxygenated steam for 100 hours at 923 K.

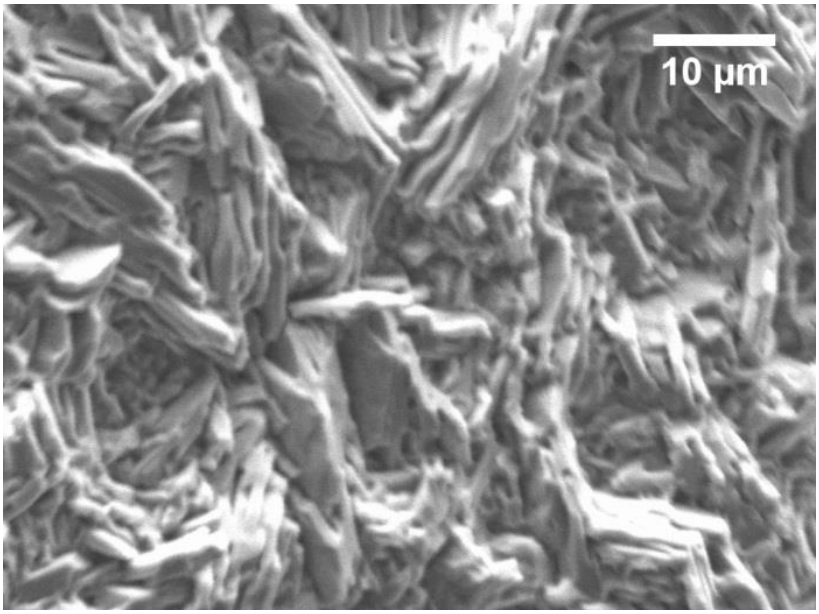

Figure 6-20 SE micrograph of the surface of TP347H FG vacuum annealed for 500 hours at 1273 K and 0.01 Pa followed by oxidation in deoxygenated steam at 923 K for 750 hours.

Cross sectional micrographs for depleted specimens exposed to deoxygenated steam for 100 hours at 923 K are shown in Figure 6-21. A duplex oxide scale consisting of an outer Fe rich scale of magnetite and inner Fe-Cr-Ni spinel grew on the Cr depleted samples similar to that seen for isothermal testing of non-depleted samples. For samples exposed for shorter vacuum annealing times of 16 hours followed by 100 hours in deoxygenated steam, a Cr rich scale started to form at the base of the Fe-Cr-Ni spinel but was not continuous due to the short oxidation time. These scales were not seen to be continuous for non-depleted samples until 300 hours oxidation and therefore were not expected to be continuous for depleted samples subsequently oxidised for 100 hours. Where vacuum annealing was carried out for shorter times, 16 – 250 hours, the oxides formed were relatively uniform. Vacuum annealing times of 500 hours and above resulted in the Fe-Cr-Ni spinel oxide layer to grow in a more undulated fashion.

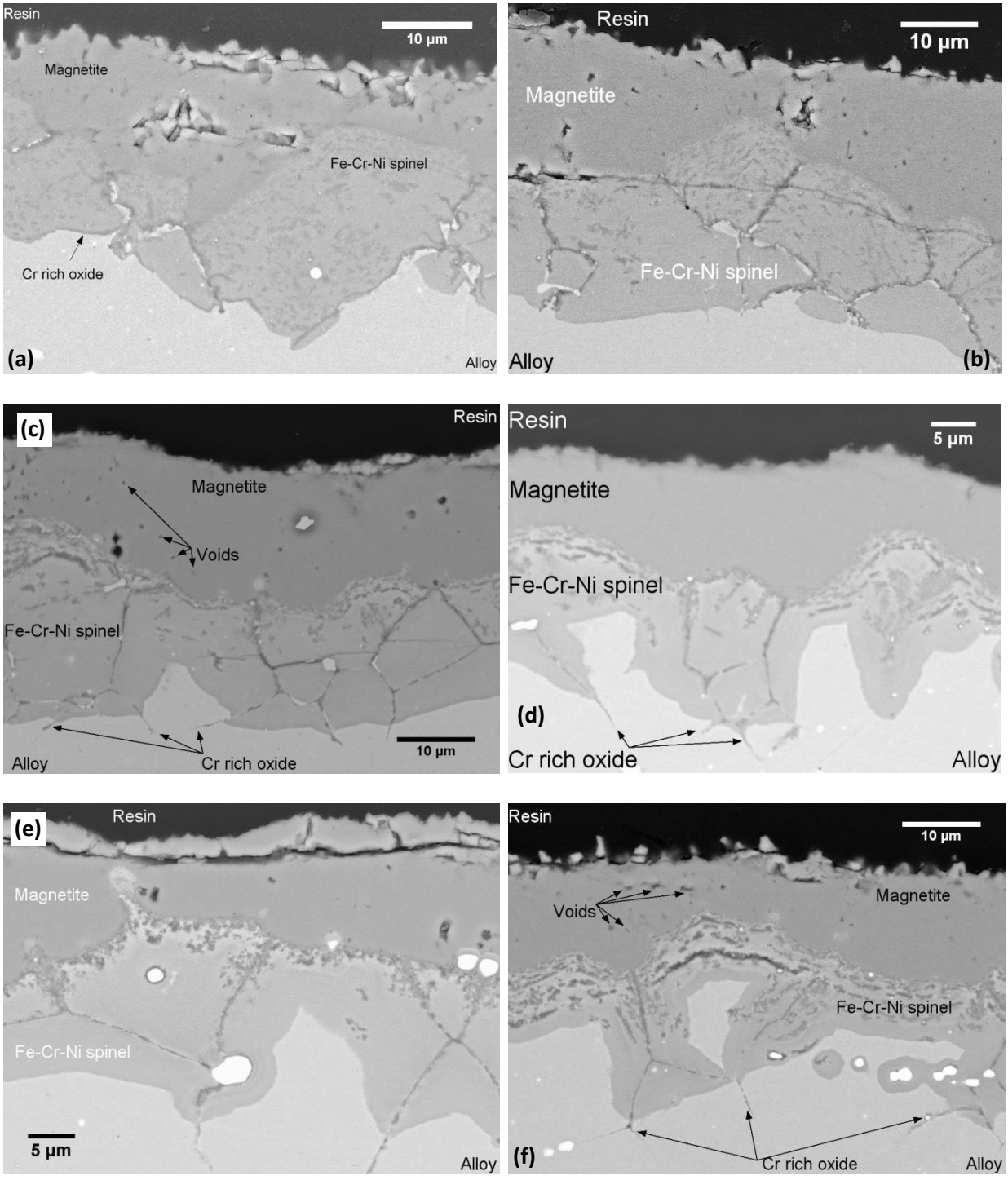

Figure 6-21 BSE cross section image of TP347H FG vacuum annealed for (a) 16 hours, (b) 100 hours, (c) 250 hours, (d) 500 hours, (e) 750 hours and (f) 1000 hours at 1273 K followed by steam oxidation for 100 hours in deoxygenated steam at 923 K.

For longer vacuum annealing times above 250 hours followed by 100 hours exposure to deoxygenated steam, intergranular penetrations into the alloy of a Cr rich oxide were observed. This was confirmed using EDS linescans, an example of which is

shown in Figure 6-22 for a sample of TP347H FG vacuum annealed for 500 hours at 1273 K and 0.01 Pa followed by 100 hours in flowing deoxygenated steam at 923 K. The linescan indicated an increase in the Cr concentration within the penetration. TEM would be required to fully characterise whether this was a layer of chromia or chromite.

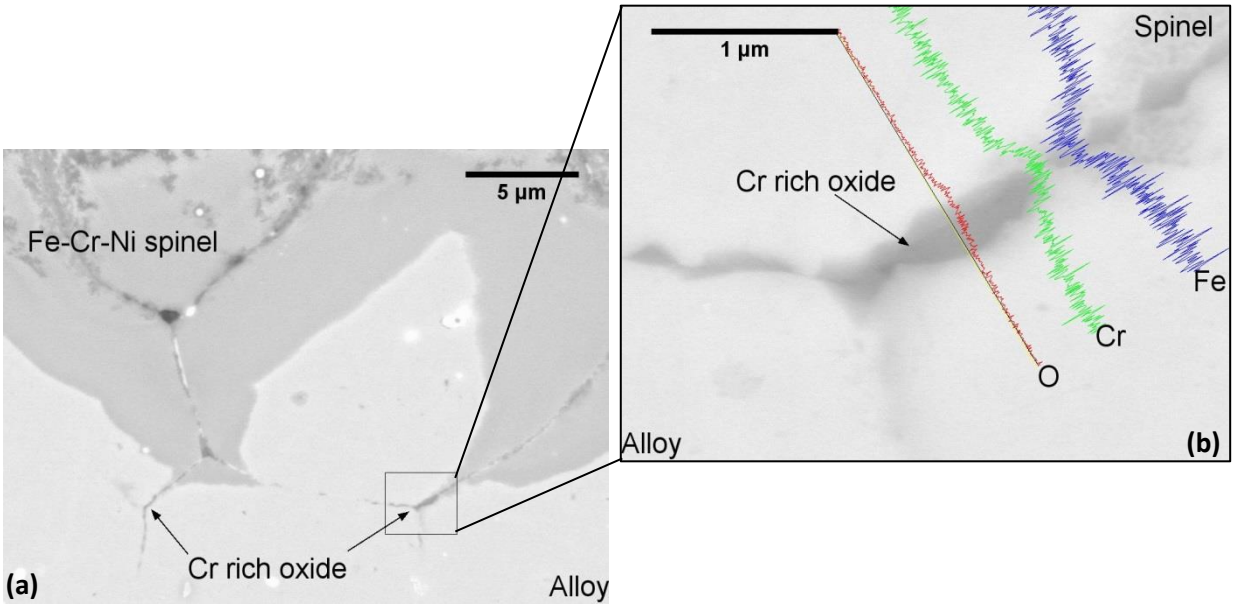

Figure 6-22 BSE cross sectional micrograph of TP347H FG vacuum annealed for 500 hours at 1273 K and subsequently exposed to deoxygenated steam for 100 hours at 923 K (a) low magnification (b) high magnification with EDS linescan results.

After 750 hours vacuum annealing at 1273 K and subsequent oxidation in deoxygenated steam for 100 hours at 923 K, Figure 6-21, cracking was observed in the outer magnetite layer but no spallation was observed.

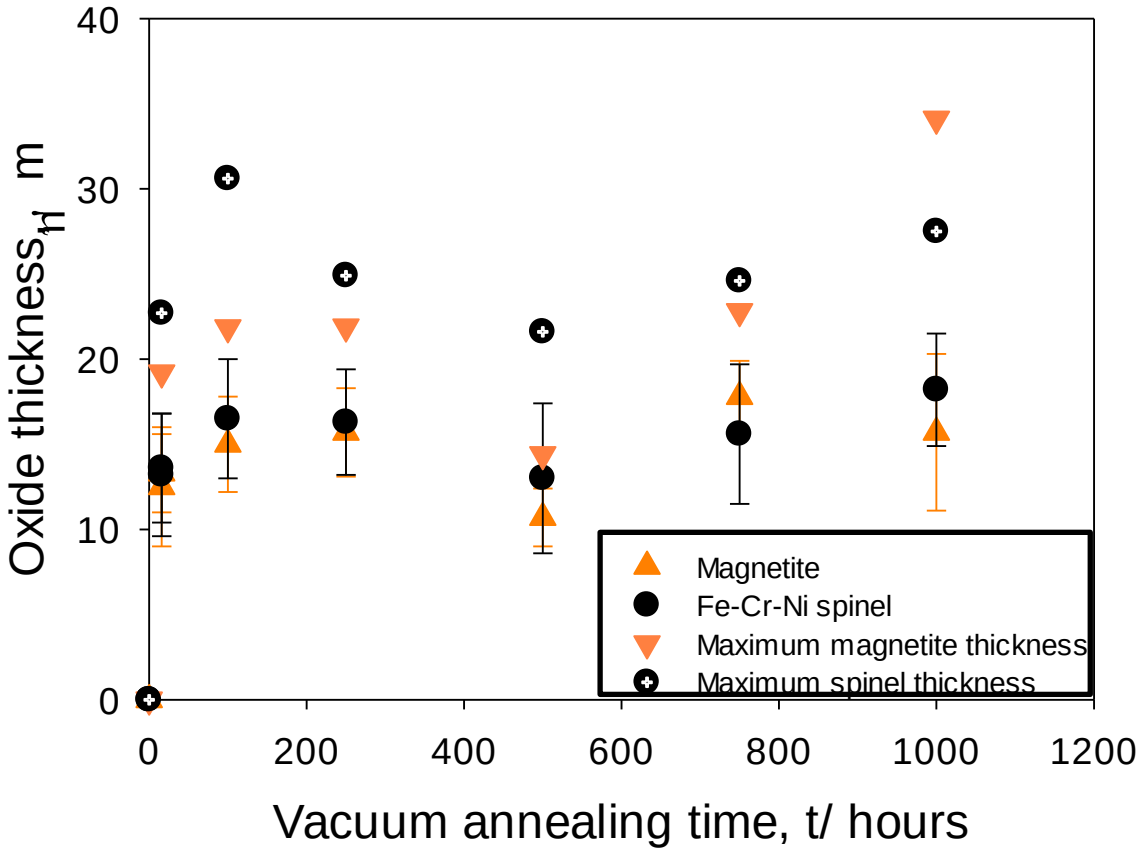

Figure 6-23 Oxide thicknesses of TP347H FG vacuum annealed for various times at 1273 K and 0.01 Pa followed by 100 hours oxidation in flowing deoxygenated steam at 923 K.

Oxide thickness measurements were recorded for each specimen exposed to deoxygenated steam subsequent to vacuum annealing. There was a general increase in oxide thickness for samples vacuum annealed for 16 hours to 250 hours. The greater the level of Cr depletion from increased annealing time would be expected to result in a decrease in oxidation resistance and hence greater oxide thickness. However, samples vacuum annealed for 500 hours and above followed by 100 hours exposure to deoxygenated steam resulted initially in a decrease in oxide thickness compared to 250 hours and then a general increase. A similar observation was noted by Lobb *et al*. [59] where the rate of oxidation was unaffected by the Cr content when the alloy was depleted to levels of 6 – 14 wt.%.

It is postulated that after 500 hours there was a grain size effect dominating the oxidation mechanism. Oxygen is able to diffuse down the grain boundaries faster than it can diffuse through the bulk of the alloy. Increased vacuum annealing times lead to an increase in the grain size and hence a decrease in the number of grain boundaries and therefore the number of diffusion paths available for oxidation. The alloy used in this study, TP347H FG, was developed to increase the oxidation resistance compared to the coarse grained version of the alloy. This is because Cr segregates to the grain boundaries and is able to form a protective Cr rich oxide more quickly with an increased number of grain boundaries although decreasing the grain size will not cause the extent of Cr diffusion down a given grain boundary to increase.

Samples vacuum annealed for 16 hours followed by 100 hours oxidation formed a non-continuous Cr rich oxide at the base of the spinel since the level of depletion was not very significant with C_s = 17.9 at.%. The depth of depletion in the sample was 10 µm and the Fe-Cr-Ni spinel oxide had grown to an average of 13 µm. The alloy therefore was no longer depleted of Cr at this point, hence the observation of the Cr rich oxide beginning to form at the base of the spinel. For 1000 hours on the other hand, the depth of Cr depletion subsequent to vacuum annealing had increased to 133 µm and the spinel thickness subsequent to oxidation in deoxygenated steam was 18.7 µm. From Equation 6-1 it was determined that the Cr concentration at a depth of 18.7 µm after 1000 hours vacuum annealing was 14.1 at.%. Although the Cr rich oxide at the base of the spinel was not shown to be continuous for any of the tests carried out for this area of the work, it was still observed to be present and would have been continuous if the oxidation time had been increased.

6.3.2. The critical Cr concentration required to form a healing layer

6.3.2.1. Introduction

Evans *et al.* [179] found that a level of 18.7 wt.% Cr was required to form a healing layer at 973 K in CO/ CO_2 environments for 20Cr-25Ni-Nb stabilised stainless steels that had undergone pre-annealing for 1000 hours at 1273 K. C_S under the conditions studied by Evans *et al*. reached 6 wt.%. The theoretical Cr depletion profiles that were predicted using Equation 6-3 in this study were used to predict the vacuum annealing time that would be required to deplete the surface of TP347H FG to a level of 12.0 at.% Cr. Once vacuum annealing was complete the samples were sectioned using the method described in Chapter 3 and subsequently exposed to steam for 100, 250, 500 and 750 hours. Each of these samples was then subsequently cross sectioned and examined using SEM. The results of these experiments are presented and discussed below.

6.3.2.2. Results and discussion

The predicted annealing time from Equation 6-3 to produce a Cr depletion level of 12 at.% was shown to be 500 hours. This was calculated using an average diffusion and transfer coefficient of other experiments that had already been calculated. The experimental value of C_S after 500 hours vacuum annealing was 12.8 at.% with a depletion depth of 80 µm. There was no visible spallation on cooling from subsequent steam oxidation exposures.

The surface of each sample was examined using SEM and micrographs are shown in Figure 6-24. The SEM micrographs of the surface of the samples indicated no

cracking or spallation of the outer oxide and the samples appeared to be uniform across the whole surface.

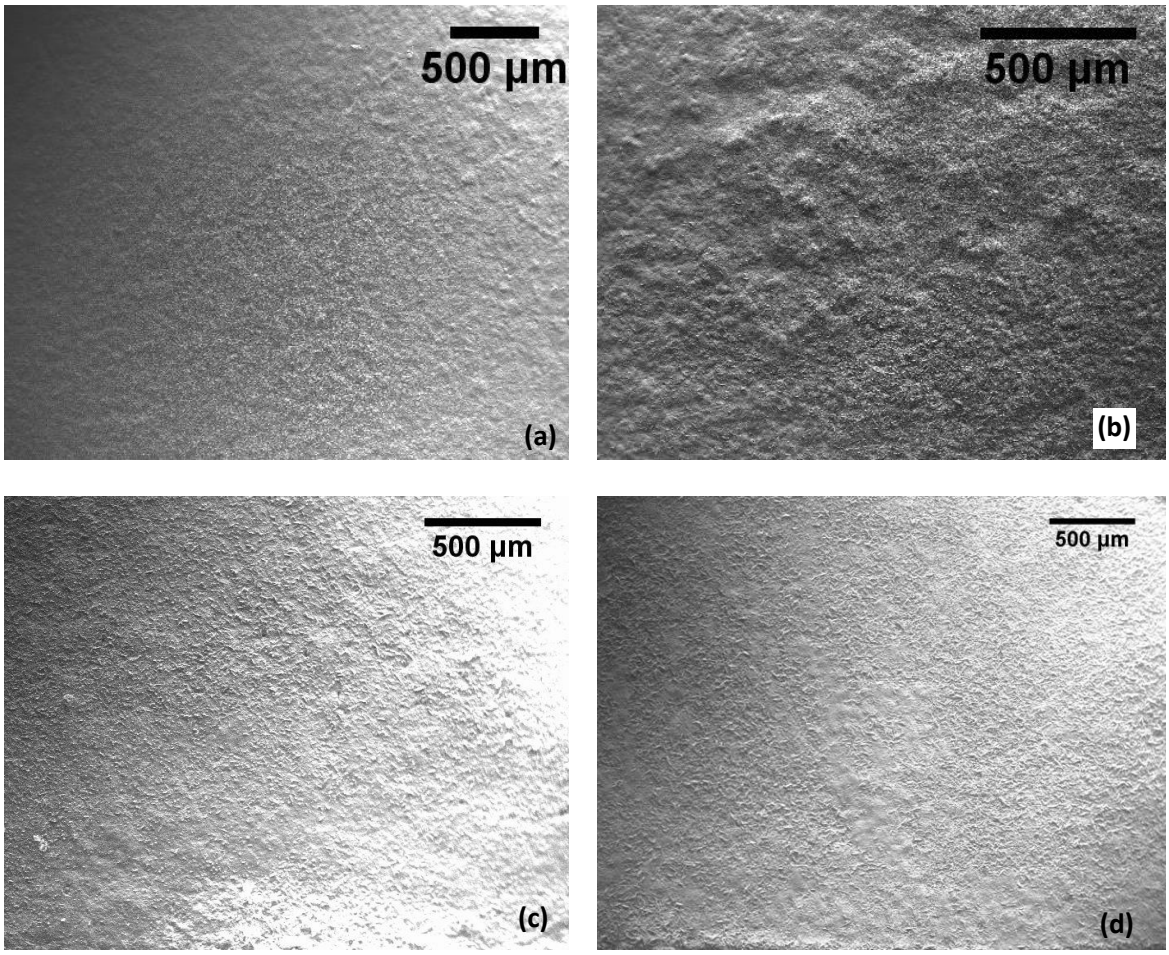

Figure 6-24 SE micrograph of the concave pickled surface of TP347H FG vacuum annealed for 500 hours at 1273 and 0.01 Pa followed by subsequent oxidation in deoxygenated steam at 923 K for (a) 100 hours, (b) 250 hours, (c) 500 hours and (d) 750 hours.

Examination of cross sections indicated that for the shorter oxidation times of 100 and 250 hours, the inner Fe-Cr-Ni spinel grew in an undulated fashion. Longer oxidation times of 500 and 750 hours on the other hand, showed the two oxides formed were relatively uniform in thickness. Alloy entrapment was also shown to occur, Figure 6-25(a). It is therefore postulated that oxidation occurs initially on the grain boundaries and as the time at temperature increases, the entrapped alloy also experiences oxidation hence a more uniform thickness with longer oxidation times.

Cross sectional analysis was also performed to determine the oxide chemistry using EDS and WDS analysis and also to determine the oxidation kinetics for samples where C_S = 12.8 at.%. A duplex oxide was observed consisting of an inner Fe-Cr-Ni spinel oxide and an outer magnetite layer. No evidence was found of haematite which was as expected as a result of the steam environment used.

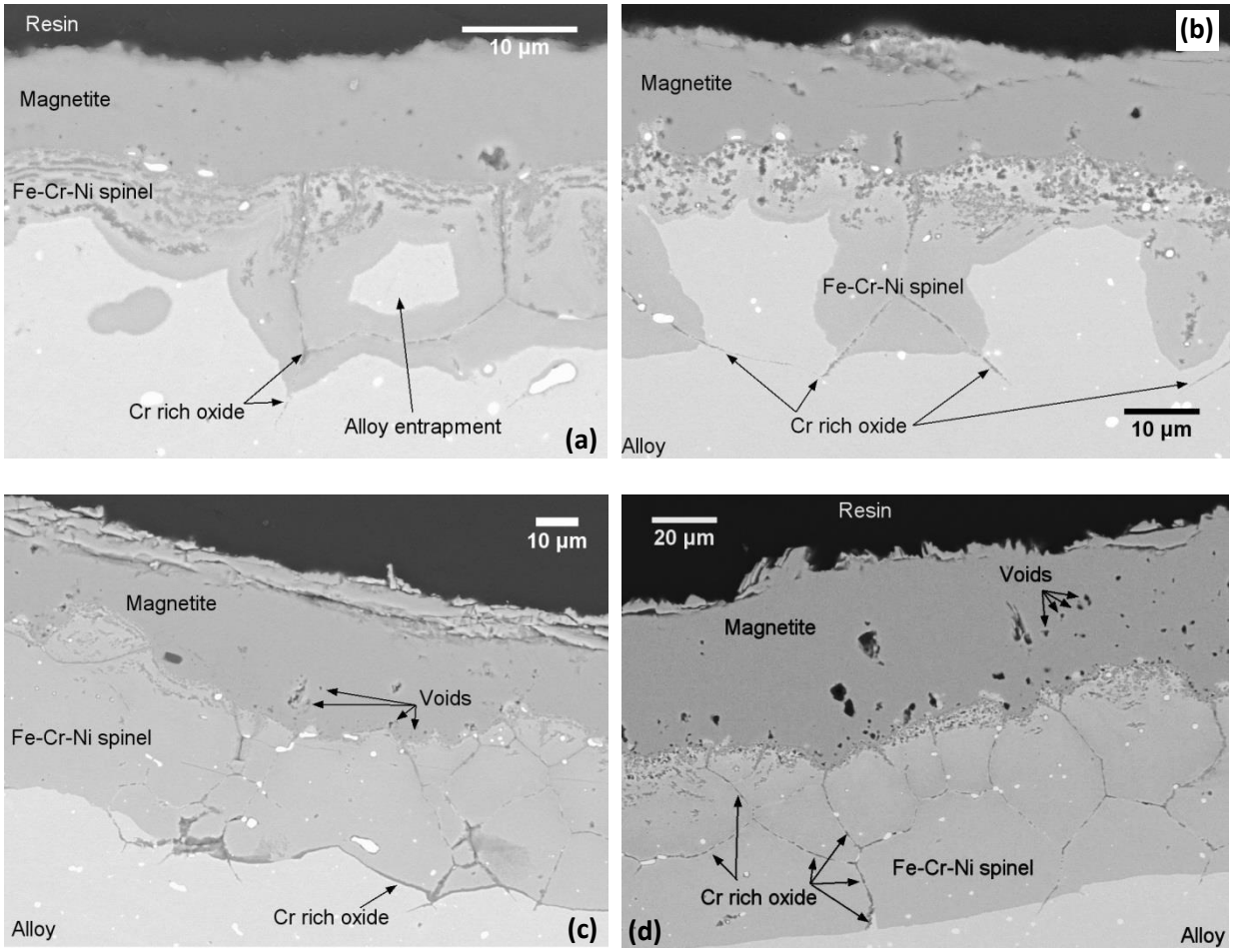

Figure 6-25 BSE cross sectional micrograph of TP347H FG vacuum annealed for 500 hours at 1273 K and 0.01 Pa followed by oxidation in deoxygenated steam at 923 K for (a) 100 hours, (b) 250 hours, (c) 500 hours and (d) 750 hours.

For samples vacuum annealed for 500 hours at 1273 K followed by oxidation in deoxygenated steam at 923 K for 100 and 250 hours, a Cr rich oxide was observed on the grain boundaries but was not continuous. Oxidation for 500 hours on the other hand showed the Cr rich oxide was beginning to form at the base of the spinel.

Intergranular penetrations down the grain boundary into the alloy were also observed. These penetrations were found to be rich in Cr, Figure 6-26.

Equation 6-3 was used to determine the theoretical concentration of Cr at the base of the spinel using the diffusion and transfer coefficients calculated earlier, Table 6-1. It was shown that after 500 hours when the Cr rich layer started to form at the base of the spinel, the Cr concentration at that point was 17.9 at.% whereas for 250 hours the concentration at the base of the spinel was 15.2 at.%, Table 6-7. A Cr concentration between 15.2 – 17.9 at.% will therefore allow a Cr rich scale to start forming at the base of the spinel.

Table 6-7 Cr concentration at the base of the spinel calculated using Equation 6-1 and the Cr diffusion and transfer coefficients calculated earlier.

Oxidation time, hours	Spinel thickness, µm	Cr concentration at depth = spinel thickness, at.%
100	10.7	14.5
250	15.5	15.2
500	38.7	17.9
750	62.0	19.3

Further increasing the oxidation time to 750 hours resulted in the growth of Cr rich oxides around the grain boundaries of the Fe-Cr-Ni spinel oxide, as well as a small amount at the base of the spinel, as shown in Figure 6-24. Further oxidation had occurred below the Cr rich oxide on the grain boundaries indicating it was not fully protective at that point. However, where it had formed at the base of the spinel no further protrusions were observed.

The critical Cr concentration required to form a healing layer has also been investigated in the literature for other alloys. Yuan *et al*. [121] found that for ferritic/ martensitic steel P92, the critical Cr concentration for healing layer formation increased when the alloy was exposed to steam compared to air environments. This was thought to be as a result of the formation of volatile Cr species formed in steam containing environments [180]. 20Cr25Ni steel exposed to CO/ CO_2 was found to require a Cr concentration of approximately 16% to form a healing layer when oxidised in the temperature range 1023 – 1173 K [59]. This value was also found to be required for 25Cr20Ni2.8Si stainless steel when exposed to air at 1286 K [122]. 304 steel with a similar composition to the one studied in this thesis also required a Cr concentration of 16 wt.% when exposed to air at 923 K [118]. It has been suggested in the literature that volatile species such as $CrO_2(OH)_2$ form under steam oxidising conditions and causes the rate of oxidation to increase relative to air due to the lack of a continuous chromia layer [77]. Generally, it has been found that chromia forming steels require a higher concentration of Cr to form a protective layer when in the presence of water vapour [47], [120], [119]. It has also been suggested by Norby [124] that Cr_2O_3 loses its protective properties when exposed to steam environments as a result of its ability to dissolve hydrogen ions.

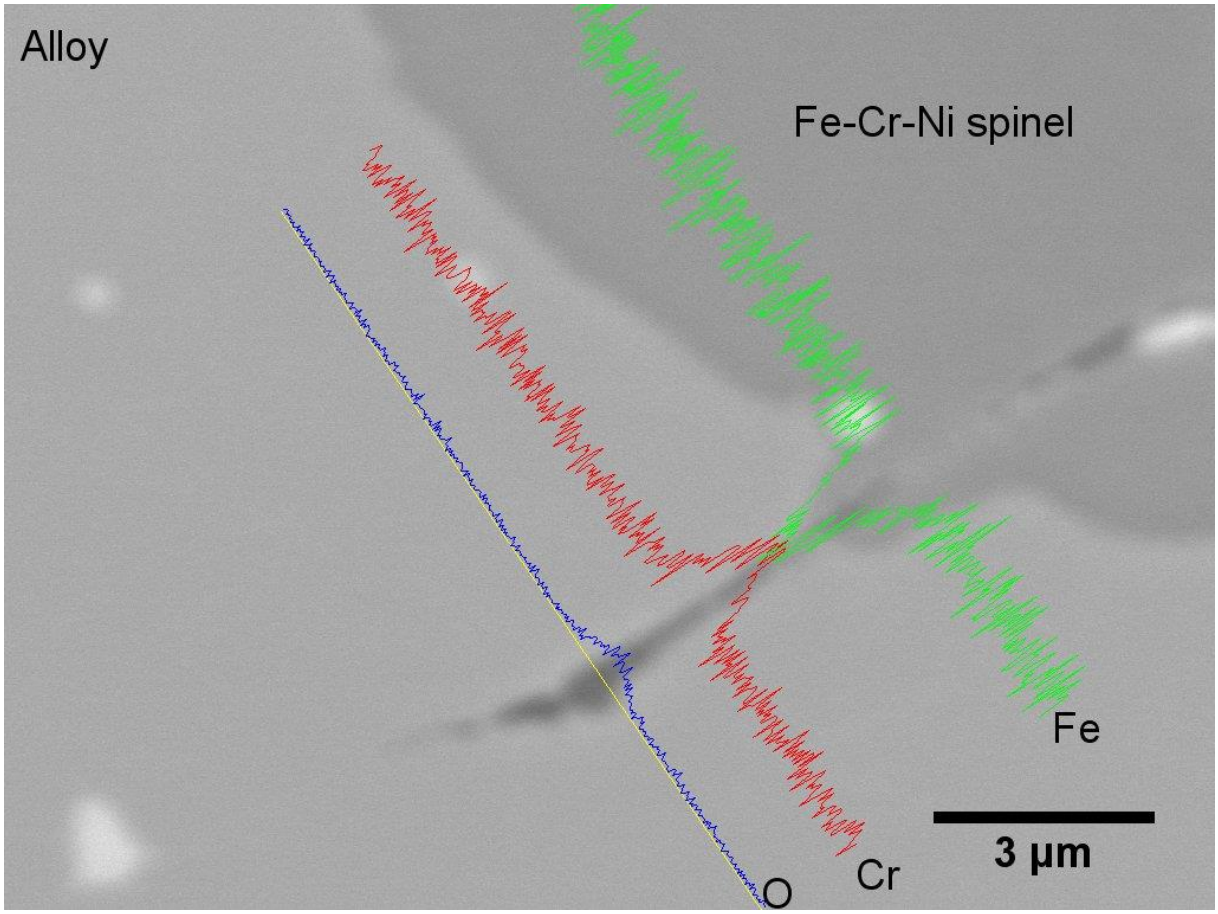

Figure 6-26 BSE cross sectional micrograph of TP347H FG vacuum annealed for 500 hours at 1273 K and 0.01 Pa followed by 250 hours oxidation in deoxygenated steam at 923 K with EDS linescan.

Oxide thickness measurements were taken for each of the oxides formed and were plotted as a function of oxidation time, Figure 6-27. There was a general increase in the thickness of each oxide and kinetics were found to be linear as per the following equation:

$$\xi = k_l t \qquad \text{Equation 6-8}$$

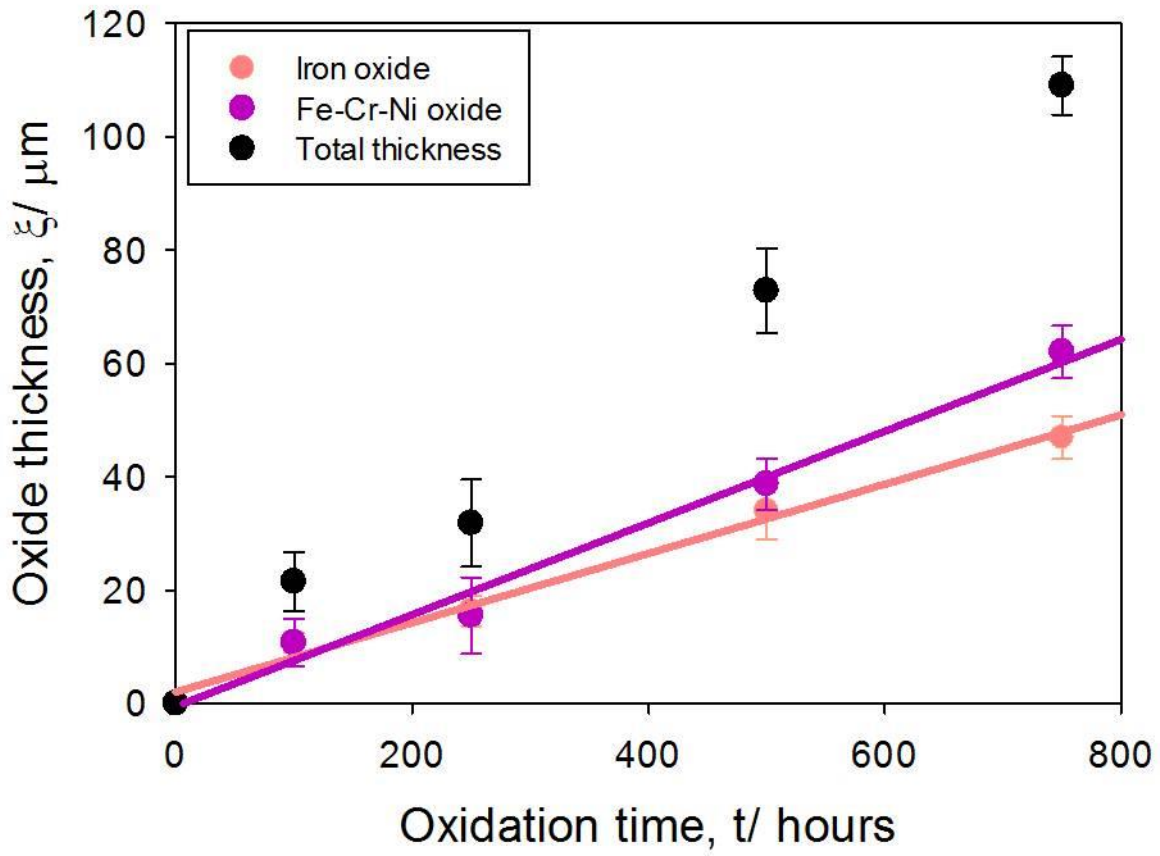

Figure 6-27 Oxide thicknesses for magnetite and Fe-Cr-Ni spinel after oxidation in deoxygenated steam at 923 K subsequent to vacuum annealing for 500 hours at 1273 K and 0.01 Pa.

Rate constants were obtained for each oxide since the gradient of the above plot = k_l and were found to be 2.3 x 10^{-11} $m.s^{-1}$ for Fe-Cr-Ni spinel and 1.7 x 10^{-11} $m.s^{-1}$ for iron oxide.

6.4. Conclusion

Vacuum annealing of TP347H FG at 1273 K and 0.01 Pa resulted in evaporation of Cr and Mn within the alloy with preferential depletion at the grain boundaries resulting in grain boundary grooving. The position of the sample within the furnace and the temperature was shown to have a significant impact on the extent of Cr evaporation.

The concentration of Cr at the surface was shown to decrease with increasing vacuum annealing time.

Equation 6-3 was shown to provide a reasonable approximation for Cr depletion and gave results for diffusion and transfer coefficients. The effective diffusion coefficients were calculated to be 2.17×10^{-15} – 3.23×10^{-15} $m^2.s^{-1}$. Equation 6-4 was used to calculate theoretical weight losses based on Cr evaporation which was found to significantly underestimate the loss seen for longer vacuum annealing times. Further investigations showed that grain boundary grooving also contributed to the mass loss but still did not account for the extent observed in this work.

Work was carried out to investigate the effect of Cr depletion on the oxidation and spallation behaviour of TP347H FG in deoxygenated steam environments at 923 K. Cr depletion caused a significant increase in oxide thickness compared to samples which were not vacuum annealed. It was found that as the grain size of the alloy increased, oxide thickness did not vary significantly and it was only up until 500 hours vacuum annealing that there were increases in oxide thickness when oxidation was carried out for 100 hours.

Investigations were carried out to determine the critical concentration of Cr required to form a healing layer at the base of the spinel. Although Cr rich oxides were identified as intergranular penetrations in all instances a complete healing layer was not observed for any of the oxidation times tested when the samples had been pre-annealed for 500 hours. The Cr rich layer was shown to begin formation between 15.2 and 17.9 at.% Cr and it is expected that this layer would be continuous at a value of more than 19.3 at.% Cr based on the sample exposed to deoxygenated

steam for 750 hours post vacuum annealing. It is thought that the alloy is close to its limit compositionally. Comparisons made to the literature indicated that Cr rich healing layers are not observed to be continuous under steam conditions but are continuous when oxidation is carried out in air environments. It was also noted that steam oxidising environments increase the critical Cr concentration required to form a healing layer relative to air oxidising environments and this is thought to be as a result of volatile species such as $CrO_2(OH)_2$ forming under steam conditions.

Chapter 7 – Discussion

The increasing aspiration to reduce CO_2 emissions in the past decade has resulted in alternative methods of power generation including increasing operating temperatures and substituting fuels. These modifications have introduced stringent materials requirements on the boiler tubing, particularly when considering biomass as a fuel. It is believed that biomass will lead to an increase in the number of shutdowns since it is not expected to be used for baseload operation therefore presenting problems in terms of material lifetime. Issues such as tube overheating and erosion of turbine blades have been reported in the literature as a result of oxide scale spallation. These problems can eventually lead to tube rupturing which can cost operating companies several hundreds of thousands of pounds for every day a power plant is inoperable. Being able to predict the onset of spallation will allow for planned maintenance shutdowns at the most opportune moment for both operator and consumer. Research gaps highlighted in the literature survey at the beginning of this thesis demonstrated the need for further understanding of the cyclic steam oxidation and spallation behaviour of alloys already employed as heat exchanger tubing in coal fired power plants. The main aims for this thesis therefore were to investigate the cyclic steam oxidation and spallation behaviour of a 300-series austenitic stainless steel, TP347H FG, and to investigate the effect of Cr depletion on the oxidation behaviour. This deeper understanding will allow spallation predictions to be made.

This thesis has investigated the oxidation behaviour of TP347H FG under both isothermal and cyclic conditions in air-saturated and deoxygenated environments at

923 K. Previous work in the literature reported duplex oxide formation under isothermal conditions indicating an inner spinel layer and outer Fe rich layers with a Cr rich oxide at the spinel/ alloy interface [2], [22], [54], [162]. Cross sectional examination carried out for this thesis highlighted an inner Fe-Cr-Ni spinel and an outer layer of magnetite with a decoration of haematite. During the course of this work it has been found that the Cr rich oxide developing at the base of the spinel layer adjacent to the alloy is composed of a layer of $FeCr_2O_4$ and a layer of Cr_2O_3 similar to that reported by Jianmin *et al*. [181]. The Cr_2O_3 layer was identified by its crystal structure using TEM studies carried out by Dr Rengen Ding at the University of Birmingham [132]. The growth rate of this Cr_2O_3 layer is in keeping with the values predicted using data from Evans *et al*. [161] for pure Cr_2O_3 and was observed to be approximately 115 µm after 1000 hours oxidation in air-saturated steam at 923 K. A mechanism for isothermal oxidation was suggested and was shown earlier in Figure 4-24.

The growth of Fe-Cr-Ni spinel on similar alloys in the literature was found to follow parabolic kinetics [21] with a k_p value of 1.7×10^{-17} $m^2.s^{-1}$. It was observed extensively in this thesis that the development of Cr_2O_3 at grain boundaries was linked to arresting inward Fe-Cr-Ni spinel growth resulting in near-cubic kinetics under isothermal conditions. Data for diffusion coefficients is shown in Appendix D and indicates that the diffusion of Fe through Cr_2O_3 is much slower than that through the alloy [182], [183]. Concentration profiles obtained through TEM/ EDS studies showed an enhancement in Fe beneath the Cr-rich oxides providing evidence that these layers prevented further outward diffusion of Fe, hence reducing the growth rate.

Under cyclic oxidation conditions Fe-Cr-Ni spinel thickness was shown to be bimodally distributed. This was thought to be as a result of the formation of the Cr rich oxides. Again, the formation of this protective layer slows down the rate of diffusion of Fe outwards and prevents further oxidation. Therefore, when the Cr rich oxides are continuous at the base of a grain, the rate of growth of Fe-Cr-Ni spinel is reduced. For grains where the Cr rich oxides are not continuous on the other hand, the Fe-Cr-Ni spinel continues growing at the same rate as that observed during isothermal conditions. This difference in growth rates results in a more undulated oxide, hence a bimodal distribution. A simple kinetic model therefore does not hold for these conditions and further work would be required to fully determine the kinetic behaviour under cyclic conditions. Comparisons were made between the Fe-Cr-Ni spinel kinetics found in this work and those available in the literature for similar alloys. It was found that there was good agreement between literature values and those observed in this work for the lower bimodal average [21]. For longer term cyclic oxidation testing it was also shown that there is some shrinkage of the Fe-Cr-Ni spinel during the second thermal exposure. It was postulated that this was as a result of the reformation of Fe_3O_4. There was a decrease in the amount of Fe diffusion available as a result of the protective Cr rich oxides. Therefore, it was thought that the reformation of magnetite at the outer surface was as a result of Fe diffusion from within the spinel layer, hence resulting in shrinkage of the Fe-Cr-Ni spinel.

A comparison was also made between isothermal and cyclic exposures of the same duration and it was shown that for shorter oxidation times, up to 300 hours in total, the Fe-Cr-Ni spinel was thicker under cyclic oxidation conditions. For tests totalling 1000 hours however the spinel was shown to be thickest under isothermal

conditions. This was postulated to be as a result of the formation of the Cr rich oxide at the base of the spinel as mentioned earlier. The Cr rich layer is shown to be continuous after 300 hours. Therefore, for cycles of 500 hours where the Cr rich layer is already fully formed at the start of the second cycle, Fe diffusion from within the alloy becomes slower.

Extensive spallation was observed during cooling in laboratory air for all isothermal experiments in air-saturated steam at 923 K. Meticulous collection of spalled particles allowed SEM investigations to be carried out which showed the spalled oxide to be that of haematite for short term testing and both haematite and magnetite for long term testing. A number of models exist to attempt to describe the spallation behaviour such as those described in Section 2.5.5 of the literature review. Previous techniques used to examine spallation of oxides lacked the ability to detect localised temperature drops at the time of a spallation event and image the specimens at the same time [65], [145], [148], [149], [150], as described in Section 2.5.4 of the literature review. In the case of this project a technique was developed to collect the strain energies developing within a cooling sample. The technique termed Simultaneous Thermographic and Optical Recording Media Examination, or STORME, was capable of collecting data on the temperature at which delamination and spallation occurred as well as the radius of the localised site from delamination to spallation. This technique also allowed identification of individual spalled particles so that spalled oxide thickness and the data obtained from thermographic images could be correlated. This was described extensively in Section 3.3.6. From this it has been determined that the haematite/ magnetite interface was the primary location of delamination and spallation, as shown in Section 4. Results obtained from STORME

allowed strain energy calculations to be made which indicated haematite had the highest contributing strain energy relative to magnetite.

It was also shown in this work that a layer of pores developed within the magnetite oxide layer. For longer times at temperature these voids coalesced resulting in a plane of weakness. STORME analysis indicated the fracture energy at this interface to be 1.6 $J.m^{-2}$.

Armitt *et al*. [136] developed a spallation model whereby critical strain values were identified as a function of the spalled oxide scale thickness for various failure mechanisms. This early spallation model was then used as the basis for other models. For instance, Schutze *et al.* [133] modified the model to include all factors that could contribute to spallation such as Young's modulus, oxide scale defects and fracture toughness. Quadakkers *et al.* also investigated the mechanism of steam oxidation and found that spallation was dependent on the type, morphology and growth of pores in the oxide scale of interest [85]. Models available in the literature and discussed in this thesis are in agreement that oxide strain energy is key to interpreting spallation behaviour. Other important parameters include the differences in thermal expansion coefficients [136], [142] between the alloy and oxides and also the thickness of the spalled oxide scale [130], [142].

The model proposed by Evans *et al*. [144] was used in this work to determine the spallation mechanism for the outer Fe oxides. This model takes into account the spalled oxide thickness and the critical temperature drop required to initiate spallation. Spallation maps were plotted for haematite only thickness, magnetite only thickness and complete spalled oxide thickness. The fracture energies of the

haematite/ magnetite and magnetite/ spinel interfaces were determined through a best fit approach. Values of γ_F were found to be 9 $J.m^{-2}$ for the haematite/ magnetite interface and 1.6 and 7.6 $J.m^{-2}$ for the magnetite/ spinel interface when taking only magnetite thickness into account and the total spalled thickness into account, respectively. The spallation maps also indicated that the failure mechanism for this system was unstable buckling. Further evidence for unstable buckling was found through cross sectional examination where crack extension could be seen beyond the original buckle. Thermographic images obtained from STORME also highlighted an increase in the radius of delamination during cooling which is indicative of unstable buckling.

The unique STORME technique has, for the first time, predicted the spallation mechanism for an alloy exposed to air-saturated steam through determination of interfacial fracture energies. The spallation mechanism for samples of TP347H FG exposed to air-saturated steam was shown to be unstable buckling under isothermal and cyclic conditions. It has previously been suggested in the literature that taking only spalled oxide thickness into consideration is not adequate enough to predict the onset of spallation and that defects such as voids should also be considered [126]. The unpredictability of these defects impedes accurate quantification hence making it difficult to interpret the extent of their contribution. It was found in this thesis that voids play a key part in the spallation mechanism however, the approach used in this work was found to model this system very well despite only taking into consideration the spalled oxide thickness.

The STORME technique was also used during cyclic steam oxidation experiments and it was found that where the second thermal exposure was carried out in air-

saturated steam, spallation occurred on cooling and there was an increase in the radius of the delaminated site from the time at which delamination occurred to complete localised spallation. The amount of visible spallation was shown to decrease with increasing number of cycles. For deoxygenated steam environments however, no visible spallation was observed on cooling. Regions of localised temperature changes were observed with STORME under these conditions and measurements of the radius of these sites indicated there was no change for the entire cooling period. These results would suggest stable buckling occurs on cooling under these conditions.

Isothermal oxidation experiments carried out throughout the duration of this project showed that haematite forms during the initial stages of oxidation when exposed to air saturated steam at 923 K. Hence, once a complete layer has been established, no further haematite formation was observed. Evidence of this was found during SEM examination of spalled particles where the thickness of the haematite layer remained relatively constant with increasing oxidation time. Furthermore, during cyclic oxidation where the haematite layer had spalled on cooling from cycle 1, there was no evidence of haematite during cross sectional examination subsequent to the second thermal exposure for the time periods investigated here. A mechanism for short term cyclic oxidation was proposed and is shown in Figure 5-44. It was postulated that there was no evidence of haematite formation during subsequent thermal cycles was as a result of it being formed initially.

Depletion of Cr in the alloy was observed during cross sectional analysis of TP347H FG as shown in Chapter 4. Thus, an investigation into the effect of Cr depletion on the oxidation behaviour of the alloy was devised. A series of vacuum annealing

exposures at 1273 K and 0.01 Pa were conducted to deplete the alloy of Cr, thus simulating the selective oxidation of Cr resulting in a depleted surface. From this the effective diffusion coefficient was determined and was found to be in the range $2.17x10^{-15}$ – $3.23x10^{-15}$ $m^2.s^{-1}$. It also became possible to determine the vacuum annealing time required to produce a certain value of Cr concentration at the surface.

A series of samples were produced with predicted Cr concentrations and exposed to a deoxygenated steam environment to be more closely representative of the conditions seen in plant. Two steam oxidation experiments were used, the first of which consisted of a number of samples vacuum annealed for various times and exposed to deoxygenated steam for 100 hours to investigate the effect of the surface concentration on the oxidation behaviour. Again a duplex oxide consisting of an inner Fe-Cr-Ni spinel and an outer magnetite layer was observed, similar to that seen for non-depleted samples subsequent to isothermal oxidation in air-saturated steam. However, the spinel formed on depleted alloys had a different morphology to samples that were not depleted of Cr. For as-received samples the Fe-Cr-Ni spinel was speckled in appearance. Depleted samples on the other hand looked relatively uniform. This study also indicated haematite did not grow during oxidation of depleted samples. Comparisons to research available in the literature [21], [167] suggest haematite would not be expected to form under these conditions. Previous studies on model alloys showed that an increase in the Cr concentration would be expected to result in a decrease in the weight gain, Section 2.3.7.4 of the literature review. Oxide thickness of both spinel and magnetite did not vary significantly for this testing matrix despite the varying levels of Cr across the samples. It was postulated that there was a grain size effect dominating the oxidation mechanism.

The second of the steam oxidation experiments carried out involved an investigation into the critical Cr concentration required to form a healing layer. A series of samples were depleted of Cr to a level of 12 at.% and subsequently exposed to deoxygenated steam for 100, 250, 500 and 750 hours at 923 K. Oxide thickness measurements of both the spinel and magnetite layer indicated linear kinetics. A Cr rich oxide was shown to form along grain boundaries for samples that were depleted of Cr. It was found that a critical Cr concentration of 15.2-17.9 at.% Cr was required for this protective layer to form at the base of the spinel. Previous studies showed that a Cr concentration of 16 - 18.7 wt.% would be required to form a healing layer on 20Cr25Ni stainless steel when exposed to CO/ CO_2 at 1023 – 1173 K [59], [179], whilst 304 was found to require 16 wt.% when exposed to air at 923 K [123]. It has been reported in the literature that an increased Cr concentration is required to form a healing layer in steam relative to air environments which is thought to be as a result of the formation of volatile Cr species such as $CrO_2(OH)_2$ forming in steam environments [121], [180]. These species are also thought to be the cause for an increase in the rate of oxidation as a result of a lack of a protective layer [77] which could be the cause for the linear kinetics observed in this thesis.

The STORME technique was used during cooling in both steam experiments studied on Cr depleted samples. No visible spallation was observed during cooling. Additionally, no localised temperature changes on the concave surface were observed on thermographic images, suggesting there was no delamination of the outer oxide either. SEM investigations of this surface also revealed a uniform surface with no cracking observed within the oxide. This provided further evidence for the requirement of haematite to result in spallation.

Chapter 8 – Conclusions

For the first time, it has been possible to obtain a complete set of delamination and spallation data using the novel monitoring technique termed STORME allowing a substantial contribution in the understanding of spallation processes. The data gathered from STORME along with the meticulous collection of spalled oxide particles has revealed the importance of haematite formation on spallation initiation. In all of the three subcategories through which this thesis was conducted, spallation was shown to occur only in regions of adherent haematite and as a result there is a decrease in the amount of visible spallation with increasing thermal cycles. Interfacial fracture energies have been determined and it has been shown that where voids are present, γ_F reduces from 9 $J.m^{-2}$ to 7.6 $J.m^{-2}$ resulting in a change in the interface at which spallation occurs. Modelling of the data obtained from STORME revealed the spallation mechanism to be that of unstable buckling. The use of this technique during thermal cycling indicated that buckles form on cooling. Where air-saturated steam was used, spallation was observed and the delamination regions highlighted in thermographic images were shown to increase with increasing cooling time. Deoxygenated steam environments on the other hand did not result in spallation and thermographic images showed delaminated regions remained stable in size with increasing cooling time.

Characterisation of the oxides formed during isothermal oxidation of TP347H FG exposed to air-saturated steam at 923 K have shown that the oxide is comprised of an inner Fe-Cr-Ni spinel and an outer magnetite layer with a decoration of haematite

which forms during the initial stages of oxidation. With continued exposure Cr rich oxides were observed to form at the base of the spinel layer. These oxides included $FeCr_2O_4$ and Cr_2O_3 and were found to be beneficial to the oxidation behaviour. No evidence was found during thermal cycling exposures to suggest that haematite reforms during the second cycle.

Oxidation kinetics for the Fe-Cr-Ni spinel have been shown to be dependent on the concentration of Cr at the surface. Under isothermal conditions, kinetics were shown to follow near-cubic behaviour with a rate constant of 1.3×10^{-15} $m^{2.9}.s^{-1}$. The formation of protective Cr rich oxides at the base of the spinel resulted in a reduced oxidation rate. As a result of this protective layer, the Fe-Cr-Ni spinel layer was shown to have a bimodal thickness during cyclic oxidation experiments which resulted in more complex kinetics. Cr depletion was found to have detrimental consequences on the oxidation behaviour of TP347H FG. It was shown that oxidation kinetics followed a linear regime when exposed to deoxygenated steam at 923 K with a rate constant of 2×10^{-11} $m.s^{-1}$. Oxide thickness measurements of the Cr_2O_3 layer observed after longer times at temperature were found to agree well with the literature.

Finally, samples that were vacuum annealed were shown to result in the evaporation of both Cr and Mn. Mass loss increased with increasing time at temperature. Mathematical modelling of the Cr depletion profiles enabled effective diffusion coefficients and transfer coefficients for each annealing time tested to be calculated. A range of diffusion coefficients was found for 16-1000 hours vacuum annealing 2.17×10^{-15} – 3.23×10^{-15} m^2 s^{-1}. Cross sectional analysis showed grain boundary

grooving along the surface of the alloy which was also thought to contribute to the mass loss. A complete Cr rich healing layer was not observed for any of the times tested but intergranular penetrations were observed. It is expected that this would be continuous once a Cr concentration of more than 19.3 at.% was achieved.

Chapter 9 – Future Work

Areas of interest that have been highlighted in this thesis and future work that could accompany the research carried out here are described in this chapter.

Detailed analysis of the oxide growth mechanisms is vital in understanding the oxidation behaviour of typical austenitic stainless steels in steam. Oxide thickness kinetics of each of the oxide layers would allow a more accurate comparison to the literature. Furthermore, it would allow a greater understanding as to why a chromite oxide layer is seen to form and not just a dense, protective layer of chromia. It has also been highlighted in this work that the steam oxidation mechanism is still not fully understood in the literature. Therefore, further investigations into the growth mechanisms would indicate whether hydrogen has a significant role in the oxide chemistry observed in steam oxidation studies or if hydrogen is the cause for void formation.

It was addressed in this thesis that void formation and other such defects influence the spallation behaviour of the outer Fe oxides and should be considered when modelling spallation. There is therefore a need to understand the mechanism through which these voids form and coalesce and, as a result, lead to a plane of weakness, in order to be able to quantify such defects. Quantification would then allow a parameter to be included to account for these flaws and hence provide a more accurate prediction into the spallation behaviour to be made.

The cyclic oxidation kinetics were briefly investigated in this thesis and it was shown that once formation of the Cr rich oxides at the base of the Fe-Cr-Ni spinel had

begun, a simple kinetic model could no longer be used. Further investigations into the kinetic behaviour would require a more in depth study for longer oxidation times. In addition, a range of oxidation temperatures would enable a greater dataset to be established hence providing a better depth of understanding.

There is also a need to understand the reason why the critical Cr concentration required to form a healing layer is apparently higher in steam containing environments compared to air. It has previously been suggested in the literature that this is as a result of Cr volatilisation. Hence, investigating this process and determining whether volatile Cr oxides are present would help in understanding this mechanism. Moreover, the Cr rich oxide observed during steam oxidation of Cr depleted samples in Chapter 6 requires further characterisation using high resolution methods such as TEM. It would be of interest to know whether Cr depletion effects the oxide chemistry observed compared to non-depleted alloys.

Chapter 10 – Appendices

A. Determination of C_0 << C_B

C_0 is the concentration of Cr in equilibrium with the vapour pressure.

The vapour pressure of Cr at 1273 K = 0.01 Pa [149].

The concentration can be calculated using the ideal gas equation:

$$\frac{n}{v} = \frac{p}{RT} \qquad \text{Equation 10-1}$$

where n is the number of moles, mol, v is the volume, m^3, p is pressure, Pa, R is the gas constant, 8.314 $J.mol^{-1}.K^{-1}$ and T is temperature, K.

and

$$C_0 = \frac{n}{v} \qquad \text{Equation 10-2}$$

where C_0 is concentration, $mol.m^{-3}$.

Therefore,

$$C_0 = \frac{p}{RT} \qquad \text{Equation 10-3}$$

Hence,

$$c = \frac{0.01}{8.314\ x\ 1273} = 9.4x10^{-6} mol.m^{-3} = 0.00049\ ppm$$

C_B = 201000 ppm

Therefore C_0 «« C_B.

B. Calculation of grain volume and conversion to mass loss

Prior to any exposure each sample was measured and weighed, as described in Section 3.2. These measurements allowed the surface area of the inner concave surface to be calculated and subsequently the density, ρ, of the sample using the following equation:

$$\rho = \frac{m}{v} \qquad \text{Equation 10-4}$$

where m is mass, g, and v is volume, m^3.

Image analysis, described in Section 3.6.3, was able to determine the average grain size of the samples post vacuum annealing and the groove depth and width. The width of the groove was subsequently used to calculate the surface area of the groove and finally the volume of the groove.

From the average grain size it was possible to determine how many grooves would be expected per unit area and hence determine a total volume for the number of grooves present per sample.

Rearrangement of Equation 10-4 enabled the mass of the grooves to be calculated by multiplying the groove volume by the density of the sample.

Hence, an estimated mass loss for grain boundary grooving could be determined.

C. MATLAB code

```
% Function to be used once optimisation completed so that the model fits

% and plots can be produced with the optimised variables.

% This function requires input vector x and z = [D,h] input scalars Cb and t.

function [CxSim] = beckyFunc(Cb,x,t,z)

N       = length(x);

CxSim   = zeros(N,1);

for i = 1:N

    Cx1 = erfc(x(i)/(2*sqrt(z(1)*t)));

    Cx2 = exp(z(2)*x(i)+(z(2)^2)*z(1)*t);

    Cx3 = erfc((x(i)/(2*sqrt(z(1)*t)))+z(2)*sqrt(z(1)*t));

    CxSim(i) = Cb*(1-(Cx1-Cx2*Cx3));

end

end



% Prior to running beckyFunc, this function with the objective of

% calculating the sum of sqaure error between the experimental and

% simulation results. This function is the objective function of an
```

```
% optimisation algrithm.

function [MSE] = beckyFuncOptimise(Cb,x,t,z,CxExp)

N       = length(x);

CxSim   = zeros(N,1);

for i = 1:N

    Cx1         = erfc(x(i)/(2*sqrt(z(1)*t)));

    Cx2         = exp(z(2)*x(i)+(z(2)^2)*z(1)*t);

    Cx3         = erfc((x(i)/(2*sqrt(z(1)*t)))+z(2)*sqrt(z(1)*t));

    CxSim(i)    = Cb*(1-(Cx1-Cx2*Cx3));

end

MSE = sum((CxSim-CxExp).^2)/N;

End



% Optimisation algorithm for concentration equation

% For equation:

% Cx =

% Cb*(1-(erfc(x/2*sqrt(D*t)-exp(h*x+(h^2)*D*t)*erfc((x/2*sqrt(D*t))+2*sqrt(D*t))))

% Optimsation using fmincon --- non linear constrained optimisation
```

```
% algorithm. The function beckyFuncOptimise has the objective function to

% reduce the mean squared error between a model function and the

% experimental results.

% Parameters for optimisation

                    %% How to run the program %%

% Copy and paste the following into the Matlab command line: BeckyOpt

%%%%%%%%%%%%%%%%%%%%%%%%%%%%%%%%%%%%%%%%%%%%%%%%%%%%%%%%%%%%%%%%%%%

% clears the matlab environment,variables and command line

clear

close all

clc

% Set parameters

t   = 3600000;

Cb  = 20.1;

% If you need to test other values change the columns in the excel file

% 'Import1.xlsx'

[ExpResfile]  = xlsread('Import1.xlsx');

x = ExpResfile(:,1);
```

```
CxExp = ExpResfile(:,2);

% Inital Parameter guesses

D = 7.16e-16;

h = 12000;

% Vector created to feed into the parameter optimisation algorithm.

z = [D h];

% Constraints for the optimisation:

zUp = [inf inf];

zLo = [0 0];

% Optimisation algorithm

% options = optimset('Algorithm','sqp');

zOpt = fminsearch(@(z) beckyFuncOptimise(Cb,x,t,z,CxExp),z);

% zOpt should have the optimised values. Now we can run the simulation for

% your model to generate your results.

MSE = beckyFuncOptimise(Cb,x,t,zOpt,CxExp);

CxSim = beckyFunc(Cb,x,t,zOpt);

figure('Name','Concentration Plot')

h = plot(x,CxSim,'--',x,CxExp,'xr');
```

```
legend(h,'Model Predictions','Experimental Results','Location','SouthEast')

title('Cr Concentration Variation with Depth')

xlabel('Depth \m')

ylabel('Cr Concentration (At.%)')

grid off

% Here is the mean squred error in the results

printf('The mean square error in the simulation is: %f ', MSE)

fprintf('\n')

fprintf('\n')

fprintf('The fitted parameters are D = %e and h = %f.', zOpt(1),zOpt(2))

fprintf('\n')

fprintf('\n')

%% END PROGRAM %%
```

6

D. Table of Diffusion Coefficients

Table 10-1 Table of diffusion coefficients.

	T (K)	D_{gb} (cm^2 s^{-1})	D_b (cm^2 s^{-1})
Fe in austenitic steel	873		2.8×10^{-16} [182]
Cr in austenitic steel	873		1.0×10^{-16} [182]
Fe in Cr_2O_3	1013	5.9×10^{-12} [183]	3.5×10^{-18} [183]
Cr in Cr_2O_3	1013	5.1×10^{-13} [183]	2.9×10^{-18} [183]
O in Cr_2O_3	923		
Fe in Fe_3O_4	923		3.2×10^{-14} [44]
O in Fe_3O_4	923		1.0×10^{-16} [184]
Fe in Fe_2O_3	923		1.6×10^{-19} [185]
O in Fe_2O_3			

References

[1] R. Viswanathan, J. Sarver and J. M. Tanzosh, “Boiler Materials for Ultra-Supercritical Coal Power Plants - Steamside Oxidation,” *Journal of Materials Engineering and Performance,* vol. 15, no. 3, pp. 255-274, 2006.

[2] I. G. Wright and R. B. Dooley, “Morphologies of Oxide Growth and Exfoliation in Superheater and Reheater Tubing of Steam Boilers,” *Materials at High Temperature,* vol. 28, no. 1, pp. 40-57, 2011.

[3] H. Government, “The UK Renewable Energy Strategy,” 2009.

[4] P. McKendry, “Energy Production from Biomass (Part 1): Overview of Biomass,” *Bioresource Technology,* vol. 83, pp. 37-46, 2002.

[5] “http://www.biomassenergycentre.org.uk/portal/page?_pageid=75,20041&_dad=portal&_schema=PORTAL,” Biomass Energy Centre. [Online]. [Accessed 30 May 2014].

[6] P. McKendry, “Energy Production From Biomass (Part 2): Conversion Technologies,” *Bioresource Technology,* vol. 83, pp. 47-54, 2002.

[7] “Computational Thermodynamics Inc.,” Calphad, 2006. [Online]. Available: http://www.calphad.com/iron-carbon.html. [Accessed 24th July 2017].

[8] D. Porter and K. Easterling, “Phase Transformations in Metals and Alloys,” Taylor and Francis Group, 1992.

[9] B. Weiss and R. Stickler, “Phase Instabilities During High Temperature Exposure of 316 Austenitic Stainless Steel,” *Metallurgical Transactions,* vol. 3, pp. 851-866, 1972.

[10] E. Rollason, Metallurgy for Engineers, Edward Arnold (Publishers) Ltd, 1975.

[11] L. Beres, “Proposed Modification to Schaeffler Diagram for Chrome Equivalents and Carbon for More Accurate Prediction of Martensitic Content,” *Welding Research Supplement,* vol. 77, no. 7, pp. 273.s-276.s, 1998.

[12] M. H. Bina, M. Jamali, M. Shamanian and H. Sabet, “Investigation on the Resistance Spot-Welded Austenitic/ Ferritic Stainless Steel,” *International*

Journal of Advanced Manufacturing Technology, vol. 75, pp. 1371-1379, 2014.

[13] G. E. Totten and M. A. H. Howes, Steel Heat Treatment Handbook, New York: Marcel Dekker Inc., 1997.

[14] T. Oshima, Y. Habara and K. Kuroda, “Efforts to Save Nickel in Austenitic Stainless Steels,” *ISIJ International,* vol. 47, no. 3, pp. 359-364, 2007.

[15] R. E. Smallman, Modern Physical Metallurgy, 4th edition, Essex: Butterworth and Co. Ltd., 1985.

[16] M. McGuire, Stainless Steels for Design Engineers, ASM International, 2008.

[17] S. Osgerby, A. Fry and M. Wright, “Oxidation of Alloys in Steam Environments - A Review,” NPL, 2002.

[18] S. M. Industries, “TP347H FG Data Sheet”.

[19] “Nippon Steel and Sumitomo Metal Corporation [JP],” [Online]. Available: https://www.nssmc.com/product/catalog_download/pdf/P008en.pdf. [Accessed 28th May 2018].

[20] T. Dudziak, M. Lukaszewicz, N. Simms and J. R. Nicholls, “Steam Oxidation of TP347H FG, Super 304H and HR3C - Analysis of Significance of Steam Flowrate and Specimen Surface Finish,” *Corrosion Engineering, Science and Technology,* vol. 50, no. 4, pp. 272-282, 2015.

[21] J. C. Rosser, M. I. Bass, C. Cooper, T. Lant, P. D. Brown, B. J. Connolly and H. E. Evans, “Steam Oxidation of Super 304H and Shot-peened Super 304H,” *Materials at High Temperatures,* vol. 29, no. 2, pp. 95-106, 2012.

[22] I. G. Wright and R. B. Dooley, “A Review of the Oxidation Behaviour of Structural Alloys in Steam,” *International Materials Reviews,* vol. 55, pp. 129-167, 2010.

[23] W.-C. Chiang, I.-S. Tseng, P. Moller, L. R. Hilbert, T. Tolker-Nielsen and J.-K. Wu, “Influence of Silver Additions to type 316 Stainless Steels on Bacterial Inhibition, Mechanical Properties and Corrosion Resistance,” *Materials Chemistry and Physics,* vol. 119, pp. 123-130, 2010.

[24] Thermal Properties of Metals, ASM International, 2002.

[25] J. R. Davis, ASM Speciality Handbook Stainless Steels, ASM International,

1994.

[26] J. R. Davis, Metals Handbook Desk Edition, 2nd Edition, ASM International.

[27] J. R. Davis, Alloy Digest Sourcebook: Stainless Steels, ASM International, 2000.

[28] O. S. Kalakhan, “Fatigue Strength of Austenitic and Martensitic-Ferritic Steels for Nuclear Power Plants,” *Materials Science,* vol. 36, no. 5, pp. 707-713, 2000.

[29] M. Kutz, Handbook of Materials Selection, New York: John Wiley and Sons, 2002.

[30] J. Dong, Y. He, G. Song, J. Jung and K. Shin, “Evolution of Carbide Morphology and Composition in Cr-Mo-V Steel After Service Exposure,” *Materials Technology,* vol. 27, no. 1, pp. 70-72, 2012.

[31] V. B. John, Introduction to Engineering Materials, 2nd Edition, Hong Kong: Macmillan, 1983.

[32] Y. F. Yin and R. G. Faulkner, “Creep Damage and Grain Boundary Precipitation in Power Plant Metals,” *Materials Science and Technology,* vol. 21, no. 11, pp. 1239-1246, 2005.

[33] I. Fedorova, A. Kipelova, A. Belyakov and R. Kaibyshev, “Microstructure Evolution in an Advanced 9 pct Cr Martensitic Steel During Creep at 923 K (650 °C),” *Metallurgical and Materials Transactions A,* vol. 44A, pp. S128-S135, 2013.

[34] A. J. Sedriks, Corrosion of Stainless Steels, Canada: John Wiley and Sons, Inc., 1996.

[35] J. O. Anderson, T. Helander, L. Hoglund, P. F. Shi and B. Sundman, “Thermo-Calc and DICTRA, Computational Tools for Materials Science,” *Calphad,* vol. 26, pp. 273-312, 2002.

[36] S. Osgerby and T. Fry, “Simulating Steam Oxidation of High Temperature Plant Under Laboratoty Conditions: Practice and Interpretation of Data,” *Materials Research,* vol. 7, no. 1, pp. 141-145, 2004.

[37] D. J. Young and B. A. Pint, “Chromium Volatilization Rates From Cr2O3 Scales Into Flowing Gases Containing Water Vapor,” *Oxidation of Metals,* vol.

66, no. 3/4, pp. 137-153, 2006.

[38] C. Donik, A. Kocijan, D. Mandrino, I. Paulin, M. Jenko and B. Pihlar, “Initial Oxidation of Duplex Stainless Steel,” *Applied Surface Science,* vol. 255, pp. 7056-7061, 2009.

[39] L. Lazzari, Engineering Tools for Corrosion: Design and Diagnosis, Woodhead publishing , 2017.

[40] H. E. Evans, “Spallation of Oxide From Stainless Steel AGR Nuclear Fuel Cladding: Mechanisms and Consequences,” *Materials Science and Technology,* vol. 4, pp. 415-420, 1988.

[41] D. M. Gorman and A. T. Fry, “The Early Morphological Development of the Near Surface Region of Pickled Grade 91 Tubing Exposed to Steam and its Long Term Implications,” *Metals,* vol. 6, pp. 62-78, 2016.

[42] B. L. Bramfitt and A. O. Benscoter, Metallographer's Guide: Practices and Procedures for Irons and Steels, ASM International, 2002.

[43] M. Schutze, M. Schorr, D. P. Renusch, A. Donchev and J. P. T. Vossen, “The Role of Alloy Composition, Environment and Stresses for the Oxidation Resistance of Modern 9% Cr Steels for Fossil Power Stations,” *Materials Research,* vol. 7, no. 1, pp. 111-123, 2004.

[44] D. J. Young, High Temperature Oxidation and Corrosion of Metals, Oxford: Elsevier Ltd, 2008.

[45] N. Birks and G. M. Meier, Introduction to the High-Temperature Oxidation of Metals, New York: Cambridge University Press,2nd edition, 2006.

[46] M. Hasegawa, Treatise on Process Metallurgy, Elsevier Ltd., 2014.

[47] P. Kofstad, High Temperature Corrosion, London: Elsevier, 1988.

[48] G. C. Wood, “The Oxidation of Iron Chromium Alloys and Stainless Steels at High Temperatures,” *Corrosion Science,* vol. 2, pp. 173-196, 1961.

[49] G. C. Wood, T. Hodgkiess and D. P. Whittle, “A Comparison of the Scaling Behaviour of Pure Iron-Chromium and Nickel-Chromium Alloys in Oxygen,” *Corrosion Science,* vol. 6, no. 3-4, pp. 129-147, 1966.

[50] G. C. Allen, J. M. Dyke, S. J. Harris and A. Morris, “A Surface Study of the

Oxidation of Type 304L Stainless Steel at 600 K in Air," *Oxidation of Metals,* vol. 29, no. 5/6, pp. 391-408, 1988.

[51] M. Arshed, M. Siddique, M. Anwar-ul-Islam, N. Hussain, K. A. Shahid and N. M. Butt, "Study of Oxidation of Alloy 1.4306S (SS-304L) in Air and Steam at 1200 °C Using the Mossbauer Technique," *Journal of Radioanalytical and Nuclear Chemistry,* vol. 224, no. 1-2, pp. 3-6, 1997.

[52] H. Asteman, J. E. Svensson, L.-G. Johansson and M. Norell, "Influence of Water Vapor and Flow Rate on the High-Temperature Oxidation of 304L; Effect of Chromium Oxide Hydroxide Evaporation," *Oxidation of Metals,* vol. 54, no. 1/2, pp. 11-26, 2000.

[53] H. Davies and A. Dinsdale, "Theoretical Study of Steam Grown Oxides as a Function of Tempertature, Pressure, and p(O2)," *Materials at High Temperatures,* vol. 22, no. 1/2, pp. 15-25, 2005.

[54] T. Dudziak, M. Lukaszewicz, N. J. Simms and J. R. Nicholls, "Impact Specimen Geometry on T23 and TP347H FG Steels Behaviour During Steam Oxidation at Harsh Conditions," *Corrosion Engineering, Science and Technology,* vol. 52, no. 1, pp. 46-53, 2017.

[55] T. Ericsson, "A Study of the Cr-depleted Surface Layers Formed on Four Cr-Ni Steels During Oxidation in Steam at 600 °C and 800 °C," *Oxidation of Metals,* vol. 2, no. 4, pp. 401-417, 1970.

[56] A. T. Fry, S. Osgerby and M. Wright, "Oxidation of Alloys in Steam Environments - A Review," *NPL Report MATC(A) 90,* 2002.

[57] D. Laverde, T. Gomexz-Acebo and F. Castro, "Continuous and Cyclic Oxidation of T91 Ferritic Steel Under Steam," *Corrosion Science,* vol. 46, pp. 613-631, 2004.

[58] N. Greenwood and A. Earnshaw, Chemistry of the Elements, Oxford: Pergamon Press, 1984.

[59] H. E. Evans, D. A. Hilton, R. A. Holm and S. J. Webster, "The Development of Localised Pits During Stainless Steel Oxidation," *Oxidation of Metals,* vol. 14, no. 3, pp. 235-247, 1980.

[60] M. Halvarsson, J. E. Tang, H. Asteman, J.-E. Svensson and L.-G. Johansson, "Microstructural Investigation of the Breakdown of the Protective Oxide Scale on a 304 Steel in the Presence of Oxygen and Water Vapour at 600 °C,"

Corrosion Science, vol. 48, pp. 2014-2035, 2006.

[61] R. C. Lobb and H. E. Evans, “An Evaluation of the Effect of Surface Chromium Concentration on the Oxidation of a Stainless Steel,” *Corrosion Science,* vol. 23, no. 1, pp. 55-73, 1983.

[62] M. Catti, G. Sandrone, G. Valerio and R. Dovesi, “Electronic, Magnetic and Crystal Strcuture of Cr2O3 by Theoretical Methods,” *Journal of Physics and Chemistry of Solids,* vol. 57, no. 11, pp. 1735-1741, 1996.

[63] J. Staun Olsen, C. S. G. Cousins, L. Gerward, H. Jhans and B. J. Sheldon, “A Study of the Crystal Structure of Fe2O3 in the Pressure Range up to 65 GPa Using Synchrotron Radiation,” *Physica Scripta,* vol. 43, pp. 327-330, 1331.

[64] R. M. Cornell and U. Schwermann, The Iron Oxides: Structure, Properties, Reactions, Occurence, and Uses, New York: Weinheim, 1996.

[65] R. K. Singh Raman, J. B. Gnanamoorthy and S. K. Roy, “Synergistic Influence of Alloy Grain Size and Si Content on the Oxidation Behavior of 9Cr-1Mo Steel,” *Oxidation of Metals,* vol. 42, no. 5/6, pp. 335-355, 1994.

[66] A. S. Khanna, P. Rodriquez and J. B. Gnanamoorthy, “Oxidation Kinetics, Breakaway Oxidation, and Inersion Phenomenon in 9Cr-1Mo Steels,” *Oxidation of Metals,* vol. 26, no. 3/4, pp. 171-200, 1986.

[67] A. N. Hansson, K. Pantleon, F. B. Grumsen and M. A. Somers, “Microstructure Evolution During Steam Oxidation of a Nb Stabilised Austenitic Stainless Steel,” *Oxidation of Metals,* vol. 73, pp. 289-309, 2010.

[68] W. Zielinski and K. J. Kurzydlowski, “TEM Studies of the Oxide Scales Formed on Type 316 Stainless Steel During Annealing at 600 °C in a Vacuum and Air,” *Scripta Materialia,* vol. 43, pp. 33-37, 2000.

[69] S. Swaminathan, N. G. Krishna and D. I. Kim, “Characteristics of Oxide Scale Formed on Cu-bearing Austenitic Stainless Steel During Early Stages of High Temperature Oxidation,” *Applied Surface Science,* vol. 353, pp. 29-39, 2015.

[70] N. Karimi, F. Riffard, F. Rabaste, S. Perrier, R. Cueff, C. Issartel and H. Buscail, “Characterisation of the Oxides Formed at 1000 °C on the AISI 304 Stainless Steel by X-ray Diffraction and Infrared Spectroscopy,” *Applied Surface Science,* vol. 254, pp. 2292-2299, 2008.

[71] V. B. Trindade, U. Krupp, P. E.-G. Wagenhuber and H.-J. Christ, “Oxidation Mechanisms of Cr-containing Steels and Ni-base Alloys at High Temperatures - Part 1: The Different Role of Alloy Grain Boundaries,” *Materials and Corrosion,* vol. 56, no. 11, pp. 785-790, 2005.

[72] G. R. Holcomb, “Steam Oxidation and Chromia Evaporation in Ultrasupercritical Steam Boilers and Turbines,” *Journal of the Electrochemical Society,* vol. 156, no. 9, pp. C292-C297, 2009.

[73] N. K. Othman, J. Zhang and D. J. Young, “Water Vapour Effects on Fe-Cr Alloy Oxidation,” *Oxidation of Metals,* vol. 73, no. 1-2, pp. 337-352, 2010 .

[74] M. J. Monteiro, S. R. J. Saunders and F. C. Rizzo, “The Effect of Water Vapour on the Oxidation of High Speed Steel, Kinetics and Scale Adhesion,” *Oxidation of Metals,* vol. 75, no. 1-2, pp. 57-76, 2011.

[75] E. Essuman, G. H. Meier, J. Zurek, M. Hansel and W. J. Quadakkers, “The Effect of Water Vapour on Selective Oxidation of Fe-Cr Alloys,” *Oxidation of Metals,* vol. 69, pp. 143-162, 2008.

[76] C. T. Fujii and R. A. Meussner, “The Mechanism of the High Temperature Oxidation of Iron-Chromium Alloys in Water Vapor,” *Journal of the Electrochemical Society,* vol. 111, no. 11, pp. 1215-1221, 1964.

[77] H. Asteman, J. E. Svensson and L.-G. Johansson, “Oxidation of 310 Steel in H2O/ O2 mixtures at 600 C: The Effect of Water-Vapor-Enhanced Chromium Evaporation,” *Corrosion Science,* vol. 44, pp. 2635-2649, 2002.

[78] P. Huczowski, W. Lehnert, H.-H. Angermann, A. Chyrkin, R. Pillai, D. Gruner, E. Hejrani and W. J. Quadakkers, “Effect of Gas Flow Rate on Oxidation Behaviour of Alloy 625 in Wet Air in the Temperature Range 900-1000 °C,” *Materials and Corrosion,* vol. 68, no. 2, pp. 159-170, 2017.

[79] J. Ehlers, D. J. Young, E. J. Smaardijk, A. K. Tyagi, H. J. Penkalla, L. Singheiser and W. J. Quadakkers, “Enhanced Oxidation of the 9% Cr Steel P91 in Water Vapour Containing Environments,” *Corrosion Science,* vol. 48, pp. 3428-3454, 2006.

[80] G. Bamba, Y. Wouters, A. Galerie, G. Borchardt, S. Shimada, O. Heintz and S. Chevalier, “Inverse Growth Transport in Thermal Chromia Scales on Fe-15Cr Steels in Oxygen and in Water Vapour and its Effect on Scale Adhesion,” *Scripta Materiala,* vol. 57, no. 8, pp. 671-674, 2007.

[81] H. Asteman, J.-E. Svensson, L.-G. Johansson and M. Norell, “Indication of Chromium Oxide Hydroxide Evaporation During Oxidation of 304L at 873 K in the Presence of 10% Water Vapor,” *Oxidation of Metals,* vol. 52, no. 1/2, pp. 95-111, 1999.

[82] S. R. Saunders, M. Monteiro and F. Rizzo, “The Oxidation Behaviour of Metals and Alloys at High Temperatures in Atmospheres Containing Water Vapour: A Review,” *Progress in Materials Science,* vol. 53, pp. 775-837, 2008.

[83] L. Nieto Hierro, V. Rohr, P. J. Ennis, M. Schutze and W. J. Quadakkers, “Steam Oxidation and its Potential Effects on Creep Strength of Power Station Materials,” *Materials and Corrosion,* vol. 56, no. 12, pp. 890-896, 2005.

[84] Z. Liang, P. M. Singh, Q. Zhao and Y. Wang, “High Temperature Oxidation of Newly Developed Alloy 282 in the Flowing-Air and Steam Condition at 900-1100 °C,” *Oxidation of Metals,* vol. 84, pp. 291-305, 2015.

[85] P. J. Ennis and W. J. Quadakkers, “Mechanism of Steam Oxidation in High Strength Martensitic Steels,” *International Journal of Pressure Vessels and Piping,* vol. 84, pp. 75-81, 2007.

[86] J. Yan, Y. Gao, Y. Gu, F. Sun, Z. Yang, J. Lu, H. Yin and Y. Li, “Role of Grain Boundaries on the Cyclic Steam Oxidation Behaviour of 18-8 Austenitic Stainless Steel,” *Oxidation of Metals,* vol. 85, pp. 409-424, 2016.

[87] H. Steiner, “Stress Effects in Cylindrical Tubes of Austenitic and Ferritic/ Martensitic Steels with Oxide Scales,” 2002.

[88] P. Y. Hou and J. Stringer, “The Effect of Reactive Element Additions on the Selective Oxidation, Growth and Adhesion of Chromia Scales,” *Materials Science and Engineering,* vol. A202, pp. 1-10, 1995.

[89] W. Quadakkers, P. Ennis, J. Zurek and M. Michalik, “Steam Oxidation of Ferritic Steels - Laboratory Test Kinetic Data,” *Materials at High Temperatures,* vol. 22, no. 1/2, pp. 47-60, 2005.

[90] R. B. Dooley, “Program on Technology Innovation: Oxide Growth and Exfoliation on Alloys Exposed to Steam,” EPRI, 2007.

[91] M. Lukaszewicz, N. J. Simms, T. Dudziak and J. R. Nicholls, “Effect of Steam Flow Rate and Sample Orientation on Steam Oxidation of Ferritic and Austenitic Steels at 650 and 700 °C,” *Oxidation of Metals,* vol. 79, no. 5, pp.

473-483, 2013.

[92] J. Zurek, M. Michalik, F. Schmitz, T. -U. Kern, L. Singheiser and W. J. Quadakkers, “The Effect of Water-Vapor Content and Gas Flow Rate on the Oxidation Mechanism of a 10% Cr-Ferritic Steel in Ar-H2O Mictures,” *Oxidation of Metals,* vol. 63, no. 5/6, pp. 401-422, 2005.

[93] H. Asteman, J.-E. Svensson and L.-G. Johansson, “Evidence For Chromium Evaporation Influencing the Oxidation of 304 L: The Effect of Temperature and Flow Rate,” *Oxidation of Metals,* vol. 57, no. 3/4, pp. 193 - 216, 2002.

[94] J. L. Marulanda, S. I. Casteneda and F. J. Perez, “Improvement in Resistance to Steam Oxidation of Aluminide-Coated AISI 304 and AISI 316 Steel Produced by Chemical Vapor Deposition in a Fluidized Bed Reactor,” *Oxidtion of Metals,* vol. 84, pp. 429-445, 2015.

[95] X. Peng, J. Yan, Y. Zhou and F. Wang, “Effect of Grain Refinement on the Resistance of 304 Stainless Steel to Breakaway Oxidation in Wet Air,” *Acta Materialia,* vol. 53, pp. 5079-5088, 2005.

[96] G. J. Yurek, D. Eisen and A. Garrat-Reed, “Oxidation Behavior of a Fine-Grained Rapidly Solidified 18-8 Stainless Steel,” *Metallurgical Transactions A,* vol. 13A, pp. 473-485, 1982.

[97] Z. D. Xiang, S. R. Rose, P. K. Datta and M. Scheeffer, “Steam Oxidation Resistance and Thermal Stabilty of Chromium Aluminide/ Chromium Hybrid Coating on Alloy Steels Formed at Low Temperatures,” *Surface and Coatings Technology,* vol. 203, pp. 1225-1230, 2009.

[98] T. Sundararajan, S. Kuroda, T. Itagaki and F. Abe, “Steam Oxidation Resistance of Ni-Cr Thermal Spray Coatings on 9Cr-1Mo Steel. Part 2: 50Ni-50Cr,” *ISIJ International,* vol. 43, no. 1, pp. 104-111, 2003.

[99] T. Sundararajan, S. Kuroda, K. Nishida, T. Itagaki and F. Abe, “Behaviour of Mn and Si in the Spray Powders During Steam Oxidation of Ni-Cr Thermal Spray Coatings,” *ISIJ International,* vol. 44, no. 1, pp. 139-144, 2004.

[100] A. Aguero, J. Garcia de Blas, R. Muelas, A. Sanchez and S. Tsipas, “Steam Oxidation Resistant Coatings for Steam Turbine Components: A Feasibility Study,” *Materials Science Forum,* Vols. 369-372, pp. 939-946, 2001.

[101] J. Yuan, W. Wang, S. Zhu and F. Wang, “Comparison Between the Oxidation of Iron in Oxygen and in Steam at 650-750 °C,” *Corrosion Science,* vol. 75, pp.

309-317, 2013.

[102] W. E. Ruther and S. Greenberg, “Corrosion of Steels and Nickel Alloys in Superheated Steam,” *Journal of the Electrochemical Society,* vol. 111, pp. 1116-1121, 1964.

[103] M. Warzee, J. Hennaut, M. Maurice, C. Sonnen, J. Waty and P. Berge, “Effect of Surface Treatment on the Corrosion of Stainless Steels in High-Temperature Water and Steam,” *Journal of the Electrochemical Society,* vol. 112, no. 7, pp. 670-674, 1965.

[104] A. N. Hansson, H. Danielsen, F. B. Grumsen and M. Montgomery, “Microstructural Investigation of the Oxide Formed on TP347H FG During Long-Term Steam Oxidation,” *Materials and Corrosion,* vol. 61, no. 8, pp. 665-675, 2010.

[105] R. B. Dooley and I. G. Wright, “Oxide Growth and Exfoliation,” in *Boiler Tube and HRSG Tube Failures and Inspections*, Baltimore, Maryland, April 19-21, 2010.

[106] L. Tan, X. Ren and T. R. Allen, “Corrosion Behaviour of 9-12% Cr Ferritic-Martensitic Steels in Supercritical Water,” *Corrosion Science,* vol. 52, pp. 1520-1528, 2010.

[107] R. Kumar, V. K. Tewari and S. Prakash, “Cyclic Oxidation Behaviour of 1Cr-0.5Mo (T11) Boiler Tube Steel and Its Weldments in Air at 900 °C,” *Oxidation of Metals,* vol. 86, pp. 89-98, 2016.

[108] V. A. C. Haanappel, Y. P. Jacob and M. F. Stroosnijder, “The Use of Thin Layer Activation in High-Temperature Cyclic Oxidation Studies,” *Corrosion Science,* vol. 44, pp. 1411-1423, 2002.

[109] Z. Du-qing, L. Guang-ming, Z. Guo-qun and G. Yan-Jin, “Cyclic Oxidation Behavior of Fe-9Cr-1Mo Steel in Water Vapor Atmosphere,” *Journal of Central South University of Technology,* vol. 16, pp. 0535-0540, 2009.

[110] J. M. Francis, M. T. Curtis and D. A. Hilton, “The Oxidation and Spalling Behaviour of 20% Cr/25% Ni/ Nb Stabilised Steel Under Thermal Cycling Conditions,” *Journal of Nuclear Materials,* vol. 41, pp. 203-217, 1971.

[111] A. Col, V. Parry and C. Pascal, “Oxidation of a Fe-18Cr-8Ni Austenitic Stainless Steel at 850°C in O2: Microstructure Evolution During Breakaway

Oxidation," *Corrosion Science,* vol. 114, pp. 17-27, 2017.

[112] A. F. Smith and R. Hales, "Chromium Depletion From Stainless Steels During Vacuum Annealing," *Werkstoffe and Korrosion,* pp. 405-409, 1977.

[113] R. C. Lobb and H. E. Evans, "Evaporation of Elements from 20Cr-25Ni-Nb Stainless Steel During Vacuum Annealing," *Metal Science,* vol. 15, no. 1, pp. 14-20, 1981.

[114] J. C. Killeen, A. F. Smith and R. K. Wild, "Chromium Depletion Profiles After Preferential Removal of Chromium From Alloys," *Corrosion Science,* vol. 16, pp. 551-559, 1976.

[115] P. J. Gellings and M. A. De Jongh, "Grain Boundary Oxidation and the Chromium-Depletion Theory of Intercrystalline Corrosion of Austenitic Stainless Steels," *Corrosion Science,* vol. 7, pp. 413-421, 1967.

[116] J. Crank, The Mathematics of Diffusion, Oxford: Clarendon Press, 1975.

[117] E. J. Opila, D. L. Myers, N. S. Jacobson, I. M. B. Nielsen, D. F. Johnson, J. K. Olminsky and M. D. Allendorf, "Theoretical and Experimental Investigation of the Thermochemistry of CrO2(OH)2(g)," *Journal of Physical Chemistry,* vol. 111, pp. 1971-1980, 2007.

[118] H. Asteman, J.-E. Svensson and L.-G. Johansson, "Effect of Water-Vapor-Induced Cr Vaporization on the Oxidation of Austenitic Stainless Steels at 700 and 900 °C," *Journal of the Electrochemical Society,* vol. 151, no. 3, pp. B141-B150, 2004.

[119] D. Caplan and M. Cohen, "The Volatilisation of Chromium Oxide," *Journal of the Electrochemical Society,* vol. 108, no. 5, pp. 438-442, 1961.

[120] S. Jianian, Z. Longjiang and L. Tiefan, "High-Temperature Oxidation of Fe-Cr Alloys in Wet Oxygen," *Oxidation of Metals,* vol. 48, no. 3/4, pp. 347-356, 1997.

[121] J. Yuan, X. Wu, S. Zhu and F. Wang, "Investigation on the Enhanced Oxidation of Ferritic/ Martensitic Steel P92 in Pure Steam," *Materials,* vol. 7, pp. 2772-2783, 2014.

[122] R. Bauer, M. Baccalaro, L. P. H. Jeurgens, M. Pohl and E. J. Mittemeijer, "Oxidation Behaviour of Fe-25Cr-20Ni-2.8Si During Isothermal Oxidation at

1286 K; Life-time Prediction," *Oxidation of Metals,* vol. 69, pp. 265-285, 2008.

[123] J. P. T. Vossen, P. Gawenda, K. Rahts, M. Rohrig, M. Schorr and M. Schutze, "Limits of the Oxidation Resistance of Several Heat-Resistant Steels Under Isothermal and Cyclic Oxidation as well as Under Creep in Air at 650 °C," *Materials at High Temperature,* vol. 14, pp. 387-401, 1997.

[124] T. Norby, "Protonic Defects in Oxides and Their Possible Role in High-Temperature Oxidation," *Journal de Physique IV,* vol. 3, no. C9, pp. 99-106, 1993.

[125] H. E. Evans, "Cracking and Spalling of Protective Oxide Layers," *Materials Science and Engineering,* vol. A120, pp. 139-146, 1989.

[126] P. J. Ennis and W. J. Quadakkers, "Mechanisms of Steam Oxidation in High Strength Martensitic Steels," *International Journal of Pressure Vessels and Piping,* vol. 84, pp. 75-81, 2007.

[127] T. Jonsson, S. Karlsson, H. Hooshyar, M. Sattari, J. Liske, J.-E. Svensson and L.-G. Johansson, "Oxidation After Breakdown of the Chromium-Rich Scale on Stainless Steels at High Temperature: Internal Oxidation," *Oxidation of Metals,* vol. 85, pp. 509-536, 2016.

[128] M. D. Abad, S. Parker, D. Frazer, M. Rebelo de Figueiredo, A. Lupinacci, K. Kikuchi and P. Hosemann, "Evaluation of the Mechanical Properties of Naturally Grown Multilayered Oxides Formed on HCM12A Using Small Scale Mechanical Testing," *Oxidation of Metals,* vol. 84, pp. 211-231, 2015.

[129] J. Zurek, E. Wessel, L. Niewolak, F. Schmitz, T.-U. Kern, L. Singheiser and W. J. Quadakkers, "Anomalous Temperature Dependence of Oxidation Kinetics During Steam Oxidation of Ferritic Steels in the Temperature Range 550-650 °C," *Corrosion Science,* vol. 46, pp. 2301-2317, 2004.

[130] J. Robertson and M. I. Manning, "Limits to Adherence of Oxide Scales," *Materials Science and Technology,* vol. 6, pp. 81-91, 1990.

[131] J.-L. Huang, K.-Y. Zhou, X.-M. Wang, Y.-Y. Tu and J.-Q. Xu, "Acoustic Emission Analysis on Tensile Failure of Steam-Side Oxide Scales Formed on T22 Alloy Superheater Tubes," *Journal of Applied Physics,* vol. 116, pp. 044907-1 - 044907-9, 2014.

[132] P. communication.

[133] M. Schutze, P. F. Tortorelli and I. G. Wright, “Development of a Comprehensive Oxide Scale Failure Diagram,” *Oxidation of Metals,* vol. 73, pp. 389-418, 2010.

[134] J. Smialek, “A Deterministic Interfacial Cyclic Oxidation Spalling Model,” *Acta Materialia,* vol. 51, pp. 469-483, 2003.

[135] M. Takeda, T. Onishi, S. Nakakubo and S. Fujimoto, “Physical Properties of Iron-Oxide Scales on Si-Containing Steels at High Temperature,” *Materials Transactions,* vol. 50, no. 9, pp. 2242-2246, 2009.

[136] J. Armitt, R. Holmes, M. I. Manning, D. B. Meadowcroft and E. Metcalfe, “The Spalling of Steam-Grown Oxide From Superheater and Reheater Tube Steels,” EPRI report FP-686, Palo Alto, 1978.

[137] G. R. Rigby, G. H. B. Lovell and A. T. Green, “Some Properties Associated with the Spinels of Some Ores,” *British Ceramic Society Transactions,* vol. 65, pp. 137-148, 1943.

[138] A. T. Gorton, G. Bitsianes and T. L. Joseph, “Thermal Expansion Coefficients for Iron and its Oxides from X-Ray Diffraction Measurements at Elevated Temperatures,” *Transactions of the Metallurgical Society of AIME,* vol. 233, pp. 1519-1525, 1965.

[139] R. F. Tylecote, “Factors Influencing the Adhernce of Oxides on Metals,” *Journal of the Iron and Steel Institute,* vol. 196, pp. 135-141, 1960.

[140] M. Schutze, Protective Oxide Scales and Their Breakdown, Wiley, 1997.

[141] J. K. Tien and J. M. Davidson, Stress Effects and The Oxidation of Metals, New York: AIME, 1975.

[142] H. E. Evans, “Stress Effects in High Temperature Oxidation of Metals,” *International Materials Reviews,* pp. 1-40, 1995.

[143] H. E. Evans and M. P. Taylor, “Creep Relaxation and the Spallation of Oxide Layers,” *Surface and coatings technology,* Vols. 94-95, pp. 27-33, 1997.

[144] H. E. Evans, G. P. Mitchell, R. C. Lobb and D. R. J. Owen, “A Numerical Analysis of Oxide Spallation,” *Proceedings: Mathematical and Physical Sciences,* vol. 440, pp. 1-22, 1993.

[145] S. Osgerby, “Oxide Scale Damage and Spallation in P92 Martensitic Steel,” *Materials at High Temperatures,* vol. 17, no. 2, pp. 307-310, 2000.

[146] A. G. Evans and J. W. Hutchinson, “On the Mechanics of Delamination and Spalling in Compressed Films,” *International Journal of Solids and Structures,* vol. 20, no. 5, pp. 455-466, 1984.

[147] C. H. Wells, P. S. Follansbee and R. R. Dils, Stress Effects and the Oxidation of Metals, New York: AIME, 1975.

[148] A. Hayashi, N. Hiraide and Y. Inoue, “Spallation Behaviour of Oxide Scale on Stainless Steels,” *Oxidation of Metals,* vol. 85, no. 1-2, pp. 87-101, 2016.

[149] A. Galerie, F. Toscan, M. Dupeux, J. Mougin, G. Lucazeau, C. Valot, A.-M. Huntz and L. Antoni, “Stress and adhesion of chromia rich scales on ferritic stainless steels in relation with spallation,” *Materials Research,* vol. 7, no. 1, pp. 81-88, 2004.

[150] M. Guerain, P. Goudeau, B. Panicaud and J. Grosseau-Poussard, “Local Stress Determination in Chromia-Former Thanks to Micro-Raman Spectroscopy: A way to Investigate Spontaneous Delamination Processes,” *Journal of Applied Physics,* vol. 113, 2013.

[151] J. L. Smialek and J. V. Auping, “COSP for Windows - Strategies for Rapid Analyses of Cyclic Oxidation Behavior,” *Oxidation of Metals,* vol. 57, no. 5/6, pp. 559-581, 2002.

[152] H. Viitala, I. Galfi and P. Taskinen, “Initial oxidation behaviour of niobium stabilised TP347H austenitic stainless steel - effect of grain size and temperature,” *Materials and Corrosion,* vol. 66, no. 9, pp. 851-862, 2015.

[153] R. E. Athey, B. J. Martin and E. Spencer, “Condensate Oxygen Control in a Combined Cycle System Without a Conventional Deaerator - Test Results,” in *Electric Power Research Institute Condensor Technology Conference*, Boston, 1990.

[154] R. Siab, C. Huvier, M. Kemdehoundja, J. Grosseau-Poussard and J. Dinhut, “On the Relation Between Damage Rate and Stress Level Evolution in a-Cr2O3 Thin Films Growing on Ni-33at% Cr,” *Corrosion Science,* vol. 51, pp. 2246-2248, 2009.

[155] H. E. Evans and R. C. Lobb, “Evaporation of Elements from 20Cr-25Ni-Nb

Stainless Steel During Vacuum Annealing," *Metal Science,* pp. 14-20, 1981.

[156] W. R. Jones, D. Jordan, R. Hill Jr and T. Jones, "Critical Melting Points and Reference Data for Vacuum Heat Treating," Solar Atmospheres Inc., 2010.

[157] C. A. Schneider, W. S. Rasband and K. W. Eliceiri, "NIH Image to ImageJ: 25 Years of Image Analysis," *Nature Methods,* vol. 9, pp. 671-675, 2012.

[158] M. D. Abramoff, P. J. Magalhaes and S. J. Ram, "Image Processing with ImageJ," *Biophotonics International,* vol. 11, no. 7, pp. 36-42, 2004.

[159] J. Crank, The Mathematics of Diffusion, Oxford University Press, 1956.

[160] R.-L. Mobbs, S. Osgerby, M. P. Taylor and H. E. Evans, "The Effect of Thermal Cycling on Steam Oxidation Behaviour of TP347H FG," *Materials at High Temperature,* vol. 35, no. 1-3, pp. 291-298, 2018.

[161] H. E. Evans, A. T. Donaldson and T. C. Gilmour, "Mechanisms of Breakaway Oxidation and Application to a Chromia-Forming Steel," *Oxidation of Metals,* vol. 52, no. 5-6, pp. 379-402, 1999.

[162] J. Jianmin, M. Montgomery, O. H. Larsen and S. A. Jensen, "Investigation of Steam Oxidation Behaviour of TP347H FG Part 2: Exposure at 91 bar," *Materials and Corrosion,* vol. 56, no. 8, pp. 542-549, 2005.

[163] H. E. Evans and R. C. Lobb, "Conditions for the Initiation of Oxide-Scale Cracking and Spallation," *Corrosion Science,* vol. 24, no. 3, pp. 209-222, 1984.

[164] D. Chicot, J. Mendoza, A. Zaoui, G. Louis, V. Lepingle, F. Roudet and J. Lesage, "Mechanical Properties of Magnetite (Fe3O4), Hematite (alpha-Fe2O3) and Geothite (alpha-FeO.OH) by Instrumental Indentation and Molecular Dynamics Analysis," *Materials Chemistry and Physics,* vol. 129, pp. 862-870, 2011.

[165] V. Panjkovic, Friction and The Hot Rolling of Steel, New York: CRC Press, 2014.

[166] B. J. Kooi, M. A. J. Somers, R. Jutte and E. J. Mittemeijer, "On the Oxidation of α-Fe and ϵ-Fe2Ni1-z: II. Residual Strains and Blisters in the Oxide Layer.," *Oxidation of Metals,* vol. 48, no. 1/2, pp. 111-128, 1997.

[167] T. Dudziak, K. Jura, A. Polkowska, V. Deodeshmukh, M. Warmuzek, M. Witkowska, W. Ratuszek and K. Chrusciel, "Steam Oxidation Resistance of

Advanced Steels and Ni-Based Alloys at 700 °C for 1000 hours," *Oxidation of Metals.*

[168] C.-Y. Hsu, K.-H. Chang, J.-A. Gong, J. Tiren, Y.-Y. Li and A. Sakoda, "Kirkendall Void Formation and Selective Directional Growth of Urchin-Like ZnO/Zn Microspheres Through Thermal Oxidation in Air," *RSC Advances,* vol. 5, pp. 103884-103894, 2015.

[169] T. Dudziak, M. Lukaszewicz, N. Simms and J. Nicholls, "Analysis of High Temperature Steam Oxidation of Superheater Steels Used in Coal Fired Boilers," *Oxidation of Metals,* vol. 85, no. 1-2, pp. 171-187, 2016.

[170] I. G. Wright, P. F. Tortorelli and M. Schutze, "Oxide Growth and Exfoliation on Alloys Exposed to Steam," EPRI report No. 1013666, 2007.

[171] A. S. Sabau, J. P. Shingledecker and I. G. Wright, "Steam-side Oxide Scale Exfoliation Behaviour in Superheaters and Reheaters: Differences in the Behaviour of Alloys," in *6th International Conference on Advances in Materials and Technology for Fossil Power Plants*, Santa Fe, 2010.

[172] S. Sureau, D. Pequillon and D. Monceau, "Numerical Simulation of Cyclic Oxidation Kinetics with Automatic Fitting of Experimental Data.," *Scripta Materiala,* vol. 56, no. 3, pp. 233-236, 2007.

[173] W. R. Jones, D. Jordan, R. Hull Jr and T. Jones, "Critical Melting Points and Reference Data for Vacuum Heat Treating," Solar Atmospheres, Inc., 2010.

[174] A. Smith and G. B. Gibbs, "Volume and grain-boundary diffusion in 20Cr/25Ni/Nb stainless steel," *Metal Science Journal,* vol. 3, no. 1, pp. 93-94, 1969.

[175] D. West, J. Hulance, R. L. Higginson and G. D. Wilcox, "sigma-phase precipitation in 347H FG stainless steel," *Materials Science and Technology,* vol. 29, no. 7, pp. 835-842, 2013.

[176] R. A. Perkins, R. A. Padgett Jr and N. K. Tunali, "Tracer Diffusion of 59Fe and 51Cr in Fe-17 Wt Pct Cr-12 Wt Pct Ni Austenitic Alloy," *Metallurgical Transactions,* vol. 4, pp. 2535-2540, 1973.

[177] P. J. Alberry and C. W. Haworth, "Interdiffusion of Cr, Mo and W in Iron," *Metal Science,* vol. 8, pp. 407-412, 1974.

[178] A. W. Bowen and G. M. Leak, “Solute Diffusion in Alpha- and Gamma-Iron,” *Metallurgical Transactions,* vol. 1, no. 6, pp. 1695-1700, 1970.

[179] R. C. Lobb and H. E. Evans, “A Determination of the Chromium Concentration for 'Healing' Layer Formation During the Oxidation of Chromium-Depleted 20Cr-25Ni-Nb Stainless Steel,” *Corrosion Science,* vol. 24, no. 5, pp. 385-296, 1984.

[180] E. Essuman, G. H. Meier, J. Zurek, M. Hansel, T. Norby, L. Singheiser and W. J. Quadakkers, “Protective and Non-protective Scale Formation of Ni-Cr Alloys in Water Vapour Containing Hihg- and Low-pO2 gases,” *Corrosion Science,* vol. 50, pp. 1753-1760, 2008.

[181] J. Jianmin, M. Montgomery, O. H. Larsen and S. A. Jensen, “Investigation of Steam Oxidation Behaviour of TP347H FG Part 1: Exposure at 256 bar,” *Materials and Corrosion,* vol. 56, no. 7, pp. 459-467, 2005.

[182] N. Otsuka, Y. Shida and H. Fujikawa, “Internal-External Transition for the Oxidation of Fe-Cr-Ni Austenitic Stainless Steels in Steam,” *Oxidation of Metals,* vol. 32, no. 1/2, pp. 13-45, 1988.

[183] A. C. S. Sabioni, A. M. Huntz, F. Silva and F. Jomard, “Diffusion of Iron in Cr2O3: Polycrystals and Thin Films,” *Materials Science and Engineering,* vol. A392, pp. 254-261, 2005.

[184] Z. D. Sharp, “Determination of Oxygen Diffusion Rates in Magnetite From Natural Isotopic Variations,” *Geology,* vol. 19, pp. 653-656, 1991.

[185] A. Atkinson and R. I. Taylor, “Diffusion of Fe in Fe2O3 Single Crystals,” *Journal of Physics and Chemistry of Solids,* vol. 46, no. 4, pp. 469-475, 1985.

[186] G. E. Totten, Y. Sun, G. M. Webster, L. M. Jarvis and C. E. Bates, “Quenching Basics,” in *Heat Treatments: Proceedings of the 18th conference*, Rosemont, 1998.

[187] J. Yuan, X. Wu, W. Wang, S. Zhu and F. Wang, “The Effect of Surface Finish on the Scaling Behaviour of Stainless Steel in Steam and Supercritical Water,” *Oxidation of Metals,* vol. 79, pp. 541-551, 2013.